The University of Strathclyde
Department of Civil and Environmental Engineering

The impact of high temperatures on suitability of NRVB cement in nuclear waste management

Rebecca Lindsey-Halls



Doctor of Philosophy (PhD)

2026

Declaration of Authenticity and Author's Rights

This thesis is the result of the author's original research. It has been composed by the author and has not been previously submitted for examination which has led to the award of a degree.

The copyright of this thesis belongs to the author under the terms of the United Kingdom Copyright Acts as qualified by University of Strathclyde Regulation 3.50. Due acknowledgement must always be made of the use of any material contained in, or derived from, this thesis.

Signed: 

Date: 5th June 2026

Acknowledgements

I would like to begin by acknowledging and thanking my supervisors, Dr Kate Dobson and Dr Mark Stillings. Their unwavering support, guidance, and encouragement has been essential in finishing this thesis.

I would also like to thank Mara and Tanya for their help and guidance in the laboratory, and for always being there whenever I needed support, whether with experiments or on a personal level. I would also like to thank Derek and Jim for helping me to make cement moulds, and for teaching me how to use various power tools. I would like to thank Dr Paul Edwards for his help with SEM and EMPA, and Dr Claire Wilson for her help with XRD, without their help I would not have the same quality or quantity of data.

I would like to acknowledge NWS who funded this PhD through the Research Support Office, and thank my NWS supervisors for their engagement and advice.

I would like to thank my friends and colleagues for their support during this PhD. The long days in the lab would have felt a lot longer without all of you.

I want to thank my Mum, my Grandparents, and my Great Grandparents for inspiring me and encouraging me to love learning and science as a child, something I have fortunately carried with me throughout my life. They also instilled a deep belief in me that I was capable of achieving anything if I worked hard enough. I have always been incredibly fortunate to have the support and encouragement of my family, including my little brothers Ben and Matthew who have spent many phone calls and evenings listening to me talk about my PhD. I also want to thank my partner, James, who has remained an unending source of support to me throughout, and from whom I could not have asked for any more.

Abstract

This thesis investigates the effect of elevated curing temperatures on Nirex Reference Vault Backfill (NRVB) cement, a candidate backfill material for use within the United Kingdom's Geological Disposal Facility (GDF). NRVB provides a highly alkaline environment, decreases radionuclide solubility, and provides a permeable pathway for gas transport. However, the thermal output of radioactive waste can alter the mineralogical and microstructural properties of the cement, which may impact its long-term performance and safety functions. The long-term performance of NRVB cement cured under the thermal conditions associated with radioactive waste disposal is poorly understood, particularly at curing temperatures above those previously studied.

This thesis characterises mineralogical evolution, pore structure development, and radionuclide sorption behaviour. A multi-technique approach was used. X-ray diffraction (XRD) was used to identify and quantify mineral phases, with method development undertaken to minimise carbonation during sample preparation and analysis. Scanning electron microscopy (SEM) and electron probe microanalysis (EPMA) were used to examine microstructural and chemical changes. X-ray computed tomography (XCT) and helium pycnometry were used to quantify porosity. Radionuclide sorption experiments were performed to assess the influence of temperature-induced mineralogical changes on radionuclide retention.

The results demonstrate a direct relationship between curing temperature, mineralogical evolution, and porosity. Elevated temperatures promoted the formation of strength-reducing mineral phases and resulted in increased porosity. Curing temperature and calcium-to-silica (C:S) ratio controlled the mineralogy. The mineral composition was also shown to influence radionuclide immobilisation mechanisms, with different mineral phases exhibiting different radionuclide interaction pathways and pH buffering capacities.

These findings demonstrate that the long-term performance of NRVB cement depends on both its mineralogical and microstructural evolution, which are controlled by curing temperature and cement composition. The work provides new insights into the behaviour of higher-temperature NRVB cements and contributes novel data on the formation of high-temperature cement minerals and their interactions with radionuclides.

Contents

Symbols ix

Abbreviations xi

List of Figures xiv

List of Tables xx

Chapter 1 Introduction 1

1.1 Introduction to the project 1

1.2 Aims and Objectives of this thesis 4

1.3 The current status of radioactive waste in the UK and the Geological Disposal Facility 7

1.4 The chemistry, composition and properties of NRVB cement 14

1.5 Research gap, and how this thesis will contribute to the GDF Safety Case 27

Chapter 2 Optimisation of sample preparation for XRD analysis including cementitious hydration arrest 30

2.1 Introduction 30

2.1.1 Importance of XRD in cement research 30

2.1.2 The effect of carbonation and hydration arrest on cements 30

2.1.3 Aims and Objectives 33

2.2 Investigation into XRD preparation 34

2.2.1 Mineralogical phase analysis using X-ray Diffraction (XRD) 34

2.2.2 Methodology for investigating the preparation technique that produces the optimum sample for XRD analysis 36

2.2.3 Testing the effectiveness of different methods of hydration arrest and XRD preparation in preventing carbonation 38

2.3 Optimal preparation for XRD analysis 40

2.3.1 Effect of Isopropanol during micronizing 40

2.3.2 Effect of micronizing versus ball milling 42

2.3.3 Effect of micronizing versus hand grinding and sieving through 63μm mesh 43

2.3.4 Testing the effectiveness of hydration arrest and XRD preparation techniques on preventing carbonation 44

2.4 Discussion 47

2.4.1 Amounts of calcite vs. XRD preparation method 47

2.4.2 The impact of pH on hydration 52

2.5 Conclusions 53

Chapter 3 Investigation into the effect of increasing the curing temperature and altering the C:S ratio of NRVB cement on the mineralogy 54

3.1 Introduction 54

3.1.1 Cement chemistry 54

3.1.2 Curing temperature 55

3.1.3 Aims and Objectives 56
3.2 Raw Materials Information 57
3.2.1 Major Oxide Composition X-ray fluorescence (XRF) 57
3.3 Experimental work 59
3.3.1 Introduction 59
3.3.2 Method 59
3.4 Part 1: Curing of NRVB at 80, 175 and 200°C 62
3.4.1 XRD analysis 63
3.4.2 XRD results from 5 and 10 day curing at 80, 175 and 200°C 65
3.5 Part 2: Phase diagram investigation 67
3.5.1 Synthesis of NRVB C:S ratios with calcium carbonate 69
3.5.2 Synthesis of NRVB C:S ratios without calcium carbonate 75
3.6 Conclusions 88
3.6.1 Key conclusions 88
3.6.2 Further work 88
Chapter 4 The effect of increased curing temperature and different C:S ratio on porosity. 90
4.1 Introduction 90
4.1.1 Importance of porosity of cements 90
4.1.2 Techniques to measure porosity of cements 92
4.1.3 Vacuum saturation 94
4.1.4 Mercury Intrusion Porosimetry (MIP) 94
4.1.5 Helium Pycnometry 94
4.1.6 Aims and Objectives of this chapter 95
4.2 A combined multi-method approach 96
4.2.1 Sample preparation 96
4.2.2 XCT 98
4.2.3 SEM and EMPA 100
4.2.4 Helium Pycnometry 100
4.3 Results 104
4.3.1 Porosity 104
4.3.2 Helium Pycnometry 107
4.3.3 SEM and EMPA of cements 110
4.4 Discussion and comparison 115
4.4.1 The effect of curing temperature and $CaO:SiO_2$ ratio on porosity 115
4.4.2 The effect of removing $CaCO_3$, $CaO:SiO_2$ ratio, and temperature on cement porosity 117
4.4.3 Distribution of minerals 123

4.4.4 Macro porosity 123
4.5 Conclusions 129
4.5.1 Further work 130
Chapter 5 Development of methods to synthesise single high temperature mineral phases 132
5.1 Introduction 132
5.1.1 Background 132
5.1.2 Aims and Objectives 133
5.1.3 Xonotlite 134
5.1.4 Calcite 135
5.1.5 Reinhardbraunsite 137
5.1.6 Jaffeite 138
5.1.7 α-C_2SH 139
5.1.8 γ-C_2SH 140
5.2 Method 141
5.3 Results 143
5.3.1 Xonotlite 143
5.3.2 Calcite 145
5.3.3 Reinhardbraunsite 145
5.3.4 Jaffeite 147
5.3.5 α-C_2SH 149
5.3.6 γ-C_2SH 153
5.3.7 TOPAS analysis of chosen mineral formulations 156
5.4 Conclusions and chosen method for investigating radionuclide retention capacity 157
5.4.1 Summary 157
5.4.2 Method to synthesise pure phase mineral 157
Chapter 6 The effect of mineralogical composition of NRVB cement on the mobility of radionuclides 159
6.1 Introduction 159
6.1.1 Cementitious minerals that formed during higher temperature curing in Chapter 3 160
6.1.2 Radionuclides selection 162
6.2 Mineral tests to study the effect on radionuclide concentration in solution 165
6.2.1 Introduction 165
6.2.2 Phase 1 166
6.2.3 Phase 2: Tests to determine the capability of the minerals to reduce the quantity of cerium in solution 190
6.2.4 Phase 3 Sorption rate tests 194

6.3 Radionuclide sorption tests XRD 209
6.3.1 Introduction 209
6.3.2 Calcite 210
6.3.3 Xonotlite 212
6.3.4 Reinhardbraunsite 214
6.3.5 Jaffeite 216
6.3.6 α-C_2SH 218
6.4 Discussion and impact 220
6.4.1 Phase 1 results summary and conclusions 220
6.4.2 Phase 2 results summary and conclusions 223
6.4.3 Phase 3 results summary and conclusions 225
6.4.4 Conclusions 225
Chapter 7 Discussion of the implications for NRVB Cement in Nuclear Waste Disposal and repository design 228
7.1 Introduction 228
7.1.1 The aims and objectives of this project 229
7.2 How Mineralogy affects the Porosity and Radionuclide Retention 229
7.3 The impact on the current GDF design 240
7.4 Recommendations for Future Work 243
7.4.1 Proposed next experiment following Chapter 6: How the spatial arrangement of the minerals within the cement affects the properties in regards to reducing the concentration of radionuclide in solution and buffering the pH. 243
7.4.2 Proposed next experiment: How does NRVB cement perform in high salinity solution; what mineralogical changes occur when NRVB cement is exposed to high salinity solution, how is the porosity affected? 245
7.4.3 Proposed next experiment: How is the mineralogy affected when the cement is cured against a temperature gradient? 247
7.5 Overall Conclusions of the Discussion 249
References 250
Appendices 271
Appendix 1 XRD pattern of cements cured at 80°C with calcite in initial mix 271
Appendix 2 XRD pattern of cements cured at 25°C with calcite in initial mix 272
Appendix 3 NRVB cement cured at 250°C 273
Appendix 4 NRVB cement cured at 200°C 273
Appendix 5 NRVB cement cured at 150°C 274
Appendix 6 NRVB cement cured at 80°C 275
Appendix 7 NRVB cement cured at 25°C 276
Appendix 8 C:S 4 cement cured at 250°C 277
Appendix 9 C:S 4 cement cured at 200°C 278

Appendix 10 C:S 4 cement cured at 150°C 279
Appendix 11 C:S 4 cement cured at 80°C..... 280
Appendix 12 C:S 4 cement cured at 25°C 281

Symbols

Category	Symbol	Definition
Units & Physical Quantities	°C	Degrees Celsius
	°	Angle (degrees)
	2θ	X-ray diffraction scattering angle
	θ	Incident/diffraction angle
	μm	Micrometre
	nm	Nanometre
	mL	Millilitre
	g	Gram
	cm^3	Cubic centimetre
	mm^3	Cubic millimetre
	$mol\ dm^{-3}$	Molar concentration
	ppm	Parts per million
	wt%	Weight percent
	rpm	Revolutions per minute
	kV	X-ray tube voltage
	mA	X-ray tube current
	s	Seconds
	min	Minutes
	h	Hours
	d	Days
XRD / Crystallography	2θ	Diffraction angle
	d	Interplanar spacing
	λ	Wavelength of X-rays
	I	Peak intensity
	hkl	Miller indices
	n	Order of reflection
	Rwp	Weighted residual factor

	χ^2	Goodness of fit statistic
Porosity & Imaging	φ	Porosity
	ρ	Density
	ρ_s	Skeletal density
	ρ_b	Bulk density
	V_p	Pore volume
	V_t	Total volume
	$I(x,y)$	Greyscale voxel intensity
Miscellaneous	λ_{min}	Minimum wavelength
	λ_{max}	Maximum wavelength
	R^2	Coefficient of determination
	σ	Standard deviation
	Σ	Summation operator

Abbreviations

Abbreviation	
A	Alumina (Al_2O_3) – cement oxide shorthand
AFm	Mono-sulfoaluminate phase
AFt	Tri-sulfoaluminate (ettringite-type) phase
a-C_2SH	Alpha-dicalcium silicate hydrate
B	Belite (β-C_2S)
BDL	Below Detection Limit
BEC	Backscattered Electron Contrast
C	Calcium oxide (CaO) in cement shorthand / Calcite in XRD notation
C_3A	Tricalcium aluminate
C_3S	Tricalcium silicate (alite)
C_2S	Dicalcium silicate (belite/larnite)
C–S–H	Calcium–silicate–hydrate gel
C-A-S-H	Calcium–aluminium–silicate–hydrate
$CaCO_3$	Calcium carbonate (calcite)
CEM I	Ordinary Portland Cement 52.5N
Ce	Cerium
CIF	Crystallographic Information File
COD	Crystallography Open Database
CO_2	Carbon dioxide
Cs	Caesium
C:S ratio	Calcium-to-silicon ratio ($CaO:SiO_2$)
DSRL	Dounreay Site Restoration Ltd
DSC	Differential Scanning Calorimetry
DESNZ	Department for Energy Security and Net Zero
EDX / EDS	Energy-Dispersive X-ray Spectroscopy
EMPA / EPMA	Electron Microprobe Analysis
EU	European Union
F	Iron oxide (Fe_2O_3) in cement shorthand
G	Gypsum ($CaSO_4 \cdot 2H_2O$) in XRD notation
GDF	Geological Disposal Facility
H	Water (H_2O) in cement shorthand

HAW	Higher-Activity Waste
HLW	High-Level Waste
HG	Hand-ground (sample preparation)
HNO_3	Nitric acid
ICP-MS	Inductively Coupled Plasma Mass Spectrometry
ICP-OES	Inductively Coupled Plasma Optical Emission Spectroscopy
ILW	Intermediate-Level Waste
IPA	Isopropanol
J	Jaffeite (XRD notation)
K	Potassium oxide (K_2O) in cement shorthand / Katoite (context-dependent)
L	Lithium oxide (Li_2O)
LFF	Long Fine-Focus X-ray tube
LLW	Low-Level Waste
LoD	Limit of Detection
LoQ	Limit of Quantification
M	Micronised (sample preparation)
MIP	Mercury Intrusion Porosimetry
MOD	Ministry of Defence
MQL	Minimum Quantification Level
N	Sodium oxide (Na_2O) in cement shorthand
NAGRA	Swiss National Cooperative for Radioactive Waste Disposal
NDA	Nuclear Decommissioning Authority
NRVB	Nirex Reference Vault Backfill
O	Oxygen (element)
OPC	Ordinary Portland Cement
P	Phosphate (P_2O_5) in cement shorthand / Portlandite in XRD notation
PEEK	Polyether Ether Ketone
ppm	Parts per million
PWR	Pressurised Water Reactor
Q	Quartz (SiO_2) in XRD notation
R	Reinhardbraunsite (XRD notation)
RT	Room Temperature
S	Silica (SiO_2) in cement shorthand / Sulphate (SO_3) in some contexts

SCM	Supplementary Cementitious Materials
SEM	Scanning Electron Microscopy
SMR	Small Modular Reactor
Sr	Strontium
T	Titanium oxide (TiO_2)
U	Uranium
UK	United Kingdom
VLLW	Very-Low-Level Waste
X	Xonotlite (XRD notation)
XCT	X-ray Computed Tomography
XRD	X-ray Diffraction
γ-C_2SH	Gamma-dicalcium silicate hydrate

List of Figures

Figure 1: A simple diagram of the GDF showing how the waste packages will be emplaced and then NRVB cement will be used to backfill the vault. 2
Figure 2: Sites in the UK that are large producers of nuclear waste and waste disposal facilities [1] 7
Figure 3: The different categories of UK nuclear waste and the difference in how they contribute to the total volume and radioactivity of waste[6]. The blue line shows the volume and the red line shows the radioactivity. 10
Figure 4: The disposal routes that will be used for the radioactive wastes identified in the NDA and BEIS 2019 Inventory report shown as a percentage of the total volume[3]. 12
Figure 5: The design for ILW and HLW waste emplacement within the GDF[26]. 13
Figure 6: Diagram to show the four components of NRVB and their primary purpose. 15
Figure 7: The components of NRVB that maintain its high pH over time[3] 17
Figure 8: The stages of hydration of Portland cement [39]. 20
Figure 9: How the shape of hydrogarnet crystals change with the % of alumina and the curing temperature [41]. 23
Figure 10: The phases found by Kyritsis and Meller et al. when synthesising various cement systems between 200 and 350°C. Codes: p = portlandite, j = jaffeite, r = reinhardbraunsite, c = calcite, a = α-C_2SH, t = tobermorite, k = katoite, x = xonotlite, f = foshagite, c = corundum, b = bicchulite, d = calcium aluminium oxide hydrate[39]. 24
Figure 11: A Phase diagram showing different phases within C-A-S-H cement[41] 28
Figure 12: A diagram showing the effect of pH on the amount of CO_2 dissolved into water[64]. 31
Figure 13: The XRD patterns of the same sample where the black line was centrifuged immediately after it was micronized, and red where it soaked overnight. 41
Figure 14: The XRD patterns of a sample that was ground in the micronizing mill (pink) and ground in the ball mill (black) with the only section that was different zoomed in. Zoomed in sections of the pattern show a calcite peak (top) and a portlandite peak (bottom). 42
Figure 15: The XRD patterns collected on the same sample where it was hand ground and sieved (black) then half was removed and micronized (red) with some sections that showed a large difference in the symmetry zoomed in on. 44
Figure 16: A graph showing the difference in quantities of minerals in the same cement sample that was prepared for XRD analysis two different ways. The difference in these two methods is the hydration arrest method, where the Meller sample was dried at room temperature in a nitrogen oven whereas the FDBM0 sample was freeze dried. 48
Figure 17: A graph showing the difference in quantities of minerals in the same cement sample that was prepared for XRD analysis two different ways. The difference in these two methods is the grinding method, the FDHGM0 sample was hand ground with a mortar and pestle whereas the FDBMM0 sample was ball milled. 49
Figure 18: A graph showing the difference in quantities of minerals in the same cement sample that was prepared for XRD analysis two different ways. The difference in these two methods is that the FDBM0 sample was not micronized, so this sample was never exposed to isopropanol. 50
Figure 19: A graph showing the difference in quantities of minerals in the same cement sample that was prepared for XRD analysis two different ways. These two methods are the most different as they were dried and prepared for XRD differently. 51
Figure 20: This graph shows the amount of calcite present in each sample when left out for 0, 2, and 24 hours for all four methods. 51
Figure 21: Diagram to show the four components of NRVB and their primary purpose. 54
Figure 22: The XRD diffractograms from the XRD analysis done on the NRVB cements cured for either 5 or 10 days at either 80, 175, or 250°C. 66
Figure 23: The phase diagram created by Meller et al.[56] showing what mineral phases form within cement when cured at 50 to 1000°C and at a CaO/SiO_2 ratio of 0 to 3.5. 68

Figure 24: The XRD Diffractograms for cements cured at 200°C with $CaO:SiO_2$ ratios between 4 and 7.27 (NRVB). 71
Figure 25: Plot showing the portlandite peak measured with XRD, and how it decreases as more SiO_2 is added to the formula. These samples were cured at 200°C. 73
Figure 26: Plot showing the Calcite peak measured with XRD and how it remains at a constant height regardless of the addition of SiO_2. These samples were cured at 200°C. 73
Figure 27: Bar chart showing the composition of each cement sample. Where red = calcite, blue = portlandite, gypsum = light pink, larnite = grey, quartz = orange, hydrogarnet = magenta, tetra calcium aluminoferrite = navy, α-C_2SH = light green, γ-C_2SH = emerald green, jaffeite = turquoise, reinhardbraunsite = teal, katoite = purple, and xonotlite = yellow. 81
Figure 28: Graph showing how the composition of strength reducing minerals changes as the curing temperature is increased. Black = C:S 4, red = C:S 5, blue = C:S 6, green = C:S 7, and purple = NRVB. 82
Figure 29: Graph showing how the quantity of portlandite within the cement changes as the curing temperature is increased. Black = C:S 4, red = C:S 5, blue = C:S 6, green = C:S 7, and purple = NRVB. 83
Figure 30: A phase diagram showing the results found in this chapter. 85
Figure 31: Heatmap to show the amount of portlandite remaining in each sample after curing... 87
Figure 32: Image taken from literature [139] to show the relationship between compressive strength and capillary porosity in cements. 91
Figure 33: A slice of the XCT scan of a NRVB cement core cured at 80°C. This shows a 2D slice through the 3D data set (main) and a zoom in of a sub region (inset) to show the texture of the image data. The sample is NRVB cement cured at 80°C. Pores (black), cement phases (from near black to mid grey depending on volume of pore within the voxel) and SiO_2 (pale grey)..... 93
Figure 34: A diagram showing how the samples were prepared for XCT, SEM and EMPA analysis. 96
Figure 35: The workflow followed in Avizo to process the XCT scans collected of the cement cores cured at different temperatures and with different $CaO:SiO_2$ ratios. 99
Figure 36: Diagram showing how the cores were arranged in each resin block to ensure each core could be identified by its position. This arrangement has no symmetry between the three blocks so the samples cannot be mixed up if the labels on the blocks were to come off. 100
Figure 37: The workflow followed in Avizo to process the XCT scans collected of the cement cores cured at different temperatures and with different $CaO:SiO_2$ ratios to get the volume of the pores. 101
Figure 38: A slice of the XCT scan to show the difference in the core during the image processing. The first image is the original slice, the second image shows the pore space filled, and the final slice shows what has been thresholded to count for the total volume of cement core and porosity. 102
Figure 39: The first image on the left is a 3D render from Avizo showing the cement core inside the PEEK cup, the second image shows the PEEK cup after it has been thresholded, and the final image on the right shows the cement core without the PEEK cup..... 103
Figure 40: The porosity of the NRVB cement cured at 80°C, the crack in the sample can be seen at the bottom of the image where it is coloured red. 105
Figure 41: A graph comparing the percentage porosity measured using XCT and Avizo of the NRVB and C:S 4 cements cured at 25, 80, 150, 200 and 250°C. 106
Figure 42: Image showing a 3D render of the pores of the samples scanned with XCT, the pores are coloured due to size where blue = smaller pores and red = larger. A greyscale 2D slide of each sample is next to the 3D render to show the pores in greyscale before processing..... 107
Figure 43: Graph showing the effect of temperature on porosity for cements with different C:S ratios measured with helium pycnometry. 109
Figure 44: A compositional scan and backscattered electron scan of the NRVB cements cured at 25, 80, 150, 200 and 250°C. The purple boxes visible in the backscattered electron scan at 200 and 250°C are areas of the image that were scanned for elemental composition. 111

Figure 45: Compositional scan and backscattered electron scan of the C:S 4 cements cured at 25, 80, 150, 200 and 250°C. The purple boxes visible in the backscattered electron scan at 200 and 250°C are areas of the image that were scanned for elemental composition. 112
Figure 46: SEM images of the NRVB and C:S 4 cements cured at 25, 80, 150, 200 and 250°C. 114
Figure 47: A SEM image of NRVB cement cured at 250°C showing a mineral within the cement that appears to have shrunk during curing. This is shown by the 'shell' visible around the large light grey mineral. 115
Figure 48: Graph showing the effect of temperature on porosity for cements with different C:S ratios measured with helium pycnometry. 116
Figure 49: Graph showing the effect of temperature on porosity for cements with different C:S ratios for cements mixed with calcium carbonate..... 118
Figure 50: A graph showing the porosity of cements cured at room temperature and 80°C that have the same C:S ratio, the cements with calcite in the starting mix are labelled with 'calcite'..... 120
Figure 51: A graph comparing the percentage porosity measured using XCT and Avizo of the NRVB and C:S 4 cements cured at 25, 80, 150, 200 and 250°C..... 124
Figure 52: A comparison of the pores that were able to be identified using the thresholding function in Avizo in NRVB at 150 (left) and 250°C (right)..... 125
Figure 53: A comparison of the pores that were able to be identified using the thresholding function in Avizo in C:S 4 at 150 (left) and 250°C (right)..... 125
Figure 54: A graph showing a comparison of measuring the porosity of the NRVB cement cores cured at 25, 80, 150, 200 and 250°C with XCT and helium pycnometry..... 126
Figure 55: A comparison of the porosity measured with XCT and helium pycnometry for the C:S 4 cement cores..... 127
Figure 56: The diffractograms of the two mixtures that were most likely to form xonotlite. The corresponding xonotlite peaks are labelled x. 144
Figure 57: The diffractograms of the two mixtures that were most likely to form reinhardbraunsite. The corresponding reinhardbraunsite peaks are labelled R. 146
Figure 58: The diffractograms of the two mixtures that were most likely to form jaffeite. The corresponding jaffeite peaks are labelled J. 148
Figure 59: The diffractograms of the two mixtures that were most likely to form α-C_2SH. The corresponding α-C_2SH peaks are labelled a and katoite peaks are labelled k. The green line represents the aCSHCEM sample and the orange line represents the aC2SHCaOH sample. . 150
Figure 60: A comparison of the XRD patterns measured from the samples aC2SH CaOH and J CaOH 5d 152
Figure 61: The diffractograms of the two mixtures that were most likely to form γ-C2SH. The corresponding γ-C2SH peaks are labelled y. 154
Figure 62: The crucibles after curing at 1100°C. The crucible on the left used CEM I, the crucible on the right contained portlandite. 154
Figure 63: The Y C2S CaOH AFRC after curing at 1350°C for 3 hours. The crucible shattered and had melted onto the base of the oven. The sample was collected and analysed. The base of the oven was concrete and the sample was contaminated with sand from it. 156
Figure 64: How radioiodine is produced in the nuclear fuels cycle[248]. 165
Figure 65: The results from testing how much radionuclide analogue calcite can remove from solution. Iodine is represented by orange, cerium is green, caesium is blue, and strontium is purple. 172
Figure 66: The results from testing how much radionuclide analogue xonotlite can remove from solution. Iodine is represented by orange, cerium is green, caesium is blue, and strontium is purple. 175
Figure 67: The results from testing how much radionuclide analogue reinhardbraunsite can remove from solution. Iodine is represented by orange, cerium is green, caesium is blue, and strontium is purple. 177

Figure 68: The results from testing how much radionuclide analogue α-C_2SH can remove from solution. Iodine is represented by orange, cerium is green, caesium is blue, and strontium is purple. 179
Figure 69: The results from testing how much radionuclide analogue jaffeite can remove from solution. Iodine is represented by orange, cerium is green, caesium is blue, and strontium is purple. 181
Figure 70: The three cements that were chosen to investigate and their mineralogical composition. 182
Figure 71: The results from testing how much radionuclide analogue C:S ratio 4 can remove from solution. Iodine is represented by orange, cerium is green, caesium is blue, and strontium is purple. 185
Figure 72: The results from testing how much radionuclide analogue NRVB cured at 200°C can remove from solution. Iodine is represented by orange, cerium is green, caesium is blue, and strontium is purple. 187
Figure 73: The results from testing how much radionuclide analogue NRVB cured at 250°C can remove from solution. Iodine is represented by orange, cerium is green, caesium is blue, and strontium is purple. 189
Figure 74: Measured cerium concentration plotted against the initial cerium concentration for each mineral studied. The black dotted line is the initial concentration, so the closer to the black dotted line less cerium has been removed from solution by the mineral. Orange is xonotlite, navy is reinhardbraunsite, blue is jaffeite, purple is α-C_2SH, and red is calcite. 191
Figure 75: Measured cerium concentration plotted against the initial cerium concentration for each mineral studied. The black dotted line is the initial concentration. Orange is xonotlite, navy is reinhardbraunsite, blue is jaffeite, purple is α-C_2SH, and red is calcite. 193
Figure 76: Graphs to show how the concentration of the radionuclide analogues changed concentration over the 8 day tests with calcite. The radionuclide analogues are orange and the concentration of calcium in solution is blue. The top left is the control, top right is caesium, bottom left is cerium and bottom right is strontium. 196
Figure 77: Graphs to show how the concentration of the radionuclide analogues changed concentration over the 8 day tests with xonotlite. The radionuclide analogues are orange and the concentration of calcium in solution is blue. The top left is the control, top right is caesium, bottom left is cerium and bottom right is strontium. 199
Figure 78: Graphs to show how the concentration of the radionuclide analogues changed concentration over the 8 day tests with α-C_2SH. The radionuclide analogues are orange and the concentration of calcium in solution is blue. The top left is the control, top right is caesium, bottom left is cerium and bottom right is strontium. 201
Figure 79: Graphs to show how the concentration of the radionuclide analogues changed concentration over the 8 day tests with reinhardbraunsite. The radionuclide analogues are orange and the concentration of calcium in solution is blue. The top left is the control, top right is caesium, bottom left is cerium and bottom right is strontium. 203
Figure 80: Graphs to show how the concentration of the radionuclide analogues changed concentration over the 8 day tests with jaffeite. The radionuclide analogues are orange and the concentration of calcium in solution is blue. The top left is the control, top right is caesium, bottom left is cerium and bottom right is strontium. 205
Figure 81: The results from measuring the pH of the solutions over the 8 day rate experiments. The top graph is the control sample, the second from top graph is the caesium solution, the third from top is the cerium solution, and the bottom graph is the strontium solution. The navy line is calcite, the orange line is xonotlite, the green line is α-C_2SH, the blue line is reinhardbraunsite, and the purple line is jaffeite. 208
Figure 82: The XRD patterns of calcite (black) after being mixed with deionised water (red), cerium (blue), caesium (green) and strontium (purple) for 8 days. C = calcite, S = strontianite, Cs = caesium carbonate. 210

Figure 83: The XRD patterns of xonotlite (black) after being mixed with deionised water (red), cerium (blue), caesium (green) and strontium (purple) for 8 days. X = xonotlite, C = calcite. 212
Figure 84: The XRD patterns of reinhardbraunsite (black) after being mixed with deionised water (red), cerium (blue), caesium (green) and strontium (purple) for 8 days. R = Reinhardbraunsite, C = calcite. 214
Figure 85: The XRD patterns of jaffeite (black) after being mixed with deionised water (red), cerium (blue), caesium (green) and strontium (purple) for 8 days. J = jaffeite, C = calcite. 216
Figure 86: The XRD patterns of α-C_2SH (black) after being mixed with deionised water (red), cerium (blue), caesium (green) and strontium (purple) for 8 days. a = α-C_2SH, C = calcite. 218
Figure 87: A graph showing the percentage of radionuclide remaining in solution after the 8 day tests. Navy = calcite, orange = xonotlite, red = reinhardbraunsite, blue = α-C_2SH, and green = jaffeite. 222
Figure 88: A graph showing the percentage of radionuclide remaining in solution after the 8 day tests. Navy = C:S 4 cured at 250°C, orange is NRVB cured at 200°C, and green is NRVB cured at 250°C. 223
Figure 89: A graph showing the percentage of cerium in solution at different start concentrations after being mixed with individual minerals for 8 days. Navy = calcite, orange = xonotlite, red = reinhardbraunsite, blue = jaffeite, and purple = α-C_2SH. 224
Figure 90: An illustration of how the properties of the backfill, the GDF design, and the safety requirements should feed into the designs and be underpinned by optimisation. 241
Figure 91: Diagram showing how the closer to the waste container the cement is cured the larger and more irregular the pores will be, this is due to the curing temperature being highest at the waste container. 242
Figure 92: A suggested experimental setup to test how effective the cement cores are at removing radionuclide from solution. 244
Figure 93: A suggested experimental setup to investigate how cured NRVB cement behaves when exposed to a saline solution that is acting as a groundwater analogue. 246
Figure 94: A suggestion for an experimental setup where a cement core is exposed to a temperature representative of the heat produced by a waste container at one end, and at the other it is exposed to the temperature of the GDF host rock. 247
Figure 95: Two schematics showing how the cement sample would be prepared for SEM/EMPA (top) and XRD analysis (bottom). 248
Figure 96: Diffractogram for cements cured at 80°C with CaO:SiO_2 ratios between 4 and 7.27 (NRVB). 271
Figure 97: Diffractogram for cements cured at 25°C with CaO:SiO2 ratios between 4 and 7.27 (NRVB). 272
Figure 98: EMPA elemental scans for the NRVB cement cured at 250°C. Starting top left Al, C, Ca, middle left Mg, S, Fe, bottom left O, Si, and the compositional elemental scan. 273
Figure 99: EMPA elemental scans for the NRVB cement cured at 200°C. Starting top left Al, C, Ca, middle left Mg, S, Fe, bottom left O, Si, and the compositional elemental scan. 274
Figure 100: EMPA elemental scans for the NRVB cement cured at 150°C. Starting top left Al, C, Ca, middle left Mg, S, Fe, bottom left O, Si, and the compositional elemental scan. 275
Figure 101: EMPA elemental scans for the NRVB cement cured at 80°C. Starting top left Al, C, Ca, middle left Mg, S, Fe, bottom left O, Si, and the compositional elemental scan. 276
Figure 102: EMPA elemental scans for the NRVB cement cured at 25°C. Starting top left Al, C, Ca, middle left Mg, S, Fe, bottom left O, Si, and the compositional elemental scan. 277
Figure 103: EMPA elemental scans for the C:S 4 cement cured at 250°C. Starting top left Al, C, Ca, middle left Mg, S, Fe, bottom left O, Si, and the compositional elemental scan. 278
Figure 104: EMPA elemental scans for the C:S 4 cement cured at 200°C. Starting top left Al, C, Ca, middle left Mg, S, Fe, bottom left O, Si, and the compositional elemental scan. 279
Figure 105: EMPA elemental scans for the C:S 4 cement cured at 150°C. Starting top left Al, C, Ca, middle left Mg, S, Fe, bottom left O, Si, and the compositional elemental scan. 280

Figure 106: EMPA elemental scans for the C:S 4 cement cured at 80°C. Starting top left Al, C, Ca, middle left Mg, S, Fe, bottom left O, Si, and the compositional elemental scan. 281
Figure 107: EMPA elemental scans for the C:S 4 cement cured at 25°C. Starting top left Al, C, Ca, middle left Mg, S, Fe, bottom left O, Si, and the compositional elemental scan. 282

List of Tables

Table 1: The main radionuclides produced from a PWR, their half-lives, the type of radionuclide they are, and the decay mode (α = alpha, β = beta, γ = gamma). 9
Table 2: The waste types that are planned for geological disposal and the maximum temperature that they could reach within the repository. 11
Table 3: The nomenclature used to describe Cementitious systems[51] 29
Table 4: XRD parameters used to measure the cement samples used to investigate XRD preparation methodology. 37
Table 5: The four XRD preparation methods that were investigated in this set of experiments. Where the Meller method is following that of Nicola Meller, FD= freeze dried, HG = hand ground, M = micronized, BM = ball milled. 39
Table 6: Quantification results for the cements that were tested to see which preparation method was most effective at preventing carbonation. Where the Meller method is following that of Nicola Meller, FD= freeze dried, HG = hand ground, M = micronized, BM = ball milled. T0 = no exposure to air, T2 = 2 hours exposure to air, T24= 24 hours exposure to air. 46
Table 7: A table showing the four ways the different XRD preparation methods and hydration arrest methods can be compared. 47
Table 8: The pH results from the four different tap locations in the Civil Engineering laboratories. 52
Table 9: The raw materials sourced to manufacture NRVB, with the commercial name they were supplied with, and a link to the website they were sourced directly from [95] [96,97]. 57
Table 10: The XRF results on the three aliquots of cement powder and the limestone powder provided by Hanson and Tarmac. 58
Table 11: Comparison of the XRF analysis of the three aliquots of cement powder to the material analysis information provided by Hanson. 58
Table 12: The quantities of raw material and water that were tested to ensure the raw materials behaved as expected when hydrated and heated. 59
Table 13: The quantities of raw material and water that were tested to ensure the raw materials behaved as expected when hydrated and heated. 60
Table 14: The measurement conditions used for XRD analysis of the raw materials and CEM I powders. 61
Table 15: The phases identified within the raw materials when nothing was done to them (raw materials), and when they were mixed with water and heated to either 80 or 250°C for 22 hours. 62
Table 16: The measurement conditions used for XRD analysis. 64
Table 17: The results from the XRD analysis done on the cements cured for either 5 or 10 days at either 80, 175, or 250°C. 65
Table 18: A comparison of the cement used in previous phase diagram investigations (Dyckerhoff Class G cement) and the cement used for NRVB and in this study (Ribblesdale PC CEM1 52.5N). 68
Table 19: The $CaO:SiO_2$ ratios chosen to extend the phase diagram. The percentage of cement replaced with silicon dioxide, and the $CaO:SiO_2$ ratio that this replacement is equivalent to. 69
Table 20: XRD scan parameters used on the Malvern Panalytical Empyrean multi-purpose platform at the University of Glasgow. 70
Table 21: The phases identified with XRD for these cements. 71
Table 22: The $CaO:SiO_2$ ratios studied, showing the percentage of CEM I powder replaced with SiO_2 and the moles of each. 75
Table 23: Quantification of the phases that are present within the various cements. 77
Table 24: The COD IDs and references to the CIF files used in TOPAS to quantify the amount of each mineral present in the cements. 80
Table 25: The parameters used to process the XCT scans in Avizo. AT = Attenuation Threshold, AD = Anisotropic Diffusion. Anisotropic Diffusion is dimensionless and has no unit. 99

Table 26: The diameter, radius and height of the cement core NRVB cured at 25°C measured with callipers. 102
Table 27: The values used to threshold the PEEK cup and cement core of the samples cured at 250°C in Avizo image processing software. 103
Table 28: The number of pixels calculated in Avizo for the PEEK cup and cement core of the samples, and the actual volume calculated. 103
Table 29: The porosities calculated for the cement cores using XCT scanning and Avizo image processing software. 104
Table 30: The results of using XCT to calculate the volume of the cement core and then using the measurement from helium Pycnometry to calculate the percentage porosity of the cement cores. *samples were corrected for PEEK cup. HePyc is short for helium pycnometry. 108
Table 31: Helium pycnometer results for cements mixed with calcium carbonate cured at room temperature and 80°C. 118
Table 32: The porosity values calculated with helium pycnometry when the cement samples were cured at 25°C. 120
Table 33: The porosity values calculated with helium pycnometry when the cement samples were cured at 80°C. 121
Table 34: The three cements chosen to study as they contain most high temperature minerals. These minerals are α-C_2SH, γ-C_2SH, jaffeite, reinhardbraunsite, katoite, and xonotlite. The minerals of interest are highlighted in blue. 133
Table 35: The conditions at which xonotlite has been found to form at 100% purity [56]. 135
Table 36: The different synthesis methods studied in this chapter, with the mineral that could be formed. 142
Table 37: The minerals identified and the COD codes used for each mineral in DIFFRAC.EVA for the mixes that were most likely to synthesise xonotlite. 143
Table 38: The minerals identified and the COD codes used for each mineral in DIFFRAC.EVA for the mixes that were most likely to synthesise reinhardbraunsite. 145
Table 39: The minerals identified and the COD codes used for each mineral in DIFFRAC.EVA for the mixes that were most likely to synthesise jaffeite. 147
Table 40: The minerals identified and the COD codes used for each mineral in DIFFRAC.EVA for the mixes that were most likely to synthesise α-C_2SH. 149
Table 41: The mix and curing conditions of two samples that showed a similar mineralogy despite having different C:S ratios and different curing times. 151
Table 42: The minerals identified and the COD codes used for each mineral in DIFFRAC.EVA for the mixes that were most likely to synthesise γ-C_2SH. 153
Table 43: The TOPAS quantification of the mineral phases chosen that contain the least number of mineral phases and contain the desired mineral phase. 156
Table 44: The methods determined in parts 2 and 3 to synthesise the minerals that will be studied in the next chapter. 157
Table 45: The radionuclides chosen to test in this chapter and their half-lives. 162
Table 46: The half-lives of the different radioisotopes of plutonium[225]. 163
Table 47: Reference salinities used by NWS that are representative of geologies the GDF could be constructed in[252]. 167
Table 48: A table showing the 15 different solutions that were made and tested with each mineral. 168
Table 49: The concentrations of the standards used to calibrate the ICP-OES. 169
Table 50: The Minimum Quantification Level of each element measured with ICP-OES. 170
Table 51: The Limit of Detection, Limit of Quantification, and % Uncertainty for the ICP-MS results. 170
Table 52: The results from testing how much radionuclide analogue calcite can remove from solution. 171
Table 53: The percentage of radionuclide remaining in solution after 8 days of being shaken with calcite. 172

Table 54: The results from testing how much radionuclide analogue xonotlite can remove from solution. 174
Table 55: The percentage of radionuclide remaining in solution after 8 days of being shaken with xonotlite. 174
Table 56: The results from testing how much radionuclide reinhardbraunsite removes from solution. 176
Table 57: The percentage of radionuclide remaining in solution after 8 days of shaking with reinhardbraunsite. 176
Table 58: The results from testing how much radionuclide analogue α-C_2SH can remove from solution. 178
Table 59: The percentage of radionuclide remaining in solution after 8 days of being shaken with α-C_2SH. 178
Table 60: The results from testing how much radionuclide analogue jaffeite can remove from solution. 180
Table 61: The percentage of radionuclide remaining in solution after 8 days of being shaken with jaffeite. 180
Table 62: The three cements that were chosen and their mineralogical compositions. 182
Table 63: The results from testing how much radionuclide analogue the cement C:S ratio 4 250°C can remove from solution. 184
Table 64: The percentage of radionuclide remaining in solution after 8 days of being shaken with the cement C:S ratio 4 250°C. 184
Table 65: The minerals that have been tested to see how much strontium they can remove from solution that are also present within this cement mix. 186
Table 66: The results from testing how much radionuclide analogue the cement NRVB 200°C can remove from solution. 186
Table 67: The percentage of radionuclide remaining in solution after 8 days of being shaken with the cement NRVB 200°C. 187
Table 68: The results from testing how much radionuclide NRVB 250°C removed from solution. 188
Table 69: The percentage of radionuclide remaining in solution after 8 days of being shaken with the cement NRVB 250°C. 188
Table 70: The composition of NRVB cured at 250°C and the % of caesium left in solution when tested against the individual components of the cement. 189
Table 71: The concentration of cerium remaining in solution after being shaken with the individual minerals for 8 days. 191
Table 72: The concentration of calcium in each solution after the different concentrations of cerium is mixed with the individual mineral for 8 days. 192
Table 73: The results of the rate tests testing how quickly the addition of calcite reduces the concentration of radionuclides (Ce, Cs, Sr) in solution. 195
Table 74: The results of the rate tests testing how quickly the addition of xonotlite reduces the concentration of radionuclides (Ce, Cs, Sr) in solution. 198
Table 75: The results of the rate tests testing how quickly the addition of α-C_2SH reduces the concentration of radionuclides (Ce, Cs, Sr) in solution. 200
Table 76: The results of the rate tests testing how quickly the addition of reinhardbraunsite reduces the concentration of radionuclides (Ce, Cs, Sr) in solution. 202
Table 77: The results of the rate tests testing how quickly the addition of jaffeite reduces the concentration of radionuclides (Ce, Cs, Sr) in solution. 204
Table 78: The pH measurement results of the different mineral tests in deionised water with caesium, cerium, and strontium. 207
Table 79: The calcite samples, the minerals they contain and the COD ID used to identify the minerals. 210
Table 80: The xonotlite samples, the minerals they contain and the COD ID used to identify the minerals. 212

Table 81: The reinhardbraunsite samples, the minerals they contain and the COD ID used to identify the minerals. 214
Table 82: The jaffeite samples, the minerals they contain and the COD ID used to identify the minerals. 217
Table 83: The α-C_2SH samples, the minerals they contain and the COD ID used to identify the minerals. 219
Table 84: A summary table from the Phase 1 tests, showing the percentage of radionuclide remaining in solution after 8 days for each mineral in each solution. 221
Table 85: A summary table from the Phase 1 tests, showing the percentage of radionuclide remaining in solution after 8 days for each cement in each solution. 222
Table 86: A summary of the results from the phase 2 tests regarding cerium. 224
Table 87: The gradients on the lines of best fit from the Phase 3 tests. Where the number is negative this shows the mineral reduced the concentration of radionuclide analogue in solution. 225

Chapter 1 Introduction

1.1 Introduction to the project

The UK produces radioactive waste from decommissioning, civil nuclear energy, medicine, defence, and research. The UK also has a significant amount of legacy radioactive waste from historical operations at sites such as Sellafield, where plutonium was produced for the weapons programme, and fuel from Magnox and Advanced Gas Cooled reactors was reprocessed. Sellafield also has facilities used to store historic radioactive waste, these include the Magnox Swarf Storage Silo (MSSS), the Pile Fuel Cladding Silo (PFCS), and the First Generation Magnox Storage Pond (FGMSP). These facilities contain hazardous wastes that are highly radioactive and in poor condition. Retrieval of these wastes is challenging, this is due to poor record keeping and the dangerous conditions posed by the degrading facilities. One retrieved the wastes are treated and stored awaiting future disposal in a suitable facility.

The UK currently has one radioactive waste disposal facility, the Low Level Waste Repository (LLWR) located in Drigg, Cumbria. This facility accepts low level radioactive waste. For a waste to be classified as low level it must not exceed 4 GBq per tonne of alpha activity or 12 GBq per tonne of beta or gamma activity[1]. The wastes being retrieved from Sellafield either exceed these limits or are not able to be segregated from higher activity waste due to the condition they are in. The activity emitted from waste as it decays is ionising and harmful to humans, animals, and the environment. The LLWR has been assessed to provide adequate containment for low level waste, therefore it is not safe for the higher activity wastes to be disposed of to the LLWR.

These current, future, and legacy wastes are a significant driver for the UK to build a Geological Disposal Facility (GDF). The GDF would ensure these wastes can be safely and reliably isolated for thousands of years. The UK's GDF is planned to be a repository built between 200 and 1000 m underground. The GDF will have both natural and engineered barriers that prevent the migration of radionuclides into the groundwater and biosphere. The natural barriers will be provided by the depth of the GDF and the surrounding host rock. The engineered barriers will consist of the waste packaging and containers, tunnel seals, and buffer/ backfill materials. As the waste

decays it will emit heat which the backfill material will be exposed to[2]. It is therefore important that the backfill material is thermally stable and can withstand the heat emitted from the decaying waste. One candidate for backfill is Nirex Reference Vault Backfill (NRVB) Cement.

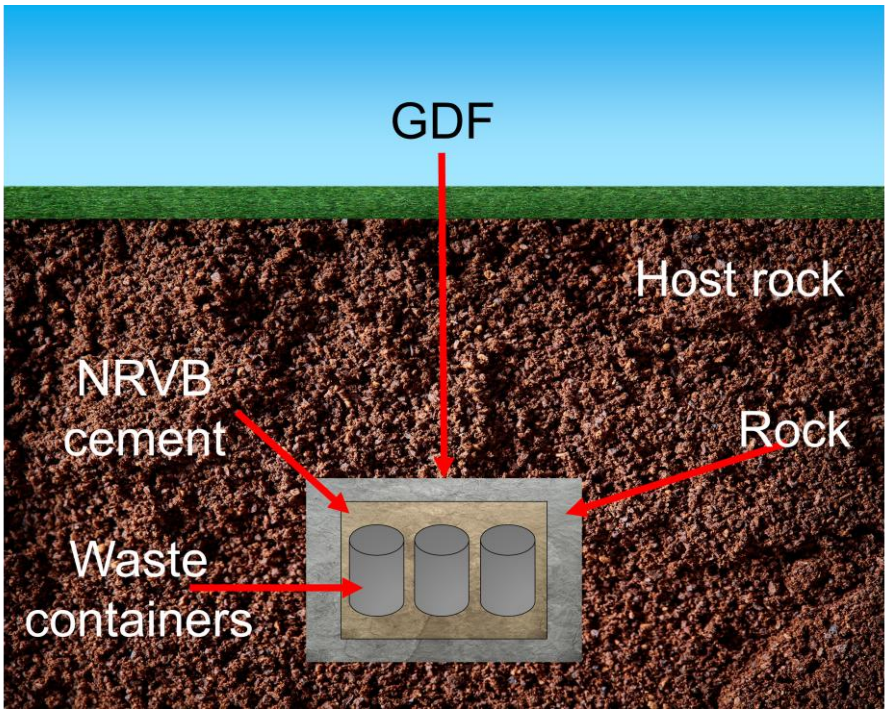


Figure 1: A simple diagram of the GDF showing how the waste packages will be emplaced and then NRVB cement will be used to backfill the vault.

NRVB cement is a cementitious backfill material designed for radioactive waste disposal. It is comprised of Portland Cement, portlandite, calcite, and water. NRVB cement is able to maintain a high pH environment of 12 to 13 by dissolving some of the mineral components into the pore water[3,4]. The high pH lowers the solubility of radionuclides and increases the amount of radionuclide sorption to the cementitious phases. NRVB cement provides structural support as the backfill of the GDF, and it has a high porosity which allows for gas transport and avoids cracking[4]. The performance of NRVB cement depends on the mineral phases that form during curing, the pore structure, and the microstructure. These properties can be affected by curing at elevated temperatures.

Different techniques can be used to study how the properties of NRVB cement are affected by curing at elevated temperatures. X-ray Diffraction can be used to study the mineral phases of cement and the quantity of them. X-ray Computed Tomography, Mercury Intrusion Porosimetry, (MIP) and helium pycnometry can be used to measure

the porosity, and SEM and EMPA can be used to analyse the microstructure and chemistry of cement. Sorption tests using ICP-OES and ICP-MS can be used to analyse the effect of curing at elevated temperatures on the radionuclide retention.

This thesis investigates the effect of elevated curing temperature on NRVB cement and how this alters its mineralogy, porosity, and radionuclide retention behaviour. XRD, XCT, helium pycnometry, SEM, EMPA, and radionuclide sorption experiments are used to characterise the evolution of the cement system under curing conditions relevant to the GDF. The work aims to improve understanding of the long-term suitability of NRVB as a backfill material within a Geological Disposal Facility. This thesis contains five research chapters and is concluded with a discussion chapter.

- Chapter 2 ‘Optimisation of sample preparation for XRD analysis including cementitious hydration arrest’ investigates preparation methods for XRD including the hydration arrest method, the grinding method, and how the samples are affected by carbonation reactions. This chapter ensures there is confidence in sample analysis in the following chapters and that the highest quality results were obtained.
- Chapter 3 ‘Investigation into the effect of increasing the curing temperature and altering the C:S ratio of NRVB cement on the mineralogy’, this chapter uses the preparation techniques developed in Chapter 2. NRVB cements were cured at temperatures between 25 and 250 °C, and silicon dioxide was added to alter the C:S ratio from 4 to 7. These samples were then analysed using XRD to determine what phases and in what abundance they form under these conditions.
- Chapter 4 ‘The effect of increased curing temperature and different C:S ratio on porosity’. In this chapter the porosity of the cements made in Chapter 3 was measured using X-ray Computational Tomography (XCT) and helium pycnometry. The cements were also measured using SEM and EMPA to study the distribution of the minerals.
- Chapter 5 ‘Development of methods to synthesise single high temperature mineral phases’. In this chapter there is an investigation in how to synthesise the high temperature mineral phases that were identified in Chapter 3 so that the properties of the minerals regarding the mobility of radionuclides can be assessed.

- Chapter 6 ‘The effect of mineralogical composition of NRVB cement on the mobility of radionuclides’. This chapter used the minerals that were synthesised in Chapter 5 and studied how effective the minerals were at decreasing the concentration of radionuclide analogue in solution.
- Chapter 7 ‘Discussion of the implications for NRVB Cement in Nuclear Waste Disposal and repository design’ discusses the impact of this research, and the implications of it on the GDF design. This chapter also discusses potential future experiments that would build on the work in this thesis.

1.2 Aims and Objectives of this thesis

There is a clear need for a Geological Disposal Facility (GDF) in the UK. To support the safety case for a GDF more research into NRVB cement as a backfill option is necessary. This project aims to investigate the effect of high temperatures on NRVB cement to provide robust scientific evidence that can help underpin a safety claim made in the safety case for the GDF. The thesis meets this aim by achieving the following objectives:

- Studying the differences in the mineral phases when the cement is cured at higher temperatures, and how the changes in mineralogy affect the properties of NRVB cement. This includes quantifying the mineral phases produced and investigating the effect on the porosity of the NRVB cement.
- Investigating the effect of the mineralogical composition of NRVB cement changing at different curing temperatures on the capacity of each cement to remove radionuclides from groundwater.

Each chapter has individual aims and objectives, these are listed below.

Chapter 1 Introduction:

- To provide a background and context of nuclear waste in the UK, the plans for a GDF, and cement chemistry and evolution during curing.
- To identify the research gap that this project fulfils.

Chapter 2 Optimisation of sample preparation for XRD analysis including cementitious hydration arrest**:**

To study the impact of:

- How well ground the sample is, a finer ground sample will have smaller size particles and a smaller size distribution. This impacts the peak shape and affects quantification as a finer ground sample will produce sharper peaks with better resolution.
- How the sample is dried. It is important to arrest the hydration of the cement quickly so that they are representative of that time point.
- The conditions the sample is exposed to, such as heat or other chemicals. Heat and chemicals can cause mineralogical alterations by interacting with minerals or dehydrating them.
- The carbonation of the sample. This will affect the amount of calcium carbonate the sample contains, as CO_2 reacts with portlandite.

Chapter 3 Investigation into the effect of increasing the curing temperature and altering the C:S ratio of NRVB cement on the mineralogy:

- To use XRD to study to identify the mineralogical changes when NRVB is cured from temperatures of 25°C to 250°C, and when the C:S ratio is adjusted from 7.27 to 4, as the current phase diagram is from a C:S ratio of 1 to 3.
- To quantify the mineralogical composition of NRVB cured at this temperature and C:S range to extend the current understanding of the NRVB cement phase diagram.

Chapter 4 The effect of increased curing temperature and different C:S ratio on porosity:

- To analyse the porosity of the cements and evaluate the impact of curing temperature and C:S ratio on porosity.
- To use SEM and EMPA to find the porosity of the cements, and to identify the minerals that form around the pores. This can be used in combination with the results from the previous chapter that analysed the mineralogy to study where minerals are forming within the cements and the impact this could have on the cements' ability to retain radionuclides.

Chapter 5 Development of methods to synthesise single high temperature mineral phases:

- To conduct a focussed literature review to find existing methods for synthesising the identified high temperature minerals. This includes research

that analyses the phases formed in cements under different conditions that may not have their primary aim to synthesise the mineral.

- To use the literature research to develop a series of experiments to replicate or improve on the efficacy of the methods found in existing research.
- To use XRD analysis then EVA and TOPAS to analyse the series of minerals made and choose the best method to synthesise high temperature minerals to use in future work to investigate their efficacy at removing radionuclide analogues from solution.

Chapter 6 The effect of mineralogical composition of NRVB cement on the mobility of radionuclides:

- **Phase 1:** The aim of this phase was to find out if any of the minerals were able to reduce the concentration of radionuclide in solution, and if so, which minerals interact with the radionuclide analogues.
- **Phase 2:** The aim of this phase was to quantify how much each mineral was able to reduce the concentration of radionuclide in solution.
- **Phase 3:** The aim of this phase was to find out the rate each mineral could reduce the concentration in solution for each radionuclide, and to determine its sorption mechanism with XRD.

1.3 The current status of radioactive waste in the UK and the Geological Disposal Facility

The United Kingdom has a long and complex nuclear history which began in 1941 with the development of the atomic bomb [5]. As nuclear research began so did nuclear waste production, in fact, almost all research and development waste is from research that began in the 1940s when the UK developed prototype and research reactors to produce both electricity for the national grid, and radioactive material required for defence programmes[6]. Two reactors built to produce plutonium for the weapons programme were the Windscale Number 1 and 2 reactors at Calder Hall, Sellafield[7]. These are currently being decommissioned, having left a legacy of highly contaminated and varied waste[8]. There are numerous sites in the UK that produce nuclear waste and several disposal facilities (Figure 2).

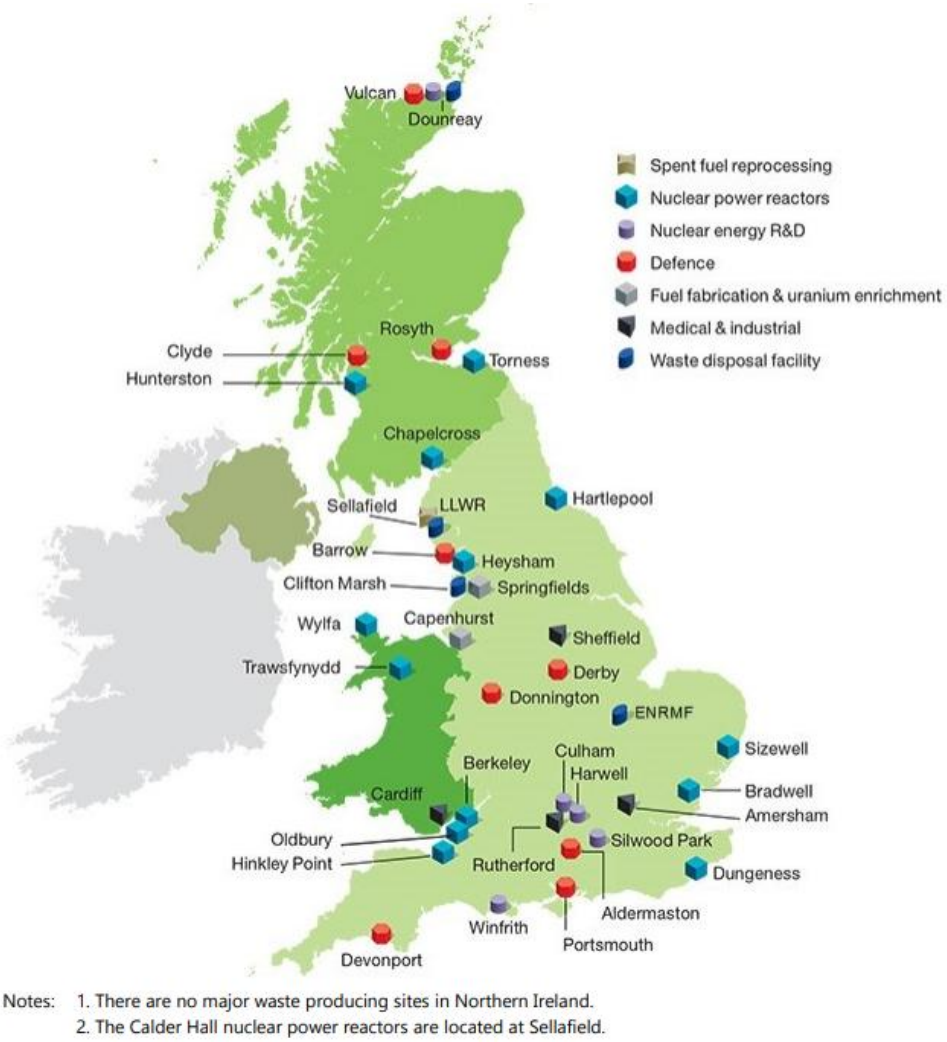


Figure 2: Sites in the UK that are large producers of nuclear waste and waste disposal facilities [1]

Other radioactive waste is produced through research facilities, medical use, industrial use, and defence. The UK's nuclear deterrent consisting of submarines powered by nuclear reactors is the largest source of waste from defence, some is also produced by other parts of the armed forces[6]. The scale of the decommissioning challenge is unprecedented with approximately 140 tonnes of plutonium held by the Nuclear Decommissioning Authority (NDA) at Sellafield and Dounreay[9], the current plan for this is vitrification then disposal in a Geological Disposal Facility (GDF).

Radioactive waste such as plutonium emits ionizing radiation whilst decaying, in the form of alpha, beta, and/or gamma radiation[10]. This radiation can be harmful to humans and non-human biota such as plants and animals. Alpha radiation has low energy and can be stopped by skin, beta and gamma radiation however require several millimetres of aluminium and one to two meters of cement respectively, to be blocked. Due to the different energies of these emissions, they are harmful in different ways; alpha radiation is only harmful if it enters the body through injection, ingestion, or inhalation. This is because it is unable to pass through the skin and leave the body. Beta and gamma radiation are most harmful through direct exposure[10].

Once radiation has entered the body it either produces stochastic or deterministic effects. A stochastic effect is when a radiation dose increases the likelihood of developing an illness, for example, increasing the probability of a certain type of cancer by 5%[11]. This can be seen in the aftermath of the accident at the Chernobyl nuclear power plant where it is estimated that the release of radiation has caused 4000 cases of various cancers and an additional 1000 cases of thyroid cancer[12].

Unlike stochastic effects, a deterministic effect will definitely occur. For example, effects could be to cause cell damage and cell death [11]. An example of this is at the Tokaimura nuclear fuel processing facility where three workers accidentally caused a critical reaction, and were exposed to an estimated 1000-4500 mSv, 6000-10,000 mSv, and 16,000-20,000 mSv doses of radiation which resulted in the death of two of the workers[13]. One worker died 12 weeks after the accident, the other died seven months later as a result of acute radiation syndrome (ARS)[14]. To prevent harmful effects from radioactive waste it is therefore essential that the waste is disposed of safely and securely, and with no chance of humans or non-human biota being exposed to it.

The UK has four main categories of radioactive waste which are classified by the activity of the radionuclides that it contains and the decay heat that the radionuclides

produce. These are Very Low Level Waste (VLLW), Low Level Waste (LLW), Intermediate Level Waste (ILW) and High Level Waste (HLW). A nuclear reactor will produce waste across these categories.

The UK currently has one Pressurised Water Reactor (PWR) reactor, Sizewell B[15], and is planning to build several Rolls Royce SMRs (Small Modular Reactors) which are based on an advanced design of the PWR (Generation III+)[16]. PWRs produce a wide range or radionuclides with different half-lives and decay modes (Table 1[17]). Radionuclides that have a half-life of months to several years can be stored until they have decayed to a lower level. Other radionuclides such as plutonium-241 that have a half-life of 24,100 years will require long term storage.

Table 1: The main radionuclides produced from a PWR, their half-lives, the type of radionuclide they are, and the decay mode (α = alpha, β = beta, γ = gamma).

Radionuclide	Half-life	Type of radionuclide	Decay mode
Cobalt-60	5.271 years	Light element	β, γ
Plutonium-238	87.7 years	Actinide	α
Plutonium-239	24,100 years	Actinide	α
Plutonium-240	6,560 years	Actinide	α
Plutonium-241	14.4 years	Actinide	β, α
Americium-241	432.7 years	Actinide	α
Americium-243	7,370 years	Actinide	α
Curium-242	162.8 days	Actinide	α
Curium-243	29.1 years	Actinide	α
Curium-244	18.1 years	Actinide	α
Strontium-90	28.78 years	Fission Product	β
Yttrium-90	2.67 days	Fission Product	β
Rhodium-106	29.9 seconds	Fission Product	β, γ
Antimony-125	2.758 years	Fission Product	β, γ
Caesium-134	2.065 years	Fission Product	β
Caesium-137	30.07 years	Fission Product	β
Barium-137	2.552 months	Fission Product	γ
Cerium-144	284.6 days	Fission Product	β
Praseodymium-144	17.28 months	Fission Product	β, γ
Promethium-147	2.62 years	Fission Product	β
Europium-154	8.59 years	Fission Product	β, γ
Europium-155	4.75 years	Fission Product	β

Despite there being the smallest volume of High-Level Waste (HLW) of 0.03%, it contributes most to the radioactivity and therefore the decay heat. Figure 3 shows the relationship between the volume of waste and its contribution to the total radioactivity. In April 2019 there were 5,100,000 tonnes of total nuclear waste within the UK, making up 4.56 million metres cubed volume[6]. It is unknown how new nuclear technologies will impact the amount of nuclear waste.

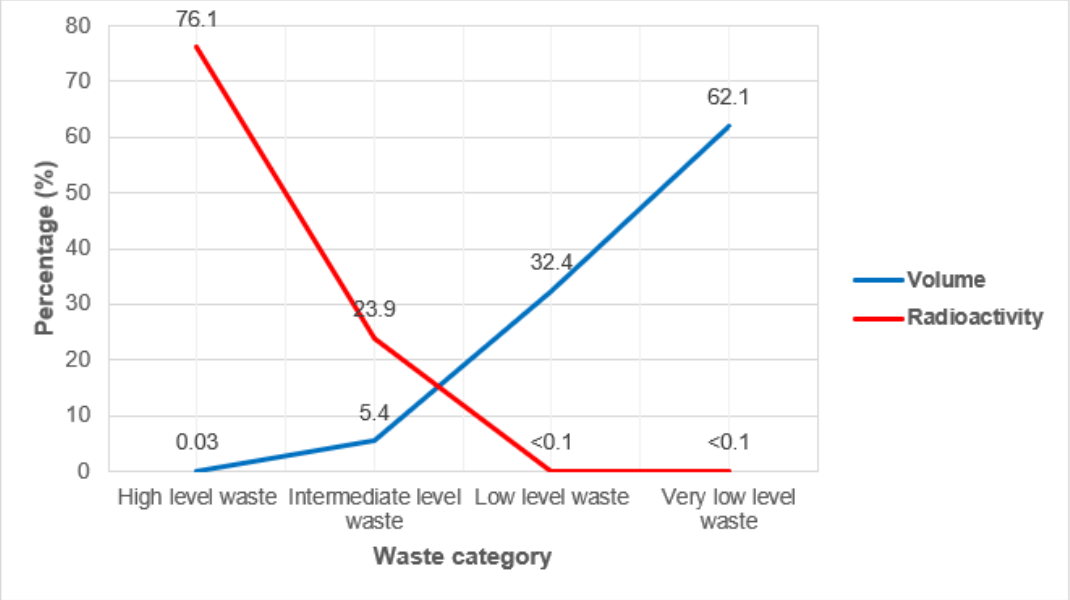


Figure 3: The different categories of UK nuclear waste and the difference in how they contribute to the total volume and radioactivity of waste[6]. The blue line shows the volume and the red line shows the radioactivity.

According to the Geological Disposal Engineered Barrier System Status Report prepared by NWS in December 2016, page 15[18], the GDF will reach a maximum temperature after closure, which will then gradually reduce. Different disposal areas are expected to reach different temperatures as shown in Table 2. The maximum 'safe' temperature is 100°C, however the concept where HLW and Spent Fuel is stored in Evaporite rock is predicted to reach 200°C[19,20]. The temperature of the repository will peak immediately after the cementitious backfill is poured as the backfill undergoes hydration reactions. The cement will therefore begin to cure at this higher temperature.

Table 2: The waste types that are planned for geological disposal and the maximum temperature that they could reach within the repository.

Waste type	**Backfill material**	**Host rock**	**Maximum Temperature (°C)**
LLW and ILW			50
ILW	Cementitious		80
HLW and Spent Fuel	Bentonite	Higher strength rock	100
HLW	Bentonite	Lower strength sedimentary rock	125
HLW and Spent Fuel		Evaporite rock	200

Radioactive waste is stored and disposed of according to its classification. Most Low-level waste (LLW) is disposed at the Low-Level Waste Repository (LLWR). Very Low-level waste (VLLW) and some LLW that has a low activity is disposed at landfill. Some LLW is stored at Sellafield, and Dounreay Site Restoration Ltd can store its own LLW and some waste from the MOD Vulcan Naval Reactor Test Establishment[6]. Since 1959 Solid Low-level waste has been disposed of at Drigg, Cumbria, in the LLWR[21,22]. Other disposal options such as metal treatment and incineration are also used (Figure 4).

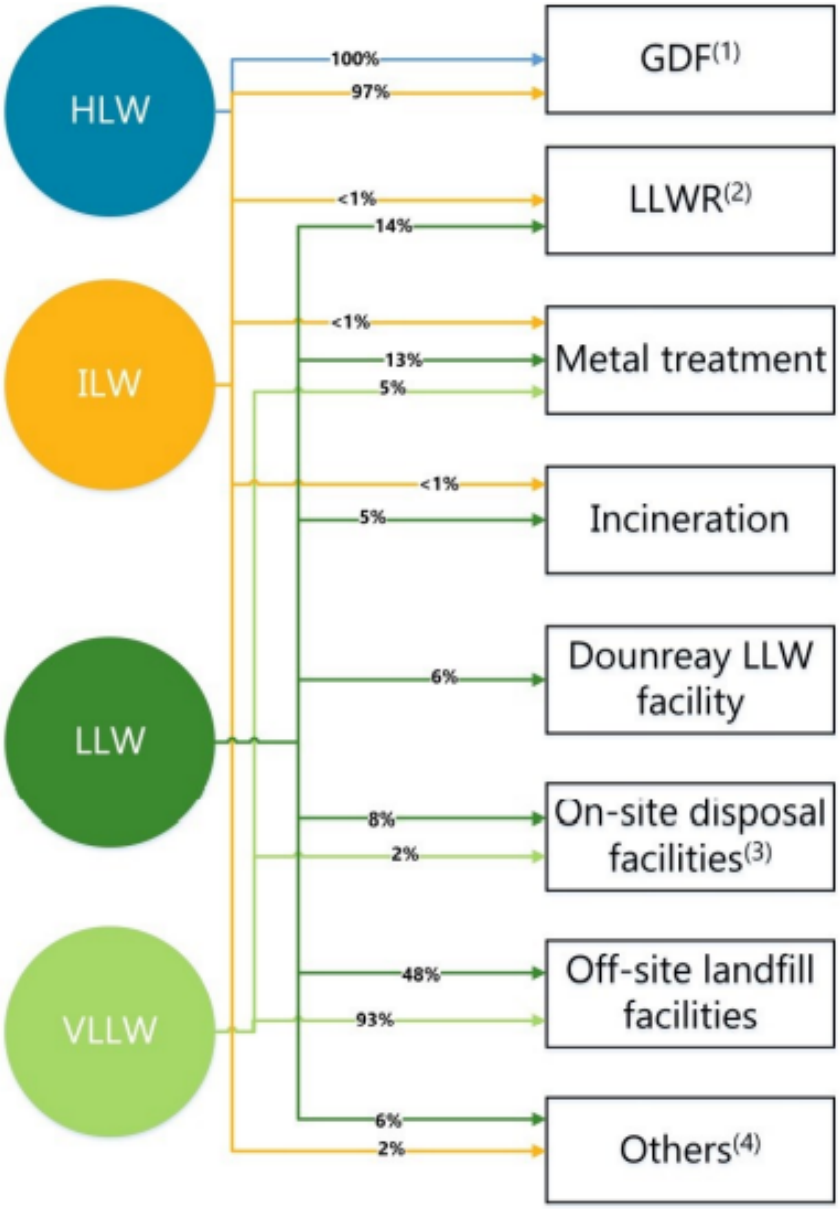


Figure 4: The disposal routes that will be used for the radioactive wastes identified in the NDA and BEIS 2019 Inventory report shown as a percentage of the total volume[3].

Higher Activity Waste (HAW) comprises High-Level Waste (HLW), Intermediate-Level Waste (ILW), and a small proportion of Low-Level Waste (LLW) that is unsuitable for disposal at existing LLW disposal facilities[23]. The UK is currently unable to dispose of HAW and the plan is to let it decay for a minimum of 50 years to reduce the activity and the amount of decay heat[21]. The plan is for the waste to then be transported for ultimate storage at a Geological Disposal Facility (GDF)[6]. The GDF is planned to be up to 1000 metres underground, utilising both engineered and natural barriers to prevent dangerous amounts of radiation escaping[24]. Therefore, the siting and design

of the GDF are vital for its efficacy, longevity, and safety. The current design for the GDF means that once the waste is transported to the storage area it will be arranged suitably so that the packages can be adequately cooled, avoiding damaging the GDF. Once the packages have been arranged the remaining space will be filled with either crushed rock, bentonite, or cement[25]. The design for ILW and HLW emplacement is shown in Figure 5. The type of cement chosen is Nirex reference vault backfill (NRVB) cement[4]. After the GDF vault has been fully sealed with backfill the surface can be reused for other purposes meaning it is essential that the natural and engineered barriers are suitable.

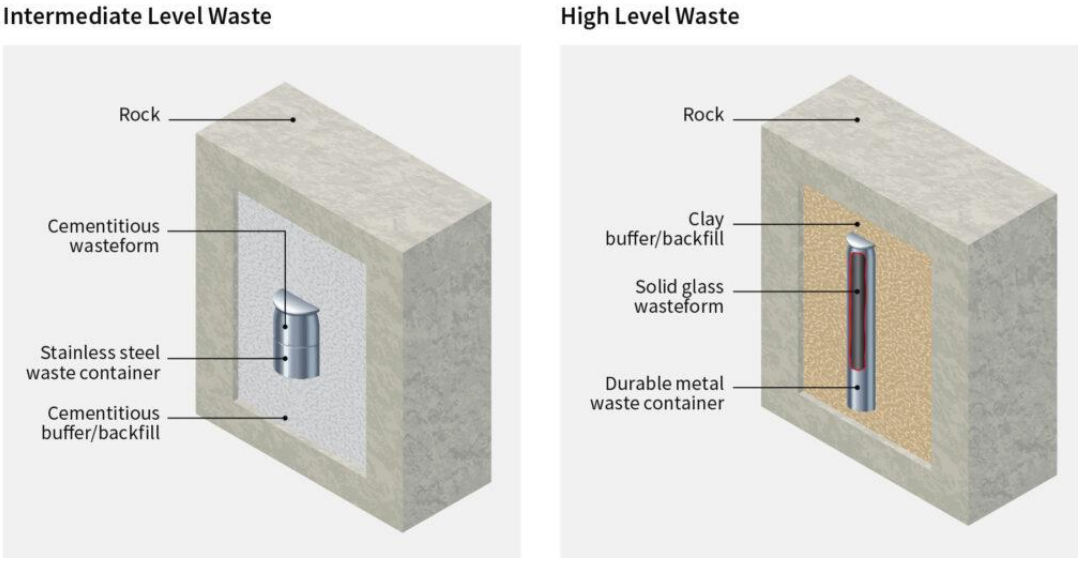


Figure 5: The design for ILW and HLW waste emplacement within the GDF[26].

The development of a Geological Disposal Facility (GDF) in England is controlled through a combination of government policy, planning legislation and regulatory requirements. UK Government policy is set out in *Implementing Geological Disposal – Working with Communities*, which establishes a consent-based process for identifying a technically suitable site with the support of a willing community[27]. Under the Planning Act 2008, as amended by the Infrastructure Planning (Radioactive Waste Geological Disposal Facilities) Order 2015, a GDF is classed as a Nationally Significant Infrastructure Project[28]. Development therefore requires a Development Consent Order, with applications considered against the National Policy Statement for Geological Disposal Infrastructure[29].

Environmental regulation of a GDF in England is the responsibility of the Environment Agency, with radioactive waste disposal regulated under the Environmental Permitting

(England and Wales) Regulations 2016[30]. The Environment Agency requires the developer to demonstrate that the disposal system will protect people and the environment during operation and following closure[31]. The Office for Nuclear Regulation (ONR) is responsible for nuclear safety, security, safeguards and aspects of radioactive material transport, with a future GDF intended to be brought within the nuclear site licensing regime established under the Nuclear Installations Act 1965[32]. These requirements are directly relevant to the long-term performance of NRVB. As a cementitious backfill, NRVB contributes to the engineered barrier system by providing a high-pH environment that can reduce radionuclide mobility, while its physical properties influence the behaviour of the backfilled vault[4]. Consequently, changes in NRVB mineralogy, porosity and chemical behaviour during the lifetime of a GDF could affect the functions for which the material was designed. Understanding how NRVB responds to conditions that may develop within a GDF is therefore important for providing evidence to support the long-term safety case.

1.4 The chemistry, composition and properties of NRVB cement

Cement will play a significant role in the GDF. It will feature as grouts, backfill, containers, tunnel linings, floors, supporting structures etc. Cement has multiple properties that lend itself to these uses, such as being an effective radiation shield, cheap, and commonly used[33]. NRVB cement will be used as backfill to encapsulate waste that is emplaced within the GDF.

How the properties of NRVB contribute to key safety functions within a GDF

Portland cement is alkaline and, when hydrated, produces highly alkaline pore solutions. Cementitious formulations may also contain supplementary cementitious materials (SCMs), such as pozzolanic materials including fly ash and silica fume. Other cementitious materials, such as ground-granulated blast-furnace slag (GGBS), may also be incorporated. GGBS is a latent hydraulic material that can react in the alkaline environment provided by Portland cement. The hydraulic materials react with products from hydration, hence helping to maintain the desired pH and pore solution[34]. These adjustments allow the cements to have similar mechanical properties to ordinary Portland cement mixtures, whilst maintaining a much higher pH[34].

The hydration conditions of cement have a large effect on the final strength of the cement[35]. The phases in Portland cement that contain silica contribute most to the strength of the cement[36]. During the early stages of hydration, tricalcium silicate (alite, C_3S) is the main contributor to strength development because it is more reactive than dicalcium silicate (belite, C_2S). The hydration of C_3S produces calcium silicate hydrate (C-S-H), which is the principal binding phase responsible for strength development in hydrated Portland cement, together with calcium hydroxide (portlandite). During later stages of hydration, dicalcium silicate (C_2S) contributes increasingly to strength development as it hydrates more slowly than C_3S but continues to react over longer periods also producing C-S-H[35].

NRVB cement is composed of 4 raw materials, each of which contributes to its properties (Figure 6). NRVB cement as backfill provides chemical benefits alongside physically supporting the containers. This includes providing an alkaline pH by dissolving some of the cement phases, preventing some radionuclides from being soluble, and increasing the likelihood of radionuclides bonding to the cement. These features prevent and slow the radionuclide's escape from the GDF and into the groundwater [37–39]. The host rock will affect the flowrate of the groundwater which will impact how the NRVB evolves over time. Previous studies have found that the NRVB is able to remain alkaline at higher flowrates than will be seen practically within the GDF once it has been built. This is important as the pH affects the sorption capacity, a high pH reduces the solubility of the radionuclides [40]. This pH of between 12 and 13 can be achieved within the pore solution of cement with a C-A-S-H system [3]. NRVB was originally designed with a low strength so that it could be removed if required,

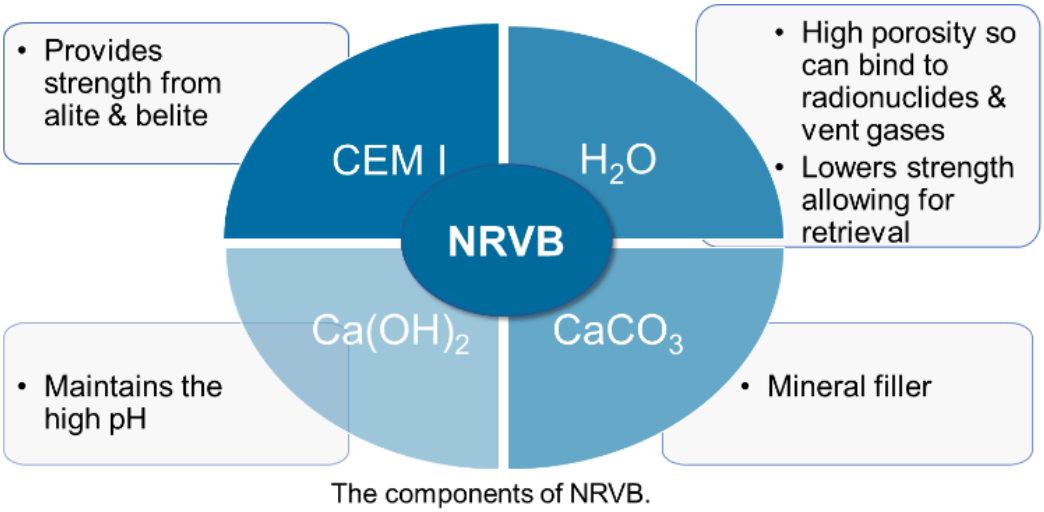


Figure 6: Diagram to show the four components of NRVB and their primary purpose.

allowing waste packages to remain retrievable during the operational period of the repository[19].

Previous studies have also found that the calcium silicate hydrate phases are the phases most responsible for binding with radionuclides. These studies have also found that their degree of crystallinity which increases as the sample ages, measured by the evolution of the peak at 100°C using Differential scanning calorimetry, has a very small impact on the cements ability to contain radionuclides [41]. This is important as radionuclide retention is another key safety feature.

In addition to the pH buffering ability, NRVB also provides a high porosity and a highly permeable environment which enables the gases that are generated by decaying fuel - such as hydrogen, methane, and CO_2[42], to pass through the cement. Therefore, this reduces pressure build up and will limit cracking, and hence degradation, within the backfill. Some of the gases are likely to contain some radionuclides, including C-14 and tritium, as a portion of the amount of methane or CO_2 emitted, with isotopes of C-14 and H-3 replacing the carbon and hydrogen atoms. A potential feature of the NRVB would be an ability to bind to these radionuclides, preventing their escape and limiting the egress of radionuclides into the surrounding soil and groundwater. Previous research has shown that atmospheric CO_2 is able to pass through the pores of ordinary Portland cement and then dissolve within the porewater, reacting with portlandite. This process reduces the pH of the cement, and the carbon atom from the CO_2 is then able to react with the calcium phases such as calcium silicate hydrate, portlandite, and calcium aluminates[42]. If this procedure still occurs with CO_2 molecules that contain radiocarbon[43] (C-14) it would be an important feature in preventing C-14 from reaching the biosphere, and investigation into the long-term implications on the longevity of the NRVB would be essential.

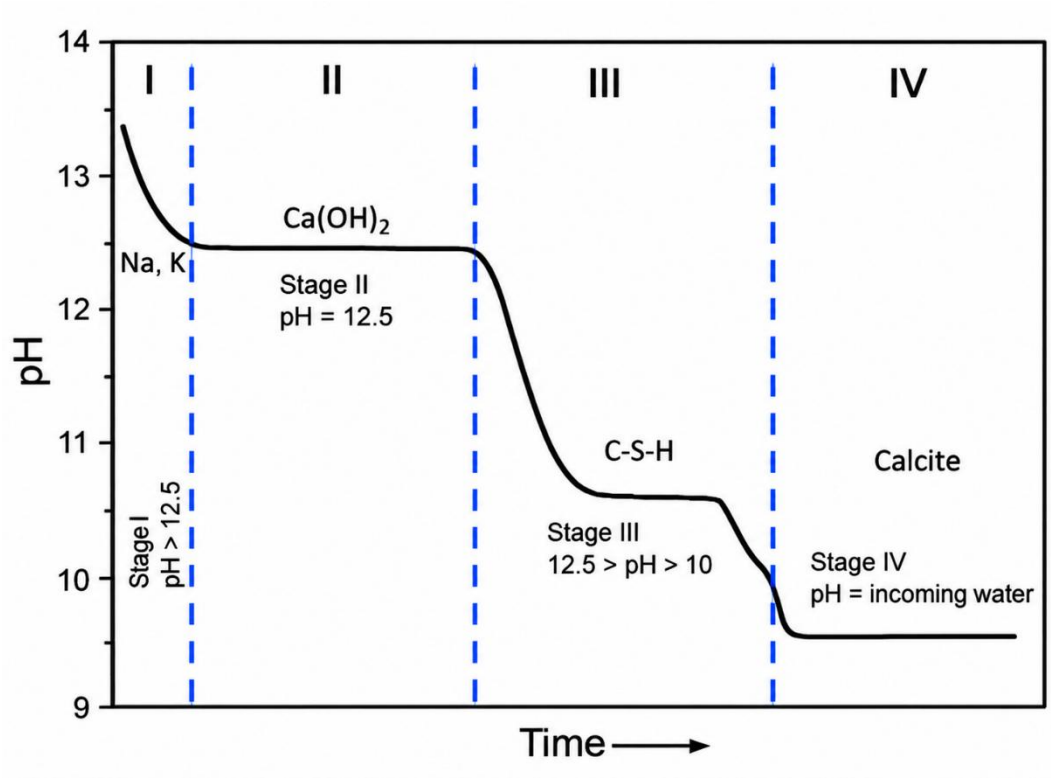


Figure 7: The components of NRVB that maintain its high pH over time[3].

In order to understand how the NRVB cement will behave over the long timescales it has previously been modelled its behaviour with groundwater (Figure 7[3]), and how the mineralogy and porosity will be affected long term. Modelling has shown that all of the phases provided by the CEM I powder will hydrate, however the portlandite will hydrate slowly over time. Later, calcium silicate hydrate and calcite will decalcify to provide the pH buffer[3,44].

NRVB has a high water to solid ratio, this gives it a relatively low strength compared to cements with a lower water to solid ratio[4]. The high-water content means the NRVB has high flowability which enables it to flow freely around the waste containers, fully encasing them and getting a high degree of coverage. A highly flowable cement would reduce the amount of operator involvement and would allow the workers to be further from the pour site. This is important when planning the construction of a GDF as if HLW is encapsulated within the GDF then the exposure to radioactivity for workers could potentially be high. To negate this exposure, protective measures could be put into place. These measures could include PPE or using robotics, reducing the exposure time, or increasing the distance between the worker and the source. Having a high flow cement means that greater volumes can be poured at once, hence increasing the distance, and decreasing the exposure time needed[45]. A high flow

cement also allows for irregular waste containers. To reduce the likelihood of reaching criticality with waste the containers are designed to make reaching criticality either impossible or very difficult, these are called Geometrically Safe Containers[46]. There is currently no GDF, so there are no conditions for acceptance. This means a variety of waste packages are being and have been historically produced with varying designs, so a flowable cement is important to ensure future disposability.

Hydration Reactions of Portland cement

Portland cement is a hydraulic cement. This means that as it hydrates it will set and gain strength. Importantly, this means that it sets as part of hydration reactions, not drying and losing water. The cement will set both in air and underwater. It can then be left underwater as it has very low solubility once it has set[47].

Portland cement has four main components: tricalcium silicate – C_3S which is known as alite, dicalcium silicate – C_2S which is called belite, tricalcium aluminate – C_3A which is known as aluminate, and tetracalcium aluminoferrite- C_4AF which is known as brownmillerite. To form this cement iron oxide, alumina, silica and lime are heated in a kiln at a series of temperatures up to 1500°C. It is at this hottest temperature which is called the 'clinkering temperature' that forms the alite and belite. The aluminate and brownmillerite are within the liquid phase at this point, during cooling they crystalise. After this mix has been heated and cooled between 3% and 5% of gypsum is added. The gypsum prevents the cement flash setting. This is then pulverized, forming Portland cement[47]. The two calcium silicate phases, alite and belite, account for over 80% of the contents of Portland cement, belite usually will not be more than 20%[47].

The final Portland cement mixture is anhydrous, and will set when mixed with water. The starting components are more soluble than the end phases so complete hydration takes place. The four main components all have different reactions when hydrated, and research has been undertaken to understand them[47].

Both alite and belite hydrate to form calcium hydroxide (portlandite) and calcium silicate hydrate. The reactions are shown below in equations 1 and 2. Alite above, and belite below. The product of this reaction is classed as semi-amorphous and is referred to as C-S-H, it is the principle binder[47].

$$2C_3S + 6H \rightarrow C_3S_2H_3 + 3CH \quad (1)$$

$$2C_2S + 4H \rightarrow C_3S_2H_3 + 3CH \quad (2)$$

After the cement is hydrated it undergoes what is known as the 'induction period'. During this phase the silica containing phases exhibit low reactivity, and have little affect on properties such as rheology. Eventually the rate of hydration increases, with alite having a much faster reaction rate than belite. Alite therefore primarilly provides the cements early setting and strength, with belite only impacting the strength when setting is complete[47].

When the silicate phases are hydrated they undergo an exothermic reaction. There are five stages of the hydration reaction; Preinduction Period, Induction Period, Acceleration Period, Deceleration Period, and the Diffusion Period[47].

During the preinduction period, which is very fast and only lasts for a few minutes, the cement is initially hydrated and mixed, causing heat to be released. C-S-H is created surrounding the C_3S. When the alite encounters water the surface of the crystal is protonated, causing the outermost O^{2-} and SiO^{4-} ions to change into OH^- and H_3SiO_4- ions. This outerlayer then undergoes the following reaction as shown in equation 3 below[47].

$$2Ca_3SiO_5 + 8H_2O \rightarrow 6Ca^{2+} + 10OH^- + 2H_3SiO_4^- \quad (3)$$

Once the solution is supersaturated with C-S-H it then precipitates, following the reaction in equation 4 below. This occurs at the interface, and assumes a C to S ratio of 1. During preinduction the lime (CaO) concentration increases as hydration progresses[47].

$$2Ca^{2+} + 2OH^- + 2H_3SiO_4^- \rightarrow Ca_2(OH)_2H_2Si_2O_7 + H_2O \quad (4)$$

The next step is the induction period. During this stage the heat produced from the reaction decreases, the C-S-H gel continues to precipitate, and calcium and hydroxide ions continue to increase in concentration. Once the concentration of the ions reaches supersaturation $Ca(OH)_2$ begins to precipitate out. Once this happens hydration begins again. This stage can last several hours when undertaken in ambient conditions. There are two different theories as to how this stage ends. One of which is the protective layer theory which proposes that the C-S-H gel has low permeability

which inhibits much hydration. Eventually the gel layer bursts which leads to a large release of alite and belite which then react to form more gel[47].

The other theory is the delayed nucleation theory (Figure 8) which states that the gel changes its morphological properties which increases its permeability, meaning water can diffuse into it and increase the rate of hydration[47].

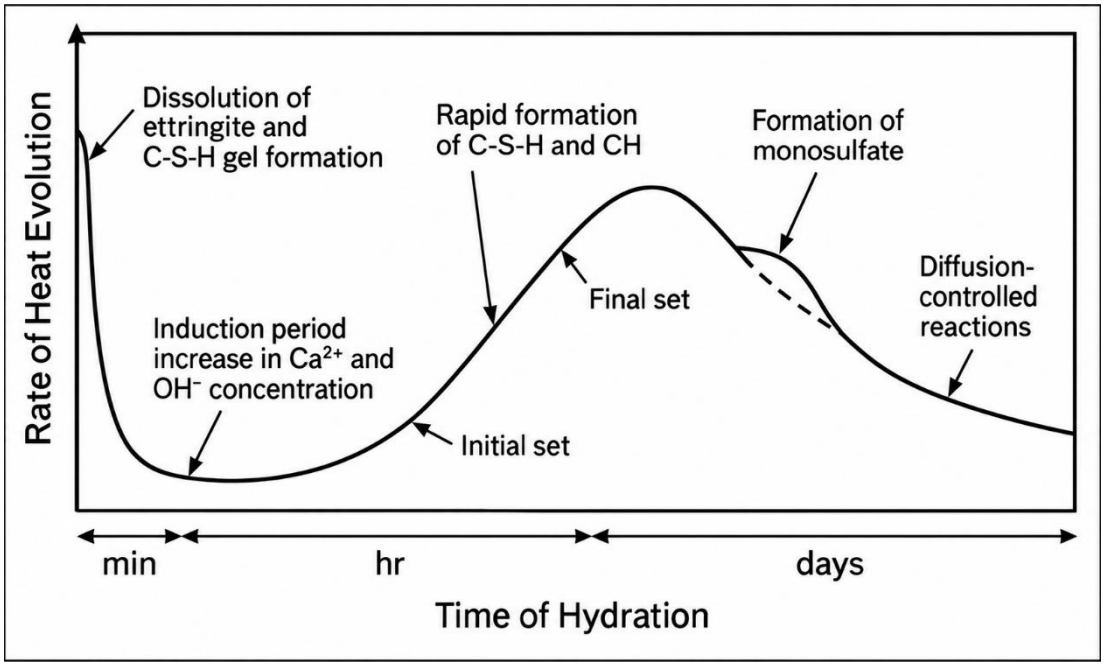


Figure 8: The stages of hydration of Portland cement [47].

After this the cement undergoes its third and fourth stage, the acceleration and deceleration periods (the setting period). Following the previous step very little alite has undergone a hydration reaction. During this step very fast hydration takes place. Whilst in the acceleration period the solid calcium hydroxide crystalises, causing the C-S-H gel to take its place, forming a network. This is what leads to the strength development of the cement, and also leads to a lower porosity. When the porosity has decreased substantially, no more C-S-H gel can move into the network, decreasing the hydration rate. This can take a few days when at ambient conditions[47].

The next and final step is known as the diffusion period. The porosity continues to decrease, slowing hydration, and increasing the strength. This period is continuous, as the portlandite crystals eventually engulf the remaining alite, preventing the system from becoming fully hydrated[47].

The formation of Ettringite within cement

Ettringite is formed when alite (C_3A) reacts with calcium and sulfate ions. Ettringite has a needle like crystal structure and can stick to the surface of other C_3A molecules, slowing hydration of the alumina phases[47]. If there is not enough sulfate present within the cement to react with all of the available C_3A then unhydrated C_3A will begin to react with ettringite, this produces $3CaO.Al_2O_3.CaSO_4.12H_2O$, monosulfate. If the sulfate concentration within the cement is then increased this can cause a reaction, called sulfate attack, that converts the monosulfate back into ettringite. If the cement is cured at high temperatures the C_3A and C-S-H will be in competition for available sulfate, this leads to hardened ettringite formation. If the cement is then cooled then a process called delayed ettringite formation can occur, where sulfate that has reacted with CSH is released to form ettringite by reacting with monosulfate. This process damages the cement[48].

During the hydration of C_3S, ettringite reacts to form monosulfate which is dispersed throughout the CSH. As the CSH continues to hydrate the permeability of the cement is reduced, by reducing the volume of the capillary porosity as its tortuosity is increased. The increased strength and lowered permeability are influenced by this slow hydration reaction[48].

When NRVB cement is placed into groundwater solutions, the sulfur concentration decreases within the groundwater, and the amount of ettringite within the NRVB increases over time. This demonstrates that NRVB will absorb sulfate from groundwater and produce additional ettringite over time. This occurred with NRVB in both groundwater and saline solution. It has also been found, using Mercury Intrusion Porosimetry (MIP) that there is very little difference between the NRVB before and after exposure to saline and groundwater[3]. However, a limitation with MIP is the large amount of pressure that is applied to the NRVB cement to assess it. NRVB cement has a low mechanical strength, so it is possible that its pore structure would be damaged or affected by the high pressures, affecting the final measurement[3]. Other porosity measurements need to be conducted alongside MIP to correlate the answers.

The impact of varying the curing and mix conditions of cements on mineralogy

Various cement mixtures have been studied at a wide range of curing temperatures up to 400°C by numerous scientific groups[49–51]. The temperature that the Portland cement is cured at has a large impact on the state of the final cement; it impacts the stability and morphology. The hydration rate of cement is increased with temperature, reducing the induction, and setting stage. An NRVB cement product generally has lower strength when it is cured at higher temperatures as hydration is hindered. The products are unaffected up to 40°C, and above 110°C the gel becomes unstable. Over 60°C ettringite destabilizes, turning into monosulfoaluminate and gypsum[47].

When Dyckerhoff cement has over 20% silica added to the cement mix by weight and the mix is then cured at 200°C within hydrothermal reactor vessels, excess 11 A° tobermorite and xonotlite is grown, and less a-dicalcium silicate hydrate is produced. This results in a stronger cement as a-dicalcium silicate hydrate causes strength retrogression in cements. Excess silica has also been found to trigger gyrolite formation as plate-like crystals. This also leads to an increase in strength within the cement[52].

If over 25% of silica is added to the cement mix, then xonotlite forms. The xonotlite forms from minerals such as octacalcium pentasilicate and reinhardbraunsite. If further silica is added then truscottite forms. This hexagonal, plate-like crystal also contributes to a stronger cement[52]. The addition of silica however leads to a decrease in permeability.

Another way to increase the strength of the cement is to add alumina to the mix. When 10% of alumina is added to a cement mix cured between 200 and 350 °C jaffeite crystals form within the cement pores. These needle-like structures grew amongst the hydrogarnet crystals, leading to an increase in strength due to a decrease in porosity[52]. When alumina is added to a cement mix, and is cured at 200 or 250°C, a similar mineralogy is formed as the jaffeite and portlandite combine with the hydrogarnet phase. At a curing temperature of 250°C no α-dicalcium silicate hydrate forms, however a reinhardbraunsite phase does. α-dicalcium silicate hydrate is usually formed in cements cured at or above 200°C. At larger amounts of alumina only jaffeite is present alongside the hydrogarnet, unreacted corundum can also be found. When the cement was cured at 300°C there is an additional crystal phase

present – calcium aluminium oxide hydrate (tetra calcium trihydrotrialuminate), and when cured at 350°C bicchulite was also found[53].

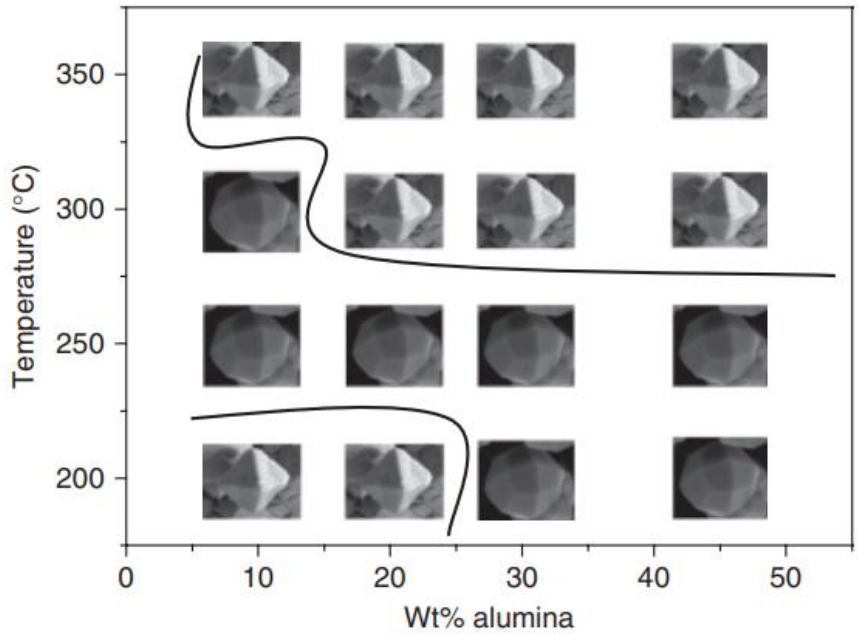


Figure 9: How the shape of hydrogarnet crystals change with the % of alumina and the curing temperature [53].

When cement is cured between 200 and 350°C and alumina is added to the mix, hydrogarnet is the main phase that forms that contains aluminium. However, the actual composition of the hydrogarnet phase relies on the quantity of silica that is present within the cement, and the temperature that the cement is cured at. For example, the size of the hydrogarnet unit cell varies depending on the composition (how many atoms are contained within the unit cell). Additionally, all of the magnesium and sulfur from the original cement mix are found within the hydrogarnet, iron can be found in the hydrogarnet and in other cement phases. Two types of hydrogarnets are formed within cements: octahedral and icositetrahedral[53] (Figure 9).

When cement is cured at temperatures above 110°C, tobermorite is formed, it then reacts further to form xonotlite or gyrolite when heated to 150°C, this reaction is dependent on the silica content. Adding alumina to the cement, however, can stabilize tobermorite up to 250°C. When gyrolite is then heated to 250°C truscottite is formed. Truscottite and xonotlite are then present to 400°C[50]. Jaffeite is metastable and is rarely found[49]. If silica is added to the cement, it slows the hydration process. This leads to an intermediate step where xonotlite and gyrolite are present within the cement, before jaffeite, α-C_2SH, and portlandite are formed. If the cement contains

alumina, then jaffeite and α-C_2SH are the intermediate step, and the end phase is a siliceous katoite hydrogarnet[51].

Adding silica and alumina to the cement mix then curing at 200°C also produces tobermorite, kilchoanite, jaffeite, corundum, and hydrogarnet to be present (Figure 10). As the amount of silica is increased kilchoanite is replaced by xonotlite, and when cured at 250°C there is no kilchoanite present at all. When cured at 300 and 350°C foshagite can be found rather than tobermorite[53]. Tobermorite stabilizes and improves the strength. When both alumina and silica are added the cement samples mineralogy's and strengths were similar when cured at either 300 or 350°C[52]. Cements cured at 300 and 350°C on average show more favourable permeability behaviour than lower curing temperatures due to the phases that are formed, the wide range of crystalline shapes associated with the phases, and how they block the pores preventing fluid ingress[52].

Proportions (wt%)			200°C			250°C			300°C			350°C		
Dyckerhoff cement	Silica flour	α-Al_2O_3	% hgnt	*y*	Other phases	% hgnt	*y*	Other phases	% hgnt	*y*	Other phases	% hgnt	*y*	Other phases
100	0	0			*p, j, a*			*p, j, r*	16	1.6	*p, j, r*	15	1.3	*p, j, r*
95	0	5	40	1.9	*p, j, a*	47	1.8	*p, j, r*	61	1.8	*p, j*	69	1.7	*p, j*
90	0	10	64	2.0	*p, j*	87	2.1	*p, j, r*	76	1.9	*p, j*	82	1.8	*p, j*
85	0	15	82	2.0	*p, j*	87	2.1	*p, j*	88	2.0	*p, j*	81	2.0	*p, j, d*
80	0	20	97	2.1	*j*	92	2.1	*j*	83	2.1	*j, d*	72	2.0	*p, j, d, b*
75	0	25	88	2.2	*j, c*	82	2.1	*j, c*	$hgnt_1 = 71$ $hgnt_2 = 3$	2.1 1.0	*j, d*	60	2.0	*j, c, d, b*
70	0	30	80	2.1	*j, c*	75	2.1	*j, c*	$hgnt_1 = 63$ $hgnt_2 = 4$	2.1 1.0	*j, d*	56	2.0	*d, b, c*
65	0	35	74	2.1	*j, c*	70	2.1	*j, c*	62	2.0	*j, c, d*	51	2.0	*d, b, c*
60	0	40	73	2.1	*j, c*	62	2.1	*j, c*	47	2.0	*j, c, d*	43	2.0	*d, b, c*
55	0	45	60	2.1	*j, c*	55	2.1	*j, c*	49	2.1	*j, c, d*	40	2.0	*d, b, c*
50	0	50	55	2.2	*j, c*	51	2.2	*j, c*	44	2.0	*j, c, d*	35	2.0	*d, b, c*
80	10	10	49	1.6	*j, k, t, c*	89	1.5	*j*	93	1.4	*j*	75	1.3	*p, j, f, x*
70	10	20	61	1.6	*j, k, t, c*	88	1.5	*c*	$hgnt_1 = 62$ $hgnt_2 = 31$	1.4 1.0	*j*	$hgnt_1 = 46$ $hgnt_2 = 33$	1.2 0.9	*p, x*
70	20	10	30	1.4	*t, x, c*	48	1.3	*t, x, c*	63	1.0	*x*	$hgnt_1 = 44$ $hgnt_2 = 35$	1.2 0.8	*x*
60	10	30	68	1.5	*j, t, c*	67	1.4	*t, c*	$hgnt_1 = 47$ $hgnt_2 = 35$	1.5 0.9	*c*	$hgnt_1 = 37$ $hgnt_2 = 36$	1.1 0.7	*x*
60	20	20	26	1.4	*t, x, c*	34	1.2	*t, x, c*	$hgnt_1 = 12$ $hgnt_2 = 21$	1.1 0.8	*x*	14	0.8	*c*
50	10	40	54	1.5	*t, c*	48	1.3	*t, x, c*	$hgnt_1 = 35$ $hgnt_2 = 28$	1.3 0.9	*x*	65	0.8	*c, b*

Figure 10: The phases found by Kyritsis and Meller et al. when synthesising various cement systems between 200 and 350°C. Codes: p = portlandite, j = jaffeite, r = reinhardbraunsite, c = calcite, a = α-C_2SH, t = tobermorite, k = katoite, x = xonotlite, f = foshagite, c = corundum, b = bicchulite, d = calcium aluminium oxide hydrate[39].

Before the cement undergoes hydration, it contains alite, belite, gypsum, and ferrite. During hydration above 100°C, the alite reacts to form jaffeite, and belite reacts to form the very weak α-C_2SH phase. After two hours the anhydrous calcium silicates are mostly gone, and that there are no more mineralogical changes within the cement[51]. The α-C_2SH phase is unstable and contributes to a reduction of strength

known as strength retrogression[51]. The loss of strength is caused by the belite mineral unit cell shrinking as it becomes α-C_2SH. To stop α-C_2SH from forming silica is added to the cement mix to reduce the C:S ratio and promote the formation of other phases with more favourable strength characteristics. Controlling the phases that form is important in knowing the characteristics of the cement and how it will behave long term[51]. In real cement samples the α-C_2SH remains present up to 200°C, and tobermorite is stable up to 300°C, when silica was added to be between 11 and 33% the weight of the cement[49].

When a Portland cement suitable for use in an oilwell is cured at 200 and 250°C with excess water it will have a composition of portlandite, jaffeite, and α-C_2SH after 5 days of curing, and anhydrous calcium silicate phases (alite, belite) will still remain present after extended curing timeframes (10 days). This is an issue as not only is the weak α-C_2SH phase created but it also has extended the time needed for the cement to set[51]. It is suggested that this could be reduced by curing at a higher temperature. There is also the possibility of the cement interacting with a silica sealant, as silica is known to slow the setting process this would mean the cement could react with chemical species within the groundwater/ host environment[51].

The properties of the minerals commonly found within cement

Different crystal phases within the cement have different properties due to their chemical composition, and structure. For example, cements with tobermorite show a lower permeability and a higher strength than xonotlite, therefore a cement that contains a significant amount of tobermorite will have higher strength and be less permeable to water. Tobermorite has two different crystal forms, one of which is ‘normal’ and is more vulnerable to heat than its ‘anomalous’ form which can remain stable at higher temperatures. This is because the ‘anomalous’ form can interact with aluminium ions to stabilise itself. If alumina is added to the cement mix it can be assumed that the ‘anomalous’ form is present over the ‘normal’[49].

Xonotlite is commonly found when the amount of silica added is more than 11% of the weight of the cement and is unaffected by alumina additions[49]. Increasing the curing temperature has been found to lead to more silica being used[49].

Kilchoanite is a metastable phase only observed at very short curing times when cured at lower temperatures or can be observed when the cement is cured above 500°C. At a curing temperature of 500°C the cements contain no sulfate phase due

to the sulfate being consumed by the jaffeite, hydrogarnets, xonotlite, gyrolite, and reinhardbraunsite phases[49].

The mineral truscottite contributes to strength more than gyrolite. Truscottite is found when cement is cured at 350°C, opposed to gyrolite which is formed at lower temperatures[52]. This is because cements formed at 350°C have been found to have a 25% higher compressive strength compared to cements cured at 200°C[52]. Truscottite has also shown to greatly reduce the permeability, providing the lowest permeability C-A-S-H cement.

At 350°C bicchulite and calcium aluminium silica hydrate form, these both reduce the overall strength. These two new mineral phases also cause a reduction in permeability. This is due to the calcium alumina silica hydrate having a plate like structure. These form between the hydrogarnet, blocking any fluids from passing through the pores. To promote the formation of truscottite, alumina and silica are required. Other cements without silica or alumina added show no formation of 11 A˚ Tobermorite present, and a reduction in strength[52].

The strength, permeability, and porosity of a cement can be gauged by the degree of crystallinity measured with X-ray Diffraction (XRD). In previous research the degree of crystallinity has been labelled as either ‘good’ or ‘poor’, with ‘poor’ meaning the sample has an XRD spectrum with widened peaks or a raised background as a result of gel content or amorphous crystals; and ‘good’ crystallinity when the spectrum has sharp peaks and a low background[50]. This classification system assumes the conditions all samples are measured will remain stable, and there is no error in gathering or evaluating the data. Alumina can increase the degree of crystallinity, and cements containing xonotlite show better crystallinity than cements that contain just silica[50].

Research into NRVB cement without additives is limited, and the research that has been undertaken has a small scope, and only uses one analytical technique to assess the data meaning it is not validated.

1.5 Research gap, and how this thesis will contribute to the GDF Safety Case

As the GDF is expected to store the radioactive waste for thousands of years it is vital that the backfill can fulfil its purpose and remain safe, and stable. This thesis investigates the effect that high temperatures, the ratio of raw materials, and the curing conditions have on the phases within NRVB cement. This is important to understand as key features of NRVB, such as its high pH, led to its selection as a key candidate for the backfill material, and any alteration to these properties could reduce its effectiveness and lead to a release of radiation to the surface/ groundwater. After the effect of curing the NRVB cement is understood then the implication of the mineralogical changes on radionuclide retention is studied.

Within the GDF the HLW will be stored in an environment that naturally provides barriers and protection. For example, the depth of the GDF is a natural separation between the GDF and the surface. Two backfill systems have been previously studied for use in the UK GDF; bentonite, and NRVB cement. The KBS-3 concept for GDF uses bentonite as a buffer system around sealed copper cannisters with cast-iron inserts[54]. Bentonite would protect the waste canisters from any geological movements and would possibly provide the additional benefit of adsorbing radionuclide leaks from the canisters. Bentonite is also able to stop the flow of groundwater into the facility through its natural properties. It is also able to undertake swelling when it is hydrated meaning there are no gaps between the engineered barriers and the natural host rock[34].

Cements can provide significant structural supports and will be used as engineered support systems and barriers. Cements within the GDF would be exposed to groundwater, porewater, the buffer, and other structural materials within the GDF. The cement will react with these different components which could lead to a change in both the cement, buffer, and host environment. Important outcomes from interactions could be a change in the pH, pore structure, pressure, hydraulic conductivity, and the composition[34]. This highlights the importance of understanding the behaviour of the backfill to support the Safety Case for the GDF, and to ensure a long term, safe storage system is in place. NRVB needs to provide effective containment of the radioactive waste emplaced within it for over 10,000 years if it is used as the backfill for the GDF, despite its interactions and changes from interacting with the host environment and stored waste (rock, groundwater, radionuclides)[3].

NRVB cement is made up of different phases, which vary depending on the ratio of materials and the conditions it is made and cured at. The different phases have different crystal structures, and ratios of elements. It is important to know what mineralogical phases the NRVB will contain at different times and temperatures as they have different properties such as strength[52].

It is also important to understand the porosity of cement as this directly impacts the durability[55]. The cement needs to have a low porosity to ensure it has sufficient strength, and a low hydration heat. Cement phases from the clinker can be present after 18 months of curing, suggesting it has a low rate of hydration. As the cement continues to hydrate over time the porosity will decrease. This is an ideal property as it will reduce the ingress of groundwater, and hence the interaction with it[33].

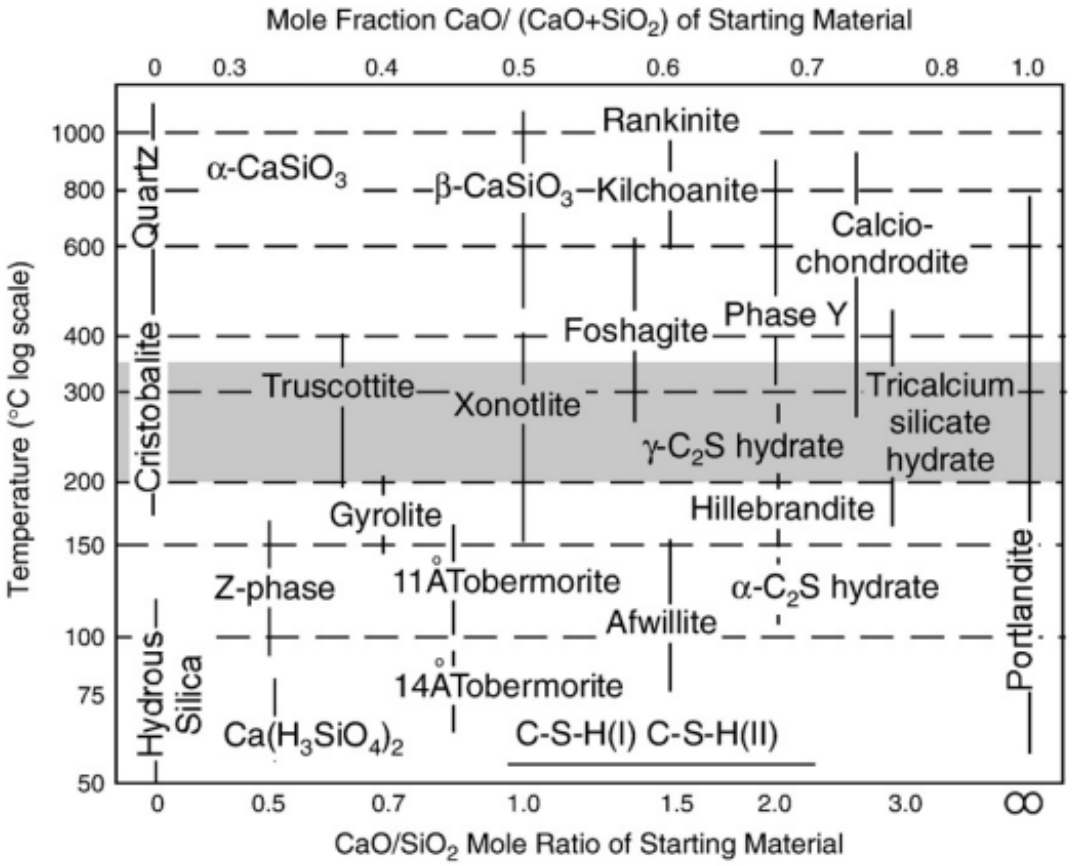


Figure 11: A Phase diagram showing different phases within C-A-S-H cement[41]

Previous work has been done to study the effect of temperature and ratio of raw materials on the phases of cement systems containing alumina (C-A-S-H)[56] (Figure 11). It is also understood that an increase of temperature will increase the rate of hydration which will increase the strength of the cement[36]. However, cement contains unstable phases such as weak α-C_2SH, which can form at high temperatures and

need to be avoided. Therefore, there is a curing temperature at which strength can be increased, however past this temperature the strength will be reduced.

Existing research has not studied NRVB at high temperatures (over 90°C). This project initially studies NRVB at temperatures up to 250°C which would be suitable for storing higher activity wastes. This research has a strong focus on method development and standardization, as analysing cements with XRD, SEM, etc. is difficult as beam damage is very common with cements, and they are very sensitive to effects from air such as carbonation[57].

Abbreviations are commonly used to describe the components of cement (Table 3). This abbreviated nomenclature is used throughout this thesis.

Table 3: The nomenclature used to describe Cementitious systems[51]

Component	**Shortened nomenclature**
CaO	C
SiO_2	S
H_2O	H
Al_2O_3	A
Fe_2O_3	F
SO_3	S
TiO_2	T
FeO	f
P_2O_5	P
Li_2O	L
K_2O	K
Na_2O	N
CO_2	$\bar{C}$
SO_3	$\bar{S}$

Chapter 2 Optimisation of sample preparation for XRD analysis including cementitious hydration arrest

2.1 Introduction

2.1.1 Importance of XRD in cement research

X-ray diffraction (XRD) is a common and effective analytical technique in cement research due to its ability to identify and quantify crystalline phases within cementitious materials[58,59]. It is usually used to investigate hydration reactions, thermal phase transformations, degradation mechanisms, and long-term mineralogical evolution[56]. In studies involving radioactive waste encapsulation materials such as NRVB cement, XRD analysis is particularly important as the mineral phases directly affect the chemical and physical behaviour of the material, including pH buffering, porosity evolution, durability, and radionuclide retention capabilities[60,61]. Quantitative phase analysis using techniques such as Rietveld refinement is therefore important in understanding the long-term performance of cementitious materials under repository-relevant conditions[62].

Despite the widespread use of XRD, obtaining reliable mineralogical data from cement systems has challenges. Cementitious materials contain a large proportion of poorly crystalline and metastable phases which are highly sensitive to environmental conditions during sample preparation and analysis[59]. Hydrated phases such as calcium silicate hydrate (C-S-H), ettringite, and portlandite can undergo significant alteration during grinding, drying, storage, and exposure to vacuum or atmospheric conditions[58]. In addition, the high amorphous content and preferred orientation effects commonly present within hydrated cements can skew both qualitative and quantitative analysis[63]. These challenges become more significant when investigating subtle phase changes, where distinguishing between genuine mineralogical evolution and preparation-induced artefacts is essential.

2.1.2 The effect of carbonation and hydration arrest on cements

One of the most significant sources of alteration during XRD preparation of hydrated cementitious materials is carbonation. Carbon dioxide (CO_2) can be introduced to the cement through atmospheric CO_2 or from CO_2 that has dissolved in the water used in

the hydration reactions. As Figure 12 shows, the amount of CO_2 dissolved in water can be measured using the pH[64].

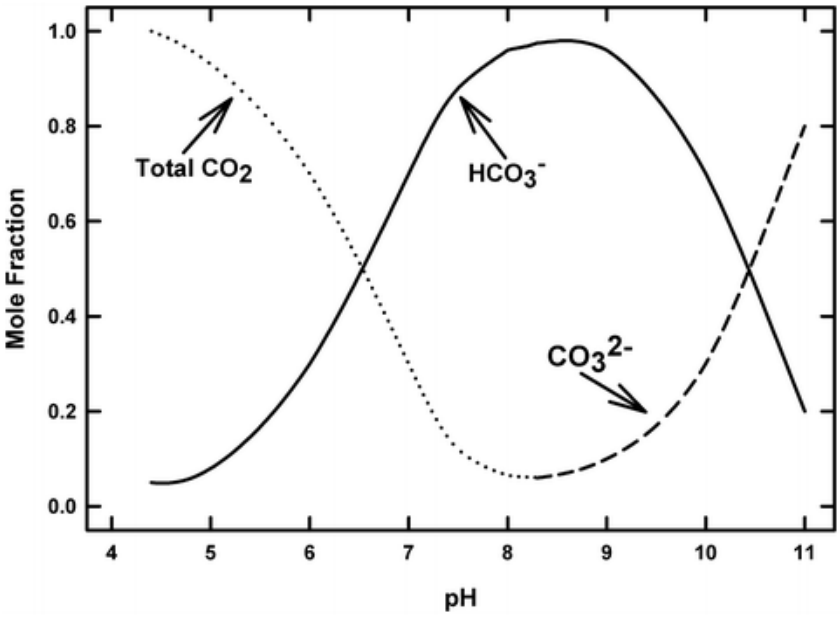


Figure 12: A diagram showing the effect of pH on the amount of CO_2 dissolved into water[64].

Carbon dioxide reacts with hydrated cement phases, particularly portlandite and C-S-H, producing carbonate phases such as calcite, aragonite, and vaterite[65,66]. Even limited atmospheric exposure can lead to measurable carbonation within Portland cement systems, altering the mineralogical phases measured during analysis. Carbonation also results in the decalcification of C-S-H phases, changing both the chemistry and structure of the material[66]. These changes are an issue when studying thermally altered cements, as carbonation products may obscure or overlap with key diffraction peaks associated with hydration and decomposition products[67].

In addition to modifying the mineralogy of the sample, carbonation can affect the interpretation of quantitative phase analysis. The formation of calcite peaks during atmospheric exposure may falsely suggest mineralogical transformations that did not occur during curing or thermal treatment. Similarly, the consumption of portlandite during carbonation can lead to underestimation of hydration products and inaccurate interpretation of hydration progression or thermal degradation[62]. Carbonation can significantly alter the microstructure and phase composition of hydrated cement pastes, highlighting the importance of minimising atmospheric exposure during sample preparation and storage[68]. This is particularly important for NRVB cement

systems, where maintaining an alkaline mineral assemblage is critical for radionuclide immobilisation within a GDF[61].

Several approaches have previously been used to minimise carbonation during cement analysis. These include solvent exchange drying, freeze drying, preparation within inert atmosphere glove boxes, vacuum storage, and the use of airtight sample holders[67]. Rapid acquisition techniques have also been used to reduce atmospheric exposure during analysis. While these methods have shown varying degrees of success, there is currently no universally accepted methodology for the preparation and analysis of hydrated cementitious materials by XRD. In many cases, preparation procedures are poorly reported or inconsistent between studies, making comparison between datasets difficult[63]. There are also limited studies that have evaluated the effectiveness of different preparation techniques specifically for thermally treated cements.

This lack of standardisation presents a significant challenge when investigating the thermal evolution of cementitious materials[69]. Elevated temperatures can induce subtle mineralogical transformations, including the destabilisation of ettringite, decomposition of portlandite, and formation of high-temperature calcium silicate phases[53,56]. If carbonation occurs during sample preparation, it becomes difficult to determine whether observed phase changes are genuine reaction products or artefacts introduced during handling and analysis. Consequently, the development of a robust methodology that minimises atmospheric alteration is essential for producing reliable and reproducible XRD data.

Carbonation occurs when CO_2 interacts with the cement by dissolving into the water contained within the cement. After curing, the cement still contains water, such as structural water, capillary water, and water contained within the C-S-H gel framework. The water contained structurally is trapped through crystallization reactions with the cement minerals and is therefore chemically bound to the cement. An option to prevent carbonation is to remove the water from the cement. This also arrests the hydration reactions occurring within the cement, giving a more representative sample of the desired time point. This water can only be removed through dehydration reactions. The water stored in the C-S-H gel is bound via hydrogen bonding and capillary tension, and can be removed via evaporation. The water stored in the capillaries and pores is unbound and available within the pore structure and contributes to further hydration reactions. It is this water that needs to be removed via

hydration arrest procedures to best produce a cement representative of that timepoint and degree of curing[67]. Without intervention capillary and pore water continues to react with the surrounding mineral phases thereby altering the mineralogy.

There are various methods of arresting hydration, and drying cement pastes[67,70]. Current research suggests that the drying method that is least destructive to the composition of cement is freeze drying. The second least is oven drying, and the method that has the greatest effect on the mineralogical composition is solvent replacement[67,70].

This chapter investigates the development of an XRD preparation methodology for hydrated cementitious materials designed to minimise carbonation during sample preparation, storage, and analysis. Different preparation and handling techniques are evaluated to determine their effectiveness in preserving the original mineralogy of the cement system. This chapter also investigates the effect of drying methods on the final mineralogical composition, developing a methodology that ensures no further hydration reactions occur and the cements tested are representative and comparable for a specific time point and degree of curing. The methodology developed within this chapter is subsequently applied throughout this thesis to investigate the mineralogical evolution of NRVB cement exposed to elevated temperatures under repository-relevant conditions.

2.1.3 Aims and Objectives

This thesis aims to answer the research question of what happens to NRVB cement when the curing temperature is increased. NRVB cement has been analysed previously using XRD to identify and quantify the mineral phases present[4]. XRD is an established and reliable technique to qualitatively and quantitatively analyse cement[71], and will be used in several chapters of this thesis.

A significant amount of XRD analysis has been undertaken during this thesis, it is therefore important that samples are prepared to a high standard for measurement. Several factors can affect the scan quality of a sample. These include:

- How well ground the sample is, a finer ground sample will have smaller size particles and a smaller size distribution. This impacts the peak shape and

affects quantification as a finer ground sample will produce sharper peaks with better resolution.

- How the sample is dried. It is important to arrest the hydration of the cement quickly so that they are representative of that time point.
- The conditions the sample is exposed to, such as heat or other chemicals. Heat and chemicals can cause mineralogical alterations by interacting with minerals or dehydrating them.
- The carbonation of the sample. This will affect the amount of calcium carbonate the sample contains, as CO_2 reacts with portlandite.

The aim of this chapter is to investigate different preparation methods to ensure the XRD scans are as accurate as possible. Therefore, the diffraction peaks need to be symmetrical and sharp, ensuring mineral identification and quantification are accurate and representative of the samples being measured.

2.2 Investigation into XRD preparation

2.2.1 Mineralogical phase analysis using X-ray Diffraction (XRD)

Different crystalline materials diffract X-rays in characteristic ways that are inherent to their atomic structure and crystal lattice arrangement. X-ray diffraction (XRD) is based on the constructive interference of monochromatic X-rays scattered by periodically arranged atoms within a material, as described by Bragg's law.

Different crystalline materials diffract X-rays in characteristic ways that are inherent to their atomic structure and crystal lattice arrangement[72]. X-ray diffraction (XRD) is governed by Bragg's law, which describes the condition for constructive interference of X-rays scattered by parallel planes of atoms within a crystal:

$$n\lambda = 2d \sin\theta \tag{5}$$

Where n is an integer, λ is the X-ray wavelength, d is the interplanar spacing, and θ is the diffraction angle[73, 74]. Each crystalline phase has a unique set of interplanar spacings, resulting in a characteristic set of diffraction peak positions.

When an incident X-ray beam interacts with a material, its chemical composition and microstructural and macrostructural features such as crystallite size, lattice strain,

preferred orientation, and the presence of multiple crystalline phases affects the resulting diffraction signal[72]. In cementitious materials, this is particularly important due to their inherently complex, multi-phase nature, which commonly includes phases such as portlandite, ettringite, calcite, and residual clinker minerals[58,75]. These factors influence not only peak positions but also peak shapes and relative intensities.

The resulting diffraction pattern, or diffractogram, can be compared with reference patterns stored in crystallographic databases such as the Inorganic Crystal Structure Database (ICSD) [76]. Phase identification is achieved by matching experimental peak positions and intensities with those calculated from known crystal structures[75].

Beyond qualitative phase identification, XRD can be used for quantitative phase analysis through Rietveld refinement, a whole-pattern fitting approach originally developed by Rietveld[73]. In this method, a calculated diffraction pattern is refined against the measured data by adjusting structural, instrumental, and microstructural parameters to minimise the residual difference between observed and calculated intensities[73,77]. The refined scale factors can be used to estimate the weight fraction (W_i) of each crystalline phase according to:

$$W_i = \frac{S_i Z_i M_i}{\Sigma(S_j Z_j M_j)} \quad (6)$$

Where S is the refined scale factor, Z is the number of formula units per unit cell, and M is the molecular weight of the phase[77]. Quantitative XRD (QXRD) is widely applied to cementitious systems to determine phase assemblages that influence mechanical performance, durability, and chemical stability[58,59,75].

Significant limitations arise when applying XRD and QXRD to NRVB systems. A large fraction of hydrated NRVB consists of poorly crystalline or amorphous phases, particularly calcium–silicate–hydrate (C–S–H), which does not produce distinct diffraction peaks and therefore cannot be directly quantified by conventional XRD[59,78]. These phases instead contribute to the amorphous background, introducing uncertainty into quantitative phase estimates. In addition, extensive peak overlap between cement hydration products, preferred orientation effects (notably for portlandite and ettringite), and the presence of minor secondary phases formed during alteration or carbonation can further reduce analytical accuracy[75]. Sample preparation procedures, such as drying, grinding, or exposure to atmospheric CO_2, may also modify NRVB mineralogy and pore chemistry, which is particularly critical for materials

used in nuclear safety assessments[79]. Consequently, XRD analysis of NRVB is most robust when combined with complementary techniques such as thermal analysis, scanning electron microscopy, or geochemical modelling to fully characterise phase assemblage and long-term behaviour[59,79,80.]

When acquiring an XRD scan of a powder, a key factor is how well ground the sample is. A finer sample ensures the phases will be evenly distributed, and the scan will be more representative. It also means the sample will pack better into the sample holder, thereby minimising the surface effects from an unevenly packed sample surface.

2.2.2 Methodology for investigating the preparation technique that produces the optimum sample for XRD analysis

There are a range of methods to prepare and measure a sample with XRD, these preparation techniques can have a direct impact on the results measured[69]. The optimal preparation and measurement conditions will differ depending on the material being measured. Regardless of how established the technique is, to ensure the material is being optimally analysed, refinement and calibration of the technique and XRD machine is needed.

To optimise the preparation of the samples studied in this thesis there are three challenges that need to be addressed:

1. What is the best method for grinding the samples that crushes them to a fine enough powder but does not cause any additional reactions or result in amorphization?
2. How can the hydration of the cements be arrested in a way that is rapid but uses a technique that does not alter the composition of the cement?
3. How can the method used for hydration arrest and XRD sample preparation be optimised to minimise carbonation of the cements?

To ensure the highest quality data was collected, without compromising either particle size or composition, a comparison of preparation methods was completed prior to collecting XRD data on this work.Optimal preparation for XRD analysis

Effect of Isopropanol during micronizing: A cement sample was cured hydrothermally for 5 days, the hydrothermal cell was rapidly cooled and the cement was removed. The sample was hand ground and sieved through a 63μm mesh. Two

lots of the sample were weighed out (2g). One portion was soaked in isopropanol for 24 hours before being centrifuged and dried, the other was put into isopropanol then immediately centrifuged and dried at 25°C in a N_2 oven to constant mass.

Effect of micronizing versus ball milling: one cement sample was split into two portions (2g each), one part was ground with a ball mill (Retsch MM200) dry at 10.1 Hz for 2 minute intervals to allow the sample to cool before being sieved through a 63µm mesh. The other sample was micronized (XRD-Mill McCrone) for 7 minutes per gram of sample at the first speed setting in isopropanol. After micronizing the cement was centrifuged and dried in a N_2 oven at 25°C to constant mass.

Effect of micronizing versus hand grinding and sieving through 63µm mesh: the same cement was split in two (2g each), the sample was hand ground and sieved, half was then removed and micronized with isopropanol. The sample was centrifuged then dried in a N_2 oven at 25°C to constant mass.

All samples were measured with the parameters described below in Table 4. All samples were stored in a N_2 oven at 25°C and were analysed with XRD within 24 hours of preparation.

Table 4: XRD parameters used to measure the cement samples used to investigate XRD preparation methodology.

Parameter	**Setting**
Detector	PIXcel3D-Medipix3 1x1 detector
X-ray tube	Empyrean Cu LFF HR (9430 033 7310x) DK431564
2θ range (2θ)	5.0064 - 79.9934
Time (hh:mm:ss)	03:15:19
Step size (2θ)	0.0131
Steps	5712
Count time (ms)	498.270
Filter	Ni
Rotation	Yes
Secondary Soller slit	dCore Soller slits 0.04 rad
Divergence	PDS for iCore 0.125°
Goniometer	240.0 mm
Kapton film	Yes

2.2.3 Testing the effectiveness of different methods of hydration arrest and XRD preparation in preventing carbonation

To investigate the effect of different components of the hydration arrest and XRD preparation method on the carbonation of the cement CEM I 52.5N it was prepared for XRD four different ways. All pastes were mixed by hand for 15 minutes before being pipetted into PEEK moulds, put into hydrothermal Parr cells, then cured at 200°C for 5 days. The Parr Cells were removed from the ovens and rapidly cooled in cold flowing water. The cement samples were removed from the moulds intact. The hydration arrest followed the cement being removed from the moulds.

One hydration arrest method that was tested was that followed by Meller et al[56]. They prepared their cement pastes for XRD by drying the pastes in a nitrogen oven, then grinding in a ball mill. The cements were then immediately analysed with XRD. They report less than 10 percent of their mass as calcite. The second method was arresting hydration reactions by freeze drying the samples. This process involves submerging the cement pastes in isopentane cooled in liquid nitrogen to approximately -159 °C, then immediately putting the samples into the freeze drier for 24 hours[81]. The samples are weighed before and after, the weight should decrease as the remaining water should be removed from this sample. If the weight has increased then water has condensed on the samples and they are left in the freeze drier for longer. After removal from the freeze drier the samples are ground with a mortar and pestle, then sieved with a 63μm mesh size. After all of the sample has been ground to <63μm 2g is weighed out and mixed with 7ml of isopropanol. This is put into the micronizer and ground for 10 minutes (5 minutes per gram of sample). The solution is decanted into a centrifuge tube, then centrifuged at 7000 rpm for 10 minutes. This is repeated once to ensure the isopropanol has separated from the cement paste. The excess isopropanol is disposed of, and the remaining paste is dried in a N_2 oven at 25 °C until constant mass. This usually takes 4 days.

The third method involves the cement paste being freeze dried and then ball milled into a fine powder. In the final method the sample is freeze dried, ball milled, and then micronized.

These four combinations of methods were chosen to identify if there is a step of the process that is causing the carbonation and can thus be altered or removed to reduce

it. Minimising carbonation is preferable as the more carbonation present in the sample, the less calcium silicate phases are present. This means the cement sample may not be representative. Table 5 summarises the four different methods, and the differences between them.

Table 5: The four XRD preparation methods that were investigated in this set of experiments. Where the Meller method is following that of Nicola Meller, FD= freeze dried, HG = hand ground, M = micronized, BM = ball milled.

Name	**Meller**	**FDHGM**	**FDBM**	**FDBMM**
Freeze Dried		X	X	X
Dried in N2	X	X	X	X
Ball milled	X		X	X
Hand ground		X		
Micronized		X		X
Comment	Not exposed to IPA Not Freeze dried Not hand ground	Method used	Freeze dried Not exposed to IPA	Freeze dried, not hand ground, exposed to IPA

After each hydration arrest method was completed, the samples were stored in the nitrogen oven at 25°C, so no further carbonation with CO_2 from the atmosphere could occur. The samples were split, 2g of each was always stored in nitrogen to provide a zero time point where all carbonation was from preparation or hydration arrest. 2g was then left open to the laboratory atmosphere for 2 hours, and a further 2g was left in the laboratory atmosphere for 24 hours, before being returned to a nitrogen atmosphere. This should be a test of the effectiveness of the hydration arrest methods. If the methods are able to remove all pore water from the samples, then theoretically no further carbonation should occur. This testing also gives an indication of the rate of carbonation in air. If there is no or a slight increase in calcite content between 0h and 2h then sample handling is unlikely to have been responsible for the

carbonation. If there is only slightly more calcite after 24 hours then the rate of carbonation is very low.

XRD analysis was then completed on the samples treated by each hydration arrest method and stored in N_2 atmosphere, and air for 2 and 24 hours. The sample holders were sealed with a very thin layer of Kapton film over the sample hole, the edges were sealed with Sellotape so the samples would not be exposed to air during scanning. The XRD patterns were then analysed using HighScore[82] to identify the mineralogy, and then quantified using TOPAS[83] to determine the amount of calcite and other minerals. The original raw cement powder did not contain any carbon containing components so no calcite should be present.

The pH of the deionized water used to mix the cement was also measured and was compared to water collected from a different location within the laboratory, deaired water, and deionised water collected from a Millipore. Each water sample was collected directly from the respective tap into sterile 50ml centrifuge tubes. Approximately 30-40 ml was collected to minimise the headspace, provide enough sample for measurement, and to allow for room inside the tube for the pH probe to be inserted. Each sample was measured 3 times to allow for the identification of any anomalous results.

2.3 Optimal preparation for XRD analysis

2.3.1 Effect of Isopropanol during micronizing

One technique to prepare a sample for XRD analysis is to grind the sample to a very small particle size that is below 10μm is to use a microniser. This requires adding 1-2 grams of sample to 7ml of liquid and grinding for a set amount of time, based on sample mass[69]. Cements can react with water, so to prevent further hydration reactions during grinding isopropanol is used as coolant/lubricant. However, previous studies have found that alcohol can affect the mineralogical composition of cement[67].

To test whether isopropanol was changing the composition of the cement the following test was undertaken:

1. Two portions of the same cement sample were prepared with the same method.

2. One portion was soaked in isopropanol over night, whereas the other was briefly immersed then removed and dried immediately.
3. The two samples were measured using XRD with the same parameters.

The results of this test are shown below in *Figure 13*.

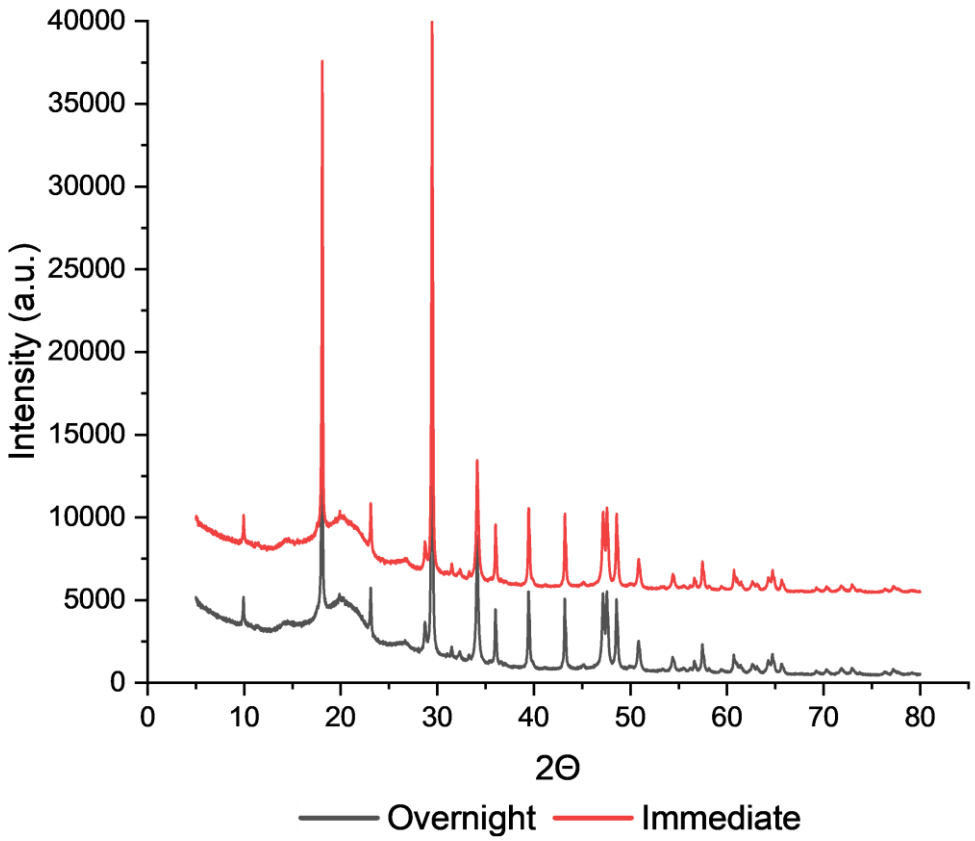


Figure 13: The XRD patterns of the same sample where the black line was centrifuged immediately after it was micronized, and red where it soaked overnight.

The XRD patterns for this experiment showed no difference in the two patterns as can be seen in *Figure 13*. This is a reasonable result, as the interaction of isopropanol with the cement would be controlled by diffusion. The equation for diffusion is below in equation 7 below. Where a is the smallest thickness.

$$t_E = \frac{a^2}{D} \tag{7}$$

After sieving the largest particle is smaller than 63μm. The value for diffusivity, D, of alcohol in cement of $1 * 10^{-11} m^2 * s^{-1}$ [67]. Therefore, the time for diffusion is a maximum of 396.9 seconds, which is approximately 6.5 minutes. This would also

reduce as the cement is in the micronizing mill and the particle size is reduced to 5-10 µm. From the equation it can be assumed that the isopropanol will have fully diffused through the cement regardless of how quickly the cement is centrifuged. However, from the test in section 2.3.2, Effect of micronizing versus ball milling, where micronizing was compared with simply hand grinding and sieving the only difference was the peak symmetry. This suggests that despite diffusing into the cement paste there is no interaction with the cement minerals that causes a change in the XRD patterns.

2.3.2 Effect of micronizing versus ball milling

To study if the isopropanol was altering the mineralogy of the cement the same cement sample was split into two, one part was ground with a ball mill dry and the other was micronized in isopropanol. The results are shown in *Figure 14*.

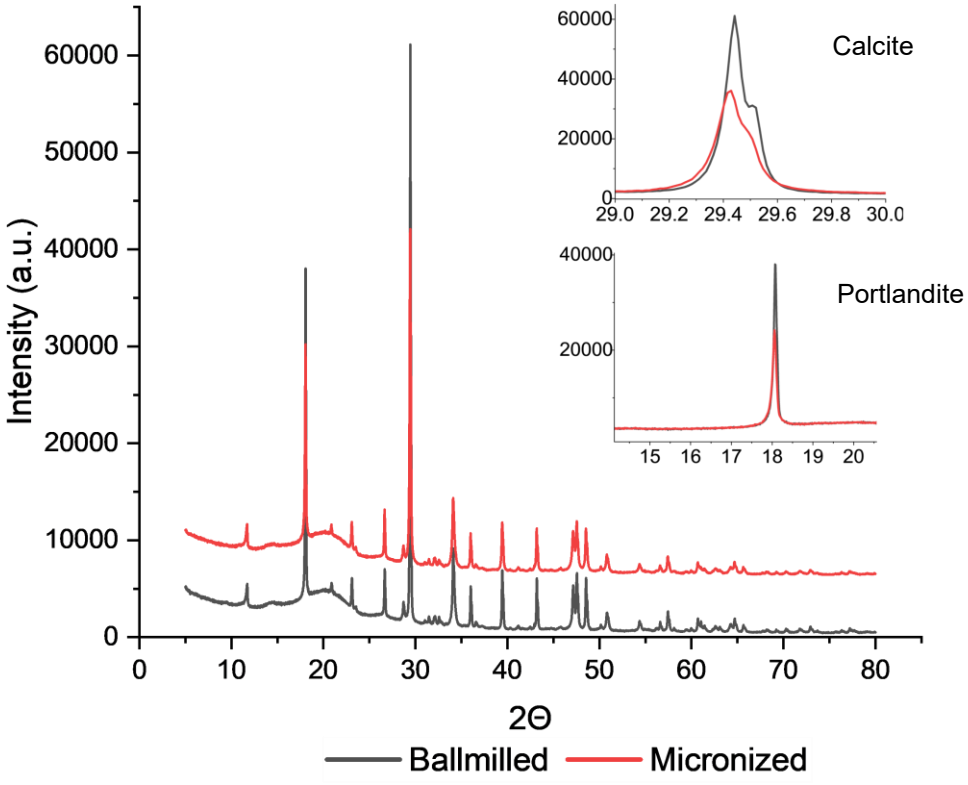


Figure 14: The XRD patterns of a sample that was ground in the micronizing mill (pink) and ground in the ball mill (black) with the only section that was different zoomed in. Zoomed in sections of the pattern show a calcite peak (top) and a portlandite peak (bottom).

The cement ground with the ball mill was dry and was ground in two-minute intervals for approximately two hours. The cement ground in the micronizing mill was combined with 7ml of isopropanol and ground for 10 minutes, as Scarlett et al. found the best grinding time to be 5 minutes per gram[69]. Only two peaks were affected, the portlandite peak and calcite peak (*Figure 14*) – both being lower in intensity when the sample is ground in the ball mill. However, the increase in height on these two peaks is likely due to preferred orientation. The 001 hkl peak on Portlandite is higher when it is more finely ground in the microniser, this is because it allows for better packing so the Portlandite crystals can better align causing preferred orientation[84]. Similarly, calcite has a stronger and more symmetrical reflection on the 104 hkl peak[85].

2.3.3 Effect of micronizing versus hand grinding and sieving through 63µm mesh

To study how effective micronizing was versus hand grinding and sieving through a 63µm mesh the same cement was split in two, the entire sample was hand ground and sieved, half of the sample was then removed and micronized with isopropanol. Both samples were stored under nitrogen. The samples were scanned with XRD, the results are shown in Figure 15.

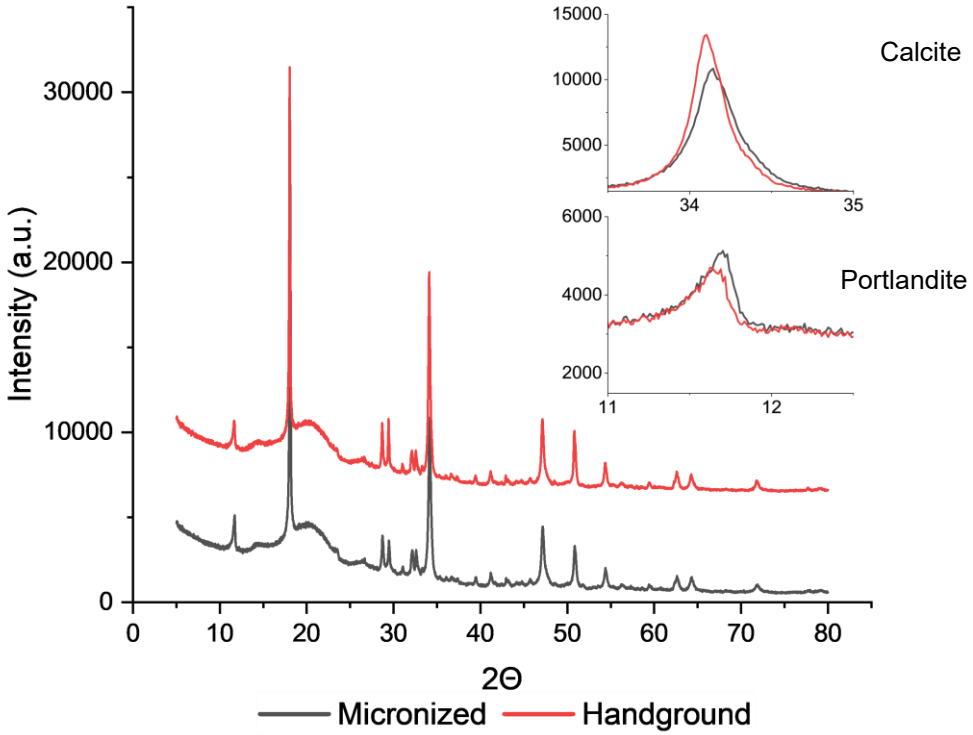


Figure 15: The XRD patterns collected on the same sample where it was hand ground and sieved (black) then half was removed and micronized (red) with some sections that showed a large difference in the symmetry zoomed in on.

Despite having similar patterns, the sample that was micronized shows better peak resolution, particularly for the portlandite peak. Given the superior resolution of the peaks in the XRD pattern this approach will be taken for cement sample preparation for XRD. Micronizing in isopropanol will ensure more reliable quantification using the software TOPAS. As better peak symmetry will allow better peak resolution and more accurate quantification. Although it has a higher amount of preferred orientation for calcite and portlandite, this can be accounted for during refinement in TOPAS.

2.3.4 Testing the effectiveness of hydration arrest and XRD preparation techniques on preventing carbonation

Carbonation takes place when carbon dioxide from the atmosphere dissolves into the cement pore water, forming carbonic acid. This then reacts with the portlandite, forming calcium carbonate, also known as calcite, which is the main product from the carbonation reaction. Carbonation is avoided when studying cements as the calcium

used to produce calcite is taken away from producing other minerals, meaning the final cement may not be representative. It is therefore important that sources of carbonation are identified and minimised if possible.

In this chapter various hydration arrest methods have been used to dry the same cement sample, the cement samples have then been scanned with XRD and their mineralogical phases identified and quantified (Table 6). The calcite column shows the percentage of the cement that formed calcium carbonate, a carbonation product. No calcium carbonate was present in the initial starting mix of the cement so any present in the final product has formed from carbonation.

Table 6: Quantification results for the cements that were tested to see which preparation method was most effective at preventing carbonation. Where the Meller method is following that of Nicola Meller, FD= freeze dried, HG = hand ground, M = micronized, BM = ball milled. T0 = no exposure to air, T2 = 2 hours exposure to air, T24= 24 hours exposure to air.

Sample	Mineral (%)					
	Calcite	**Portlandite**	**Gamma dicalcium silicate hydrate**	**Jaffeite**	**Alpha dicalcium silicate hydrate**	**Reinhardbraunsite**
FDHGMT0	7.38	14.9	38.7	12.27	15.61	11.14
FDHGMT2	7.8	14.48	38.5	12.75	14.96	11.15
FDHGMT24	7.31	13.83	40.74	13.41	14.44	10.28
Meller0	8.01	16.32	37.69	12.47	10.61	14.91
Meller2	9.93	17.31	37.96	12.15	10.59	12.06
Meller24	8.96	16.02	43.3	13.17	11.63	6.92
FDBMM0	7.27	14.96	39.08	12.82	14.9	10.98
FDBMM2	6.41	14.13	37.34	12.33	13.11	16.68
FDBMM24	7.05	13.17	41.99	13.42	13.95	10.41
FDBM0	8.4	17.16	38.76	12.7	9.62	13.35
FDBM2	8.89	16.56	38.58	11.82	10.2	13.95
FDBM24	7.74	15.4	40.82	13.7	9.08	13.25

2.4 Discussion

2.4.1 Amounts of calcite vs. XRD preparation method

Comparing different methods allows for the effect of one component of XRD preparation to be assessed (Table 7).

Table 7: A table showing the four ways the different XRD preparation methods and hydration arrest methods can be compared.

Comparison	Method 1	Method 2	Testing
1	Meller	Freeze dried then ball milled	Freeze drying
2	FDHGM	FDBMM	Grinding method
3	FDBM	FDBMM	Micronizing
4	Meller	FDHGM	Cement drying technique and grinding technique

The difference between the two methods being compared in comparison 1 is that method 2 is freeze dried before being ball milled. The Meller method is dried in a nitrogen oven at 25°C until constant weight. During the freeze drying process the sample is immersed in isopentane cooled to -198.5°C in liquid nitrogen. Some studies have found that exposing cement pastes to alcohol can affect the mineralogy, however these studies do not state how. Therefore, this comparison allows a study into the impact that isopentane exposure and being freeze dried under vacuum has on the cement composition.

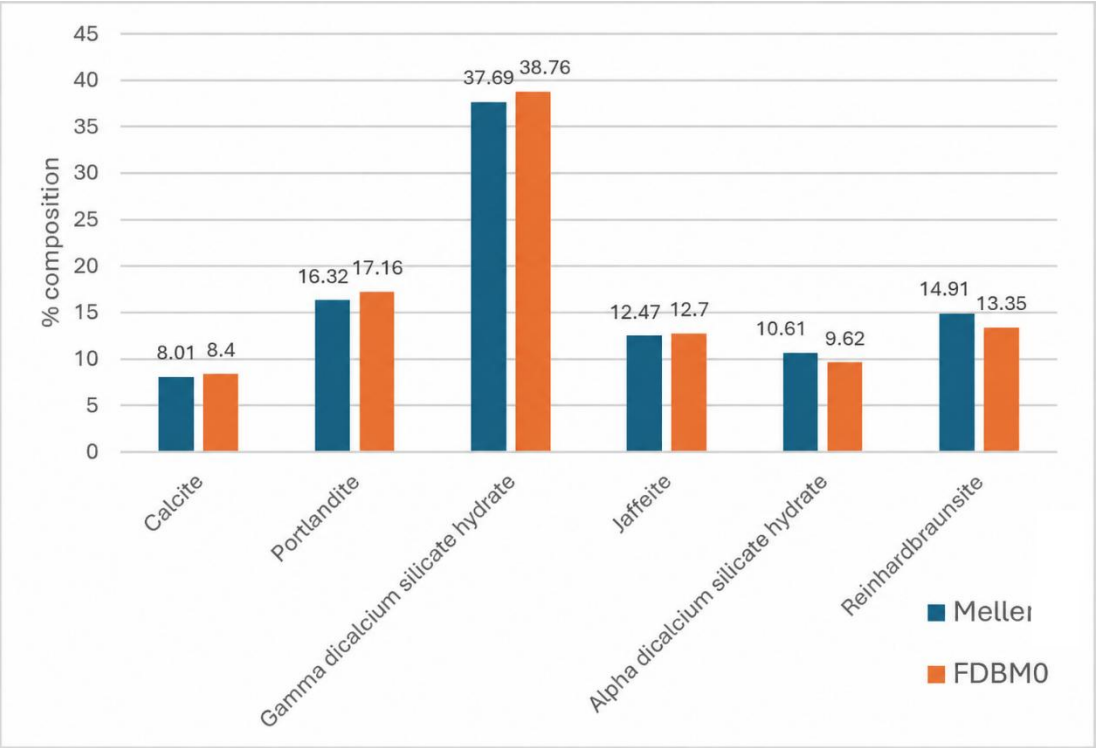


Figure 16: A graph showing the difference in quantities of minerals in the same cement sample that was prepared for XRD analysis two different ways. The difference in these two methods is the hydration arrest method, where the Meller sample was dried at room temperature in a nitrogen oven whereas the FDBM0 sample was freeze dried.

The XRD results (Figure 16) show that the Meller method produced marginally less calcite than first freeze drying the sample. Each mineral is within 1.5% of the two preparation methods, showing a similar mineralogical composition. These results suggest that drying under N_2 and freeze drying do not affect the amount of carbonation, and have little to no effect on the mineralogical composition.

The second comparison compared the results from freeze drying, hand grinding, then micronizing the sample versus freeze drying, ball milling, the micronizing the sample. Therefore these two methods are able to give an indication on whether hand grinding the sample with a mortar and pestle is more effective against carbonation versus using a ball mill. The advantage of using a ball mill is that it grinds the sample significantly faster, particularly when the samples are harder. These samples were cured at 200°C so were relatively weak, therefore hand grinding took approximately the same amount of time. Inside the ballmill the cements will be less exposed to

carbon dioxide in the atmosphere, however the ball mill creates more heat than hand grinding which can alter the composition and degrade certain minerals.

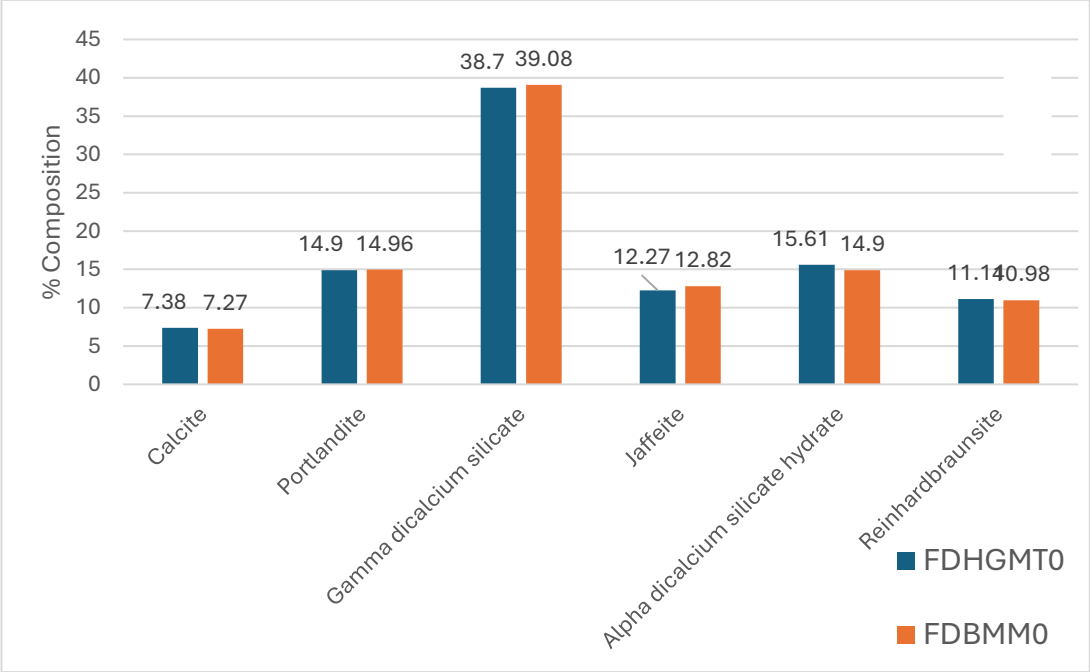


Figure 17: A graph showing the difference in quantities of minerals in the same cement sample that was prepared for XRD analysis two different ways. The difference in these two methods is the grinding method, the FDHGM0 sample was hand ground with a mortar and pestle whereas the FDBMM0 sample was ball milled.

The XRD quantification shown in Figure 17 showed very similar results for this comparison. Ball milling showed a higher amount of gamma dicalcium silicate hydrate present, and less alpha dicalcium silicate hydrate. However, the numbers are very similar so these differences could be due to other factors such as background or scan quality. The difference between these two methods is one has the additional step of micronizing the sample. The results are shown in Figure 18. During micronising the sample is soaked in IPA then ground to a particle size of less than 10µm. The micronized sample shows more alpha dicalcium silicate hydrate, and less reinhardbraunsite. This sample was exposed to IPA.

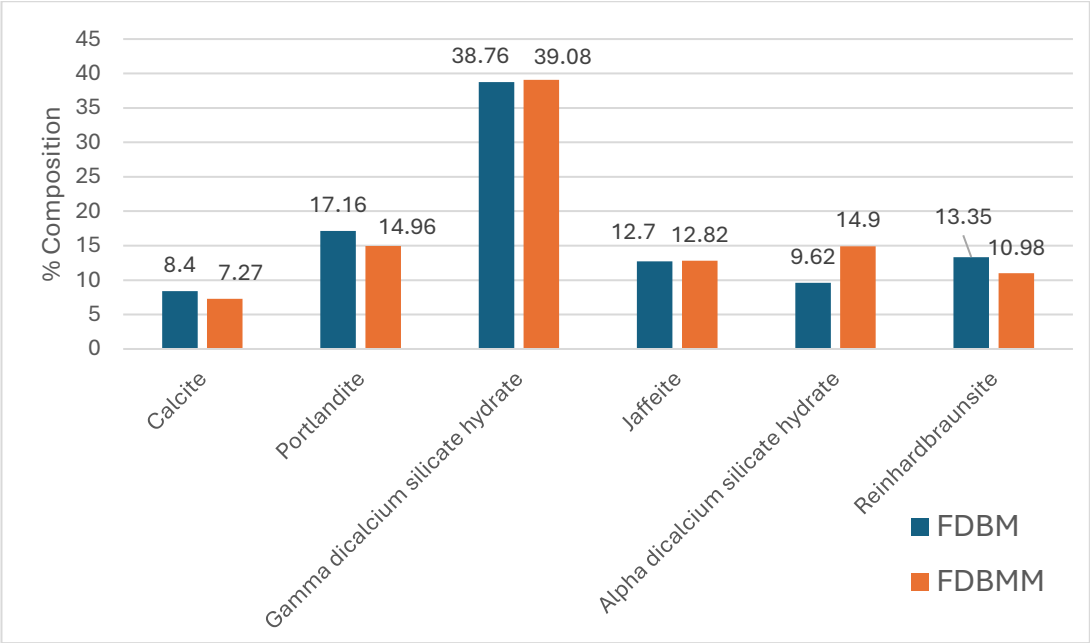


Figure 18: A graph showing the difference in quantities of minerals in the same cement sample that was prepared for XRD analysis two different ways. The difference in these two methods is that the FDBM0 sample was not micronized, so this sample was never exposed to isopropanol.

The Meller method dried their cement slowly at room temperature under nitrogen, the other sample was freeze dried so the hydration arrest would happen much faster. The Meller method was then ball milled, whilst the FDHGMT0 sample was ground using a mortar and pestle, before being micronized in IPA. The results are shown below in Figure 19. The most significant difference is the amount of alpha dicalcium silicate hydrate, and reinhardbraunsite present in each sample. The Meller method shows more alpha dicalcium silicate hydrate, and less reinhardbraunsite. This could be due to the differences in drying methods, exposure to heat in the ball mill, or exposure to IPA in the micronizer.

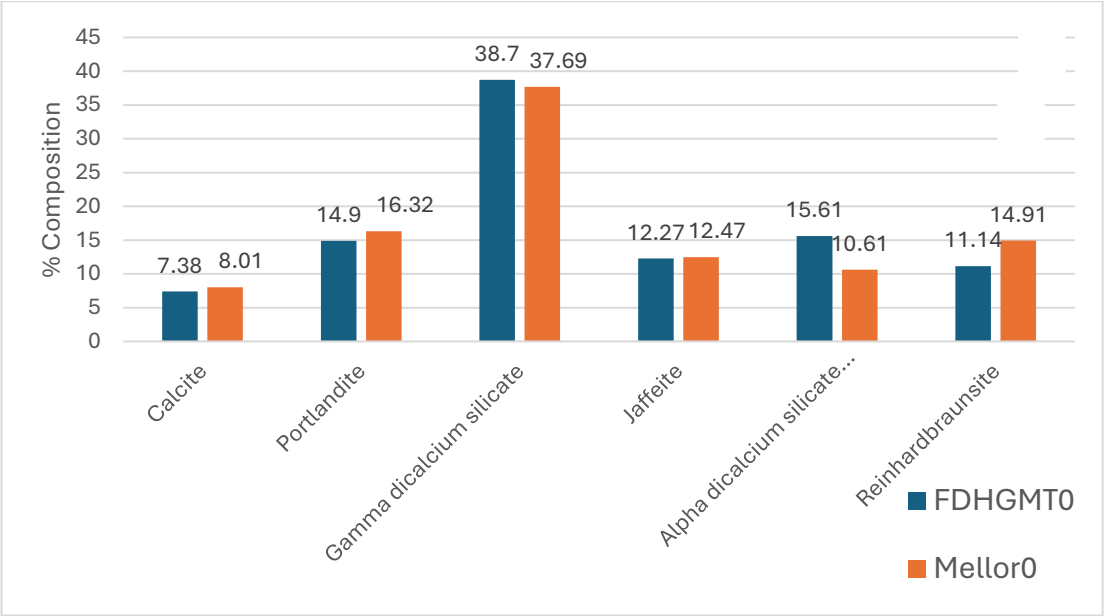


Figure 19: A graph showing the difference in quantities of minerals in the same cement sample that was prepared for XRD analysis two different ways. These two methods are the most different as they were dried and prepared for XRD differently.

Amount of calcite over 24 hours

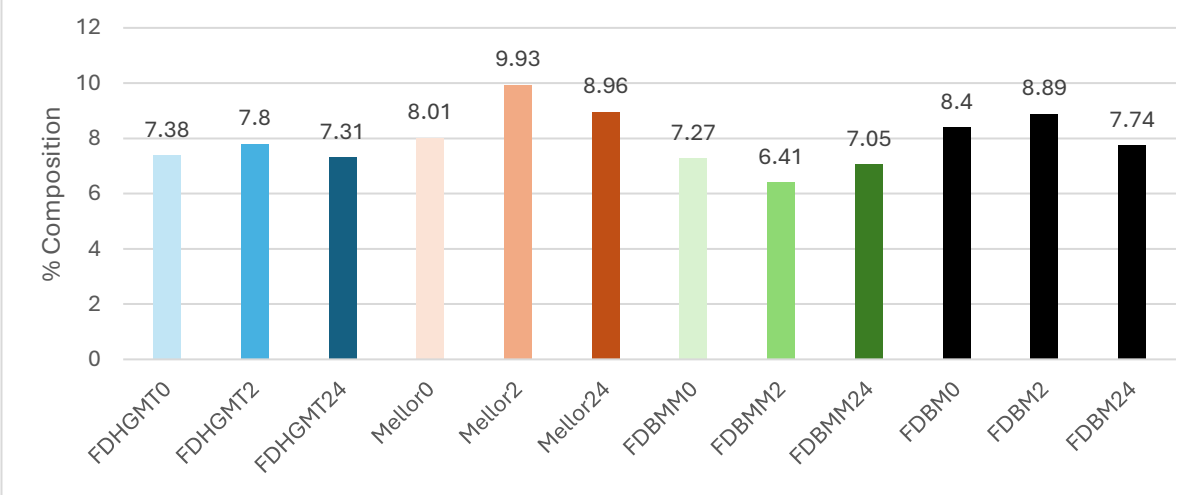


Figure 20: This graph shows the amount of calcite present in each sample when left out for 0, 2, and 24 hours for all four methods.

An amount of the four cements (2g) was exposed to the atmosphere for 0, 2, and 24 hours, after they had their hydration reactions stopped, and were ground for XRD. This was to investigate how effective the hydration arrest methods were. Carbonation occurs when cements are exposed to CO_2 which is then able to dissolve into water

contained within the cement, such as pore water. This then reacts with portlandite to produce calcium carbonate (calcite), and water.

$$CO_2 + Ca(OH)_2 \rightarrow CaCO_3 + H_2O \quad (8)$$

If the hydration arrest is effective, then all pore and excess water should be removed from the cement. This means that CO_2 will be unable to dissolve, and no further carbonation should take place, and that all calcite within the cement is caused during the initial hydration reaction with the CO_2 dissolved in the water used to mix the cement[86,87]. The results are shown in Figure 20, and showed there was no further carbonation for any of the cements. Therefore all hydration arrest methods were effective.

2.4.2 The impact of pH on hydration

One cause for the carbonation is the water used to hydrate the cement. Atmospheric CO_2 dissolves into the pore water so it is possible that this has an effect on the amount of calcite present.

Samples were taken from different locations around the laboratories including the laboratories on the first (Level 1) and second (Level 2) floors. The pH of these was then measured in triplicate, with an average being taken which is given in Table 8.

Table 8: The pH results from the four different tap locations in the Civil Engineering laboratories.

Sample	**pH**
Level 1 DI from tap	6.292
Level 2 Millipore	6.340
De aired water	6.049
Level 2 DI from tap	6.607

The water collected from various sources in the laboratories were all around a pH of 6. At this pH there is approximately 0.6 mole fraction of CO_2 dissolved in the water (Figure 12[88]).

Approximately 10% of the cement samples are carbonate, the XRD sample holders contain 0.6g of cement, so just 0.06g of the sample is carbonate. 0.06g of carbonate

would be 0.00059946 moles, and therefore 0.02638g of CO_2 would need to be dissolved in the water used to hydrate the cement to account for this level of carbonation. This suggests that CO_2 is introduced to the cements during the initial hydration step, and not from the atmosphere after curing, and is therefore unavoidable.

2.5 Conclusions

The XRD preparation method followed by Meller et al.[56] had the highest percentage of calcite when exposed to atmospheric air for 2 and 24 hours, however at 0 hours exposure it had less calcite than the sample that was freeze dried and ball milled. However, all the results are very similar and are comparable to the amount of carbonation found in literature. Meller et al found approximately 10% of calcite in their samples. This shows that the preparation method has very little effect on the rate of carbonation or the amount of calcite. From literature, it is suggested that the carbonation is from CO_2 dissolved in the water used to mix the cement[88]. The pHs found in the labs in James Weir agree with this conclusion. None of the cements carbonated further when exposed to the atmosphere. This confirms that the hydration arrest methods are effective, at least short term, and that the XRD measurements taken are representative of the desired stage of hydration. The method chosen for hydration arrest is drying to constant mass under nitrogen, and for XRD preparation to hand grind using a pestle and mortar then micronize the samples as this produced the XRD diagram with the best peak symmetry, and is therefore best for quantification analysis.

Chapter 3 Investigation into the effect of increasing the curing temperature and altering the C:S ratio of NRVB cement on the mineralogy

3.1 Introduction

Nirex Reference Vault Backfill (NRVB) is a cementitious material proposed for use as backfill in the GDF; it has a high pH [37–39] (12.5 at 25°C[89]), and low viscosity when mixed, setting as a low-strength solid cement (Figure 21).

If NRVB is to be used as the backfill material for the GDF, it must remain fit for purpose for over 10,000 years despite any interactions and changes induced by its interaction with the host environment and stored waste (i.e., rock, groundwater, radionuclides)[3].

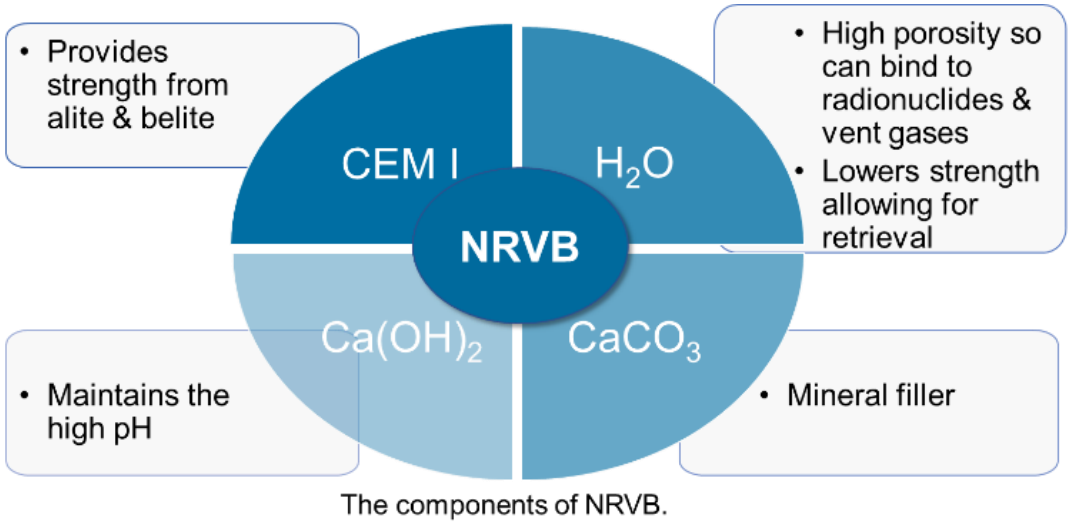


Figure 21: Diagram to show the four components of NRVB and their primary purpose.

3.1.1 Cement chemistry

NRVB cement contains four components, CEM I powder, calcium carbonate, portlandite, and water, as shown in Figure 21. After it is cured NRVB cement is made up of different mineral phases, which vary depending on the ratio of materials (CaO to SiO_2, solid to water etc.) and the conditions at which it is made and cured. The different phases have different crystal structures, and ratios of elements (Ca, Si, O, H, Al, Fe, and other metals in small quantities). It is important to know what mineral phases will be present in the NRVB as minerals are chemically altered and

transformed over anthropogenic and geological time (100 to 10,000 years) as different cement minerals have different strengths and can affect the porosity and material properties[52].

Cement minerals have different properties such as strength, calcium-to-silica ratio, and density. It is important to know what mineral phases will be present within the NRVB as this could influence the design of the GDF. For example, if only weak phases are present, then containment will be required. NRVB has a very high $CaO:SiO_2$ ratio of 7.27, previous studies have not investigated the mineralogy at this ratio and at high temperatures. NRVB typically contains portlandite, calcite, calcium silicate hydrate, ettringite, and monocarboaluminate phases[89].

NRVB has an alkaline pH. The high pH is maintained by the initial dissolution of a portion of the portlandite phase over time into the pore space, and later, when all of the portlandite has been consumed, other calcium silicate phases will dissolve[90]. High pH environments can reduce the solubility of some radionuclides and increase the likelihood of them being captured within the cement. This feature prevents and slows radionuclide escape from the GDF into the surrounding groundwater [39]. It is therefore important that portlandite is present in the NRVB. Portlandite, calcium hydroxide or $Ca(OH)_2$ reacts with the quartz powder, silicon dioxide, or SiO_2 to produce calcium silicate mineral phases. Portlandite is a key phase which prevents radionuclide migration it is consumed and produced during different cement reactions. For NRVB to be an effective cement backfill, and be able to raise the pH, some portlandite must be present in excess in the NRVB and not fully consumed during the cement hydration reactions.

3.1.2 Curing temperature

The temperature at which the Portland cement is cured has a large impact on the state of the final cement, as it impacts the stability and morphology. Cement hydration is increased with temperature, reducing the induction and setting stage. However, the final cement product generally has a lower strength when it is cured at higher temperatures as hydration is hindered. The cement reaction products are unaffected up to 40°C, and above 110°C the C-S-H gel becomes unstable. Over 60°C ettringite, a cement strengthening mineral, destabilizes, turning into monosulfoaluminate and gypsum[47], resulting in a weaker cement.

3.1.3 Aims and Objectives

NRVB is one of the backfill options being considered for encapsulating waste within the GDF. In the UK a site has not been selected for a GDF, depending on the characteristics of the site, such as the host rock, the waste encapsulated will meet different temperature requirements[91]. It is therefore important to study NRVB at a range of temperatures as it is unknown what temperature it will be cured[92]. The cement may also come into contact with waste during the lifetime of the GDF, and it is likely there will be a variable geothermal gradient within the GDF. Nagra have done modelling that shows after 10 years the canister surface temperature will be 160°C in their deep geological repository, and NWS have investigated cement stability to 300°C[91]. It is therefore important to study NRVB performance over a range of temperatures, as the actual curing and long-term thermal environment within a GDF are uncertain[93,94].

The aim of this chapter is to investigate the effects of high-temperature curing on the NRVB, and the effects of the C:S ratio on the cement mineralogy when the cement is cured at different temperatures to simulate the potential geothermal and radiological heating effects within a GDF environment. The specific objectives to achieve this aim include:

- Using XRD to study to identify the mineralogical changes when NRVB is cured from temperatures of 25°C to 250°C, and when the C:S ratio is adjusted from 7.27 to 4, as the current phase diagram is from a C:S ratio of 1 to 3.
- To quantify the mineralogical composition of NRVB cured at this temperature and C:S range to extend the current understanding of the NRVB cement phase diagram.

Meeting these aims provides supporting evidence for the use of NRVB and other cement formulations at different curing temperature within the GDF safety case.

3.2 Raw Materials Information

NRVB is composed of four components, CEM I 52.5N powder, calcium hydroxide, calcium carbonate, and water. The CEM I 52.5N powder was sourced from Hanson Cements, and the Hydrated Lime and Limestone Powder were provided by Tarmac (Table 9). The companies were identified through communication from Jacobs, and historical UK National Nuclear Laboratories (UK NNL) reports.

Table 9: The raw materials sourced to manufacture NRVB, with the commercial name they were supplied with, and a link to the website they were sourced directly from [95] [96,97].

Raw material	Commercial name	Source
CEM I 52.5N powder	Portland Cement	Castle Cement from Ribbesdale works/ Hanson Ribbesdale Bulk cement products | Hanson UK[95]
Calcium Dihydroxide ($Ca(OH)_2$)	Hydrated Lime	Hydrated Lime | Tarmac Buxton Lime[96]
Calcium Carbonate ($CaCO_3$)	Limestone Powder	Limestone Powders | Tarmac Buxton Lime[97]

3.2.1 Major Oxide Composition X-ray fluorescence (XRF)

X-ray fluorescence (XRF) is an analytical technique used to determine the elemental composition of a material by measuring the characteristic secondary (or fluorescent) X-rays emitted from the material when it is irradiated with high-energy X-rays or gamma rays[98,99]. XRF analysis was performed on the cement and limestone powders. The XRF results are presented in Table 10. All three of the aliquots of CEM I powder, provided by Hanson UK, were tested. All aliquots of CEM I come from the same batch however, one aliquot was delivered separately. The results for the Cement powder delivered vary slightly from the analysis provided in the material datasheet provided by the supplier. A comparison between the measured major oxide composition of the powders and the material data sheet are presented in Table 11[100].

Table 10: The XRF results on the three aliquots of cement powder and the limestone powder provided by Hanson and Tarmac.

	XRF (%)										
ID	Na2O	MgO	Al_2O_3	SiO_2	SO_3	K_2O	CaO	TiO_2	MnO	FeO	LOI
Cem I-1	0.31	2.47	5.37	19.68	3.47	0.71	64.33	0.29	0.05	2.28	3.48
Cem I-2	0.31	2.47	5.34	19.65	3.44	0.72	64.43	0.30	0.05	2.28	3.24
Cem I-3	0.28	2.55	5.42	19.70	3.45	0.72	64.78	0.28	0.05	2.29	3.23
Tarmac Limestone	0.00	0.68	0.10	0.37	0.04	0.00	98.49	0.00	0.03	0.05	43.24

Table 11: Comparison of the XRF analysis of the three aliquots of cement powder to the material analysis information provided by Hanson.

	XRF (%)				
Compound	**CEM I-1**	**CEM I-2**	**CEM I-3**	**Average CEM I result**	**CEM I – Hanson's website**
Na_2O	0.31	0.31	0.28	0.30	
MgO	2.47	2.47	2.55	2.50	2.78
Al_2O_3	5.37	5.34	5.42	5.38	5.16
SiO_2	19.68	19.65	19.70	19.68	21.87
SO_3	3.47	3.44	3.45	3.45	3.40
K_2O	0.71	0.72	0.72	0.72	0.60
CaO	64.33	64.43	64.78	64.51	66.18
TiO_2	0.29	0.30	0.28	0.29	
MnO	0.05	0.05	0.05	0.05	
FeO	2.28	2.28	2.29	2.28	2.26
LOI	3.48	3.24	3.23	3.32	3.05

All analysis was performed on different samples taken from the same batch. This suggests that the composition is not constant. The CEM I-1 and CEM I-2 aliquots were delivered together and show the most similar results. However, all three aliquots are different from the initial testing performed by the manufacturer which are shown

in the column labelled CEM I – Hanson's website. Although they are slightly different, this testing has provided confidence that the powders contain the correct major oxides in appropriate proportions, and therefore they should react as expected.

3.3 Experimental work

3.3.1 Introduction

Initially, experiments were conducted to investigate the effects of curing NRVB cement at high temperatures (80, 175 and 250°C) for 5 and 10 days. This was to meet the overall aim of the project: to assess whether NRVB could be used as a backfill for higher heat-generating waste and to understand the effect of curing temperature on the mineral phase composition and on the alteration of the cement pore structure.

The cement powder, calcium hydroxide, and calcium carbonate used in this investigation were also tested to ensure they were representative of raw materials used in previous studies on NRVB, and of what is proposed to be used in the GDF[3,4,42].

3.3.2 Method

The three raw materials (CEM I, Calcium carbonate, and Calcium dihydroxide) were mixed by hand with water in the same solid: liquid ratio as NRVB of 0.55[4] to investigate how they behave individually at 250°C. Exact masses of solid and material are recorded against the target mass (Table 12). Each mixture was put into a PEEK mould, and placed into the same hydrothermal cell for 22 hours at 250°C. Once removed all moulded cylinders had 'set', however the $Ca(OH)_2$ was still wet. The $CaCO_3$ was similar to how it was as a powder. The CEM I was weak and could be markable with a spatula. The amount of raw material and water used to test each material are shown in Table 12 below.

Table 12: The quantities of raw material and water that were tested to ensure the raw materials behaved as expected when hydrated and heated.

Mixture	Raw material	Target weight (g)	Actual weight (g)
CEM I	CEM I	6.4	6.39905
	Water	3.6	3.61563
Calcium carbonate	$CaCO_3$	6.4	6.39927
	H_2O	3.6	3.59993
Calcium dihydroxide	$Ca(OH)_2$	6.4	6.40295
	H_2O	3.6	3.61578

The procedure was repeated with an empty PEEK mould on the bottom to prevent water from soaking into the bottom PEEK mould. Two hydrothermal cells were prepared, one at 80°C and one at 250°C; as a result, the quantity of the mixture used was doubled (Table 13). The cement mix was put into PEEK moulds then stacked in a 125 ml stainless steel pressure vessel (type 4750 Parr Instruments) rated at 200 bar at the maximum working temperature of 350°C. These were heated for 22 hours before being removed. The raw materials were ground using a pestle and mortar and vacuum sealed to prevent carbonation.

Table 13: The quantities of raw material and water that were tested to ensure the raw materials behaved as expected when hydrated and heated.

Mixture	**Raw material**	**Target weight (g)**	**Actual weight (g)**
CEM I	CEM I	12.8	12.80114
	Water	7.2	7.19909
Calcium carbonate	$CaCO_3$	12.8	12.80572
	H_2O	7.2	7.20586
Calcium dihydroxide	$Ca(OH)_2$	12.8	12.80572
	H_2O	7.2	7.20152

The CEM I cured at 80°C was very hard as expected, and at 250°C it was very soft. The raw materials (calcium carbonate and calcium dihydroxide) were heated for 22 hours at 80 and 250°C before being removed. The raw materials appeared unchanged in response to the temperature difference and were then ground and vacuum sealed to prevent carbonation. The unmixed raw material along with the CEM I, calcium carbonate and calcium dihydroxide cured at 80 and 250°C were tested with XRD to determine the mineralogy, to see if the water and heat had caused any changes.

3.3.2.1 Mineralogical analysis using XRD of the raw materials

Portlandite, calcium carbonate and CEM I were tested as raw powders after being mixed with water and then cured at 80 and 250°C, the mineralogy was analysed using XRD, prepared to the method described in Chapter 2. The XRD results summarised in Table 15 show that for $Ca(OH)_2$ and calcium carbonate the mineralogy was unaffected as a result of mixing with water and heating to 80 and 250°C. However CEM I mineralogy was affected and cured to form the early hydration product alite, and brownmillerite.

Table 14 describes the XRD measurement conditions. The CEM I powder was first analysed with Kapton tape to remove atmospheric moisture, with the trade-off that only major phases could be identified due to the high Kapton background. The samples was reanalysed without tape and with no rotation to identify any minor phases.

Table 14: The measurement conditions used for XRD analysis of the raw materials and CEM I powders.

	Raw materials	**CEM I powders**
Detector	LYNXEYE 1D monochromator	LYNXEYE 1D monochromator
2θ range	5 – 79.998	5 – 79.998
Time	00:32:08	00:32:08
Step size	0.020°	0.020°
Steps	3668	3668
Count time	0.5s	0.5s
Filter	Ni	Ni
Rotation	Yes	No
Secondary Soller slit	2.5°	2.5°
Divergence	0.2 mm	0.2 mm
Goniometer	280.0 mm	280.0 mm
Air scattering knife	Yes	Yes
Kapton tape	Yes	No

Table 15: The phases identified within the raw materials when nothing was done to them (raw materials), and when they were mixed with water and heated to either 80 or 250°C for 22 hours.

Curing conditions and raw material	**Phases identified**
$Ca(OH)_2$ raw material	$Ca(OH)_2$ (portlandite)
$Ca(OH)_2$ 80°C	$Ca(OH)_2$ (portlandite)
$Ca(OH)_2$ 250°C	$Ca(OH)_2$ (portlandite)
$CaCO_3$ raw material	Calcite
$CaCO_3$ 80°C	Calcite
$CaCO_3$ 250°C	Calcite
CEM I raw material bucket 1	Alite, calcite, brownmillerite
CEM I 80°C bucket 1	portlandite, calcite
CEM I 250°C bucket 1	Portlandite, calcite
CEM I – raw materials (bucket 3)	Alite, calcite, brownmillerite

The $Ca(OH)_2$ and $CaCO_3$ showed no reaction after hydration and heating. They also showed that they only contained what would be expected. The CEM I powder reacted after hydration and heating which was expected. To ensure atmospheric moisture did not affect the cement mineralogy during XRD analysis, Kapton tape was used as a result only the major phases can be identified in these samples.

3.4 Part 1: Curing of NRVB at 80, 175 and 200°C

After the raw materials were tested, and their purity/ suitability was confirmed, they were used to mix NRVB cement. The temperature 80°C was chosen to study as UK NNL had done work investigating the effect of long term curing cement at this temperature. The additional temperatures of 175 and 200°C were chosen based on the cement phase diagram created by Meller et al.[56] This phase diagram showed cementitious phase changes at these temperatures, and new phases such as gyrolite and hillebrandite form between 150 and 200°C. Above 200°C phases such as xonotlite, γ-C_2S and truscottite form[49]. The temperatures 80, 175 and 250°C were chosen to complement existing research into NRVB cement curing at 80°C, and to reflect potential repository conditions.

The cements were cured for 5 and 10 days, at elevated curing temperatures the initial hydration reactions within cements have completed by 5 days[4], however these

cements were also cured for 10 days to verify this and ensure the cements had the same composition.

Portland cement (CEM I, 52.5N) (26 wt.%) supplied by Hanson UK was combined with calcium carbonate (29 wt.%) and calcium hydroxide (9 wt.%), both supplied by Tarmac, and deionised water (36 wt.%). The formulation was then mixed for 15 minutes using a stand mixer, decanted into PEEK moulds, and then placed under vacuum for 15 minutes to remove bubbles, then stacked in a 125 ml stainless steel pressure vessel (type 4750 Parr Instruments) rated at 200 bar at the maximum working temperature of 350°C. The PEEK moulds are smaller than the diameter of the hydrothermal cell, allowing steam to circulate and create a homogeneous environment. The hydrothermal cell was then placed in an oven at a set temperature (80, 175 or 250°C) for either 5 or 10 days. The hydrothermal cell was removed from the oven and cooled under cold flowing water to arrest any further chemical reactions. The cement was then removed from the PEEK moulds via coring for the 80°C samples and using a spatula for the 175 and 250°C samples as the material was too fragile to be cored. The samples were then submerged in cooled isopentane and freeze-dried under vacuum for 24 hours. This process arrested the hydration reaction and prevented carbonation. Once dried, the cores and powders were ground to <63μm and then vacuum sealed before XRD analysis.

3.4.1 XRD analysis

XRD analysis was performed on the 5 and 10 day cured NRVB samples, and the constituent raw materials. XRD analysis was carried out using a Bruker D8 Advance X-ray powder diffractometer, at 40 kV and 40 mA. Three different programmes were used to analyse the cured cements, the raw materials, and the cement powders (Table 14, Table 16). The patterns were then analysed using EVA, and information from the International Centre for Diffraction Data (ICDD). The CEM I powder was first analysed with Kapton tape to remove atmospheric moisture, with the trade-off that only major phases could be identified due to the high Kapton background. The samples were reanalysed without tape and with no rotation to identify any minor phases.

Table 16: The measurement conditions used for XRD analysis.

	Cured cements
Detector	LYNXEYE 1D monochromator
2θ range	5 – 79.998
Time	00:32:08
Step size	0.020°
Steps	3662
Count time	1s
Filter	Ni
Rotation	Yes
Secondary Soller slit	2.5°
Divergence	0.2 mm
Goniometer	280.0 mm
Air scattering knife	Yes
Kapton tape	Yes

3.4.2 XRD results from 5 and 10 day curing at 80, 175 and 200°C

The NRVB cements cured for either 5 or 10 days at either 80, 175, or 250°C were measured with XRD and analysed using Eva. The mineral phases identified are shown Table 17 and the XRD diffractograms are displayed in Figure 22 with the peaks indexed for Portlandite (P) and Calcite (C) .

Table 17: The results from the XRD analysis done on the cements cured for either 5 or 10 days at either 80, 175, or 250°C.

Sample	**Curing Temperature (°C)**	**Curing Time (days)**	**Minerals [COD code]**
NRVB 80 5d	80	5	Calcite [9001297] Portlandite [1008780]
NRVB 80 10d	175	5	Calcite [9000965] Portlandite [1008780]
NRVB 175 5d	250	5	Calcite [9000965] Portlandite [1008780]
NRVB 175 10d	80	10	Calcite [4502443] Portlandite [1008780]
NRVB 250 5d	175	10	Calcite [4502443] Portlandite [1008780]
NRVB 250 10d	250	10	Calcite [4502443] Portlandite [1008780]

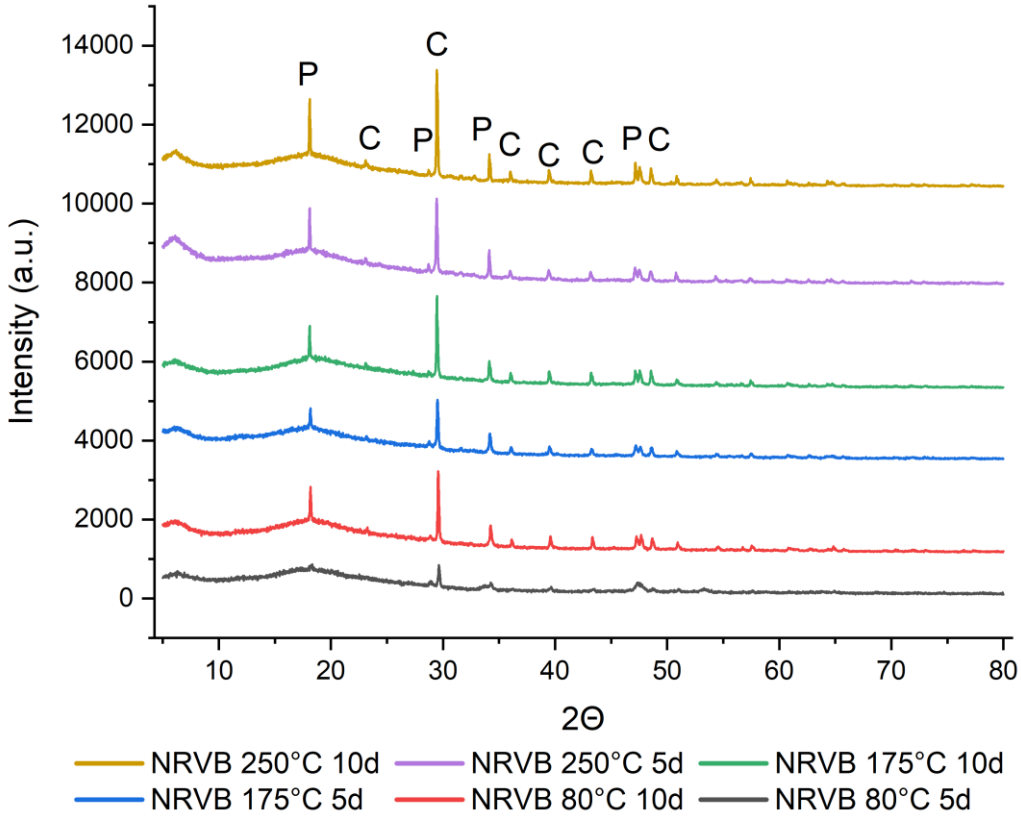


Figure 22: The XRD diffractograms from the XRD analysis done on the NRVB cements cured for either 5 or 10 days at either 80, 175, or 250°C.

The NRVB sample cured at 80°C for 5 days had a reasonably high background, which created noise over potential peaks. This would be caused by the use of Kapton tape over the sample, and the instrument conditions. This made identifying the phases that were present in smaller quantities more difficult. In this sample only calcite, brownmillerite, and portlandite, could be reliably identified. There are humps around 33 and 48 2θ that are likely several poorly resolved peaks overlapping. Some of the peaks that are probably contributing to these humps have been identified, however there are probably more minor phases that have not been found.

The NRVB samples cured for 5 days at 175°C and 250°C and all the samples cured for 10 days have a hump caused by the Kapton tape at lower 2θ values (8-26 2θ). This meant that only calcite and portlandite could be identified in these samples. Despite only these two minerals being found there are no unidentified peaks remaining. It is unlikely that only calcite and portlandite are present as other phases such as jaffeite and α-C_2SH should be present at these curing conditions[53], so it is

probable that the other peaks are present in very low quantities and are not visible over the high background caused by the Kapton tape.

The XRD analysis showed the same mineralogical composition for the NRVB cement at all curing temperatures, however the scans have significant background, which has not allowed the strength reduction at elevated curing temperatures to be explained.

3.5 Part 2: Phase diagram investigation

The work completed in part 1 showed that the current NRVB formula is weaker when cured at 250°C compared to 80°C. After analysing the NRVB samples cured at each temperature with Kapton film, it was discovered that there are key changes in the mineralogy of the NRVB heated at each temperature. As temperature is increased belite is no longer formed, and hydrogarnet, jaffeite and α-C_2SH form. Both jaffeite and α-C_2SH cause strength retrogression[101,102]. This change in phase assemblage must account for the cement weakening when cured at higher temperatures.

Cement phase diagrams only exist for C:S ratios of 0-3.5[103,104] and for an infinite C:S ratio the phase diagram shown below in Figure 23 predicts that only portlandite will be present at all curing temperatures. The findings from Part 1 show that for NRVB with a C:S ratio of 7.27 other mineral phases are present and that these minerals change with increasing curing temperature. This can be seen in Figure 21 where small peaks are present that were not able to be identified due to comprising a small proportion of the sample. To understand if a stronger cement formulation can be achieved at higher curing temperatures while retaining an excess of portlandite for radionuclide capture, the C:S ratios 4 to 7.27 were investigated at curing temperature of 25, 80 and 200°C.

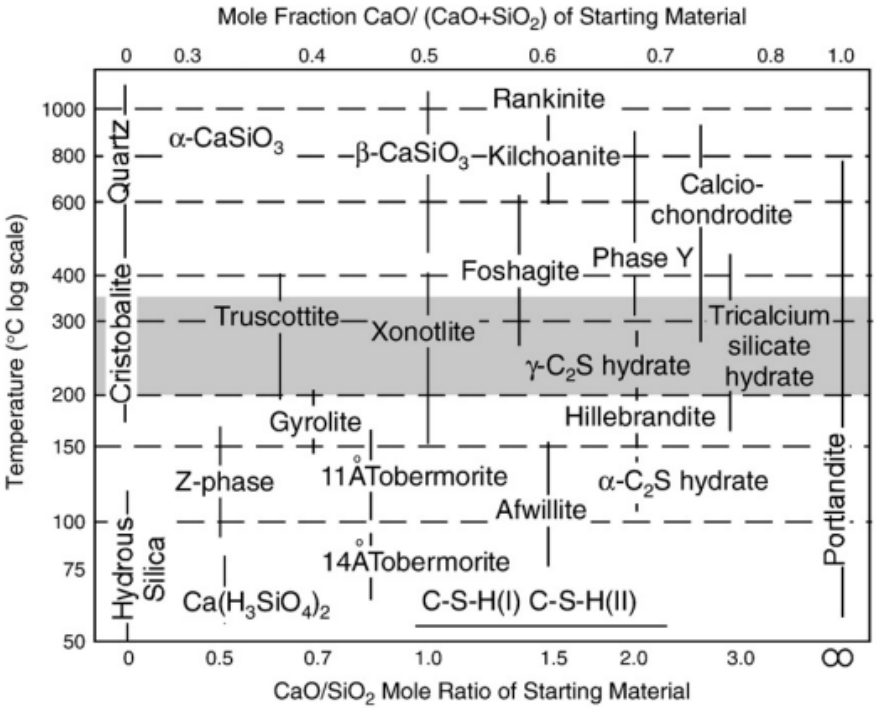


Figure 23: The phase diagram created by Meller et al.[56] showing what mineral phases form within cement when cured at 50 to 1000°C and at a CaO/SiO₂ ratio of 0 to 3.5.

The previous work to develop a phase diagram used Dyckerhoff Class G cement. The difference in composition with Ribblesdale PC CEM I is shown below in Table 18[100].

Table 18: A comparison of the cement used in previous phase diagram investigations (Dyckerhoff Class G cement) and the cement used for NRVB and in this study (Ribblesdale PC CEM1 52.5N).

	CEM I 52.5N	**Dyckerhoff Class G cement (Meller)**	**Difference**
SiO_2	21.87	22.55	-0.68
Al_2O_3	5.16	3.62	1.54
Fe_2O_3	2.26	4.53	-2.27
CaO	66.18	65.61	0.57
MgO	2.78	0.76	2.02
SO_3	3.4	1.82	1.58
K_2O	0.6	0.66	-0.06
Na_2O	0.26	0.17	0.09
Cl	0.05		0.05
TiO_2		0.17	-0.17
Mn_3O_4		0.14	-0.14

Raw material analysis done with XRF, on the CEM I 52.5N used in NRVB, and the previous phase diagram work, showed that these two cements are comparable. There were slight differences in the quantities of SiO_2 and CaO, the two major components that form alite, belite, and the other strengthening minerals. Ribblesdale PC had less than 1% less SiO_2, and less than 1% more CaO. The most significant differences are the quantity of Al_2O_3, Fe_2O_3, MgO and SO_3. As the main focus of this experimental work is to identify the Calcium Silicate phases that are stable or unstable at high temperatures, a difference in metal oxide composition should not considerably alter the calcium silicate minerals formed. Both cements have a similar SiO_2 and CaO weight percentage, therefore the calcium silicate mineral phases that form will be comparable.

3.5.1 Synthesis of NRVB C:S ratios with calcium carbonate

Silica flour was added to the NRVB formula, replacing a percentage of the CEM I powder to reduce the C:S ratio. Table 19 shows the percentage of cement and SiO_2 used to achieve each C:S ratio. The C:S ratios of 7, 6, 5, and 4 were selected as previous studies had not exceeded 3.5. For a C:S ratio of 4, almost 20% of the cement powder is replaced by SiO_2. As lower ratios were already studied, an almost 20% replacement was adequate to achieve a Ca:SiO_2 ratio of 4[105].

Table 19: The CaO:SiO_2 ratios chosen to extend the phase diagram. The percentage of cement replaced with silicon dioxide, and the CaO:SiO_2 ratio that this replacement is equivalent to.

%CEM1	%SiO_2	CaO/SiO_2 ratio
100	0	7.272
99	1	7
95	5	6
89	11	5
81	19	4

The cements were then cured at Room temperature, 80°C and 200°C for 5 days, as these produce a range of minerals at lower CaO:SiO_2 ratios (Figure 23).[49–51,53].Figure 23 The solid-to-water ratio is maintained at the same ratio as in NRVB to maintain the porosity. The solid to water ratio also affects the overall strength of the cement and can impact the mineralogy[105].

After curing, the cements were removed from their moulds then ground to a particle size of less than 63μm, the cement powders were then ground in a micronizer to a particle size of less than 5μm. Isopropanol was used as a lubricant in the micronizer. To ensure that neither micronizing the sample, nor soaking it in isopropanol affected the mineralogy, identical samples were prepared without the additional step for comparison. The results are discussed below.

3.5.1.1 Mineralogy of the cements as measured from XRD

XRD was run at the University of Glasgow in the Chemistry Department on their Malvern Panalytical Empyrean multi-purpose platform to maximise sample throughput. All samples were covered in Kapton film in the XRD holders to prevent any reactions in air, including carbonation. The scan parameters are presented in Table 20.

Table 20: XRD scan parameters used on the Malvern Panalytical Empyrean multi-purpose platform at the University of Glasgow.

	Cements
Detector	PIXcel3D-Medipix3 1x1 detector
X-ray tube	Empyrean Cu LFF HR (9430 033 7310x) DK431564
2θ range (2Θ)	5.0064 - 79.9934
Time (hh:mm:ss)	03:15:19
Step size (2Θ)	0.0131
Steps	5712
Count time (ms)	498.270
Filter	Ni
Rotation	Yes
Secondary Soller slit	dCore Soller slits 0.04 rad
Divergence	PDS for iCore 0.125°
Goniometer	240.0 mm
Kapton film	Yes

The XRD patterns were analysed using the DIFFRAC.EVA software to identify the phases within the cements. Diffractograms for the cements cured at 200°C are shown in Figure 24 with phases identified as Portlandite (P) and calcite (C). The phases identified for each C:S ratio at each temperature are given in Table 21. The phases were identified with X-ray Diffraction; C=calcite, P=portlandite, Q=quartz, H=hydrogarnet, J=jaffeite, a= α-C_2SH, B=belite, G=gypsum.

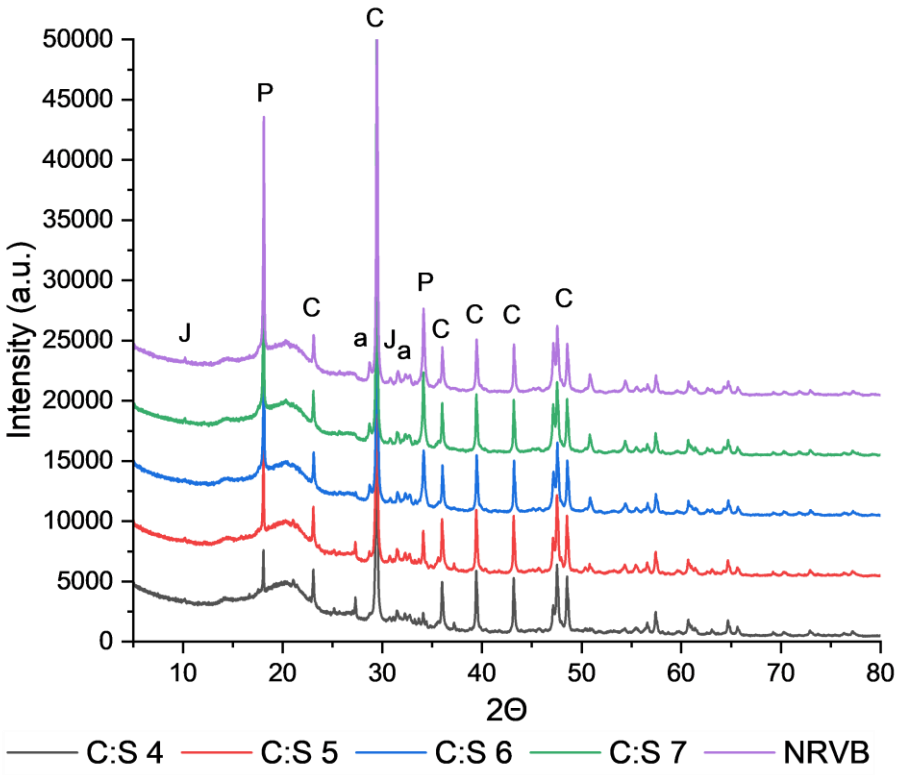


Figure 24: The XRD Diffractograms for cements cured at 200°C with $CaO:SiO_2$ ratios between 4 and 7.27 (NRVB).

Table 21: The phases identified with XRD for these cements.

Curing temperature (°C)	Approx C:S Ratio				
	NRVB	**7**	**6**	**5**	**4**
25	C, P, B, G	C, P, Q, B, G	C, P, Q, B, G	C, P, Q, B, G	C, P, Q, B, G
80	C, P, H, J	C, P, Q, H	C, P, Q, H	C, P, Q, H	C, P, Q
200	J, a, C, P	J, a, C, P	J, a, C, P	J, a, C, P	J, a, C, P

The cements cured at room temperature show calcite, portlandite, belite and gypsum (Appendix 2, Figure 97). Where SiO_2 was added to the starting mix it was also present after 5 days. No alite could be identified. As alite reacts faster than belite to form other calcium silicate minerals, it is logical that all the alite could be consumed after the 5-day curing period and hence no alite was detected. Quartz was present in all samples where additional SiO_2 was added, only the NRVB sample did not contain quartz. The presence of quartz in the room temperature samples with C:S ratios of 7,6,5,4 and lack of new calcium silicate phases indicates that the SiO_2 did not react at this temperature.

When cured at 80°C (Appendix 1, Figure 96) samples with different C:S ratio showed some variation in the mineralogy. In the NRVB formula jaffeite was present, in the other ratios jaffeite does not form until they are cured at 200°C. Jaffeite has a C:Si ratio of 3, so should form when there is a molar ratio of calcium to silicon of 3. This suggests that the higher C:S ratio means there is more calcium available to react to form higher ratio minerals. At 80°C all of the C:S ratios but 4 also produce hydrogarnet. Hydrogarnet forms from C_3A when no gypsum is present. If gypsum is present, sulphate ions from the gypsum will react with C_3A and water to form ettringite[106]. Hydrogarnet forms in C:S ratio cements 5, 6, and 7. No hydrogarnet was present in the C:S ratio 4 cement, however at lower temperatures some quartz was unreacted.

When the cements were cured at 200°C they all contained Jaffeite, α-C_2SH, calcite, and portlandite. No quartz was present in any of the samples cured at 200°C indicating that the SiO_2 was completely consumed by the reactions which formed Jaffeite, and α-C_2SH. α-C_2SH is a phase that forms over 100°C. The formation of α-C_2SH causes strength regression leading to a weaker cement[107]. Typically, the C:S is lowered to approximately 0.5 to prevent α-C_2SH formation [103,104,108].

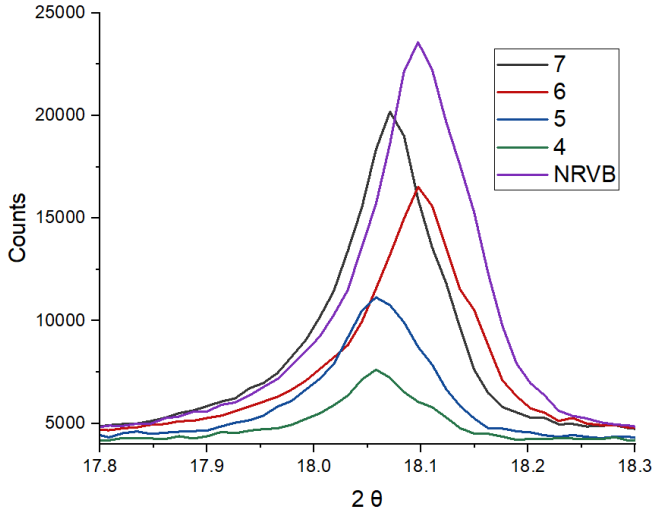


Figure 25: Plot showing the portlandite peak measured with XRD, and how it decreases as more SiO_2 is added to the formula. These samples were cured at 200°C.

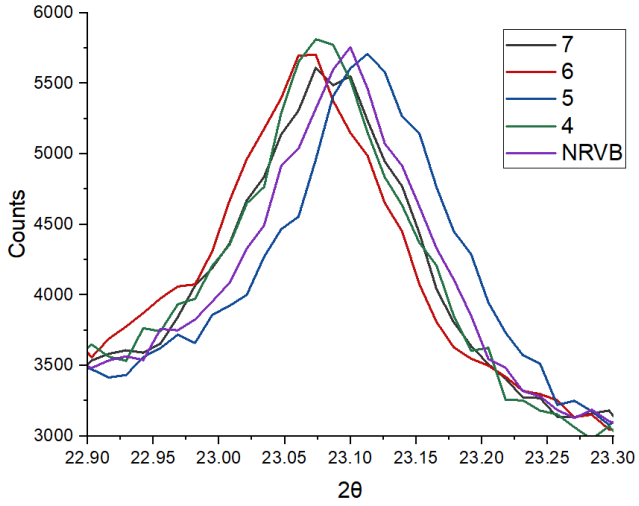


Figure 26: Plot showing the Calcite peak measured with XRD and how it remains at a constant height regardless of the addition of SiO_2. These samples were cured at 200°C.

All mixes at all curing temperature contained unreacted portlandite, and the calcite that was present in the starting mix more calcite may have formed through carbonation reactions between CO_2 in the water and portlandite during curing. Regardless of C:S ratio the amount of calcite remained constant as shown in Figure 26. As the C:S ratio was lowered, more portlandite reacted as shown in Figure 25 was consumed and the amount of calcium silicate phases (reinhardbraunsite, xonotlite, jaffeite, α-C_2SH, γ-C_2S) increased. At C:S ratio 4 cement cured at 250°C there was no portlandite present. At room temperature the cement hydration reaction was not

completed, this is indicated by the presence of belite which has slow reaction kinetics and will not be present if all hydration reactions within the cement have occurred[109,110]. Other calcium silicate hydrate phases were difficult to find in the busy pattern. As the temperature was increased more new calcium silicate phases form.

The calcite and portlandite peaks shift in both Figure 25 and Figure 26. The observed shift in diffraction peak position indicates a change in the lattice spacing of the crystalline phase. This may result from compositional variation or ionic substitution within the crystal structure; however, potential instrumental and sample-displacement effects must also be considered[111,112].

3.5.1.2 Conclusions and Discussion

These results suggest that Hydrogarnet is only stable above a C:S ratio of 4, and somewhere between room temperature and 200°C. Jaffeite is only formed and stable at a C:S ratio higher than 7 at 80°C to 200°C, or above 80°C to 200°C for a C:S ratio above 4. Neither Hydrogarnet or Jaffeite are present in the original phase diagram (Figure 23). This indicates that even curing temperatures up to 1000°C are not sufficient for these phases to form at lower C:S ratios. In addition, the weak α-C_2SH is formed somewhere between 80°C to 200°C at a C:S ratio of 4 and above. In the phase diagram Figure 23 α-C_2SH is present when C:S ratio 2 mixtures are cured between 100-150°C. While the phases identified in this investigation do not identify the exact temperature range α-C_2SH is present in all samples and hence the phase diagram can be extended showing that for a C:S ratio between 2 and 7.27 α-C_2SH is formed. More increments in C:S ratio and temperature are needed to more accurately say where phases form. However these results start to extend the previously established phase diagram (Figure 23).

The cements tested all contain high concentrations of calcite and portlandite. These minerals make it more difficult to identify other minerals present in smaller amounts. The amount of calcite remains constant regardless of the Ca:SiO_2 ratio or curing temperature. This suggests that the original calcite is unaffected by these parameters, and that any carbonation reactions occurring are independent of the amount of silica added or the curing temperature. The amount of portlandite however does change depending on the CaO:SiO_2 ratio and curing temperature. At higher temperatures, less portlandite is present in the final cement, and at higher silica additions (or lower

$CaO:SiO_2$ ratios). This shows the initial, and any forming, portlandite is reacting within the cement to form new minerals.

3.5.2 Synthesis of NRVB C:S ratios without calcium carbonate

Investigation of C:S ratios in Part 2 shows that the calcium carbonate added into the initial mix was dominating the XRD pattern, meaning some calcium silicate phases were too small to identify and quantify conclusively. The amount of calcium carbonate also remained constant, indicating that it was not reacting, unlike the portlandite which decreased as more silica flour was added, and as the cement was cured at a higher temperature. To enable quantification of the mineral assemblage in the cements the experiment was repeated without the addition of calcium carbonate but with the same percentages of silica flour added to the Portlandite. The amount of H_2O was adjusted to maintain the same solids-to-liquid ratio as the water content plays a direct role in influencing the porosity and the mineralogy of the cements. Higher amounts of water produce more hydration products; however the strength is lowered. Higher water content also produces a greater amount of calcium carbonate, and portlandite, and a lower amount of alite[113,114].

3.5.2.1 Method

The same methodology in Part 1: Curing of NRVB at 80, 175 and 200°C and Part 2: Phase diagram investigation was followed, however calcium carbonate was removed from the NRVB formula. The C:S ratios with and without calcium carbonate are shown in Table 22. The portlandite was shown to react in Part 2, so the CaO moles from it are accounted for in the new C:S ratios.

Table 22: The $CaO:SiO_2$ ratios studied, showing the percentage of CEM I powder replaced with SiO_2 and the moles of each.

$CaO:SiO_2$ ratio from Part 2	**$CaO:SiO_2$ Ratio**	**% CEM I**	**$\%SiO_2$**	**Moles CaO**	**Moles SiO_2**
7.27	4.99	100	0	0.4854262	0.09736531
7	4.79	99	1	0.4825285	0.10071901
6	4.13	95	5	0.4709377	0.11413378
5	3.38	89	11	0.4535515	0.13425595
4	2.67	81	19	0.43037	0.1610855

The cement powder and SiO_2 were added in the percentages shown in Table 22 to make a total mass of 26g, then mixed thoroughly for 15 minutes, before being pipetted into moulds. The moulds were then placed under vacuum for 15 minutes, before being sealed into hydrothermal cells. The cells were then cured at room temperature (25°C), 80, 150, 200, and 250°C for 5 days, with more temperature increments investigated to further constrain the phases present at each C:S for each temperature.

After curing the hydrothermal cells were cooled rapidly under flowing cold water. The cements were then removed from the moulds and freeze-dried under vacuum for 24 hours to stop hydration reactions within the cements. The minerals were identified using XRD and quantified using DIFFRAC.EVA and TOPAS.

3.5.2.2 Results

At room temperature the cement has not finished its initial reactions, this is shown by the presence of alite and larnite otherwise known as belite.

3.5.2.3 Quantification results

Table 23 below shows the quantification results of each mineral. This was done using Rietveld refinement in the TOPAS software. Table 24 shows the Crystallography Open Database (COD) codes used to identify the mineralogical composition and perform quantitative analysis of the cements.

Table 23: Quantification of the phases that are present within the various cements.

Amount of minerals present at 25°C Curing Temperature (%)													
C:S Ratio	**Calcite**	**Gypsum**	**Larnite**	**Quartz**	**Portlandite**	**Hydrogarnet**	**Tetra calcium aluminoferrite**	**α-C_2SH**	**γ-C_2SH**	**Jaffeite**	**Reinhardbraunsite**	**Katoite**	**Xonotlite**
4	3.252	8.141	16.134	18.892	53.581								
5	3.618	9.563	18.573	9.754	58.492								
6	5.99	1.462	22.547	5.981	64.02								
7	5.2	6.17	20.2	0.18	68.25								
7.27/ NRVB	4.356	8.575	24.601	0	62.28								
Amount of minerals present at 80°C Curing Temperature (%)													
C:S Ratio	**calcite**	**gypsum**	**larnite**	**quartz**	**portlandite**	**hydrogarnet**	**Tetra calcium aluminoferrite**	**α-C_2SH**	**γ-C_2SH**	**Jaffeite**	**Reinhardbraunsite**	**katoite**	**Xonotlite**
4	8.959			17.556	56.8873	15.431	1.193						
5	9.462			10.602	62.385	15.509	2.041						

6	9.501			4.402	67.401	17.28	1.415						
7	7.952				72.88	15.262	3.906						
7.27/ NRVB	8.373				72.803	14.11	4.714						
Amount of minerals present at 150°C Curing Temperature (%)													
	calcite	**gypsum**	**larnite**	**quartz**	**portlandite**	**hydrogarnet**	**Tetra calcium aluminoferrite**	**α-C_2SH**	**γ-C_2SH**	**Jaffeite**	**Reinhardbraunsite**	**katoite**	**Xonotlite**
4	8.083				33.781	32.97		26.166					
5	6.7				19.913	23.883		49.501					
6	5.273				43.087	23.906		27.734					
7	6.81				44.684	27.197		21.31					
7.27/ NRVB	4.076				35.343	25.884		34.697					
Amount of minerals present at 200°C Curing Temperature (%)													
	calcite	**gypsum**	**larnite**	**quartz**	**portlandite**	**hydrogarnet**	**Tetra calcium aluminoferrite**	**α-C_2SH**	**γ-C_2SH**	**Jaffeite**	**Reinhardbraunsite**	**katoite**	**Xonotlite**
4	17.27				20.628			14.18	37.595	10.324			

5	11.47				32.818			17.086	32.348	6.278			
6	9.338				45.633			13.124	25.037	6.867			
7	9.246				44.503			13.153	26.051	7.047			
7.27/ NRVB	9.146				45.499			11.573	26.684	7.097			
Amount of minerals present at 250°C Curing Temperature (%)													
	calcite	**gypsum**	**larnite**	**quartz**	**portlandite**	**hydrogarnet**	**Tetra calcium aluminoferrite**	**α-C_2SH**	**γ-C_2SH**	**Jaffeite**	**Reinhardbraunsite**	**katoite**	**Xonotlite**
4	3.84				0					11.01	60.01	0	25.14
5	8.28				12.072					4.85	59.07	15.73	
6	7.55				40.15					10.05	25.92	16.32	
7	8.25				28.7					7.83	38.91	16.3	
7.27/ NRVB	6.61				37.43					6.26	21.61	28.09	

Table 24: The COD IDs and references to the CIF files used in TOPAS to quantify the amount of each mineral present in the cements.

Mineral	**COD ID**	**Reference**
Xonotlite ($Ca_6Si_6O_{17}(OH)_2$)	9008439	[115]
Reinhardbraunsite ($Ca_5[SiO_4]_2(OH,F)_2$)	9011876	[116]
Jaffeite ($Ca_6[Si_2O_7](OH)_6$)	9012620	[117]
γ-C_2S ($Ca_5[SiO_4]_2(OH)$)	9014595	[118]
α-C_2SH ($Ca_2(HSiO_4)(OH)$)	9011378	[119]
Hemi carbonate ($(Ca_4Al_2(OH)_{12}][OH(CO_3)_{0.5}\cdot 4H_2O$)	2105252	[120]
Hydrogarnet ($Ca_3Al_2\cdot(OH)_{12}$)	9005158	[121]
Katoite ($Ca_3Al_2(OH)_{12}$)	1552359	[122]
Portlandite ($Ca(OH)_2$)	1001788	[123]
Quartz (SiO_2)	9005017	[124]
Larnite (Ca_2SiO_4)	9012789	[125]
Gypsum ($CaSO_4\cdot 2H_2O$)	1010981	[126]
Calcite ($CaCO_3$)	9000965	[127]

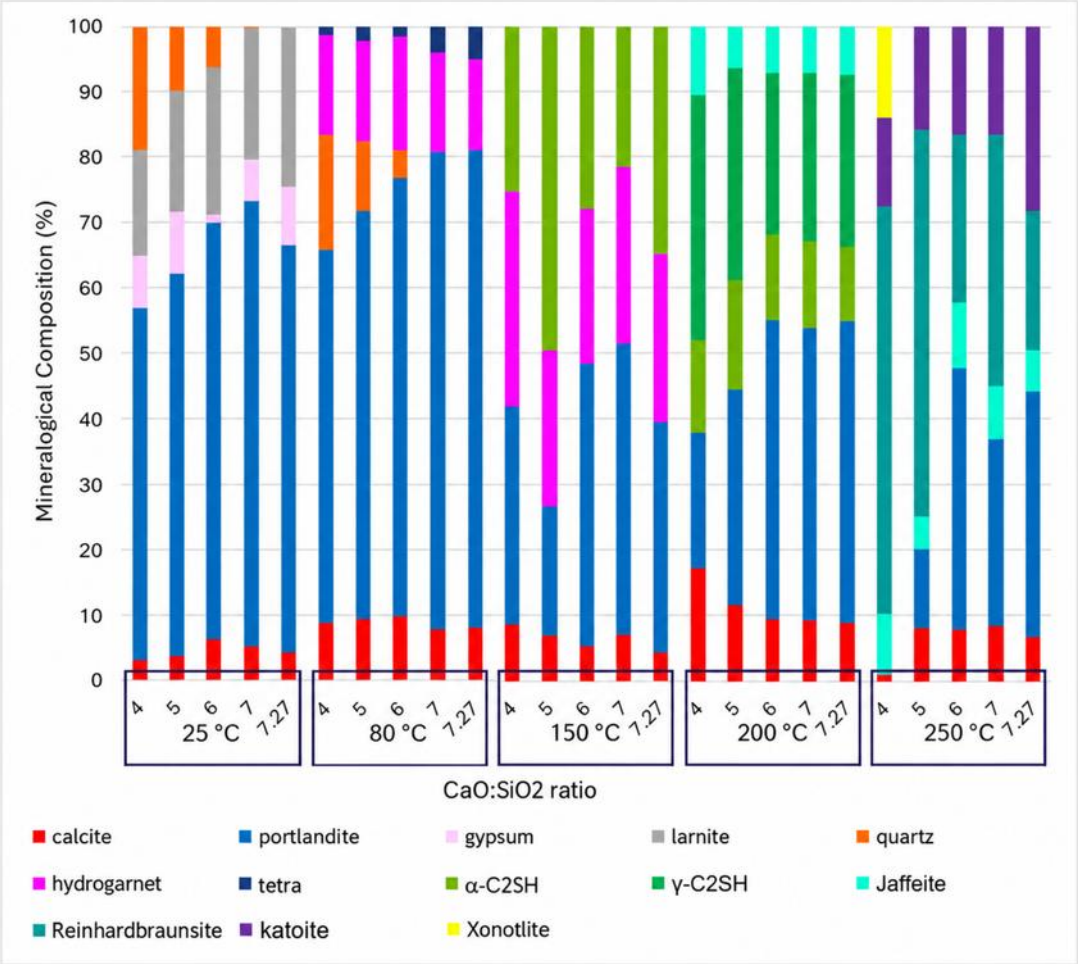


Figure 27: Bar chart showing the composition of each cement sample. Where red = calcite, blue = portlandite, gypsum = light pink, larnite = grey, quartz = orange, hydrogarnet = magenta, tetra calcium aluminoferrite = navy, α-C_2SH = light green, γ-C_2SH = emerald green, jaffeite = turquoise, reinhardbraunsite = teal, katoite = purple, and xonotlite = yellow.

The bar chart in Figure 27 shows the quantification results of the cement compositions. The amount of portlandite present after the cement has been cured reduces as the curing temperature and the amount of SiO_2 added to the mix increases.

As the curing temperature increases the amount of strength reducing minerals (jaffeite, α-C_2SH, γ-C_2SH, and reinhardbraunsite) increase within the cement composition. However, the sample with a CaO:SiO_2 ratio of 4 cured at 250°C has a composition with 14% xonotlite, which is a strengthening mineral. So it is possible at lower CaO:SiO_2 ratios than 4 strengthening minerals begin to form preferentially to strength reducing minerals.

Gypsum and larnite (belite) were not present when the cements were cured above 25°C, this shows that between 25 and 80°C the temperature is high enough for all initial hydration products to react. Gypsum reacts with alite to form ettringite which reacts further with alite to form AFm phases and other hydrates including hydrogarnet[102]. Larnite (belite) reacts to form calcium silicate hydrate, and other phases such as α-C_2SH and γ-C_2SH. The absence of gypsum and larnite in samples cured above 25°C indicates that elevated curing temperatures accelerate the completion of primary hydration reactions. This suggests that temperatures between 25 and 80°C are sufficient to fully consume the initial clinker phases and promote the formation of secondary hydrate assemblages.

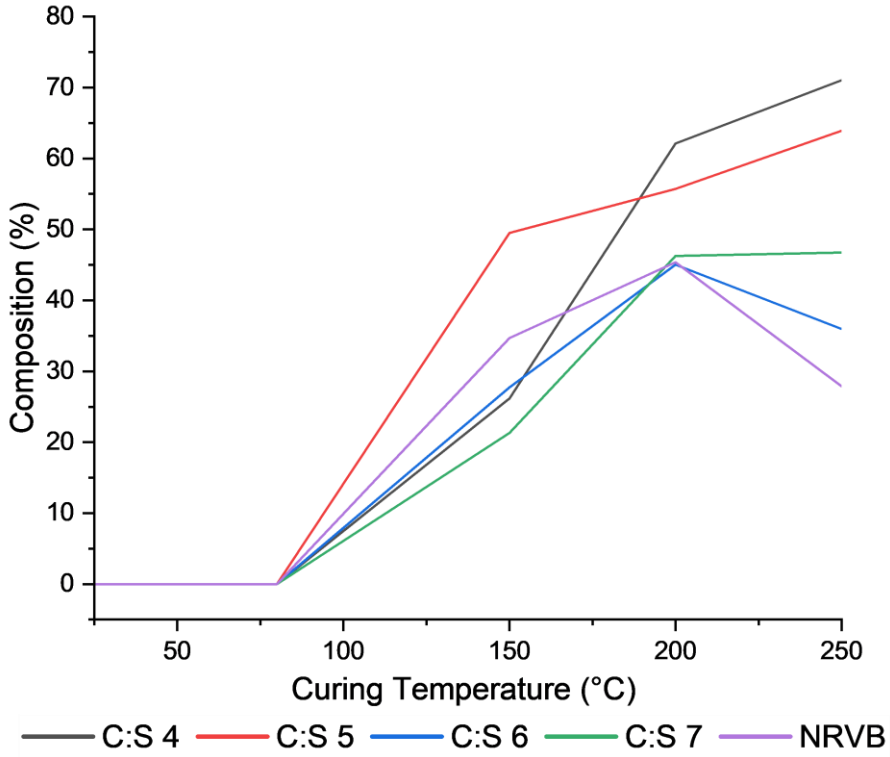


Figure 28: Graph showing how the composition of strength reducing minerals changes as the curing temperature is increased. Black = C:S 4, red = C:S 5, blue = C:S 6, green = C:S 7, and purple = NRVB.

The composition of the cement changes as the C:S ratio is altered and the curing temperature is increased (Figure 28). This changing mineralogy Increases the amount of low strength minerals in the system. All cements showed no strength reducing minerals when cured at 25 and 80°C. At a curing temperature of 150°C all cements had some strength retrogression minerals present. The amount of strength

retrogression minerals increased at a curing temperature of 200°C. The cements with a C:S ratio of 4 and 5 continued to form more strength reducing minerals when cured at 250°C, with the C:S 4 cement having the highest composition. The amount of strength retrogression minerals in NRVB and C:S 6 was less at 250°C than 200°C, whilst the composition of the cement with a C:S ratio of 7 remained fairly stable between 200 and 250°C. The increased formation of jaffeite, α-C_2SH, γ-C_2SH, and reinhardbraunsite at elevated temperatures may negatively affect mechanical performance due to their comparatively lower binding capacity and reduced contribution to cohesive C-S-H gel formation. In contrast, the formation of xonotlite in the C:S 4 sample cured at 250°C suggests that specific compositional conditions favour the development of more crystalline reinforcing calcium silicate hydrate phases at high temperature. These results indicate that the C:S ratio plays an important role in determining whether high-temperature curing favours the formation of mechanically beneficial or detrimental phases. Therefore, optimisation of both curing temperature and silica content is necessary to maximise the formation of strengthening hydrates while minimising the development of undesirable crystalline phases.

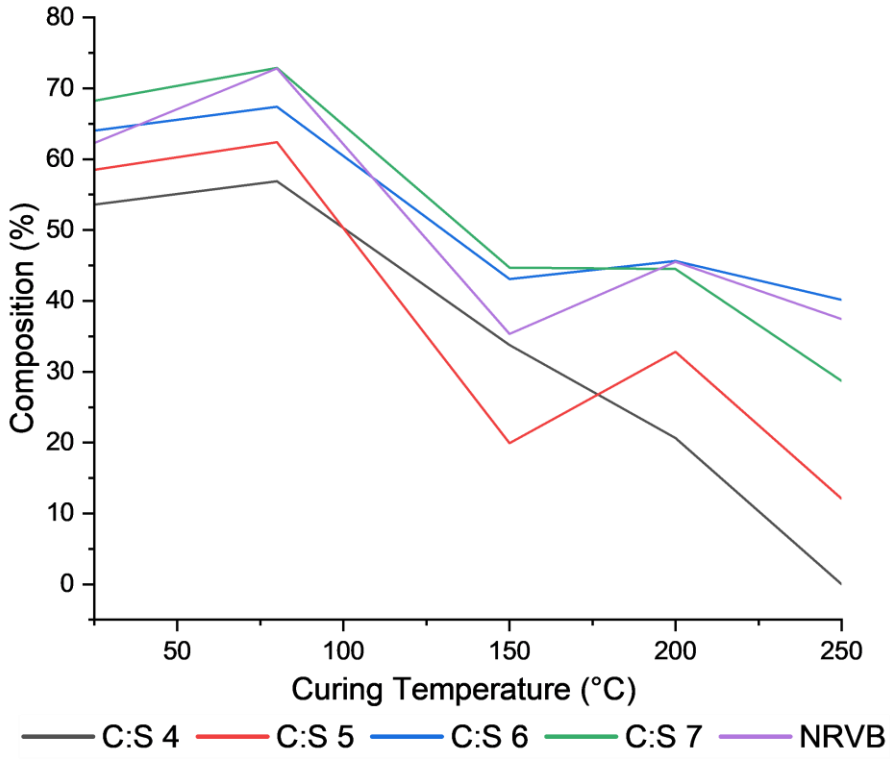


Figure 29: Graph showing how the quantity of portlandite within the cement changes as the curing temperature is increased. Black = C:S 4, red = C:S 5, blue = C:S 6, green = C:S 7, and purple = NRVB.

Figure 29 shows how the proportion of portlandite in the cements is affected by C:S ratio and curing temperature. All of the cement samples show a general trend of portlandite decreasing as the curing temperature is increased. The sample with C:S 4 and 5 show the lowest amount of portlandite regardless of curing temperature, the cements with a C:S ratio above 5 do not show a trend based on C:S ratio. This implies that the amount of portlandite present in cements with a C:S ratio above 5 is dependent on curing temperature, not the amount of SiO_2 present in the initial reaction. The reduction in portlandite content with increasing curing temperature and SiO_2 addition suggests enhanced consumption of $Ca(OH)_2$ through secondary pozzolanic and silicate hydration reactions, leading to the formation of additional calcium silicate hydrate-related phases.

The decrease in portlandite follows a similar trend to that shown in Figure 28, the amount of portlandite in all cements remains stable when cured at 25 to 80°C, and decreases when cured above these temperatures. This is similar to the amount of strength retrogression minerals present, of which there are none present at these lower curing temperature and the amount increases generally as the curing temperature increases. Overall, increasing curing temperature promoted the transformation of initial hydration products into higher-temperature calcium silicate and calcium aluminosilicate phases. This indicates that elevated-temperature curing substantially alters the equilibrium mineral assemblage of the cement system.

3.5.2.4 Discussion

The results presented in Table 23 and Figure 27 show that as curing temperature increases both strength regression and strengthening minerals form. The compositional change is represented in Figure 28. These results show two key trends when the curing temperature and C:S ratio is altered, these are the formation of minerals that cause strength retrogression and a reduction in the overall percentage of portlandite within the cured cement.

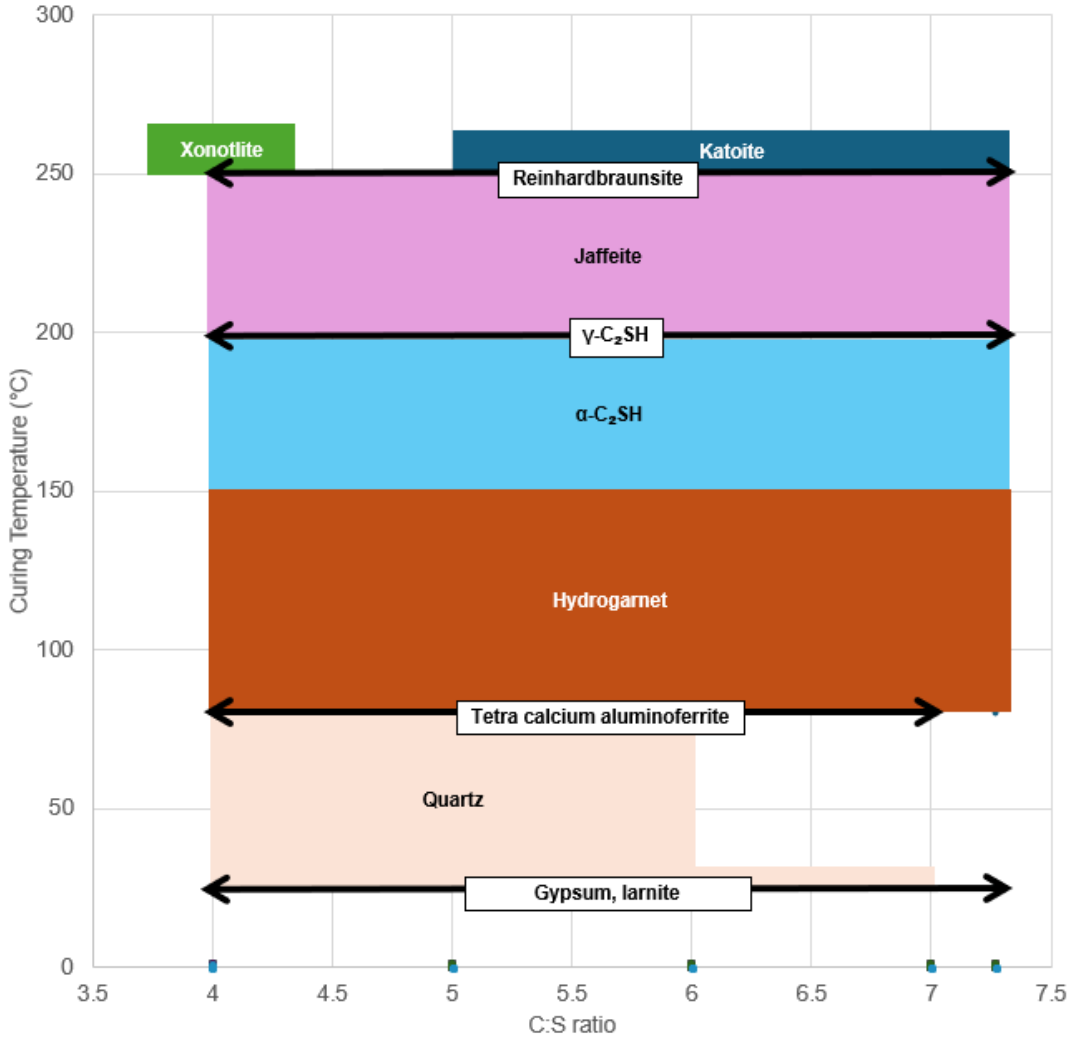


Figure 30: A phase diagram showing the results found in this chapter.

A phase diagram showing the results in part 3.5.2 is shown in Figure 30. This diagram is only representative of where the phases are present, and not their abundance. Calcite was present at every C:S ratio and curing temperature, and portlandite was present at all curing temperatures and C:S ratios apart from C:S 4 cured at 250°C.

Formation of minerals that cause strength retrogression

Minerals that cause strength regression are jaffeite, α-C_2SH, γ-C_2S, and reinhardbraunsite. C-S-H recrystalises, forming α-C_2SH. The formation of α-C_2SH from C–S–H results in a denser crystalline hydration product and a reduction in solid volume. This can cause shrinkage of the cement matrix, increasing porosity and permeability and contributing to strength retrogression[128,129] .The formation of strength reducing phases is prevented in cements used in Oil and Gas wells by adding silica [101]. Jaffeite has similar properties to α-C_2SH, its formation causes the pore structure

of cement to degrade, and a strength reduction[130]. When reinhardbraunsite forms the crystals bond poorly to each other, leaving gaps. This means reinhardbraunsite has a loose structure and is a weak, strength reducing phase[101]. γ-C_2S has a high affinity to CO_2 and can be useful for capturing C-14[131] which can form as methane as biological and cellulosic matter decays. The unit cell of γ-C_2S is 10% larger than the unit cell of β-C_2S which it forms from, this expansion in unit cell volume shatters the cement crystals into dust. γ-C_2S is a weak phase with low hydraulicity[132].

In cements with a C:S ratio of 4 cured at 250°C, Xonotlite is present and causes strengthening effects in the cement[133]. Xonotlite has a needle-like, dense structure and is thought to form from portlandite reacting with SiO_2, and polymerization reaction between C-S-H and Si-OH sites on SiO_2 [101]. Where xonotlite has formed at 250°C at a C:S ratio 4 this means the phase diagram can be extended to include xonotlite formation at this C:S ratio and temperature.

The high temperature mineral phases form in greater quantities as the amount of portlandite decreases as shown in Figure 28 and Figure 29. This reduces one of the key safety functions of NRVB; that the portlandite will dissolve into the cements pore water over time and buffer the pH to be alkaline which reduces the solubility of radionuclides that could have egressed from the waste, stopping them from entering the groundwater and migrating to the surface environment. If the portlandite is consumed during the initial curing, pH buffering will be caused by C-S-H, which is not as effective at increasing the pH as portlandite dissolution[90].

At lower curing temperatures early hydration products were present, these include larnite, gypsum, and hemi-carboaluminate. Hemi-carboaluminate ($Ca_4Al_2(CO_3)_{0.5}(OH)_{13}\cdot 5.5H_2O$) forms when calcite is initially introduced to the mix, it then becomes mono-carboaluminate as calcite content continues to increase[134]. This mineral is a carbonation precursor and is meta stable. It forms from the C_3A phase which is present during the initial hydration reaction within the cement. A previous study by Ipavec et al.[135] found this hemi-carboaluminate phase was sensitive to atmospheric CO_2, exposure to IPA, or drying, and could only be measured in situ. This cement was exposed to all of these conditions[135].

Reduction of Portlandite

In the NRVB formula, portlandite is important as it is supposed to dissolve slowly over time into the cement pore water, to maintain a high pH that reduces the solubility of radionuclides, causing them to precipitate and therefore trapping them within the cement.

During this analysis where the effect of high temperature curing, and SiO_2 addition on the mineralogy of cement was investigated, it was found that both high temperature curing, and higher additions of SiO_2 led to a reduction in the quantity of portlandite. At the most extreme temperature, 250°C, and the highest SiO_2 addition of 19% cement powder replacement (CaO:SiO2 4) all of the portlandite was consumed by hydration reactions. This is in agreement with the preliminary results from part 2, which showed the amount of portlandite decreased as the $CaO:SiO_2$ ratio decreased. Figure 31 shows a heatmap of the amount of portlandite found in the cements.

This decrease of portlandite could lead to a lower pH over time, and a less basic environment for waste. The effect of this on other infrastructure within the GDF, and the trapping of radionuclides needs to be considered for the impact to be fully understood

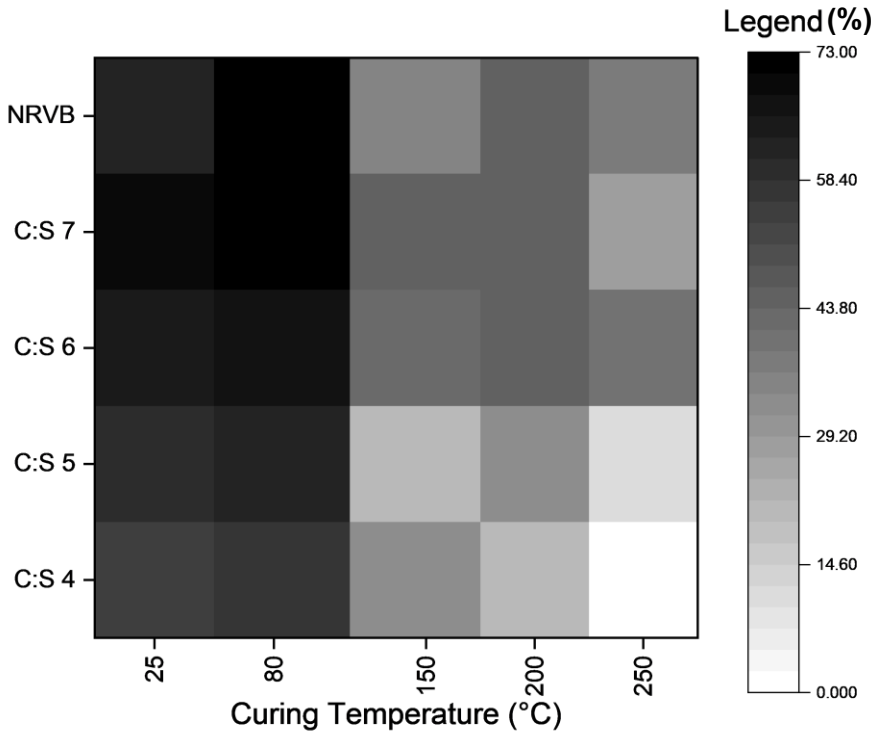


Figure 31: Heatmap to show the amount of portlandite remaining in each sample after curing.

3.6 Conclusions

During this set of experiments the phase diagram for the cement mineralogy, covering $CaO:SiO_2$ ratios of 1 to 7.27, and temperatures of 25°C to 250°C was analysed. This was achieved by curing a range of cements, then measuring them with XRD, before using EVA, Highscore, and TOPAS to fully identify and quantify their mineralogical composition.

3.6.1 Key conclusions

- The calcium carbonate in the original NRVB formula serves as a filler, and strengthener. It does not react with the other starting materials and dominates XRD patterns.
- There is a direct inverse relationship between proportion of minerals that cause strength reduction, and the curing temperature. With increasing curing temperature more strength reducing phases are present and the cements formed as a non-cohesive powder when cured at 250°C.
- At 250°C, and a $CaO:SiO_2$ ratio of 4, xonotlite forms. This is a strengthening mineral, and its formation is in agreement with literature, where SiO_2 is added to a cement mix to reduce the $CaO:SiO_2$ ratio to less than 1, to prevent the formation of mineral phases that cause strength retrogression. Xonotlite has a $CaO:SiO_2$ ratio of 1, so these reaction conditions are favourable to its formation.
- A key physical characteristic of the NRVB cement is the porosity, and pore interconnectivity. The next chapter investigates how the mineralogy evolution at elevated temperatures and with different C:S ratios affects the porosity of the cements.

3.6.2 Further work

- The cements could be remade on a larger scale to measure the pH of the pore volume. This would show how much the loss of portlandite affects the pH and give an indication of how much the pH drops and how damaging this could be to the infrastructure that it will interact with inside the GDF.
- Modelling work could be carried out to simulate the temperatures the GDF will experience, and to map the temperature gradient across the NRVB cement.

This could be used to build a map of what minerals will form where and provide an indication of the varying properties of the NRVB cement.

- Radionuclide testing of the cements cured at high temperatures where portlandite has reacted to form minerals to see if the NRVB cement is still able to trap radionuclides without the excess portlandite.

Chapter 4 The effect of increased curing temperature and different C:S ratio on porosity

4.1 Introduction

The porosity of a cement has an impact on its physical properties such as strength, transport, and ventilation. Different factors influence the porosity of a cement. These are:

- An increased water to cement ratio leads to increased porosity and decreased strength[136]. A higher water content means any excess water that is unreacted remains in the pore space, leading to a greater capillary pore volume[137,138]. The capillary porosity is the main attribute that determines the compressive strength of a cement[139]. Strength decreases as the capillary porosity increases[139]. This is due to a reduction in connected C-S-H, pores acting as flaws that cracks can propagate from, and an increased porosity facilitates greater ingress of water and chemicals that can lead to degradation.
- Curing conditions, such as time to cure, to allow for the microstructure and microporosity to fully develop.
- Incorporation of supplementary cementitious materials (SCMs) and admixtures. Previous studies have investigated the addition of SCMs to concrete and found the higher the amount of SCMs such as GGBS or Micro Silica added the lower the porosity of the concrete[139]. The addition of admixtures means the water to cement ratio can be lowered whilst the workability is maintained.

4.1.1 Importance of porosity of cements

4.1.1.1 The role of Cementitious Backfill in Deep Geological Repositories

The main purpose of cementitious backfill in engineered barrier systems is to prevent radionuclides from radioactive waste reaching the biosphere and causing harm to people, animals, or the environment. The backfill provides structural stability to hold the waste containers within the repository and perform chemical buffering to maintain a high pH to reduce the solubility of radionuclides and slow the degradation of waste containers and structural components of the repository. Cement minerals can also

chemically bond with radionuclides that escape from the waste containers to prevent their ingress into the environment. The porosity of the cement is an important parameter as it has a direct impact on the strength, transport, and ventilation properties.

4.1.1.2 Strength

The strength of a cement is impacted by its chemistry, what minerals form, the percentage porosity, and the pore distribution. Factors that impact mineral formation such as composition, curing temperature and time, and solid to water ratio also effect the porosity of the end cementitious system. The porosity in turn then has an impact on the strength, illustrating the complexity of forming an ideal cement, and the interdependencies of the system on initial mix and curing conditions.

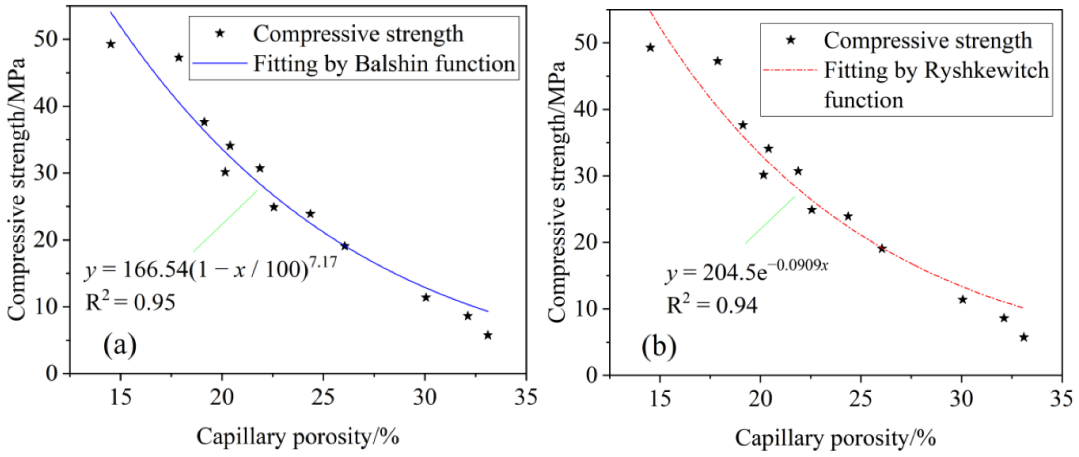


Figure 32: Image taken from literature [139] to show the relationship between compressive strength and capillary porosity in cements.

The porosity has a direct impact on the strength of a cement as is shown in Figure 32, with higher porosity reducing the strength[139]. As the water content is directly linked to the porosity, a wetter mix leads to a weaker cement. Water that is in excess, and is not consumed by the hydration reactions will also increase the capillary porosity by remaining unreacted within the cement. This causes a reduction in strength and can lead to excess cracking.

4.1.1.3 Transport of radionuclides and gases through the cement backfill

An important function of cement porosity is to limit the transport and migration of radionuclides through the hardened matrix. The pore structure within the cement acts not only as a physical barrier but also as a reactive surface where radionuclides can

be retained through adsorption, ion exchange, and surface complexation. A pore network with a high internal surface area increases the number of available binding sites, thereby enhancing the material's capacity to immobilize radionuclides and reduce their mobility over time [139]. A cement with connected pores would enhance flow through the material.

The characteristics of the pore network are strongly influenced by the cement-to-water ratio and the incorporation of supplementary cementitious materials[139]. As the cement-to-water ratio decreases and there is less unreacted water, the pore structure becomes more tortuous, creating a more complex and indirect pathway for fluid flow and diffusive transport [139]. This increased tortuosity slows the movement of dissolved species through the material. Additionally, the inclusion of fly ash has been observed to reduce pore connectivity by refining the microstructure and promoting the formation of additional hydration products, which block or constrict capillary pores. Together, these effects contribute to a denser, less permeable cement matrix that is more effective at restricting radionuclide migration.

4.1.1.4 Gas transport

The porosity of the backfill will provide ventilation for the repository. As cellulosic materials degrade methane gas is produced[140]. The corrosion of metals will also produce hydrogen gas. If these gases are not able to be vented from the repository they can build up and cause cracking. Hydrogen gas is also flammable so venting is important to prevent H_2 gas build up and explosion.

4.1.2 Techniques to measure porosity of cements

4.1.2.1 X-ray Computed Tomography (XCT) for 3D characterisation at micron scale

XCT is a non-destructive imaging technique that can be used to quantify the internal structure of materials[141]. The spatial resolution of the technique varies with the scanning system used. X-rays are generated with a user defined maximum energy, then the x-ray beam is passed through a rotating sample to a scintillator fronted CCD detector Denser, more attenuating materials absorb the x-rays, so the intensity of the beam hitting any pixel on the detector is controlled by all the phases the x-rays have passed though on the beam path By rotating the sample and collecting 1000's radiographs at different angles, we can use mathematical back projection algorithms

to reconstruct the 3D structure of the sample. During this project XCT was performed on a Nikon XT scanner operating with a 180kV transmission target. Lower energy x-rays provide more information about subtle differences in composition but the minerals within the cement samples in this study have very similar elemental compositions and bulk attenuation meaning that even with the lowest energy beam we can get good transmission (80 kV) the XCT data show very little difference in the grayscale values of different phases (Figure 33) The challenge of resolving similar phases is compounded when the grain sizes come close to the resolution of the imaging, which may also be the case here.

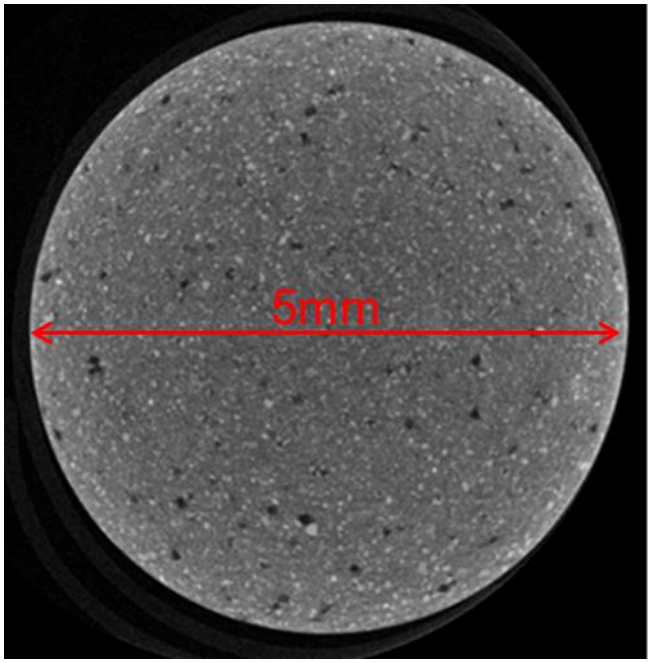


Figure 33: A slice of the XCT scan of a NRVB cement core cured at 80°C. This shows a 2D slice through the 3D data set (main) and a zoom in of a sub region (inset) to show the texture of the image data. The sample is NRVB cement cured at 80°C. Pores (black), cement phases (from near black to mid grey depending on volume of pore within the voxel) and SiO_2 (pale grey).

Pores that can be simply segmented based on greyscale value (black) form less than 1% of the sample volume. As total porosity is expected to be closer to 50%[52,142] the majority of the porosity is below the resolution of the XCT data. Each pore under approximately 5 µm (voxel size) is captured by a greyscale value between that of the cement phases and the pores, the so called “partial voxel effect”. MIP values have been used to guide the thresholding in XCT analysis to get agreement, however this is incorrect, as the porosity is dispersed across many voxels and taking a single

threshold value will incorrectly capture the distribution. It would be possible to calibrate the partial pore volume per voxel based on the greyscale of air and a piece of one of the cement mineral phases, but that cannot provide accurate understanding of the pore network geometry and connectivity without substantial higher resolution imaging. XCT is therefore used to measure the volume and geometry of the macro-porosity only.

4.1.3 Vacuum saturation

Vacuum saturation involves the cement being dried in an oven to remove all pore water, then the sample being placed under vacuum to remove all the air before de-aired water is then added to the cement. The volume of water that enters the cement is measured, giving a volume of the pores[143,144]. This method works poorly on small and low strength and when cement is rewetted hydration reactions may occur. Rewetting a cement will also cause alkali groups such as hydroxides to dissolve into the water, altering the chemistry of the cement[145] and changing the absorption capabilities. This would also change the volume. Cements cured above 80°C were too structurally weak to be rewetted. They lost all form when soaked in IPA to arrest hydration, and initially dissolved exposed to water coolant during coring (Chapter 3).

4.1.4 Mercury Intrusion Porosimetry (MIP)

MIP can measure pore sizes between 4 to 7500 nm. Mercury is non wetting, so pressure is needed to force the mercury into the pores, and the pressure is inversely proportional to the pore size. When combined with the total volume of mercury the method provides porosity and a pore size distribution [146]. While a common analytical technique to measure the pore size distribution of cement, MIP is likely to damage the fragile samples of this study and the technique was not accessible during the study[147].

4.1.5 Helium Pycnometry

Helium pycnometry is a gas-displacement technique used to determine the (skeletal) density of a material by measuring the volume that is accessible to helium gas. Helium is used because the very small molecular size allows it to penetrate very small pore

throats, and because it is chemically inert. During measurement, helium is expanded from a calibrated reference chamber into the sample chamber. The resulting pressure change allows the volume accessible to helium to be calculated using the ideal gas law. When this volume is combined with the measured mass of the sample, the true density can be determined. This method is widely used for powders, cements, ceramics, polymers, and porous solids[148].

Helium pycnometry is non-destructive, relatively fast, and highly repeatable, and it avoids the safety and handling concerns associated with liquid displacement methods such as mercury intrusion. The technique is also capable of resolving very small volume differences, making it particularly useful for characterising fine powders and highly porous materials[149]. However, the measurement only accounts for pores that are accessible to helium; closed pores are treated as part of the solid volume, which can lead to an overestimation of total porosity and an underestimation of density. Results are also sensitive to sample preparation, as moisture, adsorbed gases, or volatile components can alter the measured pressure response and introduce error. In some highly porous materials, helium adsorption at higher pressures has also been reported to affect the apparent volume measurement of cements[150].

4.1.6 Aims and Objectives of this chapter

The aim of this chapter is to analyse the porosity of the cement samples that were mineralogically characterised in the previous chapter.

The objectives are:

1. Analyse the porosity of the cements and evaluate the impact of curing temperature and $CaO:SiO_2$ ratio on porosity.
2. Use Scanning Electron Microscopy (SEM) and Electron Probe Microanalysis (EPMA) to find the porosity of the cements, and to identify the minerals that form around the pores. This can be used in combination with the results from the previous chapter that analysed the mineralogy to study where minerals are forming within the cements and the impact this could have on the cements' ability to retain radionuclides.

4.2 A combined multi-method approach

To measure both the porosity, the relationship of porosity to mineralogy, and where minerals form spatially within the cement matrix, the prepared samples (identified in section 3.5.2 above) were analysed using multiple techniques (Figure 34). Each technique provides different information about the sample.

- XCT is an imaging technique that gives information about the macroporosity, the pore shape, and changes within the sample such as cracking.
- Helium pycnometry provides a value for the total porosity including microporosity.
- SEM gives visual and elemental information for a thin section that has been polished.
- EMPA provides an elemental map of one slice of the cement core and can provide information as to where minerals are forming relating to the porosity or bulk of the sample.

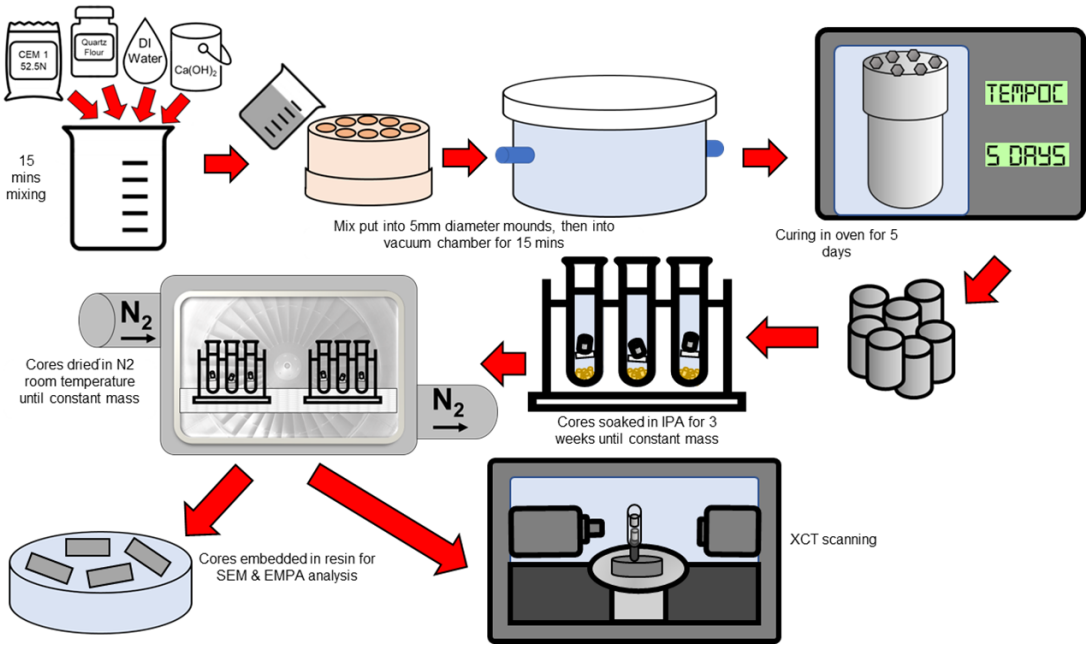


Figure 34: A diagram showing how the samples were prepared for XCT, SEM and EMPA analysis.

4.2.1 Sample preparation

Cement cores for XCT were prepared separately to the samples prepared for XRD, but prepared from the same batch of cement at the same time to ensure the samples are comparable. The cements from 3.5.2 were used in this chapter. For XCT, the cement mix was cast into small cylinders using a specially made PEEK mould. The

mould had 8 holes of 5 mm diameter and 10 mm depth. PTFE tape was used to secure a base to the mould. The filled mould was kept under vacuum for 15 minutes to remove air bubbles so that any porosity measured had formed during the curing process. The moulds were designed specifically for this project for optimal XCT scanning. The cores were then cured for 5 days at either room temperature, 80, 150, 200, or 250 °C. Following curing, the base of the moulds were removed and the cores were pushed out of the moulds. Removing calcite from the initial starting mixture also increased the strength of the cements. This meant that cores could be collected and preserved. The initial samples that contained calcite were not able to be cored due to their low strength.

Isopropanol has the most ideal properties when compared to other common solvents as it does not affect the microstructure of the cement, so it is the best alcohol to use for solvent exchange[67]. The solvent needs to be used in a more than 20:1 ratio with the specimen volume. The best solvent to use for hydration arrest has a low boiling point so that it can be easily removed without using destructive techniques such as heating, a small molecular size so that it is not hindered by size effects when diffusing and is miscible with water so that it can effectively be exchanged with water and arrest the hydration. Isopropanol is the best solvent that meets these requirements[67]. It can also be 'cleaned' of water using molecular sieves, so is cost effective and can be recycled.

Solvent exchange is a diffusion process, and the size of the sample therefore has a direct relationship with the time that is needed for the solvent to fully penetrate the cement. It is a square relationship, so increasing the core diameter from 5mm to 10mm would take 25 times longer to stop hydration. This is why cores must be taken before solvent exchange, or the cement cured in moulds of 5mm or smaller diameter. The ratio of solvent to cement dictates how often the solvent needs to be replaced. A higher amount of solvent means less replacements are needed[67]. This unfortunately leads to extremely high volumes required, so it is more efficient to conduct more frequent replacements, and to use beads to clean the solvent of water so that it can be reused.

The method for weighing the sample during solvent exchange is to remove the cement paste from the solvent, blot excess solvent from it using blue roll, and weigh it. When the weight has started to stabilize it will be removed and weighed more frequently until there are two consecutive, measurements within 24 hours of each other that show the

same weight. The least destructive method to remove the solvent is to vacuum dry the samples in a nitrogen oven at room temperature until the weight has stabilized again[70]. Four cores from each cement sample were soaked in isopropanol until they had achieved constant mass, then dried in nitrogen until they were at constant mass. They were then sealed in vacuum bags before XCT was undertaken on them.

4.2.2 XCT

Scanning parameters were optimised for the cement cores to achieve as much possible difference in the phases in the cement cores. The scanning parameters were 80 kV, 122 mA, 3141 projections, 2s exposure, and a 4.39 reconstructed voxel resolution. The 3D volumes were reconstructed using the Nikon proprietary algorithms.

4.2.2.1 Data Analysis

The scans collected were visualised and analysed using Avizo® version 2021.1. Sub volumes were taken from the centre of each sample to avoid any edge effects. The image processing workflow (Figure 35, Table 25) was developed to extract the central sub volume, crop the data, remove cone beam effects, isotropic diffusion to remove noise, then segmenting the pores by auto thresholding and measuring the total pore volume and the pore size distribution. The border kill operation was performed to remove any pores that were affected by the initial cropping.

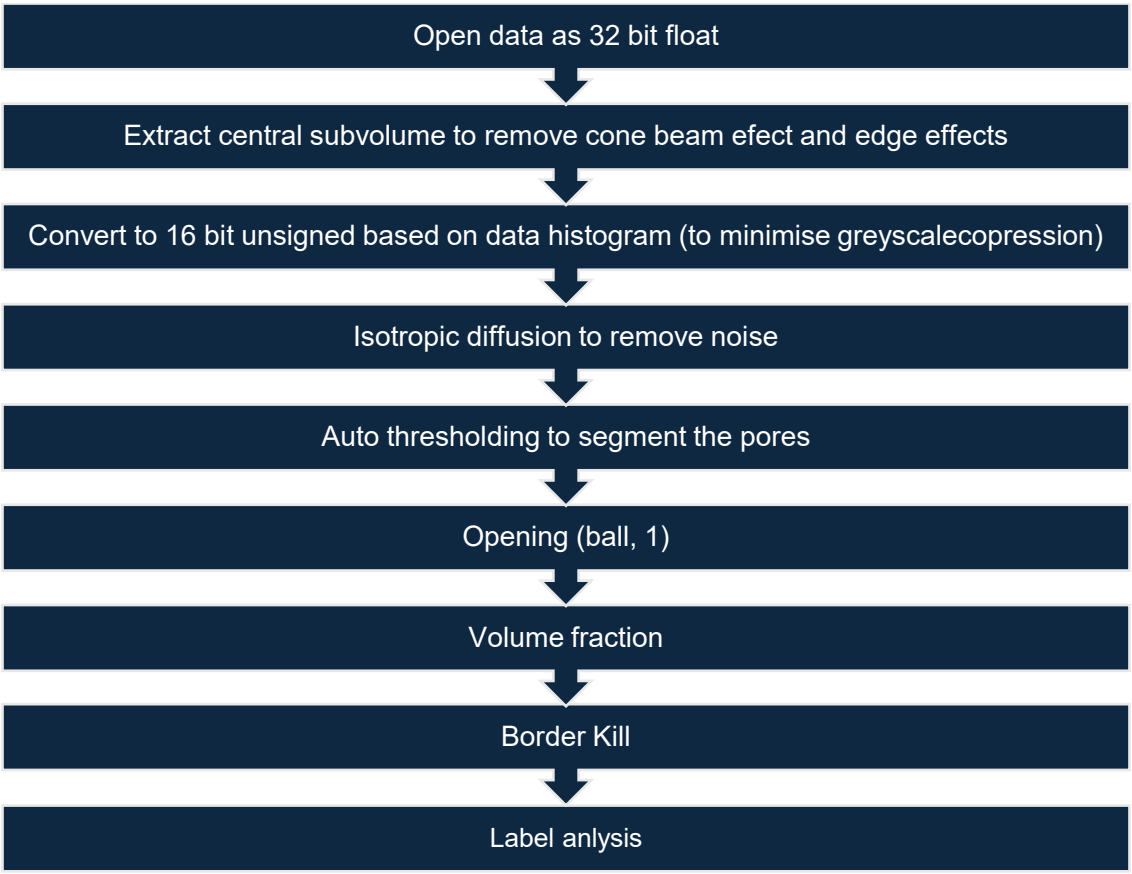


Figure 35: The workflow followed in Avizo to process the XCT scans collected of the cement cores cured at different temperatures and with different $CaO:SiO_2$ ratios.

Table 25: The parameters used to process the XCT scans in Avizo. AT = Attenuation Threshold, AD = Anisotropic Diffusion. Anisotropic Diffusion is dimensionless and has no unit.

Sample	AD	AT low (a.u.)	AT high (a.u.)	AT median (a.u.)
NRVB 25°C	7000	4000	20000	15737
NRVB 80°C	8000	0	22000	16760
NRVB 150°C	8000	0	20000	15475
NRVB 200°C	7000	8000	18000	15087
NRVB 250°C	8000	3000	20000	14653
C:S 4 25°C	4000	12000	20000	16421
C:S 4 80°C	7000	5000	22000	15749
C:S 4 150°C	3000	4000	10000	7718
C:S 4 200°C	6000	4000	15000	11864
C:S 4 250°C	7000	0	12000	7733

4.2.3 SEM and EMPA

4.2.3.1 Method

Cement cores were resin embedded in cores with a 25 mm diameter (Figure 36). They were polished under alcohol, not water, to prevent any hydration reactions on the surface. The cement cores had a diameter of 5 mm and a length of 10 mm.

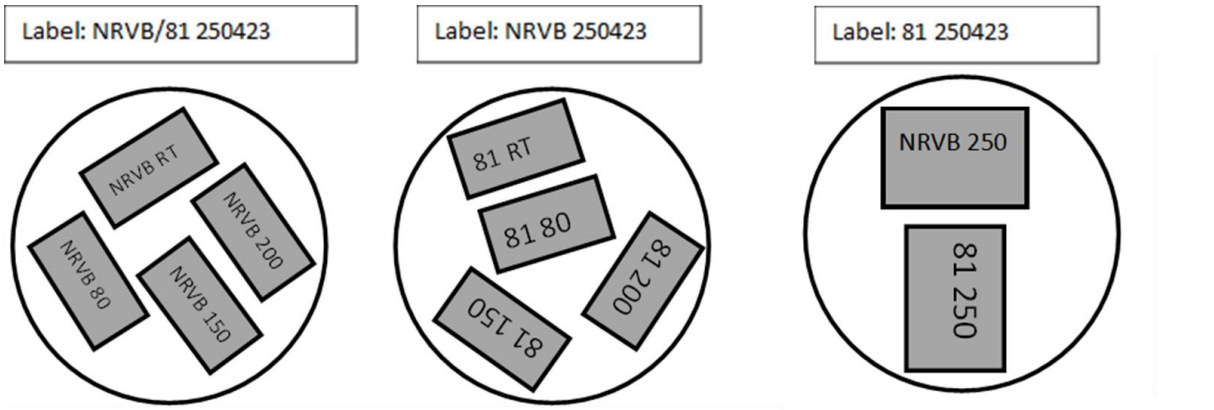


Figure 36: Diagram showing how the cores were arranged in each resin block to ensure each core could be identified by its position. This arrangement has no symmetry between the three blocks so the samples cannot be mixed up if the labels on the blocks were to come off.

Prior to SEM or EMPA analysis the embedded cores were carbon coated, and silver paint was used to paint along the edge of the sample where it met the mount. The SEM was a JEOL JSM-IT100 InTouchScope SEM, which has a tungsten source. The EPMA was a JEOL JA-8530F field-emission system which has four wavelength-dispersive X-ray (WDX) spectrometers and an energy-dispersive X-ray (EDX) detector[151]. The area of the core that was measured was recorded using the EPMA before measurement as the beam can 'dehydrate' the cement, altering its elemental properties[152]. The area that has been scanned with EMPA is avoided during SEM scanning.

4.2.4 Helium Pycnometry

4.2.4.1 Sample preparation

Extra cores that were taken from the same samples scanned with XCT were used in the helium pycnometer. This enabled the values to be directly compared to each other. The samples were stored in vacuum sealed bags to ensure they were not exposed to

air between measurements, and that the composition would remain constant and no further carbonation reactions would occur which could lead to calcite forming within the pore space. Samples less than 10% of the 10cm^3 sample chamber have lower levels of accuracy because of a small total volume; they require the addition of a metal cylinder of known weight and volume to the chamber to enable any reading to be made. This is subtracted from the final reading to give the true measurement. The cement cores were measured with and without the metal cylinder to assess what difference is seen in the measurement.

The volume of the sample was measured from XCT data because some of the cement cores are fragile and are irregular cylinders. Figure 38 shows the effect of the image processing on a slide of the scan, how the pore space is filled so that the total volume of cement core and pore space can be taken. The workflow to process the scans is shown in Figure 37.

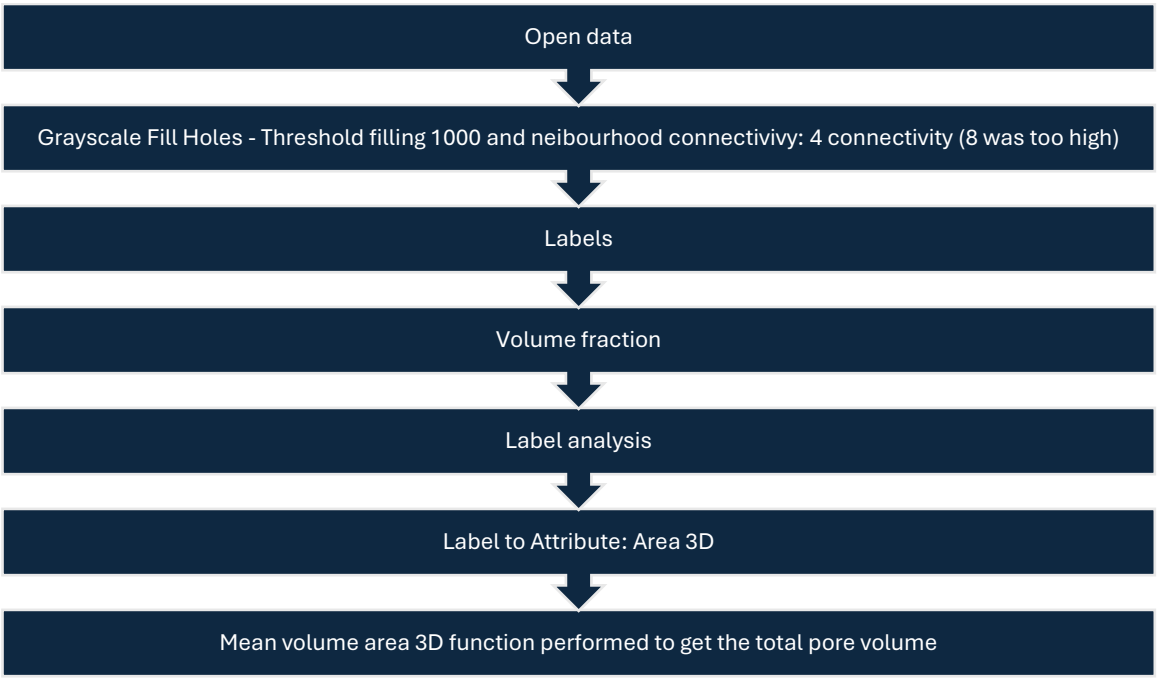


Figure 37: The workflow followed in Avizo to process the XCT scans collected of the cement cores cured at different temperatures and with different CaO:SiO$_2$ ratios to get the volume of the pores.



Figure 38: A slice of the XCT scan to show the difference in the core during the image processing. The first image is the original slice, the second image shows the pore space filled, and the final slice shows what has been thresholded to count for the total volume of cement core and porosity.

XCT was the only way to measure these samples due to how fragile they were, one NRVB sample was stable enough to measure with callipers to compare with literature values. The common method for calculating the volume of a cylinder is to measure the diameter and height using callipers. The values are then inputted into this equation $V=\pi r^2 h$ which gives the volume. The most 'regular' cylindrical core was the NRVB sample cured at room temperature, the volume was measured with callipers and was calculated to be 0.1941cm^3 (Table 26). This is a difference of 0.0109cm^3, or 5.62%. This discrepancy in values is due to the small size of the cylinder, and any irregularities along the edges that lead to a smaller volume. The values are similar though, which provides confidence in using XCT and then Avizo to calculate the volumes of the cylinders.

Table 26: The diameter, radius and height of the cement core NRVB cured at 25°C measured with callipers.

Sample	Diameter (mm)	Radius (mm)	Height (mm)	volume callipers (mm^3)
NRVB 25°C	0.504	0.252	0.973	0.1941171

4.2.4.2 Samples cured at 250°C

The samples cured at 250°C disintegrated when prepared using the standard mould method. Instead they were prepared in specially designed PEEK cups and remained in these during analysis in the Helium Pycnometer, so to know the porosity of the cement core the volume of the cup needed to be known. Using Avizo the PEEK cup was removed by using a threshold and the volume was calculated. This was then used alongside the Helium Pycnometer measurement to calculate the porosity. The values used to Threshold the cement core and the PEEK cup are in Table 27. The

thresholding was an important step in this image processing as the PEEK cup and the masking tape needed to be removed from the sample before the volume was calculated. The results of the thresholding is shown in Figure 39. Table 28 shows the volume of the PEEK cup and the cement core. These values were used to calculate the porosity of the samples cured at 250°C.

Table 27: The values used to threshold the PEEK cup and cement core of the samples cured at 250°C in Avizo image processing software.

		Threshold Minimum (a.u)	**Threshold Maximum (a.u)**
C:S 4	**Cement core**	100	1000
	PEEK cup	25	70
NRVB	**Cement core**	150	1500
	PEEK cup	25	100

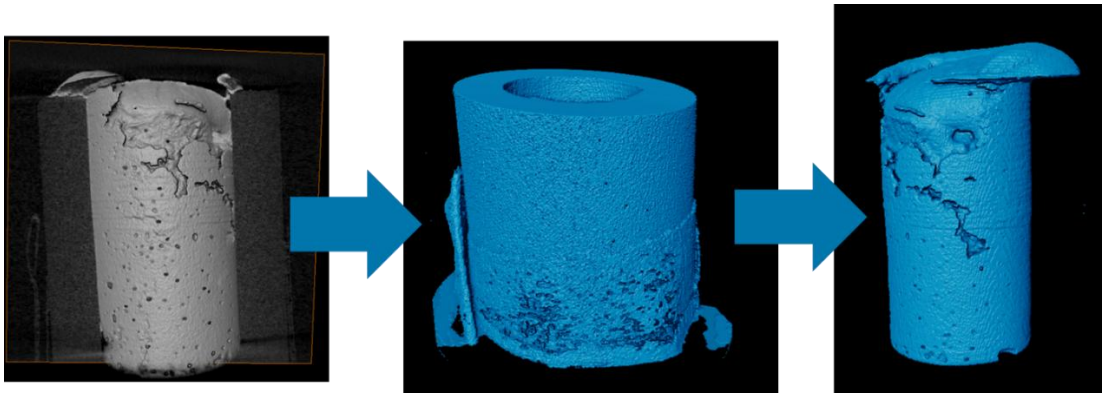


Figure 39: The first image on the left is a 3D render from Avizo showing the cement core inside the PEEK cup, the second image shows the PEEK cup after it has been thresholded, and the final image on the right shows the cement core without the PEEK cup.

Table 28: The number of pixels calculated in Avizo for the PEEK cup and cement core of the samples, and the actual volume calculated.

		Number of voxels	**Voxel size (nm^2)**	**Volume (mm^3)**
C:S 4	**PEEK cup**	18702636	1.97E-08	0.368124
	Cement core	9426872	1.97E-08	0.185549
NRVB	**PEEK cup**	22904772	1.97E-08	0.450835
	Cement core	8950621	1.97E-08	0.176175

4.3 Results

4.3.1 Porosity

The results obtained when the porosity was measured using XCT to obtain scans which were then processed in Avizo are in Table 29 and Figure 41.

Table 29: The porosities calculated for the cement cores using XCT scanning and Avizo image processing software.

Sample	**Macroporosity (%)**
NRVB 25°C	0.303398
NRVB 80°C	0.931793 with crack 0.437883 with the crack removed*
NRVB 150°C	0.53462
NRVB 200°C	0.830708
NRVB 250°C	1.38943
C:S 4 25°C	1.15795
C:S 4 80°C	0.798224
C:S 4 150°C	0.642819
C:S 4 200°C	0.657714
C:S 4 250°C	0.744047

*The sample that had the NRVB formulation that was cured at 80°C was analysed twice using Avizo. The first porosity value was calculated with the whole sample shown in Figure 40, this gave a value of 0.93% which was significantly higher than the values found at the curing temperatures of 25 and 150°C. The sample was reanalysed with the cracked area cropped out and the value was reduced to 0.44%, this value aligned with the trend shown in the other results from different curing temperatures, so it can be concluded that the crack was raising the porosity and the value of 0.44% will be used going forwards as it also aligns with the trend of porosity that can be seen in Figure 41.

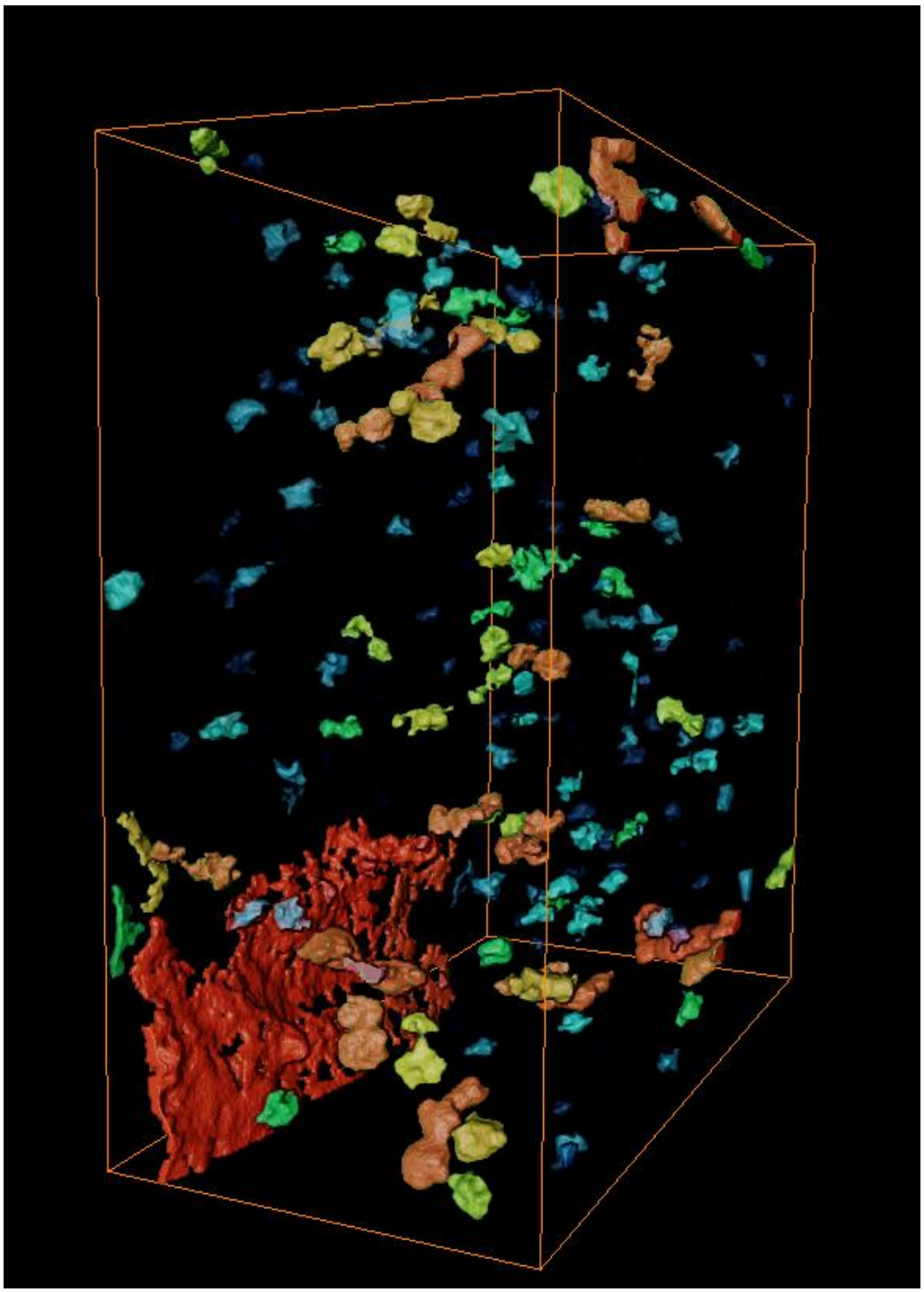


Figure 40: The porosity of the NRVB cement cured at 80°C, the crack in the sample can be seen at the bottom of the image where it is coloured red.

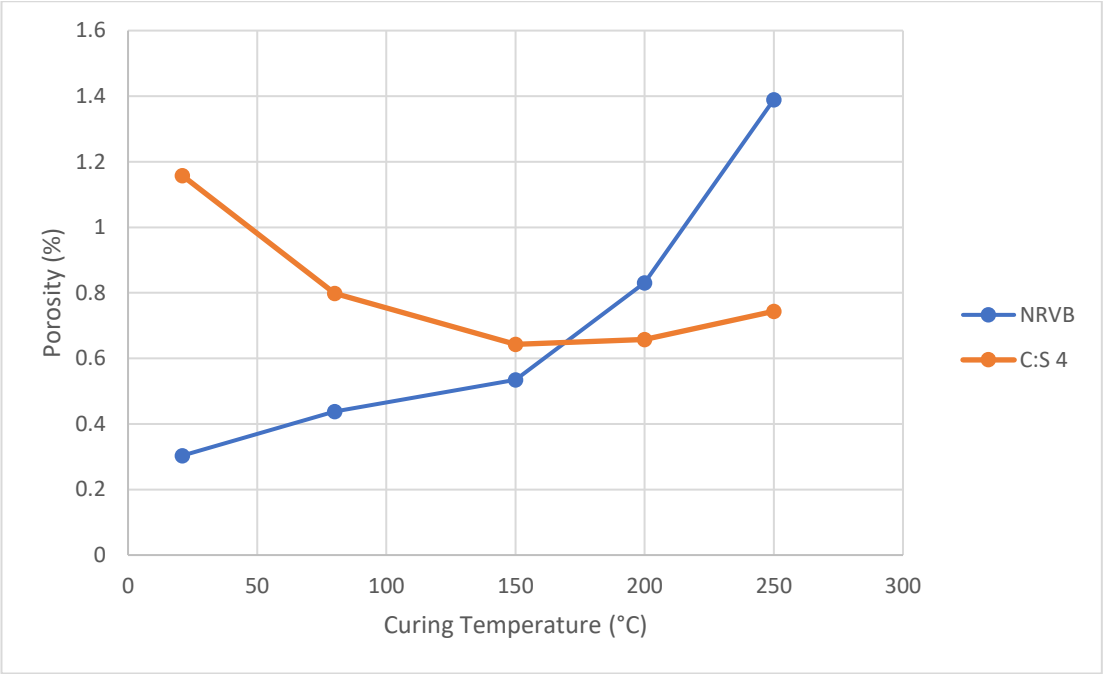


Figure 41: A graph comparing the percentage porosity measured using XCT and Avizo of the NRVB and C:S 4 cements cured at 25, 80, 150, 200 and 250°C.

Figure 41 shows the porosity measured using XCT of the NRVB cements and the C:S 4 cements. The C:S 4 cements show a decrease in porosity until a curing temperature of 150°C before a slight increase at a curing temperature of 200 and 250°C. The NRVB cement samples show a continual increase in porosity, with a sharper increase between a curing temperature of 150 and 200°C.

Figure 42 shows a render of the pores within the various cements with C:S ratio 4 and NRVB cured from 25 to 250°C. The images were created with Avizo. Only the cement samples C:S 4 and NRVB were scanned, this was due to wanting to compare the results gained from XCT with those from SEM and EMPA. These two samples are also the highest C:S ratio (NRVB has a C:S ratio of 7.27) and the lowest C:S ratio of 4, providing information on the two extremes of this project. All cement cores were 5mm wide.

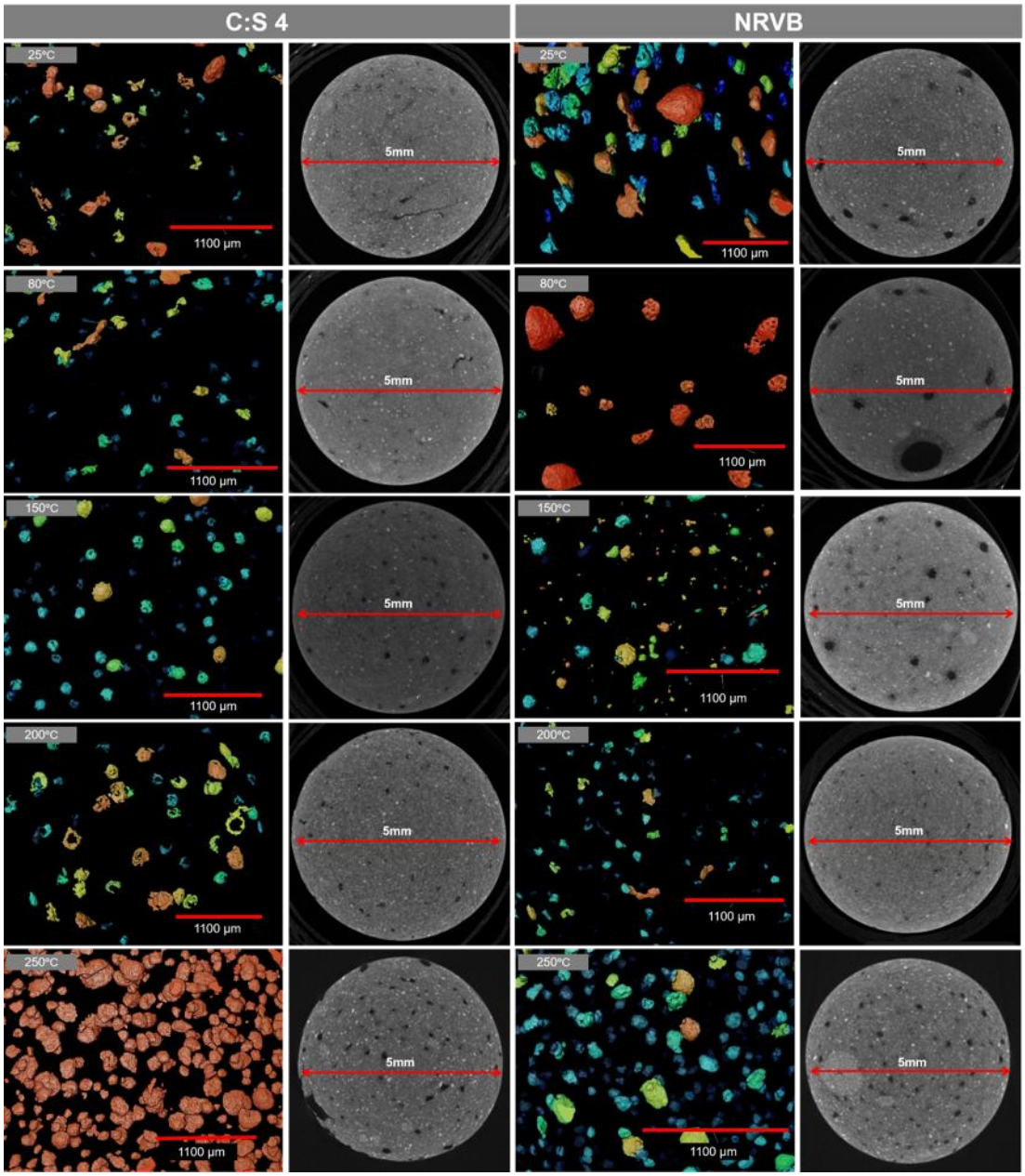


Figure 42: Image showing a 3D render of the pores of the samples scanned with XCT, the pores are coloured due to size where blue = smaller pores and red = larger. A greyscale 2D slide of each sample is next to the 3D render to show the pores in greyscale before processing.

4.3.2 Helium Pycnometry

The cement cores were scanned with XCT and processed with Avizo to calculate the total volume of cement and porosity. Cement cores from Part 3.5.1 are labelled in Table 30 with the word ‘calcite’ in their sample name. Cement cores from Part 3.5.2 do not contain the word ‘calcite’ in their sample name in Table 30. The values used to calculate the volumes of the cores studied in this chapter are in the table below. All

cores were scanned with the same resolution of 27μm for consistency and standardisation of data processing.

Table 30 shows the results of using XCT to calculate the volume of the cement core, then using helium pycnometry to calculate the percentage porosity.

*Table 30: The results of using XCT to calculate the volume of the cement core and then using the measurement from helium Pycnometry to calculate the percentage porosity of the cement cores. *samples were corrected for PEEK cup. HePyc is short for helium pycnometry.*

Sample	**Volume in voxels**	**Volume mm^3**	**HePyc volume mm^3**	**Porosity (%)**
NRVB 25°C	9308739	0.183224	0.0929	49.30
NRVB 80°C	6981408	0.137415	0.0676	50.81
NRVB 150°C	9090490	0.178928	0.0737	58.81
NRVB 200°C	6734842	0.132562	0.0665	49.84
NRVB 250°C	8950621	0.176175	PEEK Cup 0.4082 Core 0.1717*	89.51
C:S 4 25°C	9628983	0.189527	0.0953	49.72
C:S 4 80°C	7983562	0.15714	0.0779	50.43
C:S 4 150°C	8868383	0.174556	0.0833	52.28
C:S 4 200°C	6901620	0.135845	0.047	65.40
C:S 4 250°C	6.66E+06	0.131177	PEEK Cup 0.4508 Core 0.1717*	79.65
C:S 7 25°C	9612441	0.189202	0.1072	43.34
C:S 7 80°C	7557871	0.148762	0.0768	48.37
C:S 7 150°C	8272320	0.162824	0.0769	52.77
C:S 7 200°C	7702218	0.151603	0.0867	42.81
C:S 6 25°C	9016956	0.177481	0.1001	43.60
C:S 6 80°C	8587950	0.169037	0.0883	47.76
C:S 6 150°C	8212768	0.161652	0.0716	55.71
C:S 6 200°C	9597002	0.188898	0.0744	60.61
C:S 5 25°C	8990720	0.176964	0.0883	50.10
C:S 5 80°C	8602413	0.169321	0.0819	51.63

C:S 5 150°C	9039832	0.177931	0.0767	56.89
C:S 5 200°C	8432873	0.165984	0.0652	60.72
NRVB 25°C calcite	7676488	0.151096	0.085	43.75
NRVB 80°C calcite	8379688	0.164937	0.0789	52.16
C:S 4 25°C Calcite	8267518	0.16273	0.0797	51.02
C:S 4 80°C Calcite	8604232	0.169357	0.0803	52.59
C:S 5 25°C Calcite	8690070	0.171047	0.087	49.14
C:S 5 80°C Calcite	8535661	0.168007	0.0793	52.80
C:S 6 25°C Calcite	8406953	0.165474	0.0675	59.21
C:S 6 80°C Calcite	7315671	0.143994	0.0587	59.24
C:S 7 25°C Calcite	7558733	0.148779	0.0667	55.17
C:S 7 80°C Calcite	8624700	0.16976	0.072	57.59

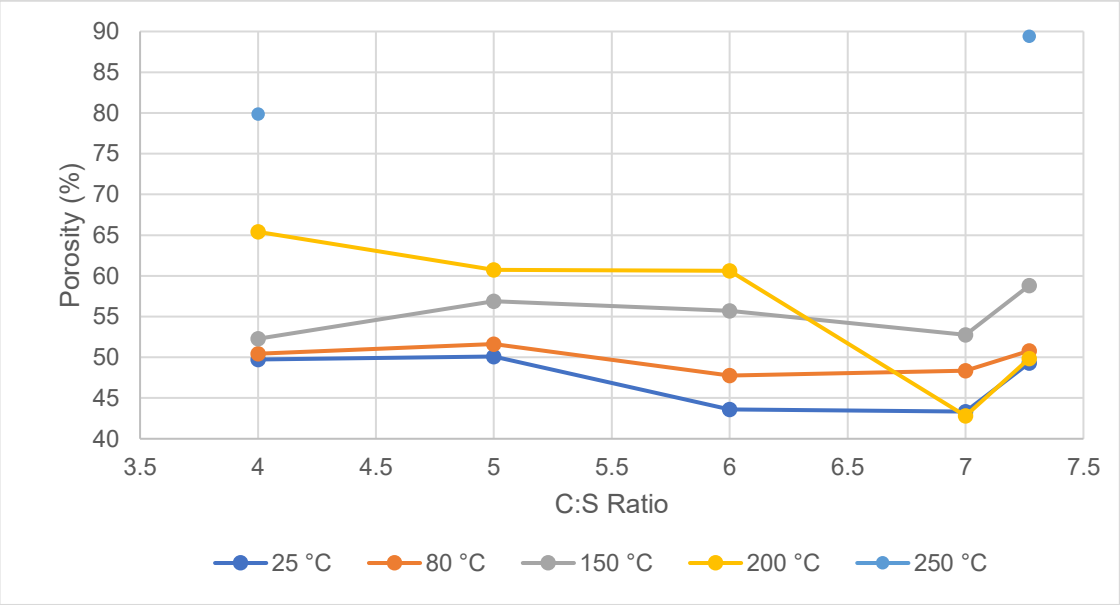


Figure 43: Graph showing the effect of temperature on porosity for cements with different C:S ratios measured with helium pycnometry.

The graph in Figure 43 shows that the porosity of the samples was affected by both the curing temperature and the C:S ratio. At lower temperatures of 25 and 80 °C, the porosity remained relatively consistent, with most samples having a porosity between approximately 43 and 51%. At 150 °C, the porosity was generally higher, ranging from approximately 52 to 59%. At 200 °C, increasing the C:S ratio generally decreased the porosity, from approximately 65% at C:S 4 to 42% at C:S 7, before increasing again at C:S 7.27. The greatest variation was observed at 250 °C, where the C:S 4 and C:S 7.27 samples had particularly high porosities of approximately 80 and 89%,

respectively. Overall, there is a general trend where cements had higher porosities when cured at higher temperatures, however cements mixed with a C:S ratio above 6 show no clear relationship between increasing temperature and porosity, suggesting that the C:S ratio and the mineral phases formed at each temperature also influenced the porosity of the samples.

4.3.3 SEM and EMPA of cements

SEM was undertaken on these samples to study the morphology of the cements in their bulk and pore space. EMPA was used to conduct elemental scans of the cements to study where mineralogy was forming. The EMPA elemental scans are shown in appendices 3 – 12.

4.3.3.1 EMPA

Figure 44 and Figure 45 show the compositional EMPA scans of the NRVB and $CaO:SiO_2$ ratio 4 in the middle column, the curing temperature of the cements in the left column, and an image taken with SEM BEC in the right column. The grayscale value of the image is related to the weight of the element that is being measured, where lighter elements appear darker and heavier elements appear lighter. In the SEM images the dark areas represent porosity.

Distinct boundaries can be seen within the compositional EMPA images for the NRVB samples cured at all temperatures. When the curing temperature reaches 200 and 250°C the solid phases are much further apart, with an apparent increase in pore space. This is in agreement with the porosity values calculated with helium pycnometry and XCT which show an increase in porosity with curing temperature.

In the EMPA results distinct mineral phase boundaries can be seen in all curing temperatures, the cement cured at 80°C appears to show the most homogeneity in its composition. The cement cured at 250°C shows the highest porosity, which is in agreement with the porosity values calculated with helium pycnometry and XCT.

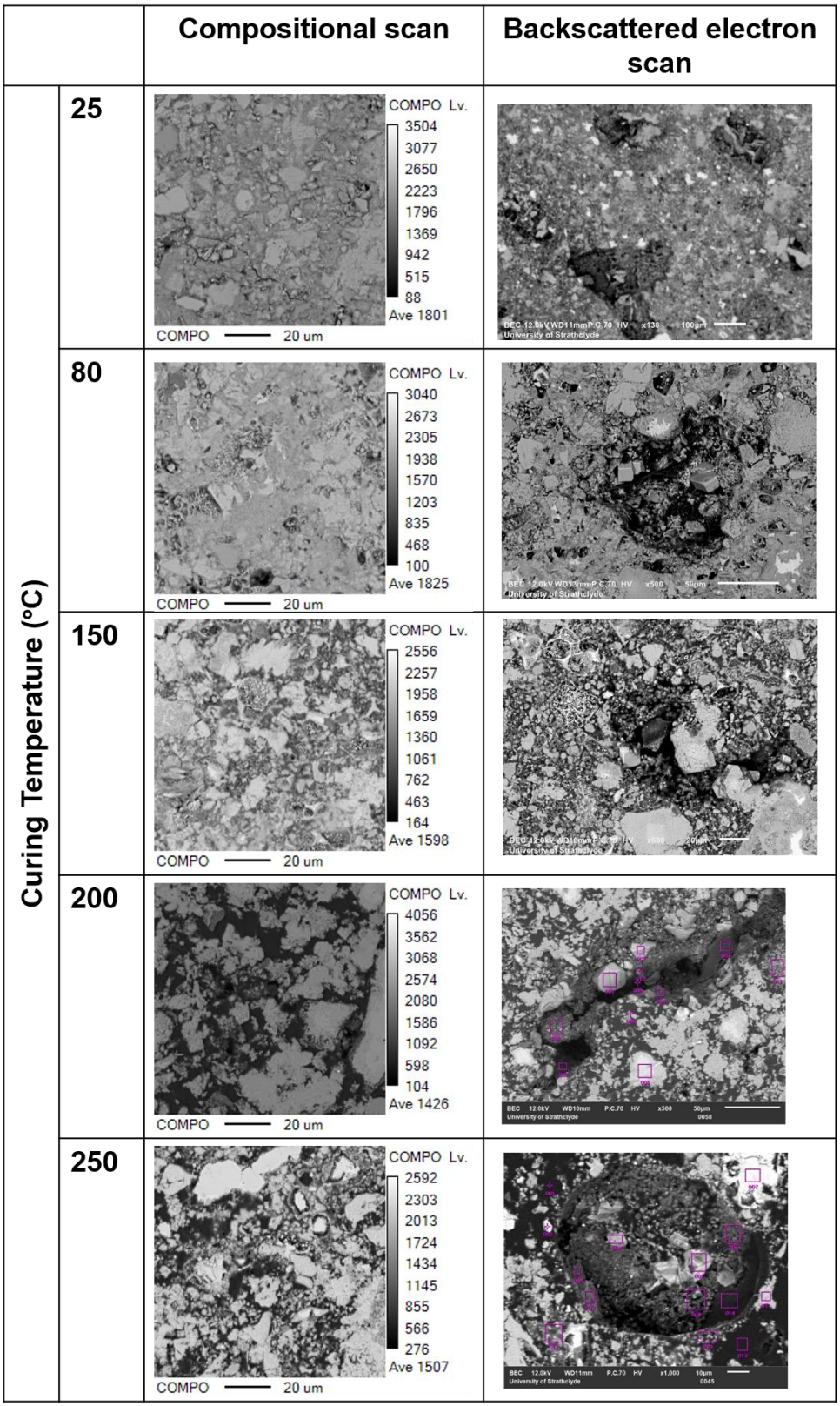


Figure 44: A compositional scan and backscattered electron scan of the NRVB cements cured at 25, 80, 150, 200 and 250°C. The purple boxes visible in the backscattered electron scan at 200 and 250°C are areas of the image that were scanned for elemental composition.

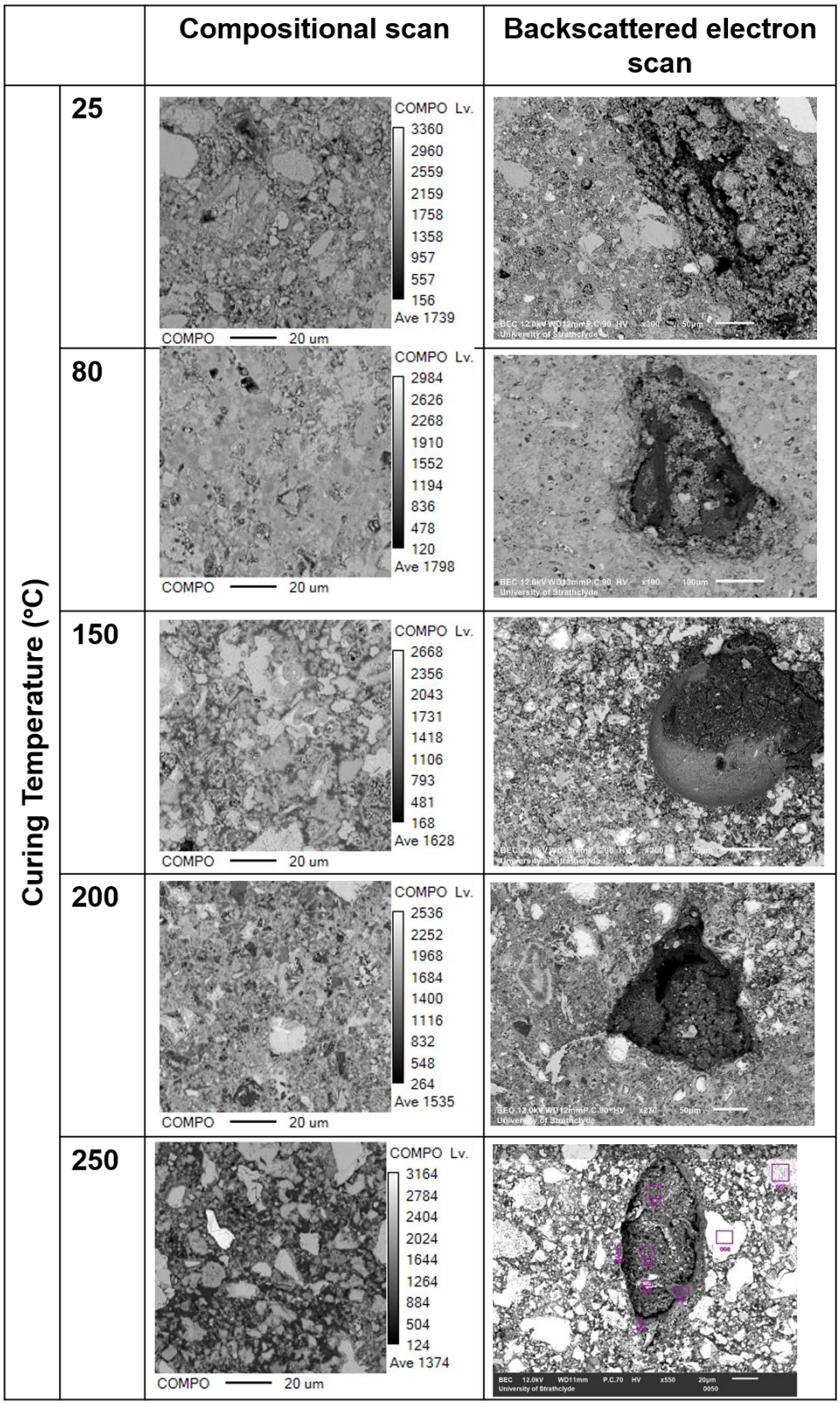


Figure 45: Compositional scan and backscattered electron scan of the C:S 4 cements cured at 25, 80, 150, 200 and 250°C. The purple boxes visible in the backscattered electron scan at 200 and 250°C are areas of the image that were scanned for elemental composition.

4.3.3.2 SEM

SEM was used to visually identify mineralogy in and around the pore space of the cements. SEM images of the samples pores are shown in Figure 46. In the NRVB sample cured at 25°C portlandite plates are visible within the pore. Amorphous content is also visible, this is likely CSH gel that has not finished hydration reactions. At 80°C the NRVB cement has formed cubic calcite crystals within the pore[153], this suggests the calcite forms from CO_2 that has dissolved in the pore water. At 150°C the pore becomes less easily defined as minerals begin to form within it. This is a crack shaped pore in a sample cured at 200°C, a calcite crystal is visible. No portlandite can be seen. At 250°C curing the pore structure is no longer visible. This is due to strength retrogression minerals forming and weakening the cement the image also shows there is a higher crystal surface accessibility and a breakdown of the matrix. Figure 47 shows a mineral that has shrunk from its original volume, this is likely either α-C_2SH or jaffeite which when they both form have a smaller unit cell than the mineral they form from. This shrinkage has caused pore space around the mineral.

In the C:S 4 sample cured at 25°C portlandite plates (flat, hexagonal) are visible within the pore. Some amorphous C-S-H gel is also visible. At 80°C the C:S 4 cement has formed long calcite crystals within the pore[153], this suggests the calcite forms from CO_2 that has dissolved in the pore water. There is also significant amounts of amorphous C-S-H gel visible within the pore. At 150°C curing temperature the pore within the C:S 4 cement has no visible minerals within it, however minerals appear to have formed at the edge of the pore. No calcite or portlandite is visible. At 200°C curing temperature the pore has minerals forming within it. There is also a visible portlandite or calcite crystal that has formed within the pore. Surrounding the pore there are several structures that appear to have a shell around them, these are minerals that have undergone shrinkage when they formed such as α-C_2SH or jaffeite. At 250°C curing the pore structure is no longer visible. This is due to strength retrogression minerals forming and weakening the cement. There are minerals that appear to have a shell around them, these have undergone shrinkage when they formed such as α-C_2SH or jaffeite.

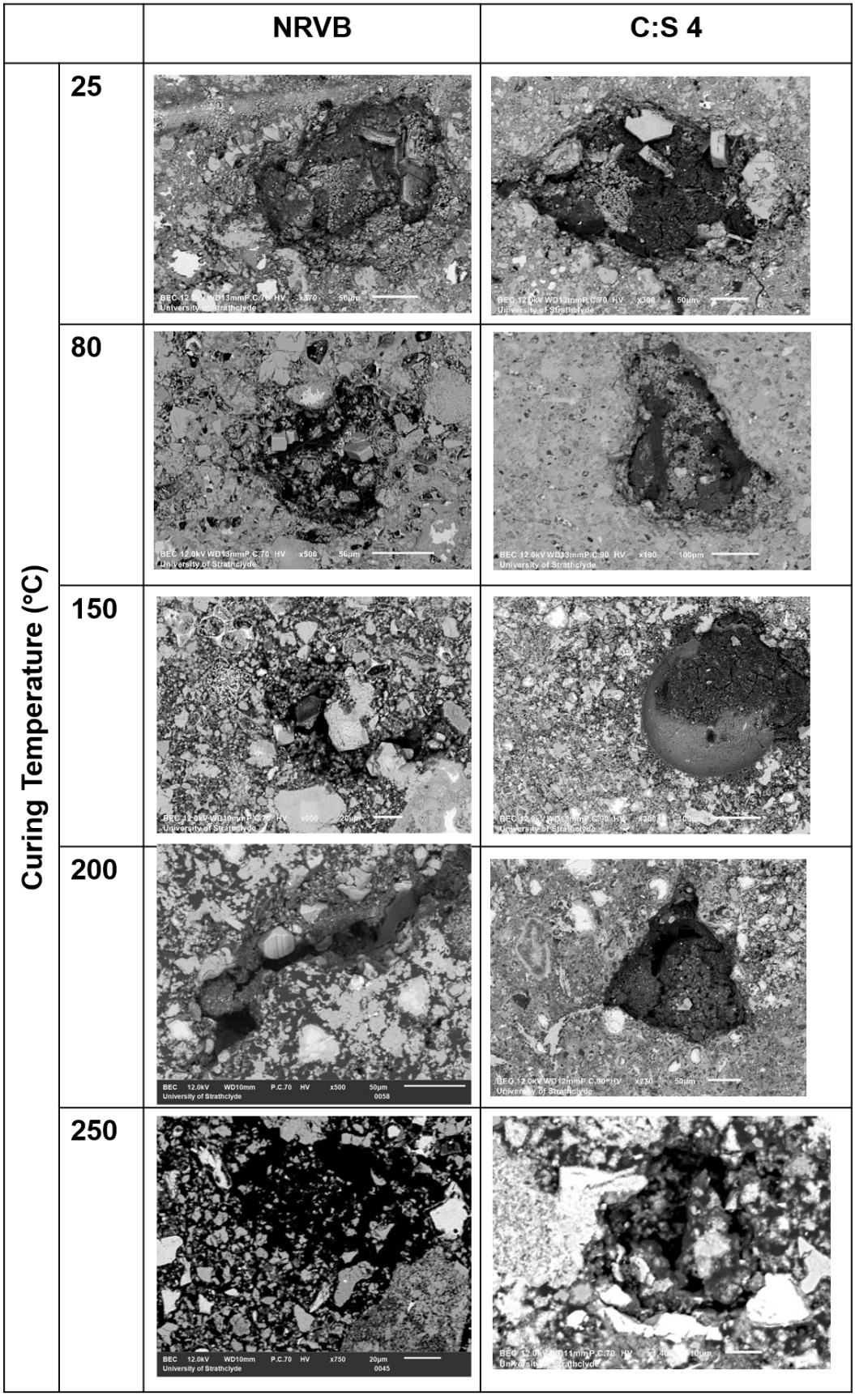


Figure 46: SEM images of the NRVB and C:S 4 cements cured at 25, 80, 150, 200 and 250°C.

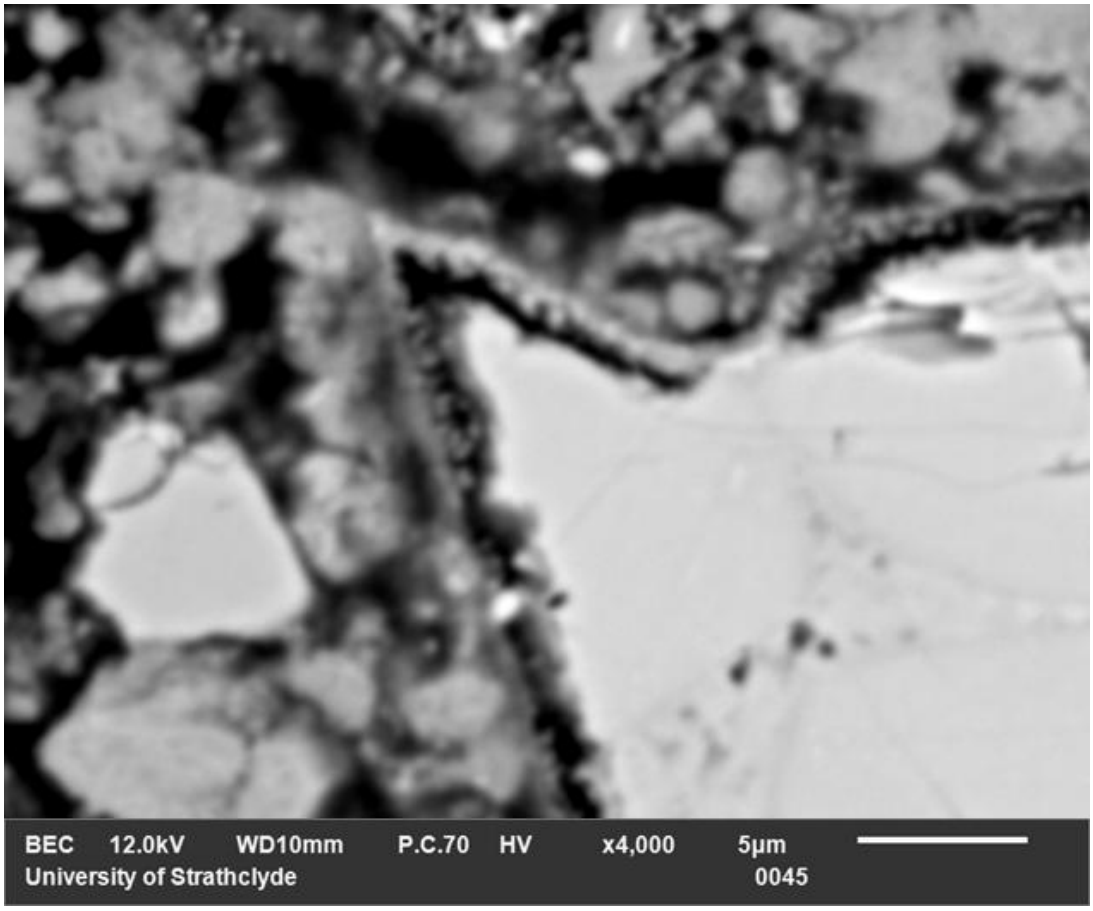


Figure 47: A SEM image of NRVB cement cured at 250°C showing a mineral within the cement that appears to have shrunk during curing. This is shown by the 'shell' visible around the large light grey mineral.

4.4 Discussion and comparison

4.4.1 The effect of curing temperature and $CaO:SiO_2$ ratio on porosity

Figure 48 shows the porosities calculated using helium pycnometry. The samples with a $CaO:SiO_2$ ratio of 4 and NRVB (7.27) were also cured at 250°C within PEEK moulds with an internal diameter of 0.5cm and a depth of 1cm. This was so they could be measured using XCT and embedded in resin to allow for EMPA and SEM scanning. These samples were also measured using helium pycnometry. However, they are excluded from the below graph. This is because no other samples were prepared this

way at 250°C, and therefore no comparison can be made and no conclusions can be reliably drawn between the effects of $CaO:SiO_2$ ratio and curing temperature of 250°C. The data however will be used further on in this chapter to look at the effects of temperature on the individual ratios.

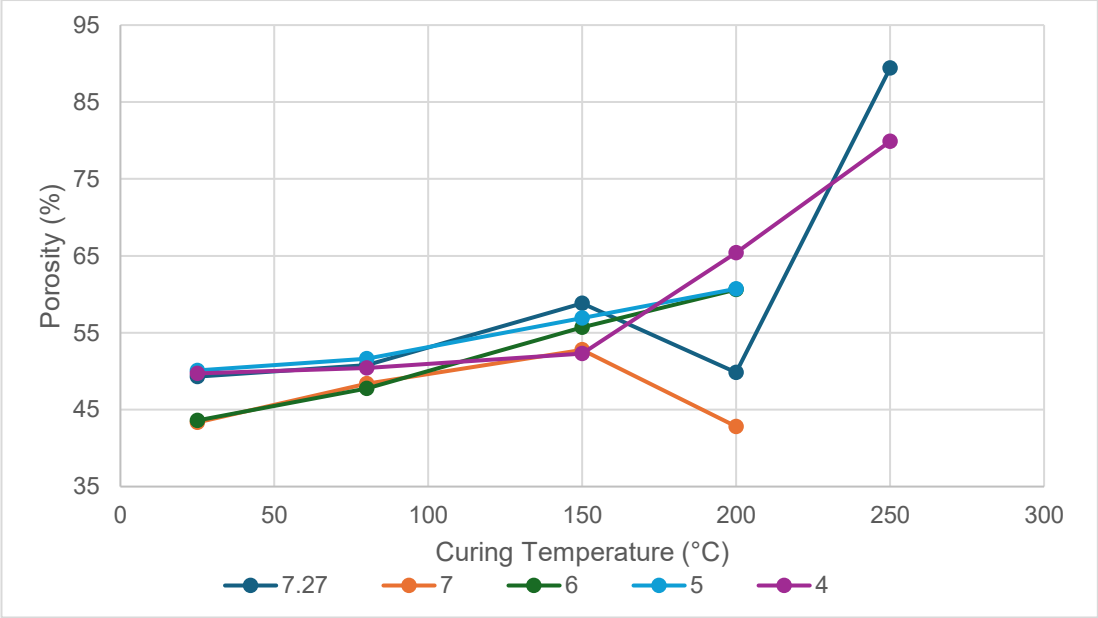


Figure 48: Graph showing the effect of temperature on porosity for cements with different C:S ratios measured with helium pycnometry.

The data up until 150°C showed an increase in porosity with curing temperature for all $CaO:SiO_2$ ratios. The sample made with a $CaO:SiO_2$ ratio of 4, where 19% of the cement powder was replaced with silicon dioxide powder, showed the lowest effect of porosity with curing temperature, having just an increase of 49.72% from being cured at room temperature to 52.27% when cured at 150°C. This sample however then showed the largest increase from being cured at 150°C to 200°C, where the porosity rose to 65.40%. A higher porosity is associated with a lower strength. This data shows that the C:S 4 cement should maintain its strength to a curing temperature of 150°C whereas the other cement mixes showed an increase in porosity which suggests a decrease in strength. However, above 150 the C:S 4 cement shows a large increase in total porosity whereas the NRVB and C:S 7 cements have a decrease in porosity. This data shows the importance of knowing the curing temperature of the cement in the repository as the C:S ratio can be altered to produce a cement that has the desired porosity and strength.

4.4.2 The effect of removing $CaCO_3$, $CaO:SiO_2$ ratio, and temperature on cement porosity

NRVB cement was mixed with and without $CaCO_3$. In the previous chapter where the effect of curing temperature and $CaO:SiO_2$ ratio was studied it was concluded that the addition and subsequent removal of $CaCO_3$ to/from the NRVB formula made no impact on the mineralogy of the final cement. The $CaCO_3$ was not found to react within the mix to form any other calcium containing minerals. The proportion of it increased as portlandite reacts with water and CO_2 to form more $CaCO_3$. The $CaCO_3$ however, was inert within the mixture. It was therefore removed to allow for mineralogical phases present in small (<10%) amounts to be identified during XRD analysis.

The mineralogical composition, however, is not the only cement property that has an impact on the strength and physical properties of the cement, such as water transport. The porosity of the cement is an important quality in the overall NRVB cement, as it effects how quickly radionuclides and other contaminants can dissolve from the storage containers, through the NRVB, and enter the biosphere. It is therefore important to understand how the quantity of $CaCO_3$ within the NRVB formula affects the porosity.

Cements that contained $CaCO_3$ were physically weaker than those with it omitted from the formula, cores were therefore only collected and dried when the cement was cured at either room temperature or 80°C. When the cements were cured at higher temperatures the cores immediately collapsed, or they broke apart during the solvent exchange and drying process.

This increased weakness when $CaCO_3$ is included in the starting mix is likely due to the high percentage of the NRVB formula that is calcite, 28%. The calcite was found not to react so it is just present as loose particles. Fick's law states that this probably gets in the way of the calcium hydroxide, cement powder, and SiO_2 reacting, leading to less overall cement minerals forming, and those that do having calcite powder interspersed between them.

Removing the $CaCO_3$ also means there is a higher proportion of components that react to form strengthening minerals, and minerals that will interact and interlock with each other, as opposed to $CaCO_3$ which is essentially ground chalk. Conversely, when calcite forms naturally from carbonation reactions during hydration or curing it has a strengthening effect.

The cement cores mixed with calcite and then cured at either room temperature (25°C) or 80°C were measured in the Helium Pycnometer following the same method as the cores that were cured with no calcite. The results are shown in the graph in in Figure 49 below. The NRVB sample showed the largest increase in porosity as the curing temperature was increased to 80°C, it also had the lowest porosity at both curing temperatures. A lower porosity is desirable as it suggests there is less of a pathway for groundwater ingress and radionuclide egress, as all cements had a lower porosity at lower temperatures it is desirable to cure the cements at lower temperatures to maintain a lower porosity.

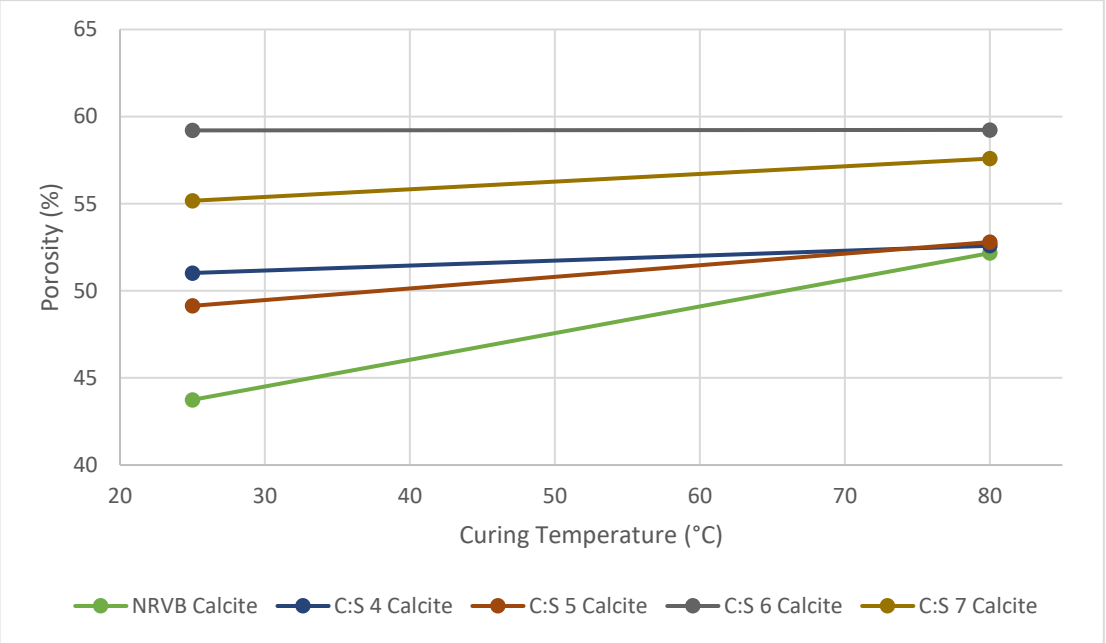


Figure 49: Graph showing the effect of temperature on porosity for cements with different C:S ratios for cements mixed with calcium carbonate.

Table 31: Helium pycnometer results for cements mixed with calcium carbonate cured at room temperature and 80°C.

	Curing Temperature (°C)		
$CaO:SiO_2$ ratio	**25**	**80**	**Difference**
C:S 7.27 NRVB	43.74449	52.16367	+8.419178
C:S 4	51.02303	52.58539	+1.562361
C:S 5	49.13668	52.7997	+3.66302
C:S 6	59.20811	59.23451	+0.026405
C:S 7	55.16827	57.58717	+2.4189

The results are shown in Figure 49 and Table 31 show that the porosity of all cement mixes increased with curing temperature. This could be due to more hydration reactions occurring due to the higher temperature. It could also be due to excess water increasing the capillary porosity and decreasing the strength. At room temperature NRVB had the lowest porosity, NRVB also has the lowest amount of SiO_2, so there is less silica to react with calcium to form minerals. NRVB also showed the greatest difference in porosity between room temperature curing and curing at 80°C, of an increase of 8.4%. This implies that the mineralogy is different at the two temperatures, and the mineralogy is reacting in or adjacent to the pore space, or at 80°C there is more unreacted water that is able to form pores and evaporate off. This is shown in Figure 46 where additional calcite minerals are present in the pore space of NRVB at 80°C that are not present at 25°C.

The cement with a $CaO:SiO_2$ ratio of 6 had a very similar to one decimal place porosity at both room temperature and 80°C curing. This suggests that the minerals forming are either very similar at both temperatures, or do not form near or within the pores.

All of the cement mixes showed an increase in porosity when cured at 80°C. There does not appear to be a trend in the porosity when compared to the $CaO:SiO_2$ ratio. This suggests that the porosity for these mixes is more dependent on curing temperature, rather than the $CaO:SiO_2$ ratio, and the main influencing factor is evaporation of water, either because the water is present in excess, or before the water is able to complete all hydration reactions.

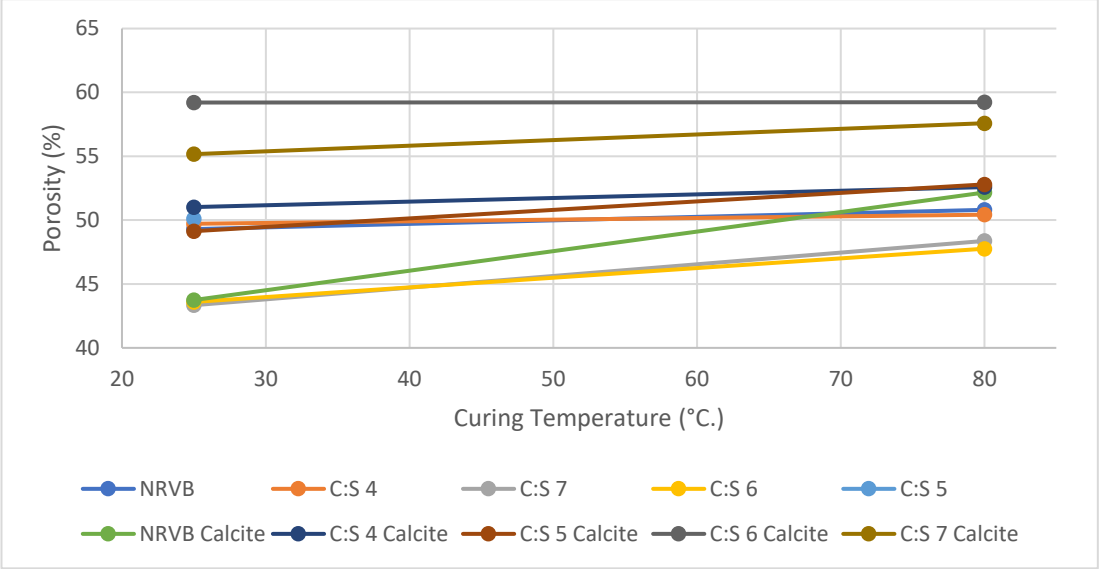


Figure 50: A graph showing the porosity of cements cured at room temperature and 80°C that have the same C:S ratio, the cements with calcite in the starting mix are labelled with 'calcite'.

The graph in Figure 50 above shows a comparison of the same cement mixes however some have the $CaCO_3$ removed. Where the $CaCO_3$ is removed the amount of water was adjusted to maintain the same water to cement ratio. This ensures that any difference in porosity is due to reactions within the cement, and not the water content. Removing the $CaCO_3$ from the cement mix made little to no difference on the porosity of the cured cement. This provides confidence that the porosity measurements made in this chapter, and the conclusions drawn from them, are applicable to NRVB cement.

Table 32: The porosity values calculated with helium pycnometry when the cement samples were cured at 25°C.

	With $CaCO_3$	**No $CaCO_3$**	**Difference**
NRVB	43.75	49.3	-5.55
C:S 7	55.16827	43.34088	+11.8274
C:S 6	59.20811	43.59952	+15.6086
C:S 5	49.13668	50.10294	-0.9663
C:S 4	51.02303	49.717	+1.30603

Table 33: The porosity values calculated with helium pycnometry when the cement samples were cured at 80°C.

	With $CaCO_3$	**No $CaCO_3$**	**Difference**
NRVB	52.16367	50.80597	+1.357697
C:S 7	57.58717	48.37377	+9.21341
C:S 6	59.23451	47.7628	+11.4717
C:S 5	52.7997	51.63042	+1.16928
C:S 4	52.58539	50.42651	+2.15888

The samples made using the same formulation as NRVB, and those with SiO_2 added to produce C:S ratios of 4 and 5, showed little difference in porosity between samples made with and without $CaCO_3$ when cured at room temperature and 80 °C (Table 32, Table 33). In contrast, samples with C:S ratios of 6 and 7 showed a considerably greater difference, with the samples containing $CaCO_3$ having approximately 9–15% higher porosity. This was unexpected, particularly as NRVB has a C:S ratio of 7.27 and might therefore have been expected to behave similarly to the samples with a C:S ratio of 7.

The effect of $CaCO_3$ on cement hydration is complex, and $CaCO_3$ cannot necessarily be considered as an inert component within the cement formulation. A previous study demonstrated that calcite can influence cement hydration by altering the distribution of calcium, aluminium and sulfate and modifying the resulting hydrate assemblage[134]. In particular, the presence of calcite can affect the formation and stability of AFm and AFt phases[134]. It has also been found that the addition of limestone was able to alter the hydrate assemblage of Portland cement, including stabilising monocarbonate and ettringite[154]. These changes affected the calculated volume of solid hydration products and consequently the predicted porosity of the cement[154]. Therefore, the presence of $CaCO_3$ in the samples studied here may have influenced the hydration reactions and resulting pore structure rather than simply acting as an inert component.

The effect of $CaCO_3$ on porosity is also dependent on the composition of the cement system. The effect of the addition of limestone on porosity varies depending on factors such as the quantity and fineness of limestone, cement composition, water-to-cement ratio and curing conditions[155]. Limestone can affect cement hydration through several competing mechanisms, including filler, nucleation, chemical and dilution effects[156]. The filler and nucleation effects can promote a denser microstructure, while at higher

replacement levels the dilution of reactive cementitious material can reduce the quantity of hydration products and increase porosity[156]. This could explain why the addition of $CaCO_3$ did not produce the same change in porosity across all the C:S ratios investigated.

This is particularly apparent for the C:S ratio 6 samples. The sample containing $CaCO_3$ had the highest porosity of all the cement samples at both room temperature and 80 °C, whereas the equivalent formulation without $CaCO_3$ had the lowest porosity at both curing temperatures. The same general effect, although less pronounced, was observed at a C:S ratio of 7. As the differences were observed independently at both curing temperatures, it is unlikely that they are solely the result of experimental variation or measurement error. Instead, the results suggest that the presence of $CaCO_3$ interacts with the cement composition at these higher C:S ratios and influences the development of the pore structure.

One possible explanation for this is an alteration in the formation and distribution of C–S–H. Calcite surfaces have been shown to provide nucleation sites for C–S–H formation, meaning that the presence of calcite can influence both the kinetics and spatial distribution of hydration products[157]. Differences in the quantity of available silica and calcium at C:S ratios of 6 and 7, combined with the presence of calcite, may have changed the formation or distribution of C–S–H and therefore the resulting pore structure. However, this mechanism cannot be confirmed from the results obtained in this study.

The C:S ratios reported here represent the bulk composition of the cement formulation rather than the C:S ratio of the C–S–H phase itself. C–S–H generally has a considerably lower C:S ratio than the bulk C:S ratios investigated here, with excess calcium accommodated within other calcium-containing phases such as portlandite and calcite[158]. Therefore, a similar bulk C:S ratio does not necessarily result in the formation of an equivalent hydrate assemblage or pore structure. This may partly explain why NRVB, despite having a bulk C:S ratio of 7.27, did not show similar porosity behaviour to the C:S 7 formulation.

The mineralogical results cannot be used to determine conclusively which mechanism caused the increased porosity at C:S ratios of 6 and 7. The high proportion of crystalline calcite within the samples made with $CaCO_3$ made the identification and quantification of lower-abundance hydration products by XRD difficult. Therefore,

differences in C–S–H or minor crystalline hydration products between the samples could not be reliably identified. Further analysis using SEM-EDX or EMPA could help determine whether differences in the distribution and composition of C–S–H occur between the samples, while thermal analysis could provide additional information on changes in portlandite and carbonate-containing phases. Nevertheless, the consistent differences observed at both room temperature and 80 °C indicate that the increased porosity associated with $CaCO_3$ at C:S ratios of 6 and 7 is likely to represent a genuine compositional effect rather than experimental variability.

4.4.3 Distribution of minerals

EMPA

The EMPA scans confirmed that when the cements are cured at temperatures of 200 and 250°C the mineral phases are further apart, with an increase in pore space and less matrix material. This is in agreement with helium pycnometry which shows an increase in total volume, and XCT which show an increase in macroporosity with curing temperature. EMPA (Appendices 3, 4, 8,and 9) also confirmed the presence of calcium silicate minerals, calcium carbonate, portlandite, and calcium silicates that also contain aluminium. This is in agreement with the mineralogical compositions identified in the previous chapter.

SEM

SEM of NRVB and C:S 4 cements at 25 and 80°C show portlandite and amorphous C-S-H gel present. At 80°C calcium carbonate growths are visible. As the curing temperature increases less portlandite is visible within the pore space, and other minerals begin to form inside the pore. At 250°C the pore structure for both NRVB and C:S 4 cement appears to have broken down, with minerals that have undergone shrinkage and strength retrogression visible. This confirms the mineralogy identified in the previous chapter.

4.4.4 Macro porosity

The samples with the NRVB formula show an increase in porosity with higher curing temperatures (Figure 51). The samples adjusted to a $CaO:SiO_2$ ratio of 4 show a decrease in porosity until a curing temperature of 150°C, then a slight increase to 200

and 250°C. This suggests that between 150 and 200°C a reaction is taking place within the cement that leads to a decrease in porosity, this could be due to minerals forming within the pore space, or minerals forming that have a larger unit cell size.

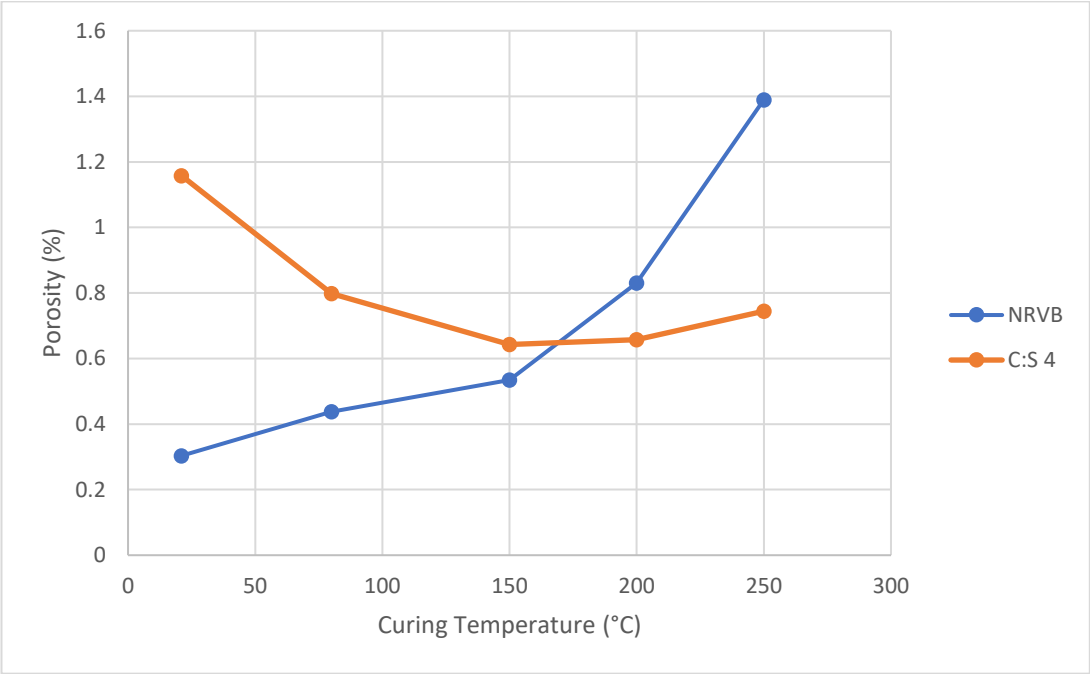


Figure 51: A graph comparing the percentage porosity measured using XCT and Avizo of the NRVB and C:S 4 cements cured at 25, 80, 150, 200 and 250°C.

Figure 52 shows a comparison of the pores that were able to be identified using the thresholding function in Avizo. The pores that formed at a curing temperature of 150°C are typically solid, and spherical. However, the pores that formed when the cement was cured at 200°C show several 'ring-like' pores, suggesting that the hydration reactions within the cement are different at the hotter curing temperature.

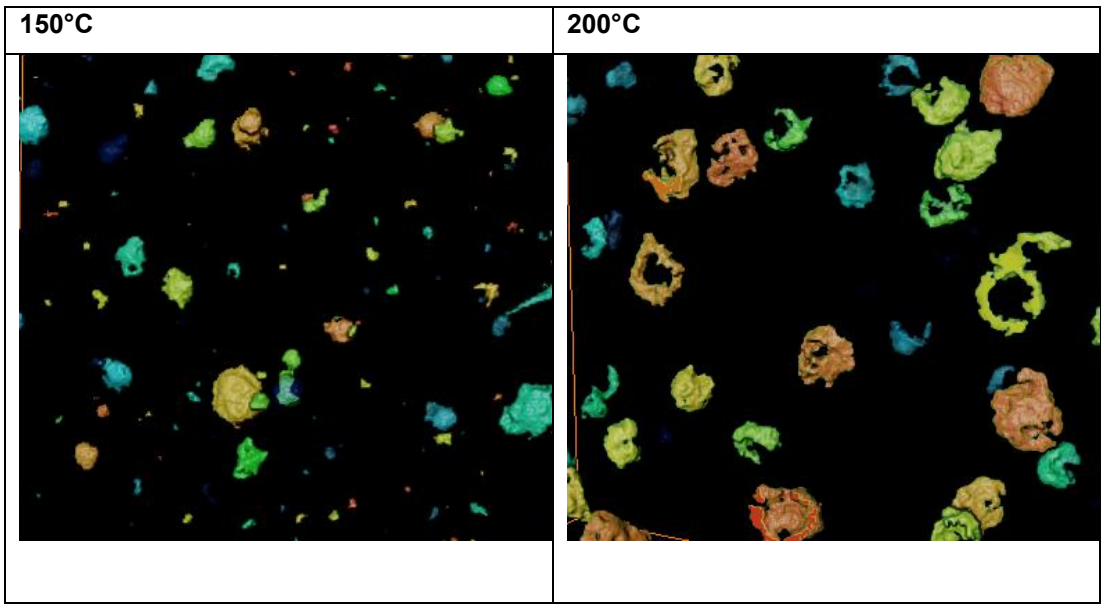


Figure 52: A comparison of the pores that were able to be identified using the thresholding function in Avizo in NRVB at 150 (left) and 250°C (right).

Figure 53 below shows the pores at the same temperatures as the table above, however for the NRVB formula. As can be seen, the pores in the NRVB cement are similar to those of C:S ratio 4 when the cements are cured at room temperature, however at 200°C the 'ring-like' pores are less pronounced. This suggests the same hydration reaction occurs at both formulations at a curing temperature of 200°C, however it is less pronounced within the NRVB cement, likely due to the presence of less SiO_2 available to react.

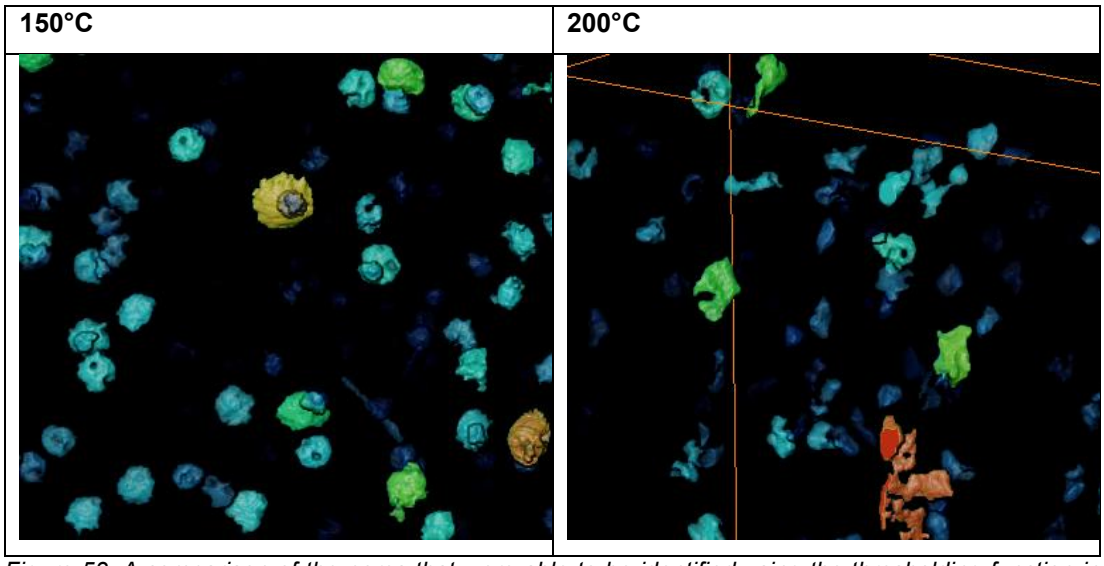


Figure 53: A comparison of the pores that were able to be identified using the thresholding function in Avizo in C:S 4 at 150 (left) and 250°C (right).

4.4.4.1 XCT vs Helium Pycnometry

NRVB formula

The two methods used to measure porosity in this chapter, XCT and helium pycnometry, provided very different results. The XCT gave values of approximately 1%, whereas the helium pycnometry gave porosity percentages that aligned far more closely to porosities found in literature[142]. The measurements from both for the cement with the NRVB formulation showed a very similar trend as shown in Figure 54, despite the porosity values from helium pycnometry being 50 times larger than those calculated from XCT. Using XCT only larger pores could be identified and measured, the similar trends of the data suggests that all pores regardless of size are affected by curing temperature similarly. This implies that the changes in porosity seen at different curing temperatures is affecting the pore size distribution equally. Alternatively, the change in curing temperature could have a much more significant effect on the larger pores which has more impact on the total porosity, and the smaller pores could remain unaffected.

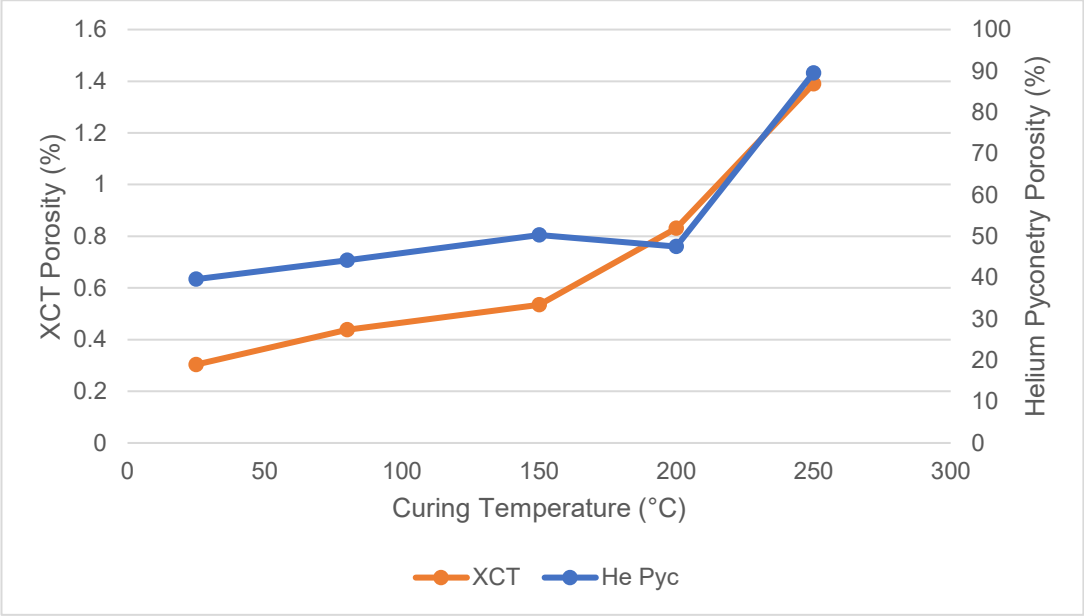


Figure 54: A graph showing a comparison of measuring the porosity of the NRVB cement cores cured at 25, 80, 150, 200 and 250°C with XCT and helium pycnometry.

$CaO:SiO_2$ ratio 4

The porosity measured with XCT and helium pycnometry for the cements with a C:S ratio of 4 show a different trend to that measured for the NRVB formula cements (Figure 55). The porosities measured using XCT show a mirror image relationship to the porosity values measured using helium pycnometry. As curing temperature increases the porosity able to be measured with XCT decreases, whereas the porosity measured with helium pycnometry increases. As XCT is only able to measure larger pores this suggests that at higher curing temperatures the pore size is reduced or fewer large pores are forming.

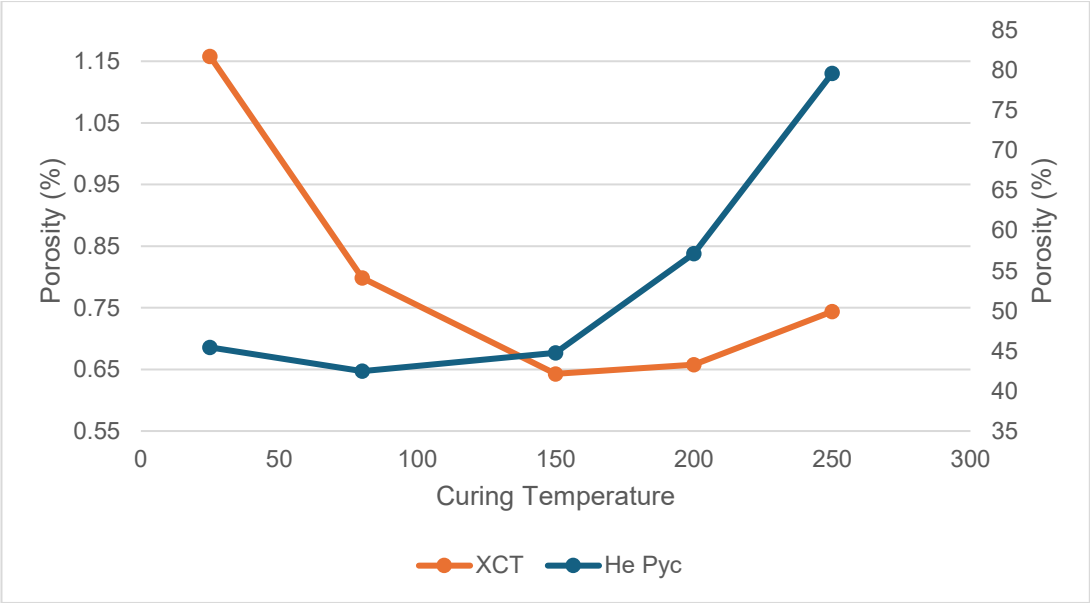


Figure 55: A comparison of the porosity measured with XCT and helium pycnometry for the C:S 4 cement cores.

Helium pycnometry measures the total porosity within the cement, as this shows the porosity increasing at higher curing temperatures this shows that despite the volume and/or number of larger pores reducing the total porosity increases. The size and/or number of pores reducing at higher curing temperatures could be due to reactions occurring within the pore space to form high temperature minerals. This is confirmed by the SEM and EMPA shown in Figure 44, Figure 45, and Figure 46 which show the formation of minerals within and on the edges of the pores when the cements are cured at higher temperatures.

The helium pycnometry results for both NRVB and cements with a C:S ratio of 4 show the same trend, where porosity increases with temperature. However when the pores

are measured with XCT the NRVB samples consistently increase in porosity whereas the cements with a C:S ratio of 4 have a reduction in porosity until they are cured above 150°C, where the porosity shows a gentle increase to a porosity value of 0.74% that is still less than the porosity when cured at 80°C (0.80%). The cements with a $CaO:SiO_2$ ratio of 4 have 19% of the cement powder replaced with SiO_2 which reduces the $CaO:SiO_2$ ratio from 7.27 to 4. This additional SiO_2 can react with the CaO containing species within the cement powder, alongside the portlandite ($Ca(OH)_2$) that is added to the mix. SEM showed less portlandite visible in the pore space as the curing temperature was increased. However, the presence of portlandite near pores does not mean that the reaction is occurring at the pore surface. It is more likely that the changes in both the portlandite and the pores are consequences of the same reaction, opposed to one causing the other. Portlandite may remain or precipitate in regions that are relatively less reacted by the increased curing temperature, while pore formation may occur where there has been local volume change, dissolution, or phase transformation. The presence of portlandite in pores at lower curing temperatures could just be resulting from a heterogeneous reaction and not be from a direct reaction at the pore surface.

The location of reactions needs to be considered in terms of the solid phases rather than the pores themselves. Reactions are likely occurring within the C–S–H or other cementitious phases, where changes in composition such as the formation of calcium silicate phases lead to a change in the matrix of the cement. The formation of these minerals can alter the porosity as a result of solid volume reduction, density changes, calcium leaching (decalcification) or localised dissolution[159,160]. In this context, pores are a product of reaction, not the site where the reaction takes place[161,162]. The pores are generated as the solid mineral phases evolve during hydration and evolution reactions[163,164]**.** The water acts as a reactant and as a transport medium for these reactions to occur. Reactions within the cement that can change the porosity are decalcification of C-S-H which can redistribute calcium and increase the stability of minerals such as portlandite[165]. This will produce a volume change, and portlandite may remain stable in certain regions where they are less reactive or where calcium is readily available.

4.5 Conclusions

In this chapter the porosity of cements with a C:S ratio of 4, 5, 6, 7 and NRVB were measured using XCT and helium pycnometry. Cements with a C:S ratio of 4 and NRVB were also analysed using EMPA and XCT.

- The sample preparation techniques used in this chapter were effective and allowed high quality data to be measured.
- Removing calcium carbonate from the cement mixture had minimal to no effect on the porosity of the cement. The calcium carbonate is used as filler in the NRVB formula and did not react when tested in the previous chapter. From this information it can be assumed that the calcium carbonate has no effect on the pore structure of the cement.
- The porosity of cements made with a C:S ratio of 4, 5, and 6 increased as curing temperature increased. The cements with C:S ratio of 7 and NRVB increased to a curing temperature of 150°C before decreasing at 200 and 250°C. This is due to minerals forming within the pore space at elevated temperatures.
- Helium pycnometry provided a more comprehensive pore measurement than XCT, this is because helium pycnometry is able to measure all porosity including microporosity, whereas XCT can only measure macroporosity above a certain resolution. Comparing the two techniques allows for an understanding about the multiscale nature and differences of the porosity.
- The XCT and helium pycnometry measurements followed a similar trend for the NRVB cement, however the trend is less similar for the C:S 4 cement. This implies the proportion of micro and macro pores is the same across the range of curing temperatures in NRVB cement. The trend being less similar implies that the proportions change in the C:S 4 cement.
- EMPA confirmed the cements were comprised of calcium silicate minerals, portlandite, calcium carbonate, and calcium silicate minerals that also contain aluminium. Further work could be done to map these minerals across the pore space.
- SEM confirmed the presence of portlandite within the pore space in both NRVB and C:S 4 at lower curing temperatures, and the formation of minerals within the pore space at higher curing temperatures. They both showed the pore space losing integrity at a curing temperature of 250°C.

The porosity of a cement is directly linked to the strength, as porosity increases the strength decreases. The results from this chapter have measured the porosity of NRVB with different C:S ratios and looked at the effect of curing the cements at different temperatures up to 250°C. The porosity was dependent on the C:S ratio and the curing temperature. As both factors affected the porosity, this shows that once the temperature of the repository is known, the C:S ratio of the cement can be altered to produce a desirable porosity that maintains the necessary strength and transport properties required of the backfill material.

4.5.1 Further work

Further work building on this chapter could focus on expanding the range of C:S ratios analysed using EMPA and SEM. Looking at a wider range of C:S ratios would help to better understand how changes in C:S ratio influence the microstructure and whether the trends observed here are consistent across a wider dataset.

Additional mineral mapping using EMPA could also be carried out with the use of calibration standards. This would allow the C:S ratio to be measured more accurately and provide more confidence in the spatial variation of composition within the samples. Improved calibration would be particularly useful when identifying subtle differences in phase chemistry that may influence pore development including identifying calcium silicate minerals that are forming around and within the pores.

Further XCT and helium pycnometry analysis could be undertaken on cements with different C:S ratios to determine whether the pore shapes and trends in total porosity observed in NRVB and C:S 4 are representative, or if they vary with composition at the temperatures studied. This would help to establish whether there is a consistent relationship between C:S ratio and pore morphology. Particularly C:S ratios between 6 and 7 as they show the greatest difference in porosity trend when heated above 150°C.

In situ XCT could also be used, where the same sample is heated and scanned repeatedly over time. This would allow the evolution of pore structures to be observed directly, providing insight into how pores evolve during curing rather than relying on measurements of the cements after they have been cured. Higher resolution XCT could be achieved by scanning smaller core samples, allowing finer-scale pore features to be resolved. In addition, nano–X-ray computed tomography could be used. This technique provides non-destructive, three-dimensional imaging at the nanoscale,

typically achieving resolutions of around 50 to 150 nm, and would allow much smaller pore structures to be examined in detail. Finally, μ-XRD could be carried out to investigate the mineralogy surrounding the pores. This would help to link local mineral composition with pore structure and provide a more complete understanding of how composition and microstructure are related.

Chapter 5 Development of methods to synthesise single high temperature mineral phases

5.1 Introduction

5.1.1 Background

In the previous chapter where the effects of curing temperature and CaO:SiO_2 ratio were explored on the mineralogy of NRVB cement several different high temperature minerals were identified. In the previous chapter it was concluded that these minerals were consuming portlandite in order to form. Portlandite plays a key role in the safety functions of NRVB, dissolving over time to buffer the pH to reduce solubility of radionuclides and prevent their escape to the biosphere.

It is therefore important to understand how the cement mixes formed at higher temperatures behave, and if any of the newly formed minerals are able to increase the performance of the cement to mitigate the loss of portlandite. To accurately evaluate the performance of the minerals at reducing the concentration of radionuclides in solution they need to be synthesised as single mineral phases or, where this is not possible, alongside another known mineral phase. This chapter describes the R&D work to try and synthesise the minerals of interest as single phases, and describes the mixes used in the following radionuclide chapter.

In the chapter where the mineralogy of the different NRVB formulas was investigated several high temperature minerals were found to have formed, these were α-C_2SH, γ-C_2SH, Jaffeite, Reinhardbraunsite, Katoite, and Xonotlite. There was no gypsum, larnite, or quartz remaining in the NRVB formulations that were cured at 150°C and the C:S ratio 4 cements cured at 200 and 250°C. The C:S ratio 4 sample cured at 250°C also had no portlandite remaining. The lack of larnite, or belite, in the cement mixes shows they had full reacted. These three mixes also contain all of the high temperature minerals between them, so they were also tested to see if the high temperature minerals performed the same when tested individually or as a mixture. The composition of these three cements is shown in Table 34. Firstly, however, a method to synthesise as many of the high temperature minerals as single mineral phases had to be developed.

Table 34: The three cements chosen to study as they contain most high temperature minerals. These minerals are α-C_2SH, γ-C_2SH, jaffeite, reinhardbraunsite, katoite, and xonotlite. The minerals of interest are highlighted in blue.

Mineral	NRVB 150°C	C:S 4 200 °C	C:S 4 250 °C
calcite	4.076	0	1.13
gypsum	0	0	0
larnite	0	0	0
quartz	0	0	0
portlandite	35.343	20.628	0
hydrogarnet	25.884	0	0
tetra	0	0	0
α-C_2SH	34.697		0
γ-C2SH	0	37.595	0
Jaffeite	0	10.324	9.2
Reinhardbraunsite	0	0	62.24
katoite	0	0	13.38
Xonotlite	0	0	14.05

5.1.2 Aims and Objectives

The aim of this chapter is to either find or develop a synthesis route to make pure Reinhardbraunsite, Xonotlite, Jaffeite, α-C_2SH and γ-C_2SH that can be used to test the minerals efficacy at removing radionuclide analogue from solution.

The objectives are:

1. Conduct a focussed literature review to find existing methods for synthesising the identified high temperature minerals. This includes research that analyses the phases formed in cements under different conditions that may not have their primary aim to synthesise the mineral.
2. Use the literature research to develop a series of experiments to replicate or improve on the efficacy of the methods found in existing research.
3. Use XRD analysis then EVA and TOPAS to analyse the series of minerals made and choose the best method to synthesise high temperature minerals to use in future work to investigate their efficacy at removing radionuclide analogues from solution.

5.1.3 Xonotlite

Xonotlite has a C:S ratio of 1 and is a needle-like, strengthening, and compact mineral. In cementitious systems, it does not form during normal hydration at ambient temperature, but instead develops under hydrothermal conditions where elevated temperature and pressure allow the existing calcium silicate hydrates to recrystallise into more thermodynamically stable phases. Xonotlite is thought to form from the recrystallisation of reinhardbraunsite and jaffeite when silica powder is added[166]. These precursor phases, which can be present in hydrothermally treated cement systems, gradually reorganise into the more ordered xonotlite structure as temperature and silica availability increase.

In typical Portland cement hydration, the dominant product is an amorphous or poorly crystalline C–S–H along with portlandite ($Ca(OH)_2$). Under hydrothermal curing, particularly above 180–200 °C, this C–S–H can transform into crystalline phases such as tobermorite, and with further temperature or time, into xonotlite[167–169]. This transformation reduces the amount of bound water in the structure and produces a more ordered, fibrous morphology. The needle-like crystals interlock within the matrix, creating a dense and compact microstructure which contributes to increased strength, reduced porosity, and improved dimensional stability, particularly at elevated temperatures[167,168].

Factors such as the C:S ratio, amount of water, and curing temperature are important in xonotlite formation. Xonotlite formation is favourable when the C:S ratio is close to 1 and temperatures are higher than those at which tobermorite is thermodynamically stable[167].

Xonotlite has been formed at a purity of 100% at the conditions described in Table 35[56]. The percentage amount of cement was replaced with quartz powder (silica flour, SiO_2) and the mixture was cured at the stated temperature for 5 days in hydrothermal cells. After curing the hydrothermal cell was rapidly cooled in a bucket of water, the cement was then ground and tested with XRD analysis.

Table 35: The conditions at which xonotlite has been found to form at 100% purity [56].

Silica flour by weight of cement (%)	Curing Temperature (°C)	Ca:Si ratio
25	350	1.199328
33.3	250	0.924576
33.3	350	0.924576
42.9	250	0.68587

Xonotlite has a C:S ratio of 1, to create the mixture with the highest likelihood of fully reacting to form just xonotlite with no starting material present selecting a mix that has a starting C:S ratio of 1 is logical. The mixes used in the previous studies do not have a C:S ratio of 1[56], therefore to optimise the results the amount of cement powder and quartz powder used will be adjusted to give a C:S ratio of 1. The same experiment will be repeated, replacing the cement powder with $Ca(OH)_2$ and maintaining a C:S ratio of 1. This will eliminate any other phases within the cement powder to isolate xonotlite.

5.1.4 Calcite

Calcite can be present in cements in two ways. The first is when it forms through carbonation reactions. This occurs when CO_2, either dissolved in the water used to hydrate the cement powders or present in the surrounding air and subsequently dissolving into the mix water, reacts with portlandite, calcium hydroxide, to form calcium carbonate. This process begins at very early ages and continues throughout the service life of the cement paste. Portlandite is particularly susceptible to carbonation due to its high solubility and reactivity with dissolved carbon dioxide, and its conversion to calcite represents one of the primary chemical changes that occur as cement hydrates are exposed to the atmosphere[58].

However, in cement systems this process is more complex, involving dissolution of CO_2 into pore solution, formation of carbonic acid, reduction of pore solution pH, and subsequent precipitation of calcium carbonate within the pore structure. The precipitation of calcite can partially block pores and locally densify the microstructure, but the accompanying reduction in alkalinity destabilises other hydration products, particularly C–S–H, which may also begin to decalcify under prolonged carbonation.

As a result, while calcite formation may initially appear to refine porosity, the overall process is associated with long-term chemical degradation of the cement matrix.

Calcite is also a common additive to cements, typically up to 5% by weight, and can have a significant impact on the mineralogy of the system. Finely ground limestone is often interground with clinker during cement manufacture, not only as a filler but also as a reactive component. The presence of calcite influences early hydration by providing nucleation sites for C–S–H growth and by reacting with aluminate phases to form carboaluminate hydrates such as monocarboaluminate and hemicarboaluminate. These reactions alter the balance of aluminate hydration products compared with systems where no limestone is present, modifying the phase assemblage and potentially refining the pore structure[170].

Despite these benefits, the presence of added calcite increases the vulnerability of cement to carbonation [170]. Limestone addition reduces the overall clinker content and therefore the quantity of portlandite produced during hydration, lowering the buffering capacity of the system against pH reduction. Furthermore, the pre-existing calcium carbonate can make it more difficult to distinguish between calcite formed through carbonation and that originally added as an ingredient when analysing hydrated samples by XRD or other mineralogical techniques[171].

In the previous chapter, where mineralogy was studied, the addition of calcite to the NRVB formula obfuscated the results, making the identification of mineral phases present in smaller amounts impossible. The strong and dominant diffraction peaks of calcite masked those of less abundant phases, particularly the calcium silicate hydrates of interest. Calcite was therefore omitted from further mineralogical studies, as the phases that could be identified with XRD showed no difference in the mineralogical results whether or not calcite was added.

The calcite used to mix the original NRVB recipe was used in these tests. XRD was repeated on it to ensure that it remained pure and that no secondary carbonation or phase changes had occurred during storage. This confirmed that any calcite detected in subsequent experiments could be attributed either to deliberate addition or to carbonation reactions occurring during curing and handling, rather than impurities within the starting material.

5.1.5 Reinhardbraunsite

The mineral reinhardbraunsite has a C:S ratio of 2.5, and its formula is $Ca_5(SiO_4)_2(OH)2$[172]. Reinhardbraunsite has been made in the past in a variety of methods. One of these was to synthesise it hydrothermally by heating tricalcium silicate (alite) at 600-700°C[173]. The crystals bond poorly to each other, leaving gaps. This means it has a loose structure and is a weak, strength-reducing phase[166].

Reinhardbraunsite develops through the recrystallisation of poorly crystalline C–S–H gels that are initially produced when portlandite ($Ca(OH)_2$) from cement hydration reacts with available silica. Under elevated hydrothermal conditions, these gels and transitional phases such as jaffeite reorganise to minimise structural water content and achieve more stable crystal structures. When additional silica is present in the mixture, the formation of reinhardbraunsite is favoured particularly where the local C:S ratio is higher than 1[174]. Microscopically, reinhardbraunsite crystals are often lath-like or needle structured, and they contribute to the developing microstructure by providing nucleation sites for further Ca–Si–H growth. The presence of reinhardbraunsite in X-ray diffraction (XRD) patterns can complicate phase identification because its peaks sometimes overlap with those of related silicate hydrates[174].

Reinhardbraunsite can be synthesised through controlled hydrothermal reactions between calcium and silica sources when the C:S ratio is higher than that which directly favours the formation of xonotlite or tobermorite. In these experiments, mixtures of $Ca(OH)_2$ (or lime) and crystalline silica (quartz or silica flour) are reacted in saturated steam at elevated temperatures, typically between 180 and 350 °C[56]. Under these conditions, the poorly crystalline C–S–H gels formed initially begin to transform into more ordered crystalline phases as the system moves toward thermodynamic stability. At intermediate C:S ratios, these transformations can produce reinhardbraunsite as a distinct intermediate phase before more stable end-members such as xonotlite dominate. Hydrothermal treatment of $CaO–SiO_2–H_2O$ mixtures under these conditions produces a range of crystalline products including hillebrandite, jaffeite, reinhardbraunsite, and xonotlite, showing that phase selection depends strongly on Ca:Si ratio and curing temperature[175].

These syntheses are usually carried out in sealed hydrothermal autoclaves where a slurry of $Ca(OH)_2$ and silica is maintained above the boiling point of water under

autogenous pressure for several days. Crystalline silica favours the formation of ordered hydrates rather than amorphous C–S–H, and slow heating combined with high curing temperatures encourages transformation to lower water-content phases like reinhardbraunsite. With continued thermal exposure or adjustments to the C:S ratio, the system can progress toward xonotlite. Because reinhardbraunsite occupies a metastable region of the Ca–Si–H system, careful control of reactant ratios, temperature, and curing time is essential for its formation and retention[176].

5.1.6 Jaffeite

Jaffeite is a crystalline calcium silicate hydrate phase with the approximate chemical formula $Ca_6Si_2O_7(OH)_6$, and it can form under hydrothermal curing conditions in cementitious systems when poorly crystalline C–S–H gels convert to more ordered phases at elevated temperature and pressure. As cement hydrates in the presence of water at temperatures above ~150–200 °C, the initial amorphous C–S–H products begin to reorganise into crystalline compounds with higher C:S ratios, such as α-C_2SH and jaffeite, before eventually progressing toward phases like reinhardbraunsite and xonotlite if conditions continue to favour further transformation[177].

The formation of jaffeite is strongly dependent on both temperature and C:S ratio. Studies have shown that at typical hydrothermal curing temperatures, higher temperatures and pressures increase the amount of jaffeite observed, even when supplementary silica or pozzolanic additions are used to alter the reaction pathways[178].

For example, in hydrothermal curing of blended Portland cement pastes, crystalline jaffeite is detected at intermediate stages, indicating that the system has undergone significant structural reorganisation beyond poorly crystalline C–S–H but has not yet favoured formation of low-water end members like xonotlite. Electron microscopy and X-ray diffraction analyses confirm that jaffeite crystals form as discrete, recognisable phases under these conditions and tend to persist alongside other intermediate hydrates until temperatures and reaction times allow further transformation or until the C:S ratio shifts due to reactant consumption[128]. Jaffeite has similar properties to α-C_2SH. Jaffeite causes the pore structure of cement to degrade, and a strength reduction in the cement[179].

The formation of jaffeite is strongly dependent on temperature, curing time, and the C:S ratio of the starting mixture. Studies show that jaffeite appears most readily under

hydrothermal conditions when the C:S ratio is between 1.1 and 1.5, and when the mixture is cured in saturated steam at temperatures of 180–250 °C for periods of 3–7 days. Within this window, the initially amorphous or poorly crystalline C–S–H gels transform into more ordered crystalline phases, with jaffeite forming alongside intermediate phases such as hillebrandite and reinhardbraunsite. Increasing the temperature or silica content in the mixture shifts the phase evolution toward xonotlite, while lower temperatures or shorter curing times favour retention of transitional or partially hydrated phases[180,181].

5.1.7 α-C_2SH

α-C_2SH (alpha dicalcium silicate hydrate) forms under controlled hydrothermal conditions when calcium and silica sources react at elevated temperatures and appropriate C:S ratios. Studies have shown that α-C_2SH can be synthesised from a mixture of CaO (or $Ca(OH)_2$) and silica sources with a $CaO:SiO_2$ molar ratio of between 1.5 to 2, making it a dibasic calcium silicate hydrate phase distinct from both amorphous C–S–H and other crystalline hydrates like tobermorite or xonotlite. For example, hydrothermal synthesis at approximately 175 °C for 16 hours produces detectable α-C_2SH when using CaO and silica as starting materials and increasing the temperature to ~200 °C accelerates its formation, with α-C_2SH becoming a dominant phase after ~8 hours of curing under saturated steam pressure. At 175 °C, significant amounts only appear after longer durations (~16 h), but at 200 °C the growth is faster and more pronounced, reflecting the strong influence of temperature and time on phase evolution in these systems[182,183]. α-C_2SH and jaffeite can form from alite under specific conditions, such as temperature and pressure[184]. At the time of this research alite was not available to order online.

α-C_2SH forms as the poorly crystalline C–S–H recrystallises under elevated temperature or hydrothermal conditions. During this process, the amorphous or semi-crystalline gel reorganises into a more ordered, layered structure with a smaller unit cell compared with the original C–S–H. This reduction in unit cell dimensions leads to a slight shrinkage of the solid phase, which can create additional void space and increase the overall porosity of the material. The increased porosity weakens the microstructure locally, as fewer interlocking particles are present to transfer stress effectively. This phenomenon is commonly referred to as strength retrogression[166],

where the initial gains in crystallinity and microstructural order are offset by the formation of micro voids and the loss of cohesive strength within the paste[58].

Strength retrogression is particularly noticeable in high-temperature cured or autoclaved cement systems where α-C_2SH becomes the dominant calcium silicate hydrate phase, as the densification associated with other crystalline phases such as xonotlite does not fully compensate for the porosity introduced during unit cell shrinkage. Understanding this behaviour is critical when designing cementitious materials for high-temperature applications, as it directly impacts both early and long-term mechanical performance.

5.1.8 γ-C_2SH

γ-C_2SH, commonly referred to as γ-dicalcium silicate or γ-belite, forms through the polymorphic transformation of β-C_2S when the material is cooled slowly from a high temperature. Unlike the hydraulically active β-C_2S phase found in belite cements, γ-C_2S is non-hydraulic and does not react with water to produce strength-giving hydrates; instead, it remains largely inactive in normal cement hydration. The transformation from β- to γ-C_2S involves a change to a more stable crystal structure at ambient temperatures, accompanied by a volume increase that disrupts the integrity of the original grains and significantly reduces hydraulicity and mechanical performance, effectively shattering the clinker particles into dust during cooling if not controlled[185].

Despite its lack of hydraulic reactivity, γ-C_2S has been shown to have a high carbonation affinity, reacting readily with CO_2 to form calcium carbonate and silica gel phases. When exposed to CO_2 in the presence of moisture, γ-C_2S exhibits rapid carbonation with high CO_2 uptake efficiency, and the resulting calcium carbonate can significantly decrease porosity and develop strength through a carbonation mechanism rather than hydration[186]. For example, γ-C_2S has been used as the main carbonate binder in coatings where carbonation leads to compacted $CaCO_3$ formation, reduced porosity, and rapid early strength gain within the first few hours of carbonation curing. Similarly, carbonation studies demonstrate that stronger, denser microstructures arise as carbonate polymorphs and silica gel fill pore space, showing that although γ-C_2S is weak as a traditional hydration phase, it can become functionally strong through controlled CO_2 activation and carbonation curing

Synthesis of γ-C_2S typically involves high-temperature sintering of calcium and silica precursors at around 1250–1500 °C, followed by slow cooling to promote the β- to γ-C_2S transformation; rapid cooling is avoided to reduce the formation of hydraulic β-C_2S and to ensure complete conversion to the stable γ phase. During this transformation, the crystal lattice expands by approximately 10 %, which disrupts the continuity of the original β-C_2S grains and produces microcracks within the material. This phase is structurally stable but mechanically weak, its structural openness gives γ-C_2S a high affinity for CO_2[187,188]. This allows carbonation to proceed rapidly and densifies the microstructure through calcium carbonate precipitation, which can partially offset its weakness [186,189].

5.2 Method

The results from different mixes in the previous chapter informed the mixes made to attempt to synthesise single pure phase minerals, alongside methods found in literature. A range of mixes with different CaO:SiO_2 ratios were made, and then cured at different temperatures. These ratios were repeated using $Ca(OH)_2$ or OPC CEM I 52.5N powder as the CaO source, with the amount of SiO_2 adjusted when cement powder was used to account for the additional SiO_2 source. The mixes and curing conditions are detailed in Table 36.

Table 36: The different synthesis methods studied in this chapter, with the mineral that could be formed.

Sample name	C:S ratio	Curing temperature (°C)	Curing time	Potential mineral	Cement/ $Ca(OH)_2$	Reference
2.5CaOH300	2.5	300	1d	Reinhardbraunsite	$Ca(OH)_2$	[53]
2.5CEM300	2.5	300	1d	Reinhardbraunsite	Cement	[53]
RCaOH5d	2.5	250	5d	Reinhardbraunsite	$Ca(OH)_2$	[53]
RCEM5d	2.5	250	5d	Reinhardbraunsite	Cement	[53]
2CaOH300	2	300	1d	aC2SH/ YC2S	$Ca(OH)_2$	[53]
2CEM300	2	300	1d	aC2SH/ YC2S	Cement	[53]
aC2SH CaOH	2	200	12 hrs	aC2SH	$Ca(OH)_2$	[53]
aCSHCEM	2	200	12 hrs	aC2SH	Cement	[53]
YC2SCaOH	2	1100*	3hrs	YC2S	$Ca(OH)_2$	[185]
YC2SCEM	2	1100*	3hrs	YC2S	Cement	[185]
YC2SCaOH	2	1350	3hrs	YC2S	$Ca(OH)_2$	[185]
JCaOH5d	3	200	5d	Jaffeite	$Ca(OH)_2$	[53]
JCEM5d	3	200	5d	Jaffeite	Cement	[53]
Jaffeite5d	3	250	5d	Jaffeite	Cement	[53]
3CaOH300	3	300	1d	Jaffeite	$Ca(OH)_2$	[53]
3CaOH250	3	250	5d	Jaffeite	$Ca(OH)_2$	[53]
3CEM300	3	300	1d	Jaffeite	Cement	[53]
XCaOH250	1	250	5d	Xonotlite	$Ca(OH)_2$	[53]
XCEM250	1	250	5d	Xonotlite	Cement	[53]

*This γ-C_2S mix was only heated to 1100°C despite literature recommending 1350°C. This was due to oven availability. The purpose of this chapter was to develop new mineral synthesis methodologies therefore testing whether this mineral could be created at a lower temperature was worthwhile as a lower synthesis temperature would reduce the time needed to heat and cool ovens and the cost of running the ovens.

The raw materials were mixed with deionised water until homogeneous. The mixture was then put into PEEK moulds before being sealed within a hydrothermal cell. The hydrothermal cell was then heated to the corresponding temperature and duration as detailed in the table above. After heating the cells were rapidly cooled under running water. The sample was removed from the moulds then dried under nitrogen at room

temperature until constant mass. The mineral samples were then vacuum sealed until analysis.

5.3 Results

The samples were prepared for XRD following the method developed in Chapter 2. The XRD scans were analysed using DIFFRAC.EVA using the same parameters as described in Table 16 to identify the different mineral phases that had formed within the mixes. The mixes that showed the lowest number of mineral phases were then quantified using TOPAS and Rietveld refinement.

5.3.1 Xonotlite

The XRD analysis using DIFFRAC.EVA to identify the mineral phases is in . The Diffractograms are plotted in Figure 56. The COD and ICSD codes used to identify the mineral compositions in EVA are listed in Table 37 below.

Table 37: The minerals identified and the COD codes used for each mineral in DIFFRAC.EVA for the mixes that were most likely to synthesise xonotlite.

Mineral	**Code**	**Reference**
Xonotlite	9008437	[190]
Calcite	9000095	[191]

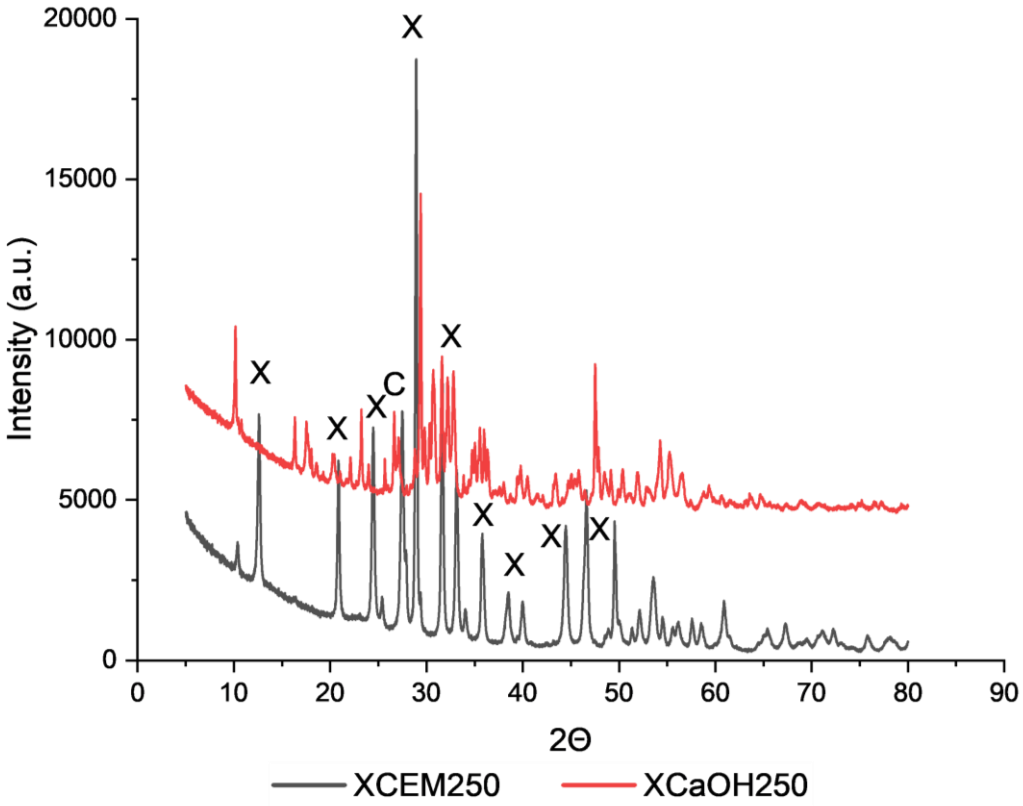


Figure 56: The diffractograms of the two mixtures that were most likely to form xonotlite. The corresponding xonotlite peaks are labelled x.

The sample XCem250 that was mixed with cement powder produced a cement that contained just xonotlite and calcite. The cement XCemCaOH also produced a cement with just xonotlite and calcite. Both samples intended to make pure phase xonotlite were successful, and showed similar mineralogical compositions. Both the sample using cement powder, and $Ca(OH)_2$ contained just xonotlite and calcium carbonate. The sample made with $Ca(OH)_2$ contained less calcite. These samples were both prepared by adjusting the $CaO:SiO_2$ ratio to 1, then mixing until homogeneous. The samples were then heated for five days hydrothermally at 200°C. After curing, the samples were removed from the moulds and dried under nitrogen gas at room temperature to constant weight.

Both samples contain just calcite and xonotlite, however, the sample where cement powder provided the calcium oxide had an additional amorphous peak around 17.5 2θ that was unable to be identified. This is likely to be an additional reaction product from the cement powder, as it contains different metals in addition to calcium oxide

and silica dioxide. Both EVA and Highscore was used to attempt identification of this peak, however, due to the sample using $Ca(OH)_2$ as the CaO source being successful and only containing Xonotlite and Calcite, further investigation into this unlabelled peak could not be justified as an appropriate synthesis pathway to obtaining Xonotlite had been found. It was therefore decided to use the method with $Ca(OH)_2$.The sample made with $Ca(OH)_2$ also had a smaller peak for calcite, and as previously said will not contain any other impurities that result from using cement powder.

5.3.2 Calcite

This is available as a raw material. The raw material was tested using XRD analysis and showed pure calcite was present. This was therefore suitable to use in further tests.

5.3.3 Reinhardbraunsite

The COD and ICSD codes used to identify the mineral compositions in EVA are listed in Table 38 below. The diffractograms are shown in Figure 57.

Table 38: The minerals identified and the COD codes used for each mineral in DIFFRAC.EVA for the mixes that were most likely to synthesise reinhardbraunsite.

Mineral	**Code**	**Reference**
Reinhardbraunsite	1529964	[192]
Calcite	9000095	[191]
Killalaite	1519934	[193]
Hibschite	9009299	[194]
γ-C_2S	9012681	[195]

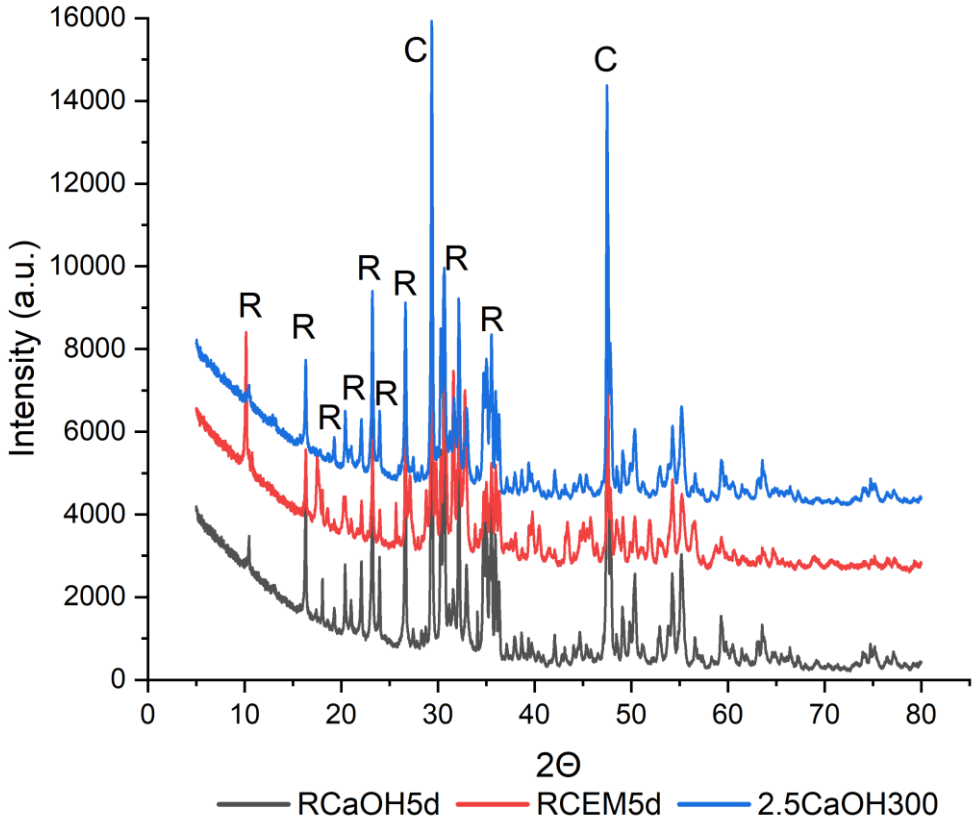


Figure 57: The diffractograms of the two mixtures that were most likely to form reinhardbraunsite. The corresponding reinhardbraunsite peaks are labelled R.

The sample 2.5CaOH300 which was mixed with a C:S ratio of 2.5 then cured at 300°C showed just reinhardbraunsite and calcite present in the final cement.

The RCaOH5d sample was prepared by mixing a $CaO:SiO_2$ ratio of 2.5, then curing at 250°C for 5 days. This method was based on results from previous mineralogy studies within this project. The final cement showed reinhardbraunsite, calcite, and killalaite present.

The RCEM5d sample was prepared following the same method as the sample above, however OPC 52.5N Cement powder was used instead of $Ca(OH)_2$ with the quantity adjusted to maintain a $CaO:SiO_2$ ratio of 2.5. This mix using cement powder had calcite, hibschite, jaffeite, γ-C_2S, and reinhardbraunsite present.

5.3.4 Jaffeite

The COD and ICSD codes used to identify the mineral compositions in EVA are listed in Table 39 below. The XRD diffractograms are shown in Figure 58.

Table 39: The minerals identified and the COD codes used for each mineral in DIFFRAC.EVA for the mixes that were most likely to synthesise jaffeite.

Mineral	**Code**	**Reference**
Portlandite	1008781	[196]
Calcite	9000095	[191]
Jaffeite	9012620	[197]
Ellestadite (OH)	9010137	[198]
Reinhardbraunsite	9013687	[192]
α-C_2SH	9011378	[199]
Quartz	9000776	[200]
Katoite	1552361	[201]
γ-C_2S	9012681	[195]

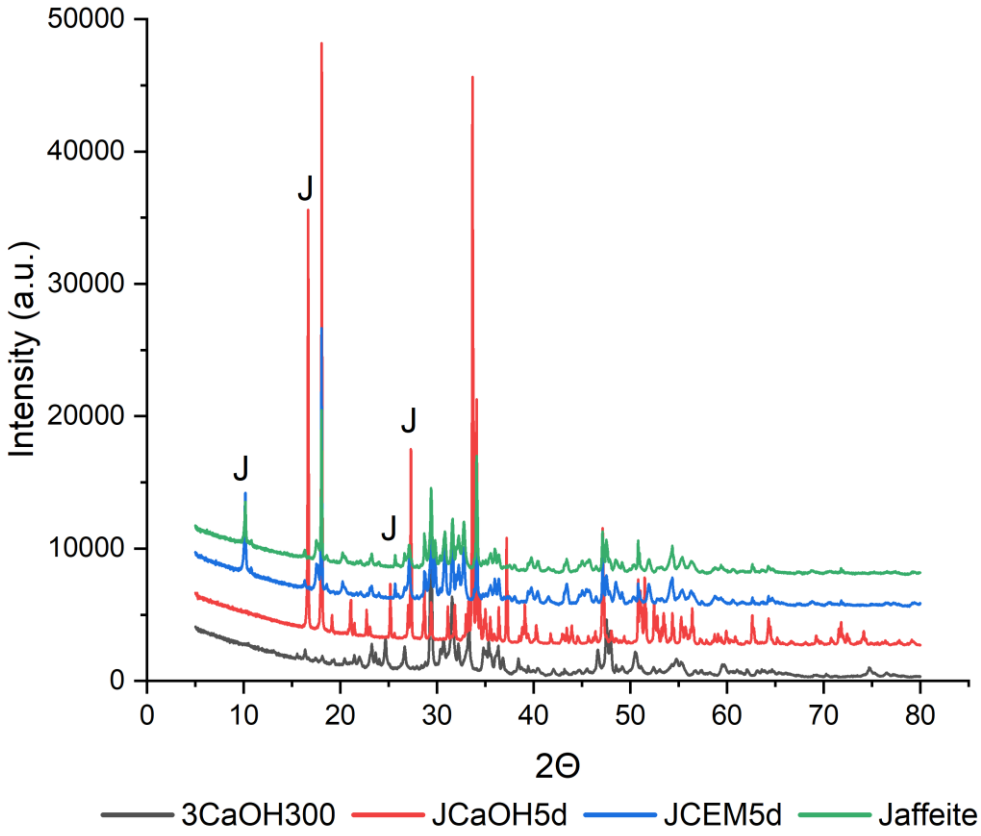


Figure 58: The diffractograms of the two mixtures that were most likely to form jaffeite. The corresponding jaffeite peaks are labelled J.

The sample JCEM5d showed a mixture of minerals present, these included portlandite, calcite, jaffeite, ellestradite, and reinhardbraunsite. The cement 3CaOH250 contained poldervaartite and quartz and no jaffeite was formed.

The cement JCaOH5d contained only Portlandite, Calcite, and Poldervaartite otherwise known as α-C2SH present. There is, however, a significant discrepancy between the measured peak size on the pattern, and the peak size on the CIF file for α-C_2SH on the peak at 16.657 2θ, or the peak with the hkl coordinates 0, 0, 2. There is limited information in literature about preferred orientation in XRD scans of α-C_2SH. The peak shape does not suggest that there is an overlapping mineral that is contributing to the peak height. The α-C_2SH peak has almost exactly the same peak shape as that for portlandite. Portlandite is an extremely crystalline mineral that produces sharp peaks, therefore any imperfections of the portlandite peak are due to instrument and/or preparation conditions. Both peaks show a slight amount of tails, this shows how well the data works with the fitting method used by the software. As

the peak shape suggests that only one reflection is responsible for it, its excess height must be due to preferred orientation of the 0, 0, 2 α-C2SH peak. This was accounted for during Rietveld refinement using TOPAS to quantify the mineral phases.

The final cement tested was labelled jaffeite and was CEM I powder heated to 250°C for 5 days. This contained the most significant jaffeite peaks, it also contained portlandite, calcite, γ-C_2S and katoite.

5.3.5 α-C_2SH

The COD and ICSD codes used to identify the mineral compositions in EVA are listed in Table 40 below. The XRD diffractograms are shown in Figure 59.

Table 40: The minerals identified and the COD codes used for each mineral in DIFFRAC.EVA for the mixes that were most likely to synthesise α-C_2SH.

Mineral	**Code**	**Reference**
α-C_2SH	9011378	[199]
Calcite	9000095	[191]
Jaffeite	9012620	[197]
Ellestadite (OH)	9010137	[198]
Katoite	9002707	[201]

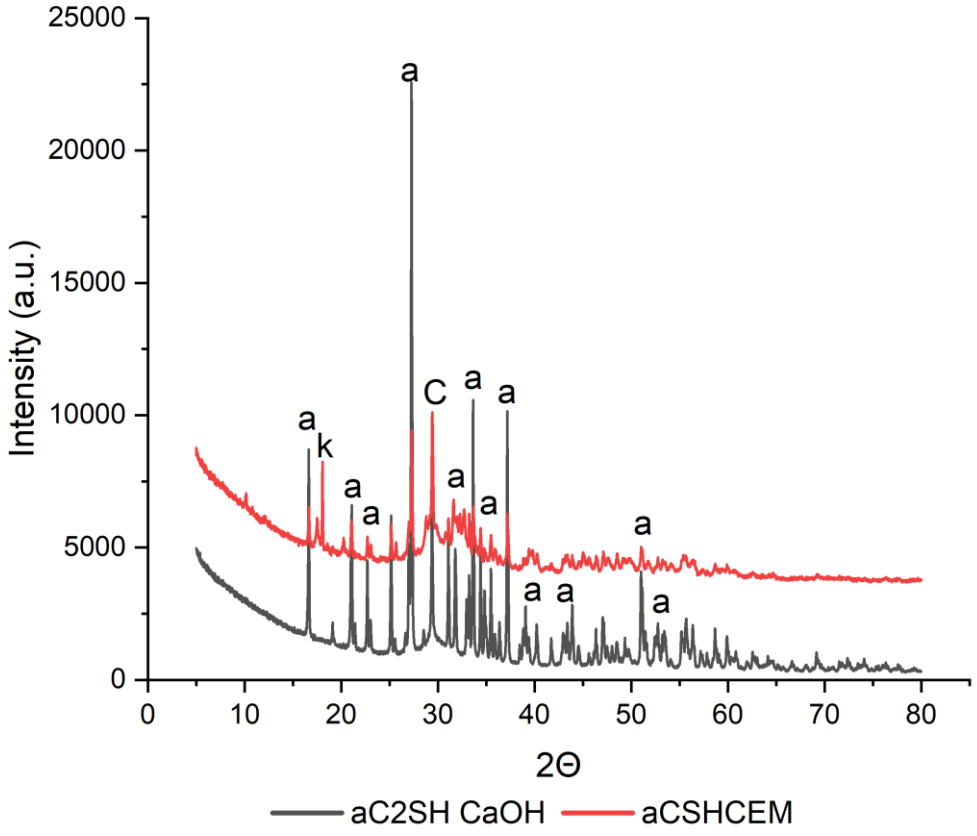


Figure 59: The diffractograms of the two mixtures that were most likely to form α-C_2SH. The corresponding α-C_2SH peaks are labelled a and katoite peaks are labelled k. The green line represents the aCSHCEM sample and the orange line represents the aC2SHCaOH sample.

The sample α-C_2SH CEM was mixed with CEM I powder not portlandite. This cement contained calcite, ellestradite-(OH), α-C_2SH, katoite, and jaffeite. This mix contains many different minerals and is not suitable for single phase mineral synthesis of α-C_2SH.

The sample α-C2SH CaOH was prepared by mixing $Ca(OH)_2$ with SiO_2 and water at a CaO:SiO_2 ratio of 2, then heating it at 200°C for 24 hours. The sample was then dried in a nitrogen atmosphere at room temperature until constant mass. This sample contained α-C_2SH and calcite after curing.

Interestingly, this sample has a similar composition to the sample labelled J CaOH 5d. The differences in preparation are in Table 41. The two main differences are the J CaOH 5d sample contains a greater amount of $Ca(OH)_2$ in the starting mix with a C:S

ratio of 3 compared to a C:S ratio of 2, and it was left to cure for five days rather than one.

The main difference between the mineralogical compositions is the presence of portlandite in the J CaOH 5d sample. Portlandite is one of the three starting components ($Ca(OH)_2$), so this is leftover and unreacted in the mix. Neither sample contained any remaining SiO_2 also known as quartz. This means that somewhere between a $CaO:SiO_2$ ratio of 2 and 3 the portlandite becomes saturated with quartz, and there is no more quartz able to react. This could be useful information regarding the final formulation of the backfill cement, as portlandite is a key component that is intended to remain present for a long time. The portlandite is supposed to dissolve slowly over time, buffering the pore water to remain at a high pH. This high pH reduces the solubility of some radionuclides, trapping them within the backfill and inhibiting their transport out and into the surrounding groundwater.

Table 41: The mix and curing conditions of two samples that showed a similar mineralogy despite having different C:S ratios and different curing times.

Sample	**$CaO:SiO_2$**	**Curing temperature (°C)**	**Curing time**
J CaOH 5d	3	200	5 days
a-C2SH CaOH	2	200	1 day

A comparison of the two XRD patterns is shown in Figure 60. The J CaOH 5d sample is red, and the a-C2SH CaOH sample is black. The a-C2SH sample shows less preferred orientation. This could be due to differences in how the samples were prepared for XRD, however they were both prepared at the same time so it is unlikely for there to be that much difference. The preferred orientation could be caused by the J CaOH 5d sample growing differently. As the $Ca(OH)_2$ was present in that mixture at a higher proportion it is reasonable to assume the reaction would have occurred slower, this is because there was proportionately less SiO_2 to encounter and react with. The sample was also cured for five time as long. A longer curing time has been found to increase the crystallinity of C-S-H[202], so it is possible the same is true when synthesising α-C_2SH. Therefore, despite very similar compositions, a mixture with a $Ca:SiO_2$ ratio of 2, and curing for 24 hours are the best conditions to synthesis α-C_2SH.

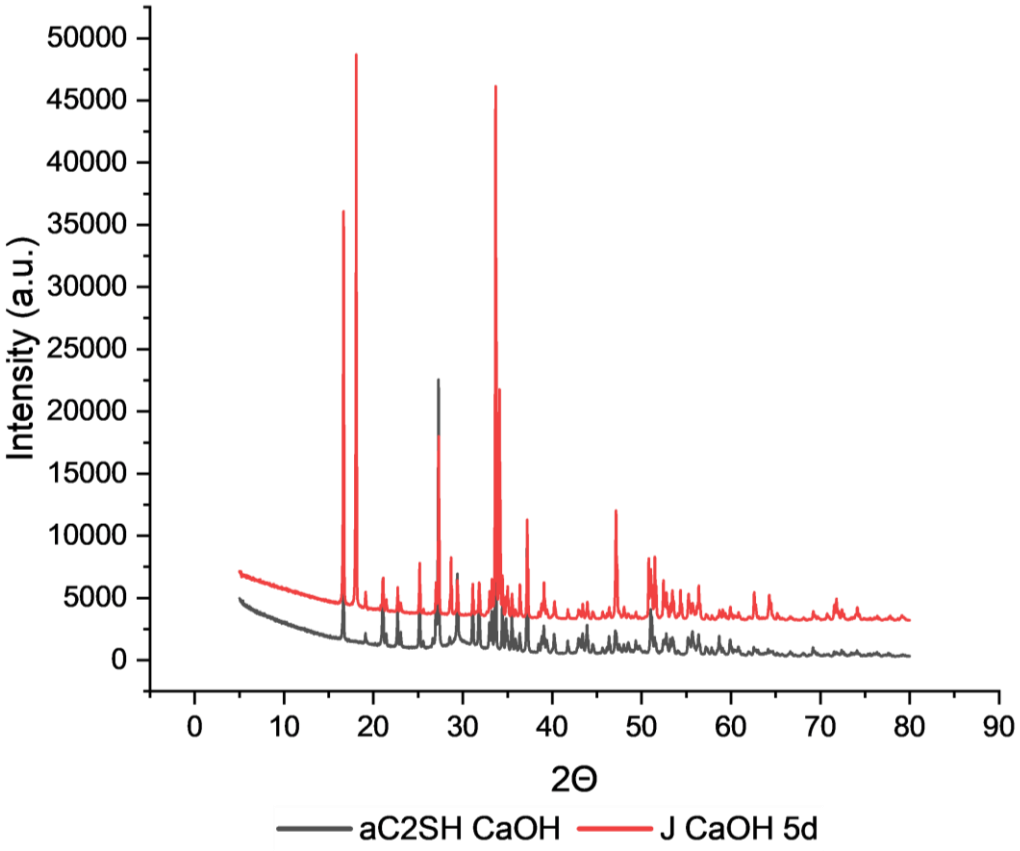


Figure 60: A comparison of the XRD patterns measured from the samples aC2SH CaOH and J CaOH 5d

5.3.6 γ-C_2SH

The COD and ICSD codes used to identify the mineral compositions in EVA are listed in Table 42 below. The XRD diffractograms are shown in Figure 61.

Table 42: The minerals identified and the COD codes used for each mineral in DIFFRAC.EVA for the mixes that were most likely to synthesise γ-C_2SH.

Mineral	**Code**	**Reference**
Larnite	9012792	[125]
Ye'elimite	9009938	[203]
Anhydrite	9004096	[204]
Lime	1011095	[205]
Quartz	9000775	[200]
Krotite	9016800	[206]
γ-C_2S	9012681	[195]
Rankinite	9012094	[207]
Cristobalite	9008224	[208]
Portlandite	9006834	[196]

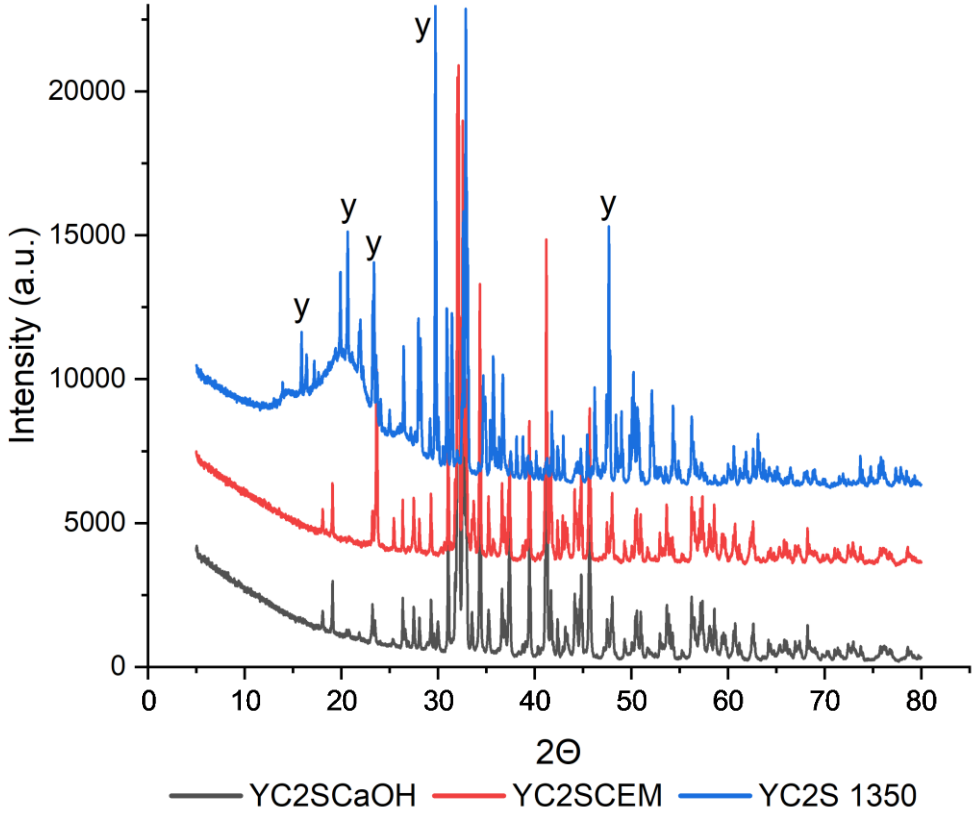


Figure 61: The diffractograms of the two mixtures that were most likely to form γ-C2SH. The corresponding γ-C2SH peaks are labelled y.



Figure 62: The crucibles after curing at 1100°C. The crucible on the left used CEM I, the crucible on the right contained portlandite.

The Y C2S CEM sample was supposed to be cured at 1350°C for 3 hours, however it was instead heated to 1100°C for 3 hours, as the oven was unable to heat to 1350°C, and the sample had already been mixed. The method being followed included results for curing at 1100°C, and claimed belite was formed, so it was useful to test the validity of other conditions of the method. Belite also may be investigated in future work or

may have been useful to synthesise as part of a two step process to make a different pure phase mineral. This sample contained belite and ye'elemite[209]. The method followed used pure CaO, so the presence of ye'elemite is from other components within the cement powder. Ye'elemite has a distinct brown colour which can be seen in Figure 62.

The Y C2S CaOH sample was prepared the with the same procedure as the YC2SCem sample, however instead of OPC 52.5 CEM1 powder, $Ca(OH)_2$ was used as the CaO source. The $CaO:SiO_2$ ratio was kept constant, and the amount of $Ca(OH)_2$ and SiO_2 was adjusted. This sample showed Larnite/ Belite present as the main phase. This is in agreement with the previous analysis found in literature [185]. This sample also had CaO, which forms from calcium carbonate at high temperatures. There was also a small amount of Y-C2S present. A mineral called Krotite was identified in the cement, this is a calcium aluminate phase, and has been found previously in cements cooked above 1000°C[206]. However, there was no aluminium present in the starting mixture, so it is not clear how it formed. The most likely source is contamination from the crucible, despite cleaning it, it is used at temperatures up to 1200 °C so will have material baked on that cannot be removed. To avoid potential cross contamination when preparing the pure phases for radionuclide analysis a different crucible will be used.

Three formulations were planned to synthesise pure phase γ-C_2SH. Two were cured at the University of Strathclyde. The final mix (Y C2S CaOH AFRC) was cured at the Advanced Forming Research Centre (AFRC) as they were the only facility that could be found with an oven that could reach 1350°C. The materials were pre weighed out at the University of Strathclyde then transported and mixed at the AFRC. This sample contained rankinite, cristobalite, and portlandite. The cristobalite is most likely sand residue from the oven used to cure the cement. The sample after curing can be seen in Figure 63. No γ-C_2SH was present.

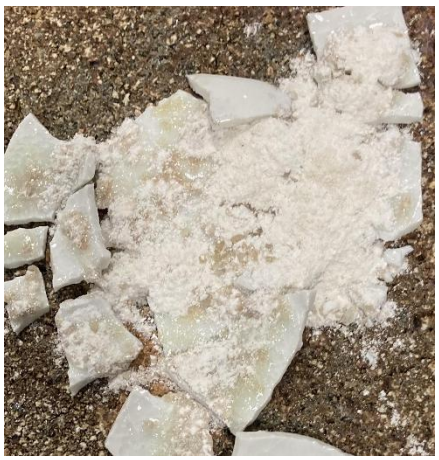


Figure 63: The Y C2S CaOH AFRC after curing at 1350°C for 3 hours. The crucible shattered and had melted onto the base of the oven. The sample was collected and analysed. The base of the oven was concrete and the sample was contaminated with sand from it.

5.3.7 TOPAS analysis of chosen mineral formulations

The formulations that were identified as containing the least amount of mineral phases and also contained the desired mineral phases were quantified. These are listed in Table 43 below.

Table 43: The TOPAS quantification of the mineral phases chosen that contain the least number of mineral phases and contain the desired mineral phase.

Sample	**Minerals [% of composition]**	**Pure phase mineral?**
2.5CaOH300	Reinhardbraunsite [90.82], Calcite [9.18]	Reinhardbraunsite
aC2SH CaOH	Calcite [12.91], poldervaartite [87.09]	α-C_2SH
Jaffeite CEM	Jaffeite [31.08], Portlandite [11.44], Calcite [13.10], Katoite [31.94], γ-C_2S [12.45]	Jaffeite
XCaOH250	Xonotlite [98.72], Calcite [1.28]	Xonotlite

The formulations to make reinhardbraunsite, α-C_2SH and xonotlite were successful as the minerals were made alongside calcite and the mixtures contained only these two minerals. The formulation to make jaffeite which was just hydrated and heated

CEM I powder contained a mixture of minerals which included jaffeite, portlandite, calcite, katoite and γ-C_2S. Although this mixture is impure it will provide information on the ability of these minerals to reduce the concentration of radionuclide in solution so it will be investigated.

5.4 Conclusions and chosen method for investigating radionuclide retention capacity

5.4.1 Summary

A synthesis method to make xonotlite, reinhardbraunsite, and α-C_2SH alongside either calcite or portlandite was determined. A method to synthesise jaffeite as a mixture containing other minerals of interest was found. No method to synthesise γ-C2S could be found in literature that worked or could be created experimentally.

5.4.2 Method to synthesise pure phase mineral

After the experiments in part 2 were analysed a synthesis route for each of the minerals of interest was decided based off the purity of the XRD mineral identification and quantification. These are described in Table 44 below.

Table 44: The methods determined in parts 2 and 3 to synthesise the minerals that will be studied in the next chapter.

Mineral	**Calcium source**	**C:S ratio**	**Curing temperature (°C)**	**Curing time**
Xonotlite	Calcium hydroxide	1	250	5 days
Jaffeite	CEM1 52.5N OPC	3	250	5 days
Reinhardbraunsite	Calcium hydroxide	2.5	250	24hrs
γ-C2SH	Calcium hydroxide	2	200	12hrs

This chapter built off work from the previous chapter where the mineralogy of high temperature and high C:S ratio cements was investigated. The aim of that chapter was to identify and characterise the mineralogy present within cements with a C:S ratio of 4-7.27 and at temperatures from 25 to 250°C. The mineralogy chapter identified several minerals that formed at high temperatures of 200 - 250°C, these included xonotlite, reinhardbraunsite, jaffeite, α-C_2SH and γ-C_2S.

This chapter focussed on either identifying or developing a method to synthesise these minerals as pure phase. Although the minerals were not able to be synthesised as single phase; xonotlite, reinhardbraunsite and α-C_2SH were able to be made alongside calcite or portlandite. Jaffeite was able to be synthesised as a mixture that contained other minerals of interest. A synthesis route for γ-C_2S was unable to be developed due to the high temperatures that are required.

The next chapter uses these mineral mixtures to investigate their effect on the concentration of radionuclide analogues in solution. The synthesis methods in Table 44 will be used to make 50g of each mineral mixture.

Further work could be done to investigate further purification of the minerals such as removing the calcite and then studying the effect on the mineral phase remaining. More investigation into developing a pure phase synthesis method for jaffeite could be done by altering the amount of water, the curing time, and the curing temperature.

Chapter 6 The effect of mineralogical composition of NRVB cement on the mobility of radionuclides

6.1 Introduction

In this Chapter the effect of different individual mineral phases on the mobility of radionuclides is investigated. In a previous chapter (Chapter 3) mineralogical characterisation was performed on NRVB cements cured between 25 and 250°C, and with a $CaO:SiO_2$ ratio of 4, 5, 6, 7, and 7.27. When cements are cured at elevated temperatures (above 150°C) high temperature minerals are formed, these are jaffeite, xonotlite, reinhardbraunsite, α-C2SH, and y-C2S. It is important to understand the impact of the formation of these minerals, particularly as they appear to form at the expense of portlandite (calcium hydroxide) on the key safety function performed by portlandite: buffering the pH to decrease radionuclide solubility.

In a cement encapsulant or backfill material, the role of calcium hydroxide is to dissolve slowly over time in the groundwater, thereby buffering the pH to remain highly alkaline[60,210]. The high groundwater pH generated by calcium hydroxide causes precipitation of radionuclides as solid hydrous oxide or hydroxide phases[211] and reduces the solubility of radionuclides[212] (e.g. uranium, nickel, caesium, barium, cadmium, europium, plutonium, selenium and chlorine[212]) that could potentially leak from the waste into the backfill. The buffering capacity of NRVB cement encourages the entrapment of the radionuclides thereby immobilising the radionuclides in the cement barrier. The high pH also serves the purpose of inhibiting microbial activities, which degrade cellulosic material, creating methane in the process[213–215]. This is one route for C-14, a radionuclide found in irradiated steel and graphite[216,217], to reach the biosphere and cause harm to humans and wildlife. High pH groundwater environments have additional benefits as the conditions inhibit steel corrosion. Inhibition of steel corrosion means that the ILW, HLW waste containers and structural components of the GDF will last longer. Hence, it provides longer containment and delays any radionuclide, hydrogen gas, and methane release. Once the ILW waste packages have been corroded, groundwater will ingress. This will increase the amount of radionuclides such as plutonium, caesium and strontium that are in contact with groundwater. Once a grouted ILW package has groundwater ingress this can

allow chloride and sulphate attack of the cement backfill thereby increasing the mobility of radionuclides by up to 9×10^{-5} wt%/year[218].

As the high temperature minerals form at the expense of the excess portlandite, investigating whether the NRVB cement is still effective at arresting radionuclides and preventing/ slowing their transport in groundwater is important as the loss of portlandite could lead to earlier container degradation, meaning the radionuclides will not be contained for as many half-lives leading to a potentially greater amount of radioactive material reaching the environment in a shorter time frame. This puts additional responsibility on the backfill material as a barrier to radionuclide release.

6.1.1 Cementitious minerals that formed during higher temperature curing in Chapter 3

How minerals were chosen

In previous work (Chapter 3) where the mineralogy of the different NRVB formulas was investigated several high temperature minerals were found to have formed, these were α-C_2SH, γ-C_2SH, jaffeite, reinhardbraunsite, katoite, and xonotlite.

There are four main ways that minerals can interact with radionuclides to reduce their concentration in solution. These are:

- Surface complexation: radionuclides are present as cations and are able to form inner-sphere complexes on the silicate and calcium sites in C-S-H[219].
- Solid solution (Interlayer uptake): radionuclides enter the interlayer sites in the C-S-H structure, this forms a solid solution phase[220].
- Coprecipitation/ Structural incorporation: actinides that are trivalent are captured within the C-S-H structure and are incorporated, not adsorped[221].
- Surface precipitation and secondary phases: radionuclides precipitate onto the surface of the mineral, this can cause secondary precipitates to form and can induce changes in structural coordination[221].

Calcite

Calcite can be present in cements in two ways. The first is when it forms through carbonation reactions, this occurs when CO_2 that is either dissolved in the water used to hydrate the cement powders, or in the air that subsequently dissolves into the water

used to mix the cement, reacts with portlandite, calcium hydroxide, to form calcium carbonate. Calcite is also a common additive to cements, up to 5% weight, and can have an impact on the mineralogy, as well as increasing a cement's vulnerability to carbonation[222].

Calcite can lower the concentration of radionuclides in soil and groundwater primarily through precipitation and sorbtion[223]. Radionuclides such as strontium, uranium oxide, and cerium can coprecipitate with calcite[224]. At the calcite–water interface, uranium(VI) is sorbed predominantly as uranyl triscarbonate-like surface complexes when dissolved uranium(VI) concentrations are below about 500 μM. At higher U(VI) concentrations above 500 μM), uranium(VI) hydroxide- and carbonate-containing precipitates begin to form on or near the calcite surface[225]. Europium (III) can be incorporated into the calcite crystal structure during recrystalisation[226]. Calcite is also able to sorb carbon-14 which is then recrystalised into the calcite structure[227].

Reinhardbraunsite

Few studies exploring the radionuclide interactions with reinhardbraunsite exist in literature. Reinhardbraunsite crystals bond poorly to each other, leaving gaps. This means it has a loose structure and is a weak, strength reducing phase[166]. Reinhardbraunsite has a Calcium to silicon ratio of 2.5, radionuclides interact with calcium so the high proportion of calcium could interact with radionuclides in solution[212]. Calcium is also more readily available to dissolve into the solution and increase the pH.

Xonotlite

Xonotlite has a C:S ratio of 1, and is a needle like, strengthening, and compact mineral. Xonotlite is thought to form from the recrystallisation of reinhardbraunsite and jaffeite when silica powder is added[166]. Xonotlite can be used to remove cobalt from a solution through a coupled dissolution-precipitation replacement mechanism where xonotlite dissolves and is replaced by cobalt containing mineral phases[228]. There is limited information available about xonotlite's ability to interact with other radionuclides.

α-C_2SH

C-S-H recrystalises, forming α-C_2SH. α-C_2SH has a smaller unit cell, this means there is a shrinkage and an increase in the porosity. This is called strength retrogression[166]. No studies explore radionuclide interactions with α-C_2SH.

γ-C_2SH

γ-C_2SH forms from β-C_2S, commonly known as belite. γ-C_2SH has a high affinity to CO2 and has been found to be useful for capturing C-14. It is 10% larger than the β-C_2S it forms from, this shatters the cement crystals into dust meaning it is a weak phase[229].

Jaffeite

Jaffeite has similar properties to α-C_2SH. Jaffeite formation causes the pore structure of cement to degrade, and a strength reduction[179]. There are limited direct studies on the interaction of jaffeite with radionuclides.

6.1.2 Radionuclides selection

Radionuclides that are present in nuclear reactors and spent fuel were chosen for these experiments. These are waste products that will be classified as ILW, HLW, HHGW or HAW and will be disposed of in the GDF, so will likely come into contact with the NRVB cement barrier in the future. The following highlights the key radionuclides selected for investigation and the rationale behind their selection:

- Cerium is a proven analogue for plutonium[230], a fission product.
- Strontium and caesium are fission products of uranium and plutonium[231].
- Iodine is a fission product from nuclear reactors[232].

The half-lives of the radionuclide analogues chosen to investigate in these experiments are shown in Table 45 below.

Table 45: The radionuclides chosen to test in this chapter and their half-lives.

Radionuclide	**Isotopes**	**$T_{1/2}$**	**Reference**
Cerium	Ce-144 Ce-139 Ce-141	284.893 days 137.64 days 32.501 days	[233]
Strontium	Sr-90	28.8 years	[234]
Caesium	Cs-135 Cs-137	2.3 million years 30 years	[235]
Iodine	I-129	1.6x107 yr	[236]

Cerium

Cerium has 35 radioisotopes, only the three listed in the table above have a half-life of over 30 days. The other radioisotopes have half-lives between 4 days and just 10 minutes. Despite its radioisotopes having short half-lives that should have had time to go through 10 decays before the waste containers have degraded to the point where radionuclides could interact with groundwater, it was still chosen for this investigation due to its other properties.

Cerium is often used as a non-radioactive analogue to plutonium due to their similar chemical properties. This is because they have a similar atomic radius, and 4f subshell electron properties. Both plutonium and cerium also form solid solutions[237]. They are both also oxidised from a +3 to +4 state and have similar coordination geometries[230]. Cerium is easy to access and as it is a proven analogue for plutonium will be used in its stead as a plutonium simulant for these experiments.

Table 46: The half-lives of the different radioisotopes of plutonium[225].

Radionuclide	**$T_{1/2}$**
Pu-238	87.8 years
Pu-239	24,100 years
Pu-240	6,560 years

The radioisotopes of plutonium have the half-lives shown in Table 46[238]: Plutonium-239 is the most common radioisotope if plutonium , it's half-life of 24,100 years means that it will still be present in the GDF when its engineered barrier begins to fail, allowing water ingress and the transport of the radionuclides from the waste containers and to the backfill, and potentially the groundwater and biosphere. The current government strategy for plutonium is to vitrify it and then store the vitrified product within the GDF[239]. The UK has the world's largest stockpile of plutonium of 140 tonnes[240], meaning a significant amount of plutonium will be disposed of within the GDF[241]. There is current research into glass dissolution, and how to create a stable vitrified plutonium waste form that will not leach into the groundwater. However, if leaching does occur over 10,000 year time scales it is likely there will be active plutonium given the very long half life of plutonium-239 so it is important to understand how it will interact with a backfill exposed to higher temperatures if NRVB backfill is to be used under higher temperature conditions.

Strontium

Strontium-90 is a fission product from uranium and plutonium. Strontium-90 bioaccumulates, and has been found in milk following the 2011 Fukushima Daiichi accident[242]. Strontium-90 is taken up by plants from air, water, and soil. Once consumed by animals or humans it behaves like calcium, causing radiation exposure and calcium deficiencies[243].

Strontium-90 has a biological half-life of 7 years so it will take 7 years before the concentration of strontium-90 in the body is halved, and 99% of it once ingested accumulates in bone marrow, teeth, and bones. Strontium-90 decays to yttrium-90, emitting a β particle, increasing the risk of bone cancer[244].

Radiative strontium is difficult to remediate as it behaves like calcium. It is likely it will interact with the cement minerals as they contain calcium and if there is any dissolution it is possible the strontium will replace the calcium within the mineral.

Caesium

Caesium is a common fission product in nuclear reactors. Caesium has 41 isotopes, however many of these are very unstable and only exist for seconds or fractions of a second. The two isotopes that need to be considered for the GDF are Cs-135 and Cs-137. Caesium can react with chlorine to form caesium chloride and easily dissolves in water. Once it reaches the surface it can be taken up as Cs-137 by plants from the soil[245]. Cs-137 is a gamma emitter, making consumption of contaminated plants dangerous.

Cements are already used to encapsulate caesium, Cs-137 has been found to be soluble in cement[246]. Hence, it is important to understand if the high temperature cement phases effect the mobility of Caesium in groundwater and in cement encapsulated waste in interim storage.

Iodine

Iodine forms at several different points of the nuclear fuel cycle, including fission, reprocessing, and disposal as shown in Figure 64. Iodine forms two radionuclides of concern, I-131 which has a half life of 8.04 days, and I-129 which has a half life of 1.57×10^7 years[247].

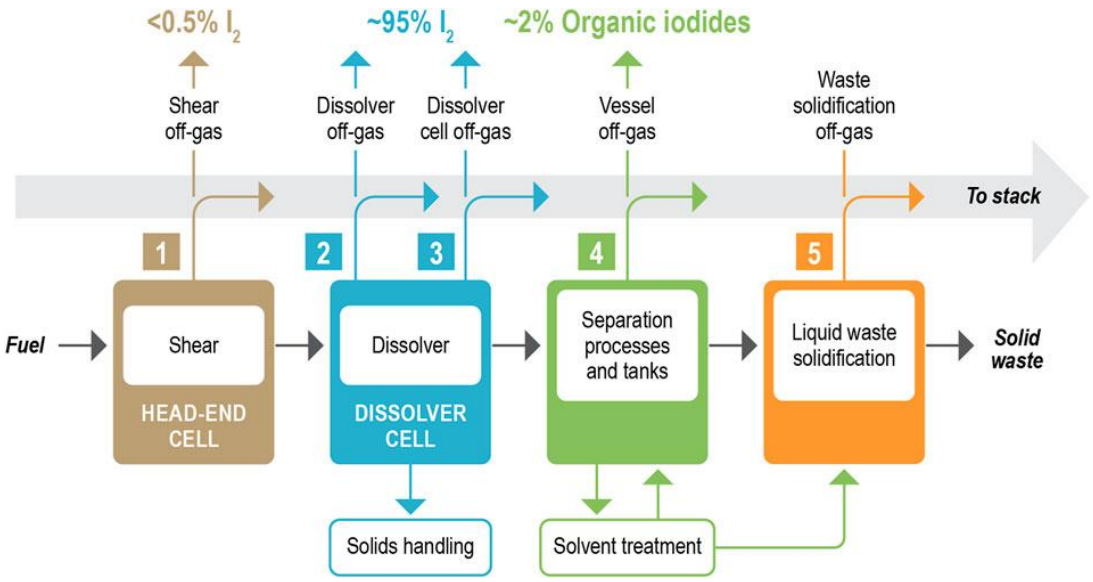


Figure 64: How radioiodine is produced in the nuclear fuels cycle[248].

Iodine 129 is toxic to humans, decaying through β and γ emission[249], and has a long half-life of $1.6x10^7$ years[236], this means it will be present in the GDF when the engineered barriers fail causing radionuclides to escape from the waste containers and into the backfill, and eventually the host rock of the GDF. The host rock has an effect on the mobility of radioiodine; iodine reaches the surface slower in evaporates whereas it moves faster in granite[247]. Metals have been found to be effective in binding to liquid iodine, the mineral Argentite (Ag_2S) takes 15 days to reach equilibrium. Malachite ($Cu_2CO_3(OH)_2$), azurite ($Cu_3(CO_3)_2(OH)_2$), and cuprite (Cu_2O) are also able to react with iodine and can reach equilibrium in 4 hours[250].

6.2 Mineral tests to study the effect on radionuclide concentration in solution

6.2.1 Introduction

To test the sorption and radionuclide retardation capabilities of the minerals that form within the cements at high temperatures the minerals were made as pure single phases where possible, and where this was not possible the minerals were formulated as a mixture of other known minerals that were also tested. They were then mixed with radionuclide analogue solutions before ICP-OES or ICP-MS was performed to see the change in radionuclide analogue concentration.

These experiments were carried out in three different phases which are introduced below.

Phase 1: The aim of this phase was to find out if any of the minerals were able to reduce the concentration of radionuclide in solution, and if so, which minerals interact with the radionuclide analogues.

Phase 2: The aim of this phase was to quantify how much each mineral was able to reduce the concentration of radionuclide in solution.

Phase 3: The aim of this phase was to find out the rate each mineral could reduce the concentration in solution for each radionuclide, and to determine its sorption mechanism with XRD.

6.2.2 Phase 1

6.2.2.1 Method

The method set out by S Cumberland et al.[251] was followed to investigate whether any of the pure phase minerals were able to interact with the radionuclides. In their work they soaked cement blocks in either 500ppm or 1000ppm strontium solution for 8 days and used ICP-OES to measure the concentration of the strontium in the solution to then calculate the amount that has been removed from the solution. The concentration of 1000ppm was chosen for these tests as they found the concentration of strontium was halved in solution, so 1000ppm is high enough to show a difference in concentration after the reaction.

To do this, 50mg of each pure phase mineral (calcite, reinhardbraunsite, xonotlite, jaffeite, and α-C_2SH) was weighed into a 15ml centrifuge tube. Three different solutions were tested: deionised water, high pH, and high salinity. Deionised water was used as a control.

High pH water was prepared by adding 1.2g of $Ca(OH)_2$ to 1 litre of deionised water and dissolving it at room temperature. This corresponds to a pH of 12.5. This was included as NRVB pore water has a pH of approximately 12.5. This is due to the excess portlandite ($Ca(OH)_2$) it contains which dissolves slowly over time into the pore water. This high pH reduces the solubility of radionuclides which helps to trap them within the cement pores, preventing their ingress into the environment and ground water. As this is a key feature of NRVB cement this was replicated in these tests.

Portlandite is present in all of the NRVB high temperature mixes apart from the cement with a $CaO:SiO_2$ ratio of 4 cured at 250°C. Testing the minerals efficacy at reducing the concentration of radionuclides in solution with and without portlandite present will show if this formulation will still be effective as it has common minerals with formulations that still have some portlandite present.

High salinity water was prepared as an analogue for the environment the GDF could be built in. Example environments are the Mercia Mudstone Group (MMG) and the Ancholme Group (AG) samples. To calculate a value to use as a salt concentration the molar amounts of NaCl were calculated for each reference saline[252] (listed in Table 47).

Table 47: Reference salinities used by NWS that are representative of geologies the GDF could be constructed in[252].

Sample Name	**MMG High Salinity**	**MMG Low Salinity**	**AG High Salinity**	**AG Low Salinity**
Na amount mg/l	121193	69090	10968	1757
Cl amount mg/l	192216	110697	19726	2176
Moles of Na	5.27	3.01	0.48	0.076
Moles of Cl	5.42	3.12	0.56	0.061

The MMG High Salinity sample had the highest molar amount of Na and Cl. It showed a higher molar amount of chlorine than sodium, the samples contained many other ions so it is probable that not all chlorine present was from the sodium chloride. Therefore, the molar amount of sodium was taken to be representative of the NaCl concentration.

No other ions were present in a significant amount, so to avoid additional variables only sodium chloride was used to increase the salinity to a value of 5.27 moles per dm^3. 1 litre of each solution was made 5 times, for a total of 15 different solutions. A series of solutions detailed in Table 48 were made.

Table 48: A table showing the 15 different solutions that were made and tested with each mineral.

Radionuclide	Chemical used	Solution		
		Deionised water	High salinity	High pH
Ce	Cerium (III) chloride heptahydrate	✓	✓	✓
Cs	Caesium chloride	✓	✓	✓
I	Sodium iodide	✓	✓	✓
Sr	Strontium chloride hexahydrate	✓	✓	✓
Control (blank)	N/A	✓	✓	✓

The radionuclide analogue was made up to a concentration of 0.0114 mol per dm^3. A 10ml of solution was added to the 15ml centrifuge tubes. The tubes were then mixed at 150 rpm in an orbital shaker for 8 days before a 0.1ml sample was taken from each one. The tubes were then left for another 8 days before an additional sample was taken. Finally, at 30 days a final sample was taken.

6.2.2.1.1 ICP-OES

To measure the radionuclide, calcium, and silicon concentrations present in the solution the samples were prepared for ICP-OES. A concentration of 1000ppm is above the maximum concentration for detection by ICP-OES. Samples were diluted into the calibration range using an appropriate dilution factor, and sample using the original stock solutions were tested to confirm the starting concentration.

A sample of each stock solution was prepared to a dilution factor of 100 and 1100. The method for dilution was: 0.1ml sample in 9.9ml of 3% nitric acid to make a 100x diluted sample. Then 1ml of the diluted sample in 10ml of 3% nitric acid to make a 1100x diluted sample. These samples were subsequently analysed by ICP-OES and were run in triplicate.

At dilution factor of 100 there was a carry over effect from the samples containing iodine. Approximately 20% of the iodine was transferred to the next sample, this was observed to reduce to around 10% by the sample after and trace by the third. At a

dilution factor of 1100 less than 10% was carried over, with none detected by the next sample. It was therefore decided to dilute the iodine samples by 1100 times, and to run a blank sample of 3% nitric acid between each sample to act as a rinse.

The samples containing cerium and strontium had too high a concentration of cerium, strontium, and calcium at a dilution factor of 100. They exceeded the maximum quantifiable concentration of the ICP-OES, and were over the range of the standard calibration curve the machine and provide the maximum and minimum quantification level. At a dilution factor of 1100 the quantities of cerium, strontium, and calcium were within the calibration curve and hence more reliable as the concentration sits within the linear range of the calibration standards.

During method development it was discovered that the quantity of iodine in the standard solutions was decreasing after two days. This could be due to the nitric acid causing the iodine to precipitate and/or evaporate when sample tubes were opened for analysis. As a result, the samples for iodine analysis were tested in small batches to avoid evaporation.

Standards for ICP-OES were prepared to Table 49 below:

Table 49: The concentrations of the standards used to calibrate the ICP-OES.

	Element (ppm)				
Standard	**Calcium**	**Silicon**	**Cerium**	**Strontium**	**Iodine**
1	0.5	0.1	0.1	0.01	0.03
2	2.5	0.5	0.5	0.05	0.15
3	5	1	1	0.1	0.3
4	25	5	5	0.5	1.5
5	50	10	10	1	3

During the initial tests it was determined that these ranges were appropriate and gave a suitable minimum quantification level shown in Table 50.

Table 50: The Minimum Quantification Level of each element measured with ICP-OES.

Element	Minimum Quantification Level (MQL) (ppm)
Ca	0.016
Ce	0.001
Si	0.003
Sr	0.00008
I	0.006

6.2.2.1.2 ICP-MS

Caesium is unable to be measured with the ICP-OES and is commonly measured using ICP-MS as the Cs is easily ionised. The challenges of measuring caesium with ICP-OES are due to its two main emission wavelengths, at 455.531 nm and 459.320 nm, being atomic emissions and less sensitive. The other wavelength, at 894.347 nm has a higher intensity but it is not commonly within the range for ICP-OES to have the capability to measure to this wavelength[253] .

The samples containing caesium where therefore analysed using the ICP-MS facility at the University of Leeds. Samples were first diluted to have a concentration of 10ppb of caesium using 3% HNO_3. Only the samples collected during phase 1 at the 8 day time point were analysed. This was due to the fact the aim of the phase 1 experiments were to identify if there is a reduction in concentration in an initial 8 day period. Other mineralogical tests were run for longer to see if the concentration continued to reduce over time. Minerals tested after the initial experiments (including the whole cement systems) were only measured at 8 days, so data collected after this timepoint is only comparable to some results. The samples at the University of Leeds were measured and had the Limit of Detection (LoD), Limit of Quantification (LoQ), and uncertainties shown in Table 51 below.

Table 51: The Limit of Detection, Limit of Quantification, and % Uncertainty for the ICP-MS results.

	Si	Ca	Cs	Ce
LOD / mg L-1	3.25E-02	1.33E-02	7.40E-02	9.52E-03
LOQ / mg L-1	1.08E-01	4.44E-02	2.47E-01	3.17E-02
% Uncertainty	11.7	3.1	1.3	1.2

6.2.2.2 Results

The results from the ICP-OES measurements are in the tables below. The results presented in these tables are the molar concentrations of the radionuclides in the solution at the different time points. These results are averaged from the values obtained from three experimental samples that underwent the exact same reaction conditions, giving three experimental repeats. The results shown below in Table 52 are the average of these three experimental repeats. The concentration of calcium and silicon were also measured.

Calcite

Table 52: The results from testing how much radionuclide analogue calcite can remove from solution.

		Amount of radionuclide remaining in solution after [days] (mol/dm^{-3})			
Solution	**Radionuclide**	**[0]**	**[8]**	**[16]**	**[30]**
Deionised water	Iodine	0.005714	0.003972	0.00441	0.006929
	Strontium	0.010769	0.003572	0.00327	0.003462
	Cerium	0.009994	0.000819	0.000191	0.000191
	Caesium	0.012069	0.0116	-	-
High pH	Iodine	0.006011	0.000968	0.00411	0.00682
	Strontium	0.009285	0.010178	0.010967	0.009237
	Cerium	0.008015	BDL	BDL	BDL
	Caesium	0.011962	0.011720	-	-
High Salinity	Iodine	0.006011	0.001014	0.004051	0.007423
	Strontium	0.009285	0.004364	0.004183	0.003462
	Cerium	0.009028	0.009415	0.008732	0.007827
	Caesium	0.010458	0.010223	-	-

Table 53: The percentage of radionuclide remaining in solution after 8 days of being shaken with calcite.

Solution	Radionuclide	Radionuclide remaining in solution after 8 days (%)
Deionised water	Iodine	69.5135
	Strontium	33.1693
	Cerium	8.19492
	Caesium	96.114
	Control	-
High pH	Iodine	16.1038
	Strontium	109.618
	Cerium	0
	Caesium	97.9769
	Control	-
High Salinity	Iodine	16.8691
	Strontium	47.0005
	Cerium	104.287
	Caesium	97.7529
	Control	-

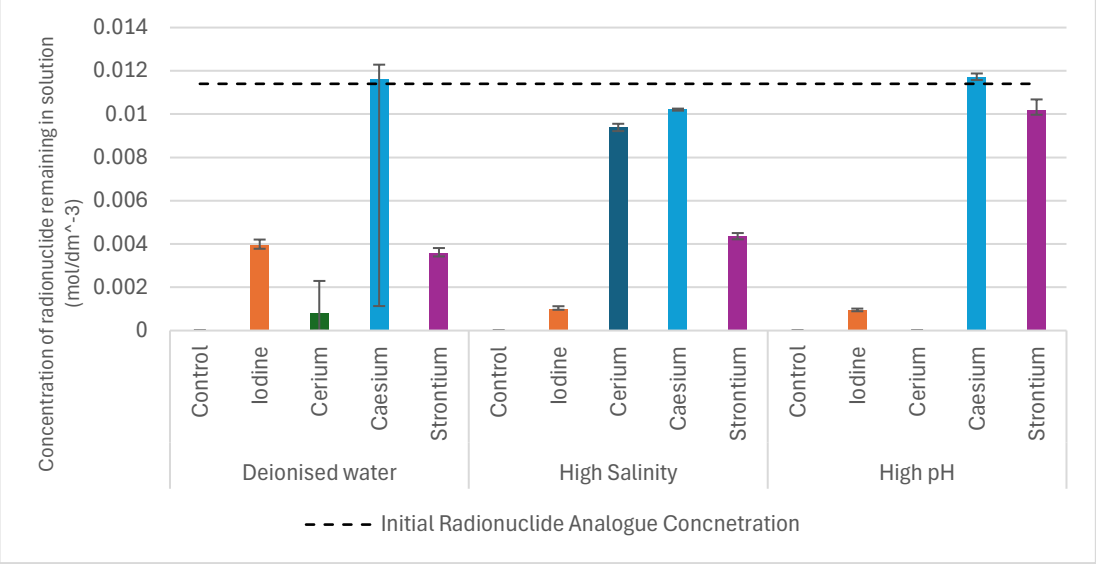


Figure 65: The results from testing how much radionuclide analogue calcite can remove from solution. Iodine is represented by orange, cerium is green, caesium is blue, and strontium is purple.

Calcite performed differently in each matrix as shown in Table 52, Table 53 and Figure 65. The iodine concentration in solution decreased is in all three solutions after 8 days,

from approximately 0.006 mol/dm^{-3} to approximately 0.004. It had the lowest concentration at 16 days in the high salinity solution. This could be due to the availability of sodium within the solution, sodium could interact with the calcite making it easier for calcium to be released. The concentration of iodine in solution can be reduced as iodine can be incorporated into the calcite mineral structure. One method of this by adding sodium ions to solution, these can substitute into the Ca^{2+} positions within the calcite. The iodine anion and sodium cation has a smaller atomic distance between them than iodine and calcium, and is more energetically favourable making the incorporation of iodine more likely[254]. However, the precipitation and incorporation of iodine into calcite is dependent on pH, and is more favourable at a pH of 8. This incorporation decreases as the pH increases[255] which is seen in the results as iodine concentration decreases the most in the high pH solution.

Cerium concentration was most reduced in the high pH solution. This is likely due to the availability of calcium in solution increasing the pH, and causing the cerium to precipitate. The concentration of cerium was also greatly reduced in deionised water to approximately 10% of its starting concentration. In deionised water calcite increased the pH to approximately 9 as the carbonate is able to dissolve into the solution. Cerium exists as an aqueous 3+ phase until above pH of 10.4 when it will precipitate solely as $Ce(OH)_3$, a stable solid[256]. $Ce(OH)_3$ will coexist with Ce^{3+} at lower pH values[256]. At the elevated pH of 9 both $Ce(OH)_3$ and Ce^{3+} are present.

In deionised water and high salinity solution the addition of calcite decreased the amount of strontium in solution. The presence of calcite reduced the strontium concentration in the 1000ppm strontium deionised water to approximately 33% and in high salinity to 47%. The addition of calcite to the high pH strontium solution caused no change in the strontium concentration.

Caesium concentration was unaffected by the presence of calcite regardless of the solution matrix. In deionised water caesium remains within the experimental error of the measurements at a concentration of 96% its original value, and in high pH and high salinity it is present at 97% .

Xonotlite

The results of how much xonotlite reduced the concentration of radionuclide analogue in solution are shown below in Table 54, Table 55 and Figure 66.

Table 54: The results from testing how much radionuclide analogue xonotlite can remove from solution.

		Sample point (days)			
Solution	**Radionuclide**	**0**	**8**	**16**	**30**
Deionised water	Iodine	0.005714	0.00403	0.003572	0.006664
	Strontium	0.010769	0.00966	0.010009	0.008916
	Cerium	0.009994	0.008683	0.007306	0.007306
	Caesium	0.012069	0.011194		
High pH	Iodine	0.006011	0.004018	0.003287	0.006993
	Strontium	0.009285	0.010843	0.010922	0.009436
	Cerium	0.008015	0	0	0
	Caesium	0.011962	0.011566		
High Salinity	Iodine	0.006011	0.003806	0.004431	0.007926
	Strontium	0.009285	0.008861	0.00831	0.008097
	Cerium	0.009028	0.008329	0.007628	0.006325
	Caesium	0.010458	0.010246		

Table 55: The percentage of radionuclide remaining in solution after 8 days of being shaken with xonotlite.

Solution	**Radionuclide**	**Radionuclide remaining in solution after 8 days (%)**
Deionised water	Iodine	70.5285
	Strontium	89.7019
	Cerium	86.8821
	Caesium	92.75
High pH	Iodine	66.8441
	Strontium	116.78
	Cerium	0
	Caesium	96.6895
High Salinity	Iodine	63.3173
	Strontium	95.4335
	Cerium	92.2574
	Caesium	97.9728

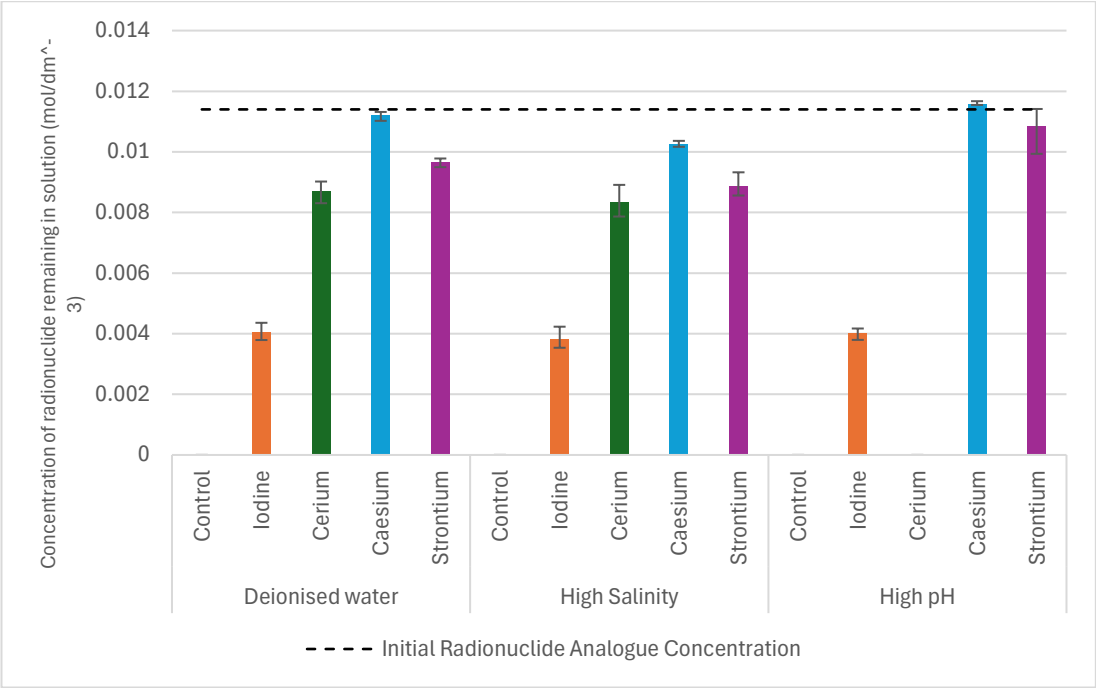


Figure 66: The results from testing how much radionuclide analogue xonotlite can remove from solution. Iodine is represented by orange, cerium is green, caesium is blue, and strontium is purple.

Xonotlite showed increased radionuclide analogue reduction capabilities when the matrix was deionised water versus high salinity or high pH. In deionised water it was able to reduce all four radionuclide analogues, however, in the high pH solution the cerium concentration was reduced to 0. This is due to the cerium precipitating in the high pH solution, as cerium precipitates to a stable solid above pH 10.4[256]. In the high salinity solution strontium and caesium remained at a higher concentration. Xonotlite reduced the concentration of strontium by 5% of its original value, compared to 10% in deionised water.

Reinhardbraunsite

The results of how much reinhardbraunsite reduced the concentration of radionuclide analogue in solution are shown below in Table 56,

Table 57, and Figure 67.

Table 56: The results from testing how much radionuclide reinhardbraunsite removes from solution.

		Sample point (days)			
Solution	**Radionuclide**	**0**	**8**	**16**	**30**
Deionised water	Iodine	0.005714	0.003747	0.002813	0.005913
	Strontium	0.010769	0.010358	0.010156	0.009165
	Cerium	0.009994	0	0	0
	Caesium	0.012069	0.011536		
High pH	Iodine	0.006011	0.00339	0.00279	0.006449
	Strontium	0.009285	0.010701	0.010336	0.010058
	Cerium	0.008015	0	0	0
	Caesium	0.011962	0.0115357		
High Salinity	Iodine	0.006011	0.003867	0.003054	0.006421
	Strontium	0.009285	0.009289	0.009354	0.008554
	Cerium	0.009028	0	0	2.62E-06
	Caesium	0.010458	0.010327		

Table 57: The percentage of radionuclide remaining in solution after 8 days of shaking with reinhardbraunsite.

Solution	Radionuclide	Radionuclide remaining in solution after 8 days (%)
Deionised water	Iodine	65.5758
	Strontium	96.1835
	Cerium	0
	Caesium	95.5837
High pH	Iodine	56.3966
	Strontium	115.25
	Cerium	0
	Caesium	96.44
High Salinity	Iodine	64.3321
	Strontium	100.043
	Cerium	0
	Caesium	98.7474

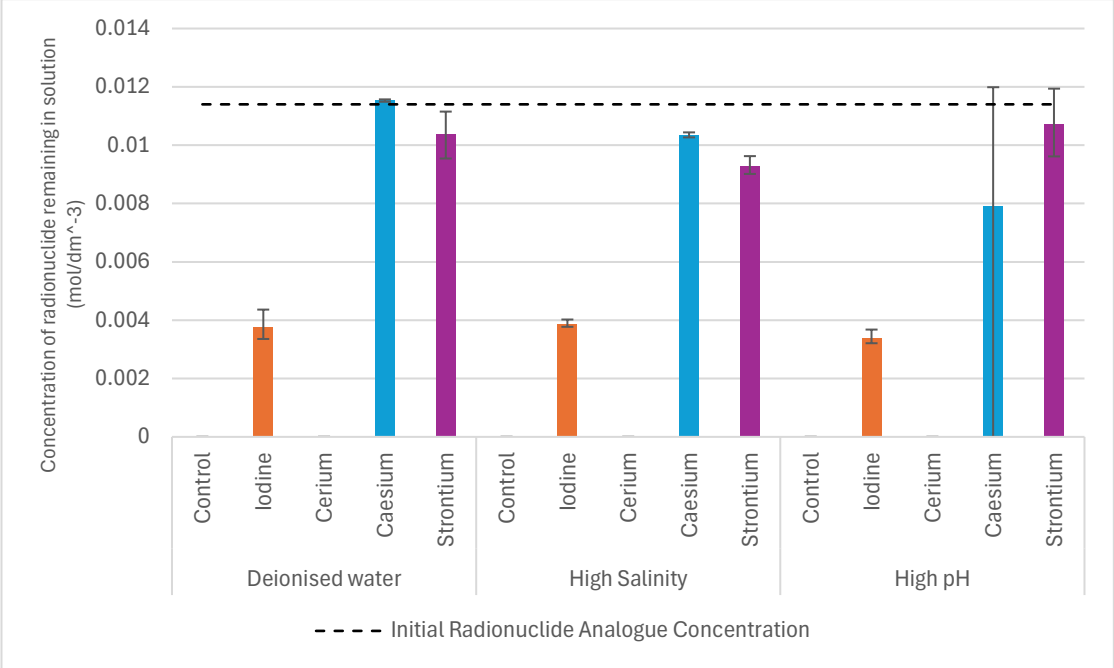


Figure 67: The results from testing how much radionuclide analogue reinhardbraunsite can remove from solution. Iodine is represented by orange, cerium is green, caesium is blue, and strontium is purple.

The tests with the mineral reinhardbraunsite showed precipitation of the cerium in all three solutions. In deionised water it showed a slight reduction of strontium concentration, and a similar small reduction in caesium. In a high pH solution and high salinity solution there was no reduction of concentration of strontium. The strontium concentration remaining constant in high pH and high salinity solution suggests the slight reduction in deionised water is not driven by pH reducing the solubility, and either a sorption process has taken place or a reaction between the strontium and reinhardbraunsite has occurred resulting in strontium uptake. The amount of iodine in all three solutions was reduced by approximately the same amount.

α-C_2SH

The results of how much α-C2SH reduced the concentration of radionuclide analogue in solution are shown below in Table 58, Table 59, and Figure 68.

Table 58: The results from testing how much radionuclide analogue α-C_2SH can remove from solution.

		Sample point (days)			
Solution	**Radionuclide**	**0**	**8**	**16**	**30**
Deionised water	Iodine	0.005714	0.002897	0.002738	0.005468
	Strontium	0.010769	0.009487	0.008705	0.007588
	Cerium	0.009994	0	0	0
	Caesium	0.012069	0.011529		
High pH	Iodine	0.006011	0.003228	0.00216	0.004953
	Strontium	0.009285	0.010091	0.010238	0.009098
	Cerium	0.008015	0	0	2.62E-06
	Caesium	0.011962	0.011621		
High Salinity	Iodine	0.006011	0.002599	0.00289	0.006458
	Strontium	0.009285	0.008824	0.008318	0.00752
	Cerium	0.009028	0	0	5.23E-06
	Caesium	0.010458	0.010128		

Table 59: The percentage of radionuclide remaining in solution after 8 days of being shaken with α-C_2SH.

Solution	Radionuclide	Radionuclide remaining in solution after 8 days (%)
Deionised water	Iodine	50.7
	Strontium	88.0955
	Cerium	0
	Caesium	95.5257
High pH	Iodine	53.7015
	Strontium	108.681
	Cerium	0
	Caesium	97.1493
High Salinity	Iodine	43.2374
	Strontium	95.035
	Cerium	0
	Caesium	96.8445

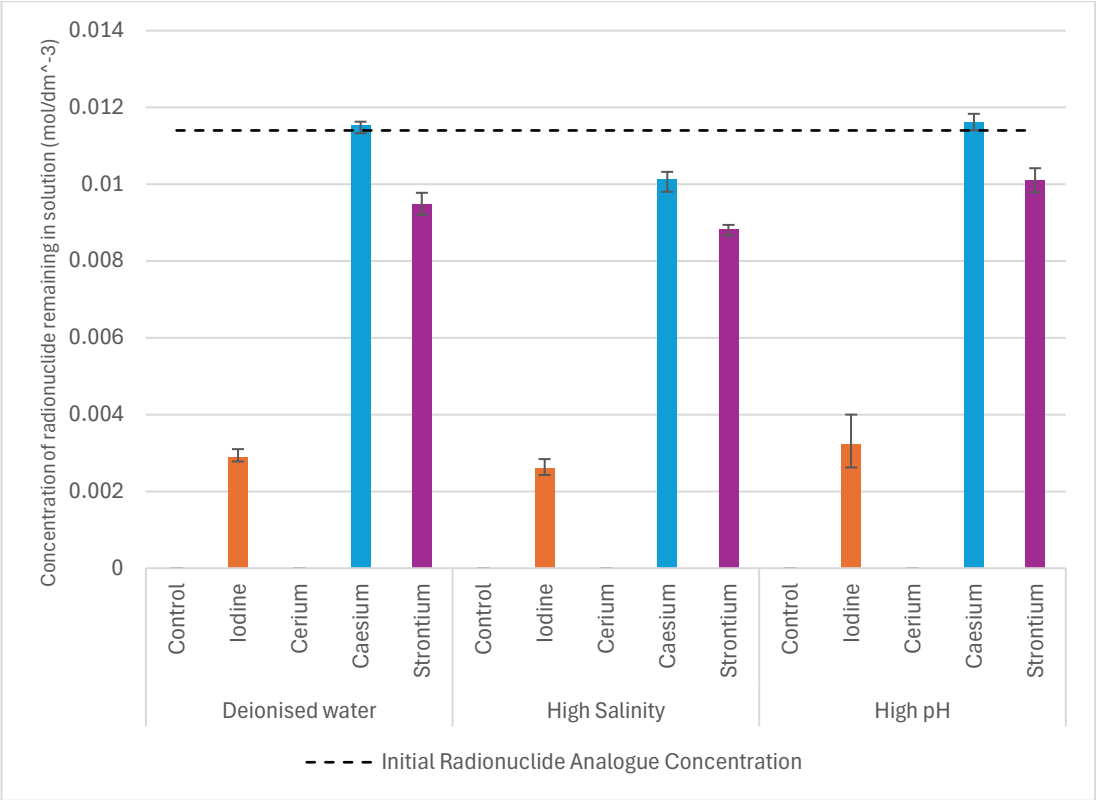


Figure 68: The results from testing how much radionuclide analogue α-C_2SH can remove from solution. Iodine is represented by orange, cerium is green, caesium is blue, and strontium is purple.

α-C_2SH showed a reduction of strontium concentration in deionised water and high salinity solution, there was no reduction in the high pH solution. This is likely due to the pH in deionised water and high salinity being raised by the portlandite present in this mix eliminating pH effect as a variable. It is possible that the portlandite present in the high pH solution is reacting or sorbing to the minerals present within this mineral preferentially over the strontium, implying that using a lower pH cement with a lower portlandite concentration would be a better barrier for preventing strontium entering the biosphere.

Jaffeite

The results of how much jaffeite reduced the concentration of radionuclide analogue in solution are shown below in Table 60, Table 61, and Figure 69.

Table 60: The results from testing how much radionuclide analogue jaffeite can remove from solution.

		Sample point (days)	
Solution	**Radionuclide**	**0**	**8**
Deionised water	Strontium	0.010769	0.0104048
	Cerium	0.009994	0
	Caesium	0.012069	0.0120675
High pH	Strontium	0.009285	0.0102640
	Cerium	0.008015	0.0000036
	Caesium	0.011962	0.0119866
High Salinity	Strontium	0.009285	0.0096249
	Cerium	0.009028	0.0001772
	Caesium	0.010458	0.0104739

Table 61: The percentage of radionuclide remaining in solution after 8 days of being shaken with jaffeite.

Solution	Radionuclide	Radionuclide remaining in solution after 8 days (%)
Deionised water	Strontium	96.6181
	Cerium	0
	Caesium	99.9876
High pH	Strontium	110.544
	Cerium	0.04492
	Caesium	100.206
High Salinity	Strontium	103.661
	Cerium	1.96278
	Caesium	100.152

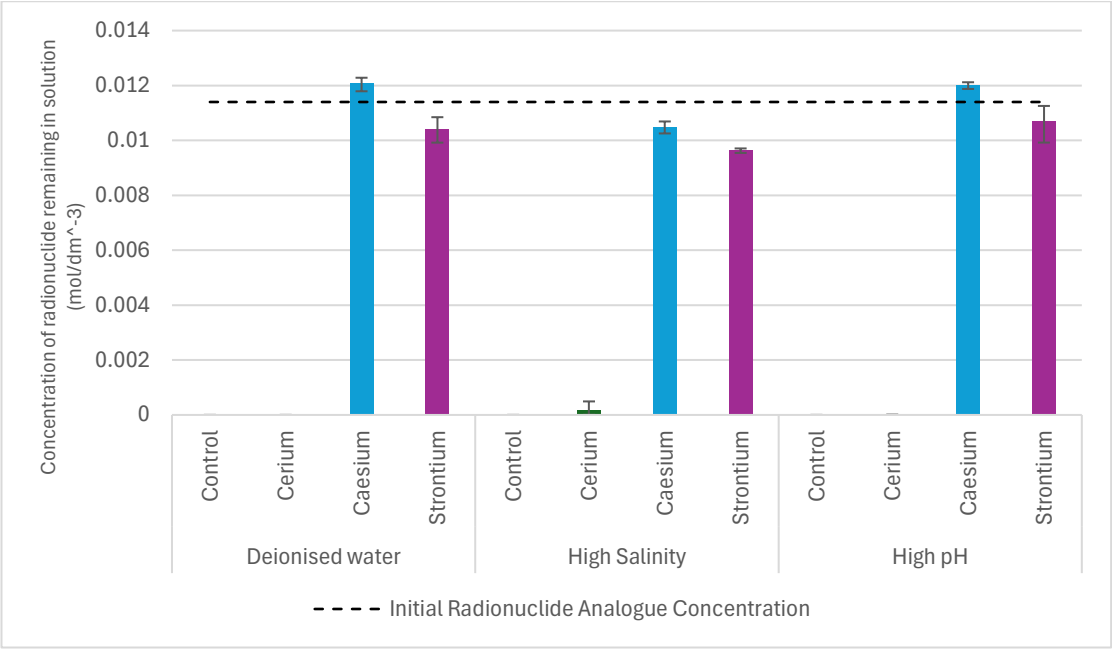


Figure 69: The results from testing how much radionuclide analogue jaffeite can remove from solution. Iodine is represented by orange, cerium is green, caesium is blue, and strontium is purple.

Jaffeite showed very similar results to α-C_2SH, it was able to reduce the concentration of cerium to 0 in deionised water, less than half a percent in the high pH solution, and less than two percent in high salinity solution. Jaffeite was able to reduce the strontium by less than four percent in deionised water, and was not able to reduce it in the high pH or high salinity solution. The amount of caesium remained at approximately 100% of its starting concentration in all three solutions.

6.2.2.3 Cement tests

The tests from phase 1 were repeated with three cement mixes from the mineralogy chapter (Chapter 3), these were C:S ratio 4 cured at 250°C, NRVB cured at 250°C, and NRVB cured at 200°C. These three cements were chosen based on their mineralogical composition as they contained minerals that had been chosen to be tested, and minerals that were present but could not be synthesised successfully (Table 34).

The aim of these experiments using whole cement systems was to ascertain whether the minerals that could not be synthesised had sorption capacity, and how a cement system performed. The three cements that were chosen and their mineralogical composition are in Table 62 and Figure 70.

Table 62: The three cements that were chosen and their mineralogical compositions.

	C:S ratio 4 250°C	NRVB 200°C	NRVB 250°C
Calcite (%)	1.13	9.146	6.61
Jaffeite (%)	9.2	7.097	6.26
Reinhardbraunsite (%)	62.24		21.61
Katoite (%)	13.38		28.09
Xonotlite (%)	14.05		
γ-C_2S (%)		26.684	
α-C_2SH (%)		11.573	
Portlandite (%)		45.499	37.43

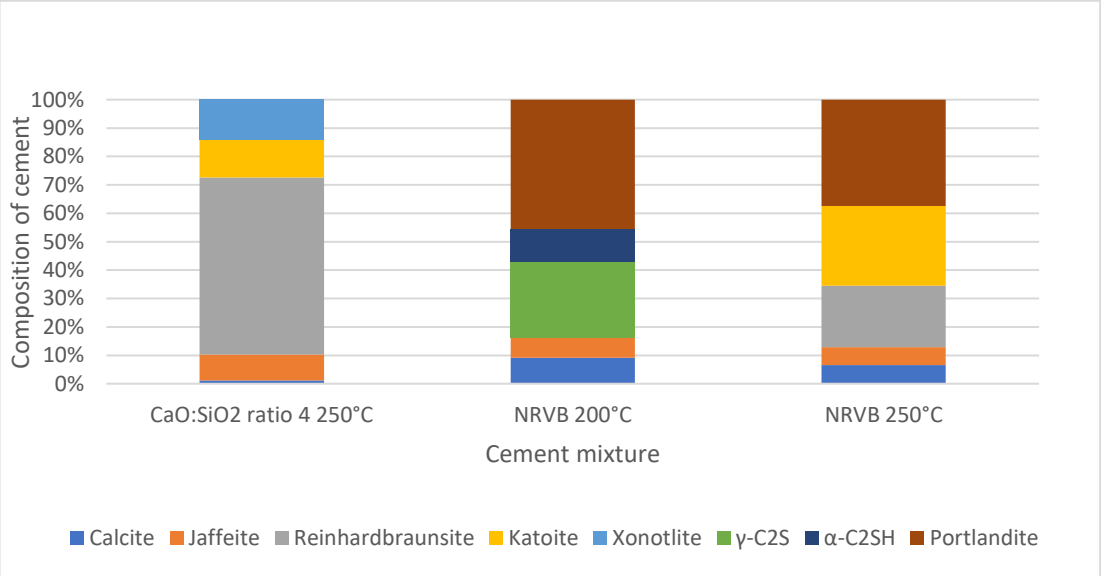


Figure 70: The three cements that were chosen to investigate and their mineralogical composition.

The cement mix C:S ratio 4 cured at 250°C was chosen as it contained the mineral katoite, an aluminium containing calcium silicate. It also contains calcite, jaffeite, reinhardbraunsite, and xonotlite. All of these have been tested as individual pure phase minerals so if this cement shows a difference in its performance then it will be either due to the mixture of minerals or the katoite. If the minerals are present in a mixture the behaviour could be altered, for example reinhardbraunsite which contains a higher proportion of calcium than calcite might dissolve more readily, meaning strontium cannot react with calcite to form strontianite.

This cement (C:S ratio 4 cured at 250°C) also contained no portlandite whereas the other two NRVB samples (cured at 200 and 250°C) did, so this will show the impact of the portlandite on buffering the pH and causing precipitation of the radionuclide analogues. The C:S ratio 4 cured at 250°C is the only cement to contain xonotlite which is a mineral that increases the strength of a cement. If a stronger backfill cement becomes more desirable then the cement mix and curing conditions could be altered to favour the formation of xonotlite, so understanding how it behaves as part of a mixture and not just individually is important to understand the safety functions of the backfill.

Only the NRVB sample cured at 200°C contained α-C_2SH and γ-C_2S, only the α-C_2SH was able to be made as a pure phase and tested. This sample will show the impact on other minerals on its efficacy, and if the performance is very different from the single pure phase tests for all minerals then it indicates that γ-C_2S is effective at reducing the concentration of radionuclides in solution.

All three cements chosen cover the minerals previously identified so will provide evidence as to whether they are effective at slowing or stopping radionuclide release. A difference in performance will also provide insight as to whether the minerals perform better in a mixture or as single phases. The exact same method that was used to test the single phase minerals was used to test the cements including the same solutions of radionuclide analogue. Therefore, a direct comparison can be made as any effects from weighing or dilution are mitigated against.

$CaO:SiO_2$ ratio 4 250°C

The results of how much the cement C:S ratio 4 cured at 250°C reduced the concentration of radionuclide analogue in solution are shown below in Table 63, Table 64, and Figure 71.

Table 63: The results from testing how much radionuclide analogue the cement C:S ratio 4 250°C can remove from solution.

		Sample point (days)	
Solution	**Radionuclide**	**0 (mol/dm^3)**	**8 (mol/dm^3)**
Deionised water	Strontium	0.010769	0.008899
	Cerium	0.009994	0.0000169
	Caesium	0.012069	0.012116
High pH	Strontium	0.009285	0.0094625
	Cerium	0.008015	0.0000067
	Caesium	0.011962	0.0118759
High Salinity	Strontium	0.009285	0.0100331
	Cerium	0.009028	0.0000259
	Caesium	0.010458	0.0104846

Table 64: The percentage of radionuclide remaining in solution after 8 days of being shaken with the cement C:S ratio 4 250°C.

Solution	**Radionuclide**	**Radionuclide remaining in solution after 8 days (%)**
Deionised water	Strontium	82.6353
	Cerium	0.1691
	Caesium	100.389
High pH	Strontium	101.912
	Cerium	0.08359
	Caesium	99.2802
High Salinity	Strontium	108.057
	Cerium	0.28689
	Caesium	100.254

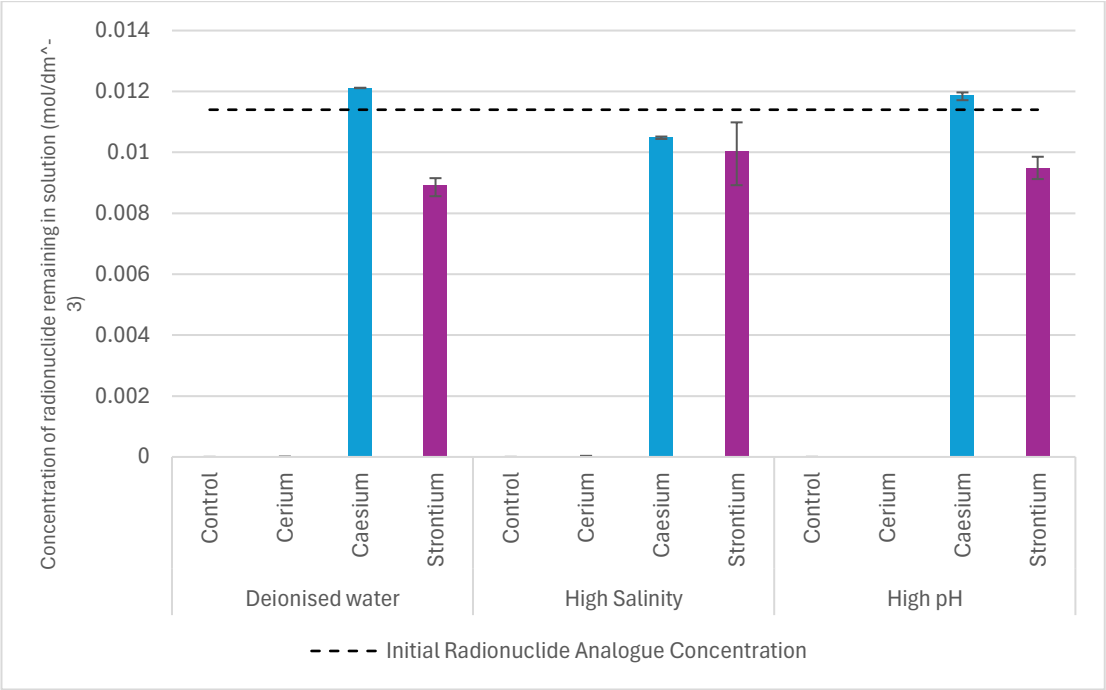


Figure 71: The results from testing how much radionuclide analogue C:S ratio 4 can remove from solution. Iodine is represented by orange, cerium is green, caesium is blue, and strontium is purple.

This cement mixture (C:S ratio 4) contained approximately 1% calcite, 9% jaffeite, 62% reinhardbraunsite, 13% katoite and 14% xonotlite. Similarly to most minerals the cement reduced the amount of cerium in all three solutions to less than one percent of the starting concentration. The concentration of strontium was most reduced in deionised water, and this was to 82% of the starting concentration. The only minerals that showed a reduction in strontium that are present in this mixture were calcite, xonotlite, jaffeite and reinhardbraunsite. Calcite is only present at 1%, which is 0.5mg total. There was approximately 10mg of strontium present, so if all of the calcite reacted with the strontium this would reduce the concentration by 5%. Xonotlite reduced the amount of strontium to approximately 90% when it was present as a single phase. Reinhardbraunsite and Jaffeite reduced the amount of strontium by less than 4%.

Table 65 shows how much strontium would be reduced by each mineral if they behaved the same as they did in the single phase tests. The total mass reduced is just 0.478mg, only 5% of the total concentration of strontium. This means that either the katoite is removing the other 12.4% from solution, or the minerals are affecting each other's efficacy.

Strontium can be incorporated into katoite through substitution for calcium within the hydrogarnet structure, owing to their similar ionic radii and charge. However, this incorporation is typically limited and depends on local chemical conditions, with other cement phases such as C–S–H often acting as the dominant sinks for strontium[257].

Table 65: The minerals that have been tested to see how much strontium they can remove from solution that are also present within this cement mix.

Mineral	**Single phase test reduction**	**Proportion (%)**	**Mass (mg)**	**Mass Sr (mg)**	**Mass Sr reduced normally (mg)**	**Mass Sr reduced scaled to the mineral proportion (g)**
Calcite	0.66831	1	0.5	10	6.68307	0.066831
Jaffeite	0.03382	9	4.5	10	0.33819	0.030437
Reinhardbraunsite	0.03817	62	31	10	0.38165	0.236623
Xonotlite	0.10298	14	7	10	1.02981	0.144173

NRVB 200°C

The results of how much NRVB cured at 200°C reduced the concentration of radionuclide analogue in solution are shown in Table 66, Table 67, and Figure 72.

Table 66: The results from testing how much radionuclide analogue the cement NRVB 200°C can remove from solution.

		Sample point (days)	
Solution	**Radionuclide**	**0 (mol/dm^3)**	**8 (mol/dm^3)**
Deionised water	Strontium	0.010769	0.0105471
	Cerium	0.009994	0.0000036
	Caesium	0.012069	0.0121139
High pH	Strontium	0.009285	0.0104607
	Cerium	0.008015	0.0000074
	Caesium	0.011962	0.0118939
High Salinity	Strontium	0.009285	0.0090854
	Cerium	0.009028	0.0000328
	Caesium	0.010458	0.0104433

Table 67: The percentage of radionuclide remaining in solution after 8 days of being shaken with the cement NRVB 200°C.

Solution	Radionuclide	Radionuclide remaining in solution after 8 days (%)
Deionised water	Strontium	97.9395
	Cerium	0.03602
	Caesium	100.372
High pH	Strontium	112.662
	Cerium	0.09233
	Caesium	99.4307
High Salinity	Strontium	97.8503
	Cerium	0.36331
	Caesium	99.8594

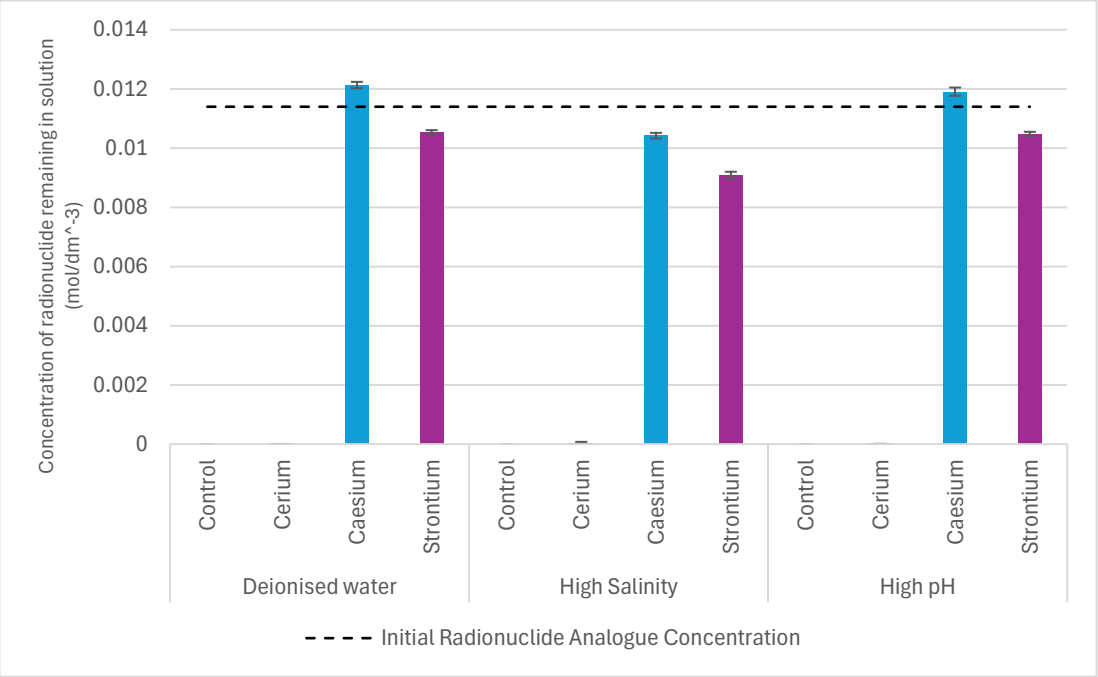


Figure 72: The results from testing how much radionuclide analogue NRVB cured at 200°C can remove from solution. Iodine is represented by orange, cerium is green, caesium is blue, and strontium is purple.

This cement mix (NRVB cured at 200°C) is composed of 9% calcite, 7% jaffeite, 27% γ-C_2SH, 12% α-C_2SH, and 45% portlandite. This cement was able to reduce cerium to less than 1% in all three solutions. This is similar behaviour to the jaffeite and α-C_2SH, and is expected from a cement that contains high amount of portlandite as this raises the pH and causes the cerium to precipitate. There was no other significant or

unexpected reduction seen with this mix. Calcite, α-C_2SH and jaffeite all reduced the concentration of strontium in solution by a similar amount to this cement mix.

NRVB 250°C

The results of how much NRVB cured at 250°C reduced the concentration of radionuclide analogue are shown below in Table 68,

Table 69, and Figure 73.

Table 68: The results from testing how much radionuclide NRVB 250°C removed from solution.

		Sample point (days)	
Solution	**Radionuclide**	**0 (mol/dm^3)**	**8 (mol/dm^3)**
Deionised water	Strontium	0.010769	0.0104565
	Cerium	0.009994	0.0001394
	Caesium	0.012069	0
High pH	Strontium	0.009285	0.0101446
	Cerium	0.008015	0.0000064
	Caesium	0.011962	0.0119392
High Salinity	Strontium	0.009285	0.0060926
	Cerium	0.009028	0.0000033
	Caesium	0.010458	0.010719

Table 69: The percentage of radionuclide remaining in solution after 8 days of being shaken with the cement NRVB 250°C.

Solution	Radionuclide	Radionuclide remaining in solution after 8 days (%)
Deionised water	Strontium	97.0982
	Cerium	1.39484
	Caesium	0
High pH	Strontium	109.258
	Cerium	0.07985
	Caesium	99.8094
High Salinity	Strontium	65.6177
	Cerium	0.03655
	Caesium	102.496

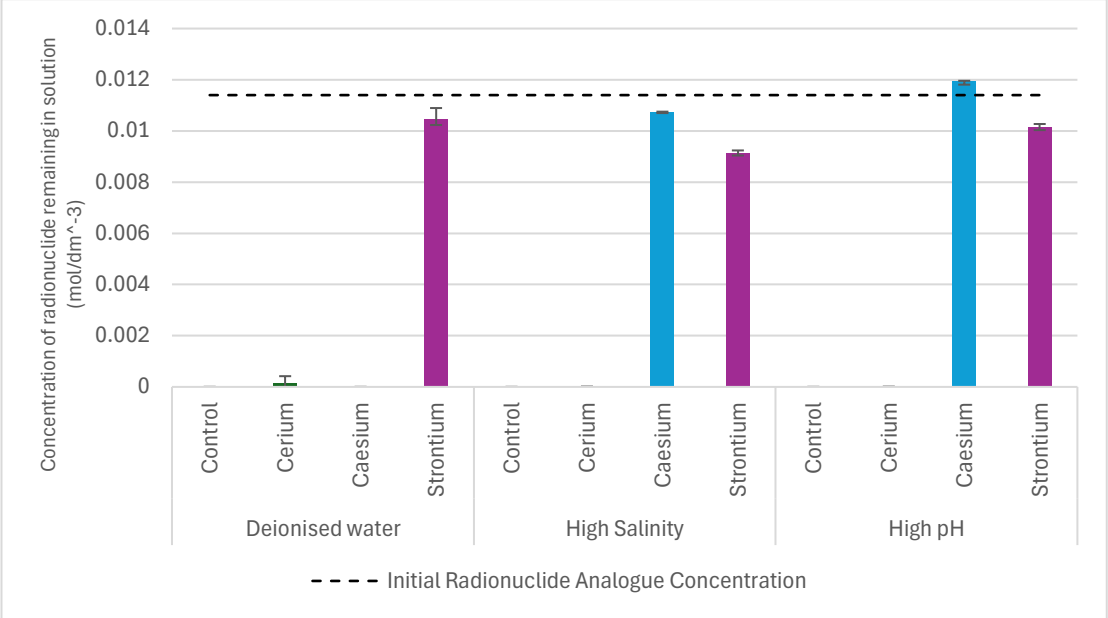


Figure 73: The results from testing how much radionuclide analogue NRVB cured at 250°C can remove from solution. Iodine is represented by orange, cerium is green, caesium is blue, and strontium is purple.

In the cement that was NRVB cured at 250°C in deionised water the caesium concentration seemingly decreased below analytical detection limits. This is unexpected result as the other two matrices tested showed no change in caesium from the starting solutions. All the other minerals present in the mixture which have been tested individually have shown similar percentages of caesium remaining in solution regardless of the solution they are in as shown in Table 70. It is unexpected that the deionised water matrix appears to have removed all caesium and this is likely due to analytical or sampling errors.

Table 70: The composition of NRVB cured at 250°C and the % of caesium left in solution when tested against the individual components of the cement.

Mineral	**% composition of NRVB cured at 250°C**	**% caesium remaining in solution in single phase experiments**
Calcite	6.61	96.114
Portlandite	37.43	*
Jaffeite	6.26	99.9876
Reinhardbraunsite	21.61	95.5837
Katoite	28.09	**

*Portlandite was not tested as a single phase mineral as it was used to adjust the pH in the high pH solutions. As there was no significant difference in the amount of caesium remaining in the high pH solutions for the other cement samples tested ($CaO:SiO_2$ ratio 4 cured at 250°C and NRVB cured at 200 °C) compared to the deionised water solutions when other minerals and cements were tested it can be assumed that portlandite would not have reduced the concentration of caesium in solution and this would be 100% remaining.

**Katoite was not tested as a single phase mineral. This was due to it not appearing in cements cured below 250°C.

6.2.3 Phase 2: Tests to determine the capability of the minerals to reduce the quantity of cerium in solution

The initial results found in phase 1 showed that some of the minerals were able to reduce the concentration of some of the radionuclide analogues. Not all minerals were effective across the different solutions. The ICP-OES results showed that the sorption capacity of iodine and strontium were reached in all of the tests, across all minerals and solutions. The ICP-MS showed that the sorption capacity of cerium was also reached in all minerals.

Most minerals were able to buffer the pH, allowing for precipitation of all or most of the cerium, this suggests the minerals could buffer the pH further and precipitate higher concentrations of cerium out of solution. Therefore, further tests were required to find the total amount of radionuclide that can be precipitated by the minerals from solution.

6.2.3.1 Method

The same procedure was followed with these solutions; 10 ml of solution was added to 50mg of mineral and agitated for 8 days. The minerals were only tested in deionised water as previous tests did not show a significant difference in high salinity or high pH solution compared to the samples tested in deionised water. The centrifuge tubes were shaken for 8 days before sampling.

6.2.3.2 Results

Cerium

The results are shown in Table 71 below.

Table 71: The concentration of cerium remaining in solution after being shaken with the individual minerals for 8 days.

Initial Radionuclide concentration (mol/dm^3)		**0.241276**	**0.113506**	**0.071693**	**0.014688**	**0.006985**
Concentration after mixing with mineral (mol/dm^3)	Calcite	0.232807	0.1212	0.061825	0.005003	0.000141
	Xonotlite	0.248366	0.124054	0.070551	0.011318	0.004772
	Reinhardbraunsite	0.20031	0.094845	0.032506	0.000251	0.000163
	Jaffeite	0.234425	0.09603	0.040257	0.00012	0.000118
	α-C2SH	0.223053	0.09702	0.036013	0.000464	0.00017

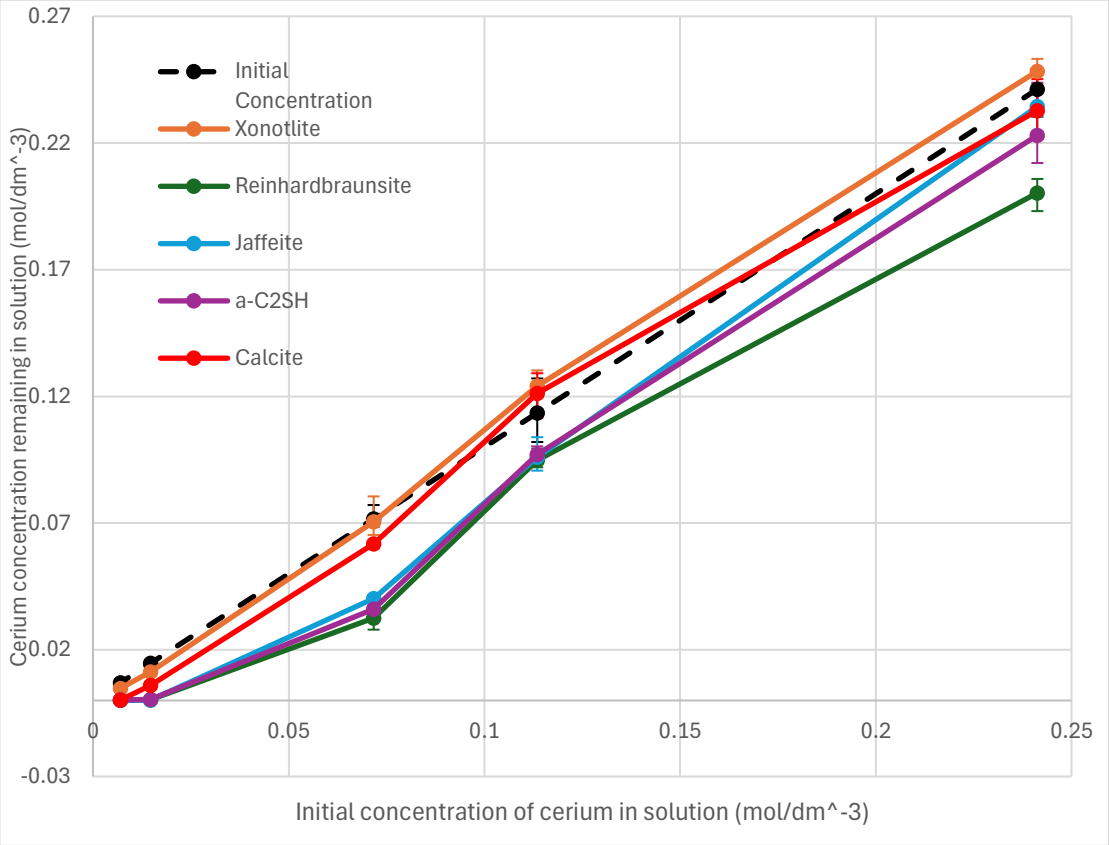


Figure 74: Measured cerium concentration plotted against the initial cerium concentration for each mineral studied. The black dotted line is the initial concentration, so the closer to the black dotted line less cerium has been removed from solution by the mineral. Orange is xonotlite, navy is reinhardbraunsite, blue is jaffeite, purple is α-C_2SH, and red is calcite.

The results are shown in Figure 74 which shows the plotted measured cerium concentration against the initial cerium concentration for each mineral. The black dashed line represents the concentration if no cerium was removed from solution, so the closer to the black dashed line the less cerium has been precipitated from solution. When the concentration of cerium in solution was above 0.0114 moldm^{-3} all minerals were not able to reduce the concentration of the cerium in solution to 0. At the concentration of 0.0114 moldm^{-3} Xonotlite reduced the concentration the least, calcite reduced the concentration the second least. Jaffeite, reinhardbraunsite and α-C_2SH were able to reduce the concentration of cerium in solution to 0. These three minerals were able to reduce the concentration of cerium in solution at higher concentrations. At the highest concentration of cerium in solution (0.228moldm^{-3}) reinhardbraunsite was able to reduce the concentration of cerium the most.

Calcium

The results are shown in Table 72 below.

Table 72: The concentration of calcium in each solution after the different concentrations of cerium is mixed with the individual mineral for 8 days.

Initial Radionuclide concentration (mol/dm^3)		**0.241276**	**0.113506**	**0.071693**	**0.014688**	**0.006985**
Mineral	Calcite	0.001269	0.003448	-6E-05	0.00532	0.002683
	Xonotlite	0.000546	4.66E-05	-0.00157	-0.00306	-0.00293
	Reinhardbraunsite	0.031118	0.040346	0.037445	0.016797	0.007653
	Jaffeite	0.027842	0.02724	0.027405	0.014949	0.008051
	α-C2SH	0.023471	0.020693	0.032365	0.012148	0.005887

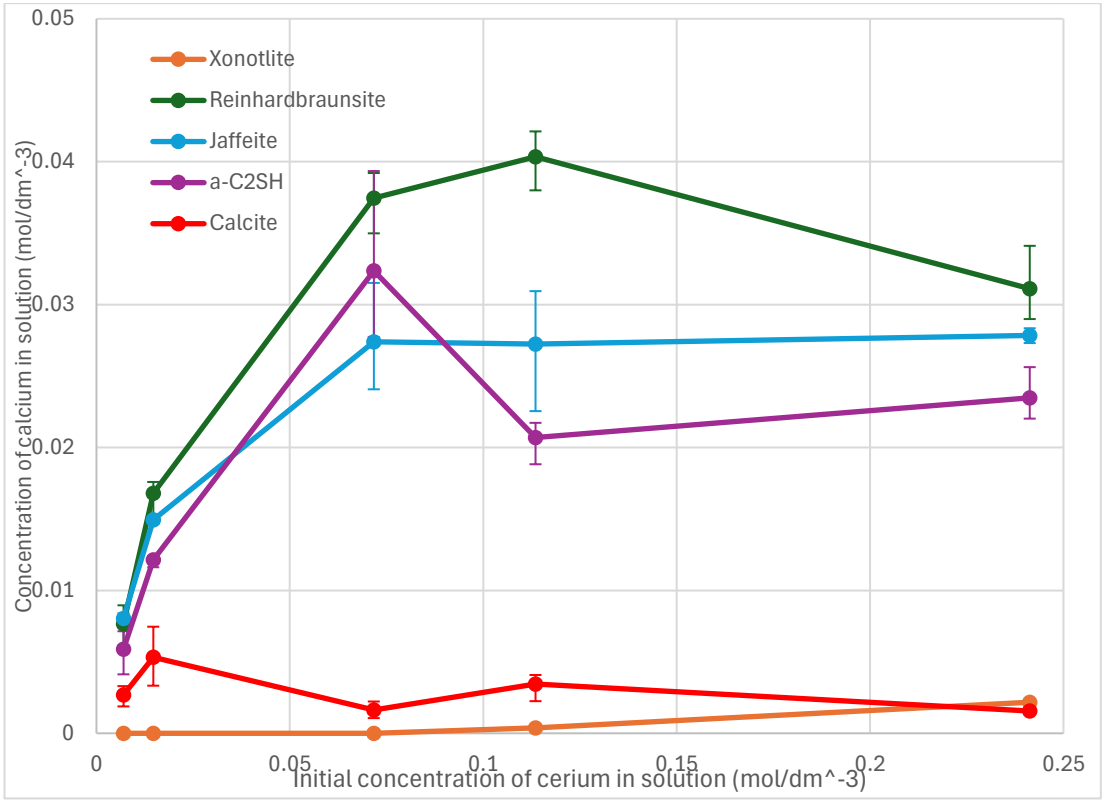


Figure 75: Measured cerium concentration plotted against the initial cerium concentration for each mineral studied. The black dotted line is the initial concentration. Orange is xonotlite, navy is reinhardbraunsite, blue is jaffeite, purple is α-C_2SH, and red is calcite.

The graph in Figure 75 above shows the amount of calcium in solution against the initial amount of cerium in solution. These tests were carried out in deionised water so any calcium should have come from the mineral.

Calcite and xonotlite both released the least calcium into solution. Reinhardbraunsite released the most calcium, and was the most effective at reducing the concentration of cerium in solution. This suggests there is a trend that minerals that can release more calcium are better at reducing the concentration of cerium in solution, and implies the mechanism where calcium is dissolved/released from the mineral is linked to the way cerium is removed from solution. This effect could be caused by the release of calcium into solution raising the pH and reducing the solubility of cerium.

Reinhardbraunsite is the most effective high temperature mineral at buffering the pH. The mechanism to buffer the pH is by the release of calcium ions into solution, causing the pH to rise and the precipitation of cerium hydroxide. The presence of reinhardbraunsite could therefore provide radionuclide retardation in a higher

temperature GDF and provides some of the safety functions of the GDF backfill, where the pH needs to be alkaline to reduce the solubility of radionuclides.

6.2.4 Phase 3 Sorption rate tests

The results in phase 1 showed that the minerals reacted in the solutions to reduce the concentration of the various radionuclides by different amounts. Most mineral solutions reduced the concentration of cerium by all or almost all of its original concentration. All of the mineral solutions also showed a reduction in the concentration of strontium. The ICP-MS results for caesium had not been received yet so the effect of the minerals on the caesium concentration was unknown. Therefore, all three radionuclides were chosen to look at the rate they are removed from solution when mixed with the different minerals. Knowing the rate at which the minerals are able to react in solution and cause a decrease in the concentration of radionuclide is useful in understanding how these minerals can contribute to the safety function of the backfill. For example, if there is a crack in the container of the nuclear waste that will allow a release of radionuclides into the backfill, knowing how quickly the minerals are able to trap radionuclides will help to inform the final containment design. If the reaction is quick then a lower volume of backfill is required to stop the radionuclides, this would mean there would be more space for storing waste in the GDF and would have cost savings. However, if the reaction is slow then a greater volume of backfill is needed to ensure the radionuclides are trapped.

6.2.4.1 Method

The method set out in part 1 was followed. 50mg of mineral was placed in an individual centrifuge tube. 10ml of 0.0114 mol dm^{-3} of each radionuclide analogue was added to the tube. Enough tubes were prepared so there were three repeats for each timepoint. The centrifuge tubes were then placed into an orbital shaker. At 2 hours, 24 hours, 48 hours, 96 hours, 192 hours three samples were removed, centrifuged, then filtered where necessary to remove the mineral from the solution. The solutions were then diluted with nitric acid and the concentrations measured with ICP-OES or ICP-MS depending on the radionuclide analogue that was being measured.

6.2.4.2 Results

6.2.4.2.1 ICP-MS and ICP-OES

Calcite

Table 73 below shows the results of the rate tests testing how quickly the addition of calcite reduces the concentration of radionuclides (Ce, Cs, Sr) in solution.

Table 73: The results of the rate tests testing how quickly the addition of calcite reduces the concentration of radionuclides (Ce, Cs, Sr) in solution.

Test	**Time (hours)**					
Control	**0**	**2**	**24**	**48**	**96**	**192**
Ca concentration ($moldm^{-3}$)	0	0	0	0	0	0
Caesium	**0**	**2**	**24**	**48**	**96**	**192**
Ca concentration ($moldm^{-3}$)	0	0	0	0	0	0
Cs concentration ($moldm^{-3}$)	0.011918	0.011349	0.010657	0.01148	0.012212	0.011777
Cerium	**0**	**2**	**24**	**48**	**96**	**192**
Ca concentration ($moldm^{-3}$)	0	0	0	0.002577	0.002019	0
Ce concentration ($moldm^{-3}$)	0.010537	0.014574	0.012609	0.012654	0.010648	0.001426
Strontium	**0**	**2**	**24**	**48**	**96**	**192**
Ca concentration ($moldm^{-3}$)	0	0.001057	0.002849	0.004959	0.006062	0.01181
Sr concentration ($moldm^{-3}$)	0.008147	0.00735	0.005306	0.004125	0.003555	2.66E-06

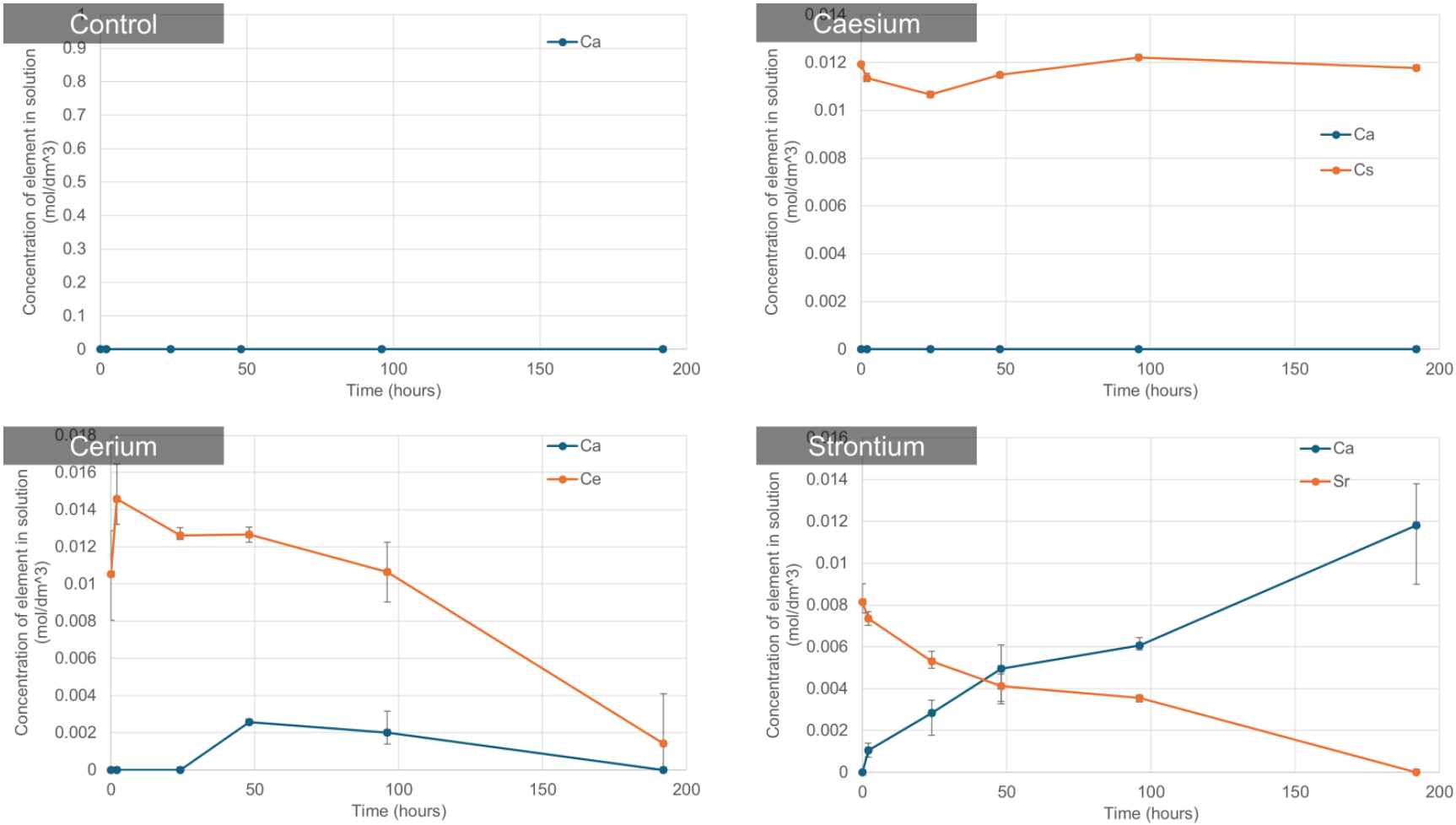


Figure 76: Graphs to show how the concentration of the radionuclide analogues changed concentration over the 8 day tests with calcite. The radionuclide analogues are orange and the concentration of calcium in solution is blue. The top left is the control, top right is caesium, bottom left is cerium and bottom right is strontium.

As can be seen in Figure 76 The control that contained just calcite showed the concentration of calcium in solution remained at zero. In the tests with calcite the concentration of caesium in solution over the 8 days was not reduced and remained essentially constant, the concentration of calcium in solution also remained at 0.

The concentration of cerium steadily decreases over the 8 days, with a sharper decrease between four and eight days than the first four days. The concentration of calcium remains at zero until 24 hours before it rises then slowly decreases again. The amount of calcium and strontium in solution is mirrored almost exactly. As the amount of strontium in solution decreases the amount of calcium increases. This suggests strontium is being substituted into calcium sites within the calcite which is causing a release of calcium into the solution. In the tests described in section 6.2.2 calcite is shown to reduce the concentration of strontium to approximately 0.003 mol/dm^{-3}, this is a very similar value to the concentration reached after 96 hours in the tests in this section. Both sets of experiments were repeated in triplicate, however in section 6.2.2 the same test tube was used for all time points, with 0.1ml of solution being removed before the tube was placed back on the shaker. This would have removed dissolved calcium from solution, and changed the solid to liquid volume ratio therefore it can be assumed that the results shown in Figure 76 are more accurate. Figure 76 also shows that after 96 hours the amount of calcium in solution continues to increase at approximately a 1:1 ratio with the amount of strontium decreasing, this further suggests that calcite is able to remove all strontium from solution.

Xonotlite

Table 74 below shows the results of the rate tests testing how quickly xonotlite was able to reduce the concentration of radionuclides in solution.

Table 74: The results of the rate tests testing how quickly the addition of xonotlite reduces the concentration of radionuclides (Ce, Cs, Sr) in solution.

Test	**Time (hours)**					
Control	**0**	**2**	**24**	**48**	**96**	**192**
Ca concentration ($moldm^{-3}$)	0	0	0	0	0	0
Caesium	**0**	**2**	**24**	**48**	**96**	**192**
Ca concentration ($moldm^{-3}$)	0	0	0	0	0	0
Cs concentration ($moldm^{-3}$)	0.011918	0.011316	0.01116	0.011486	0.012024	0.011673
Cerium	**0**	**2**	**24**	**48**	**96**	**192**
Ca concentration ($moldm^{-3}$)	0	0	0.000522	8.32E-05	0.001041	0.002119
Ce concentration ($moldm^{-3}$)	0.010537	0.013781	0.013491	0.011935	0.010936	0.009913
Strontium	**0**	**2**	**24**	**48**	**96**	**192**
Ca concentration ($moldm^{-3}$)	0	0	0	0	0	0
Sr concentration ($moldm^{-3}$)	0.008147	0.011659	0.011081	0.010368	0.010897	0.008929

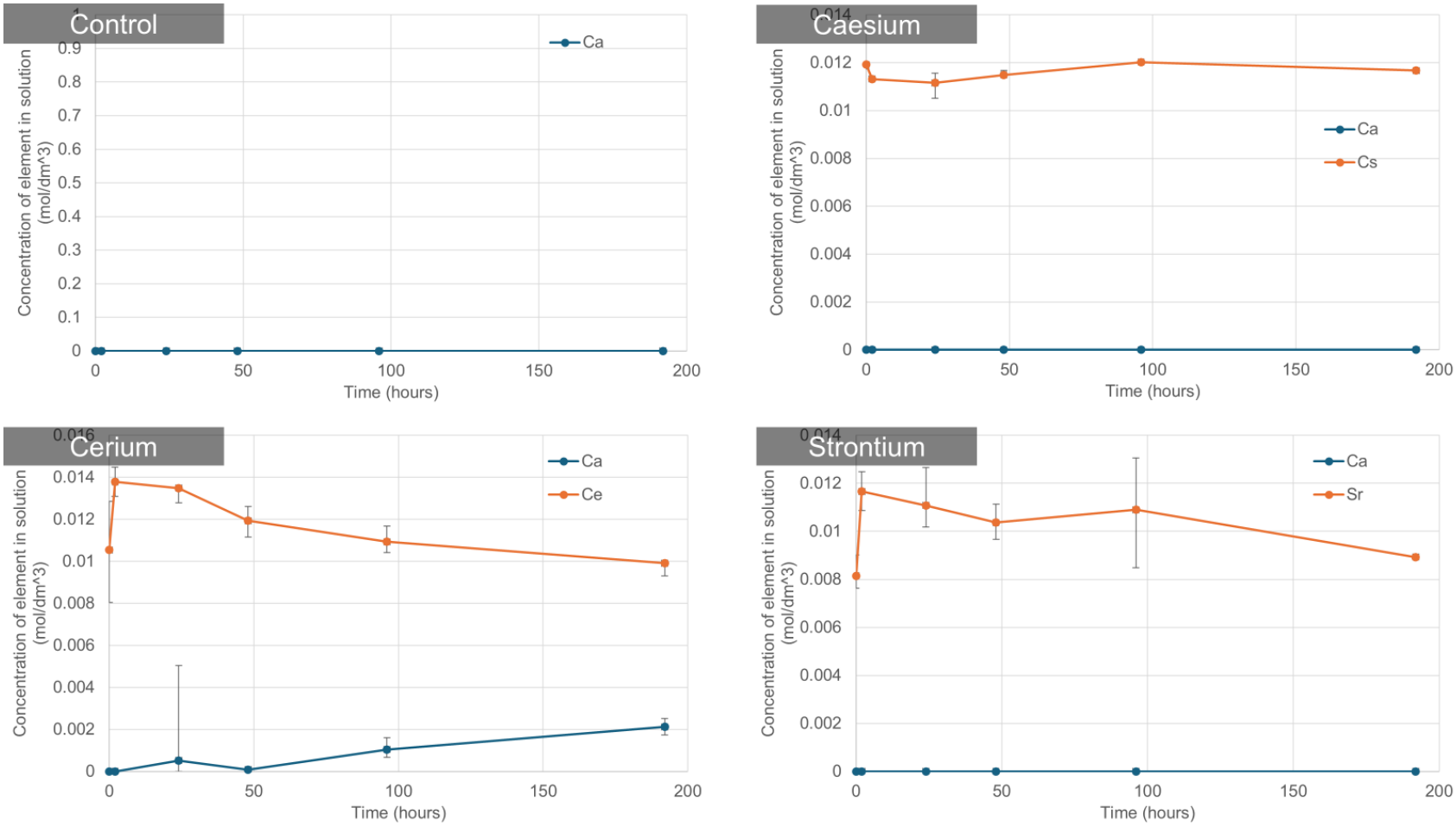


Figure 77: Graphs to show how the concentration of the radionuclide analogues changed concentration over the 8 day tests with xonotlite. The radionuclide analogues are orange and the concentration of calcium in solution is blue. The top left is the control, top right is caesium, bottom left is cerium and bottom right is strontium.

The control sample showed the concentration of calcium in solution remained at zero as is shown in Figure 77. The tests using xonotlite as the mineral showed no reduction in the concentration of caesium in solution. The concentration of calcite also remained at zero. When xonotlite was tested in the cerium solution the concentration of cerium was reduced over the 8 days, the concentration of calcium in solution increased over the experiment. In the control the concentration of calcium in solution remained at zero, the increase of calcium in solution when the xonotlite is mixed with a cerium solution suggests the cerium is causing the calcium to dissolve from the xonotlite. When the mineral xonotlite was tested with the strontium solution the concentration of strontium was slightly reduced over the 8 days. The concentration of strontium in solution remained fairly constant until the fourth day when it decreased to day 8. The concentration of calcium in solution remained at zero through the test.

α-C_2SH

Table 75 below shows the results of the rate tests testing how quickly α-C_2SH was able to reduce the concentration of radionuclides in solution.

Table 75: The results of the rate tests testing how quickly the addition of α-C_2SH reduces the concentration of radionuclides (Ce, Cs, Sr) in solution.

Test	**Time (hours)**					
Control	**0**	**2**	**24**	**48**	**96**	**192**
Ca concentration ($moldm^{-3}$)	0	0.002256	0.003078	0.003885	0.005508	0.002939
Caesium	**0**	**2**	**24**	**48**	**96**	**192**
Ca concentration ($moldm^{-3}$)	0	0.000853	0.004765	0.003314	0.006216	0.003138
Cs concentration ($moldm^{-3}$)	0.011918	0.011432	0.011568	0.011536	0.012257	0.011817
Cerium	**0**	**2**	**24**	**48**	**96**	**192**
Ca concentration ($moldm^{-3}$)	0	0.014106	0.013707	0.015622	0.017844	0.01334
Ce concentration ($moldm^{-3}$)	0.010537	7.26E-05	0.000644	1.57E-05	1.14E-05	0.000107
Strontium	**0**	**2**	**24**	**48**	**96**	**192**
Ca concentration ($moldm^{-3}$)	0	0.001863	0.003601	0.004515	0.006843	0.004752
Sr concentration ($moldm^{-3}$)	0.008147	0.011658	0.010218	0.009903	0.011133	0.008554

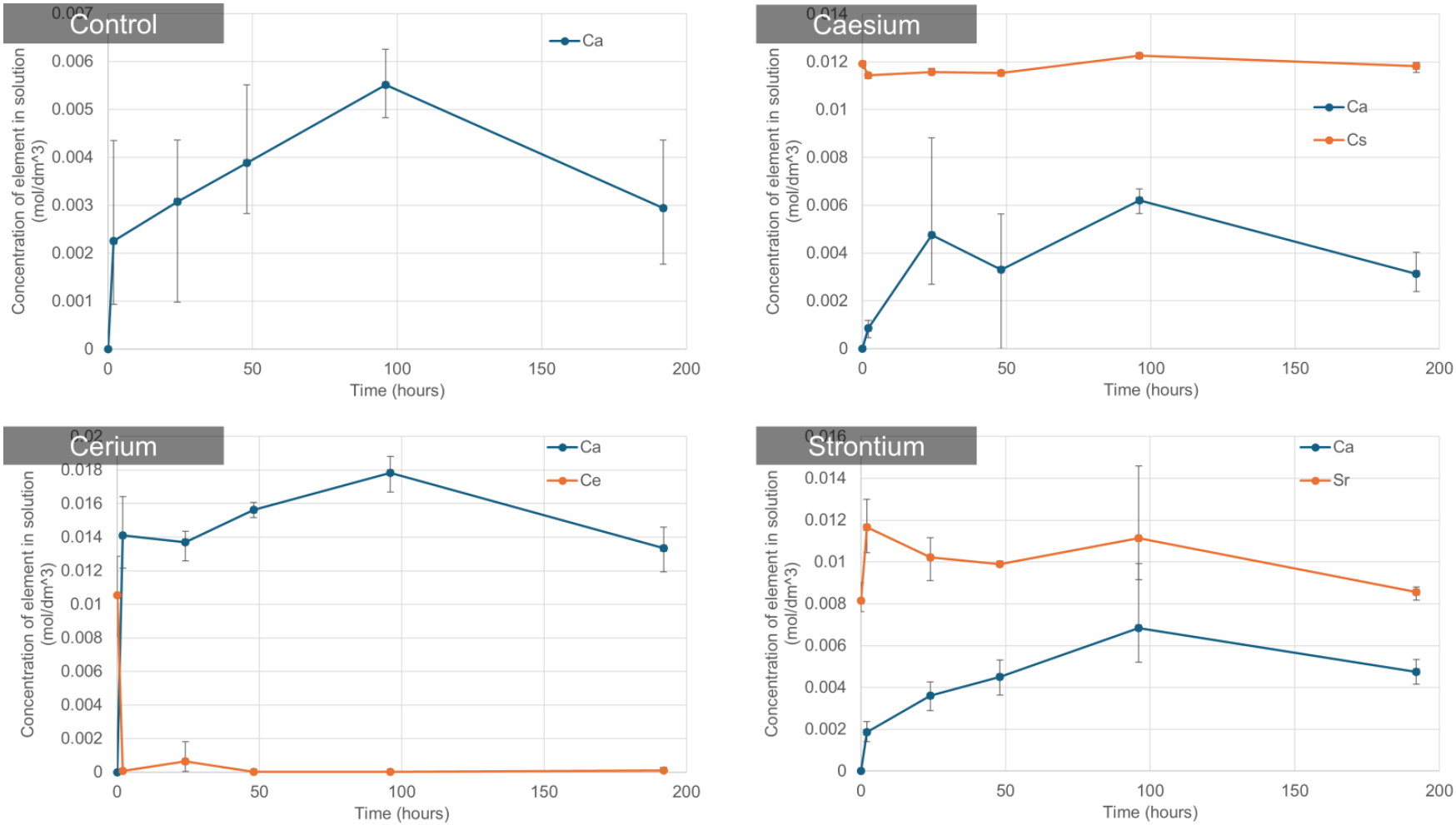


Figure 78: Graphs to show how the concentration of the radionuclide analogues changed concentration over the 8 day tests with α-C_2SH. The radionuclide analogues are orange and the concentration of calcium in solution is blue. The top left is the control, top right is caesium, bottom left is cerium and bottom right is strontium.

The graphs in Figure 78 show the sample of α-C_2SH mixed with deionised released calcium steadily until day four, it then decreased between day four and eight. This shows with no radionuclides calcium is released. The concentration of caesium remained constant in the tests with the mineral α-C_2SH. The amount of calcium appears to increase to day four before decreasing to day eight, similarly to the control test performed in deionised water. The concentration of calcium in the cerium solution increased to day four before decreasing to day eight, as the other tests in deionised water and caesium solution did. The concentration of cerium in solution dropped to approximately zero in just two hours, at 24 hours the average was slightly higher than zero however zero is within the error bars. The α-C_2SH mineral mixed with a strontium solution followed the same trend as the other solutions and deionised water where the concentration of calcium in solution increased to day four before decreasing to day eight. The concentration of strontium in solution decreased slowly, before a slight increase at day four and then a decrease to day eight.

Reinhardbraunsite

Table 76 below shows the results of the rate tests testing how quickly reinhardbraunsite was able to reduce the concentration of radionuclides in solution.

Table 76: The results of the rate tests testing how quickly the addition of reinhardbraunsite reduces the concentration of radionuclides (Ce, Cs, Sr) in solution.

Test	**Time (hours)**					
Control	**0**	**2**	**24**	**48**	**96**	**192**
Ca concentration ($moldm^{-3}$)	0	0.000269	0.002202	0.003016	0.005294	0.004053
Caesium	**0**	**2**	**24**	**48**	**96**	**192**
Ca concentration ($moldm^{-3}$)	0	0.000213	0.002147	0.003678	0.004711	0.003732
Cs concentration ($moldm^{-3}$)	0.011918	0.011369	0.011389	0.01168	0.011507	0.011742
Cerium	**0**	**2**	**24**	**48**	**96**	**192**
Ca concentration ($moldm^{-3}$)	0	0.016719	0.01787	0.019495	0.020956	0.017588
Ce concentration ($moldm^{-3}$)	0.010537	6.47E-05	3.62E-05	7.14E-06	0	9.97E-05
Strontium	**0**	**2**	**24**	**48**	**96**	**192**
Ca concentration ($moldm^{-3}$)	0	0.000178	0.001657	0.003901	0.003623	0.004203
Sr concentration ($moldm^{-3}$)	0.008147	0.011138	0.010619	0.010978	0.00961	0.009219

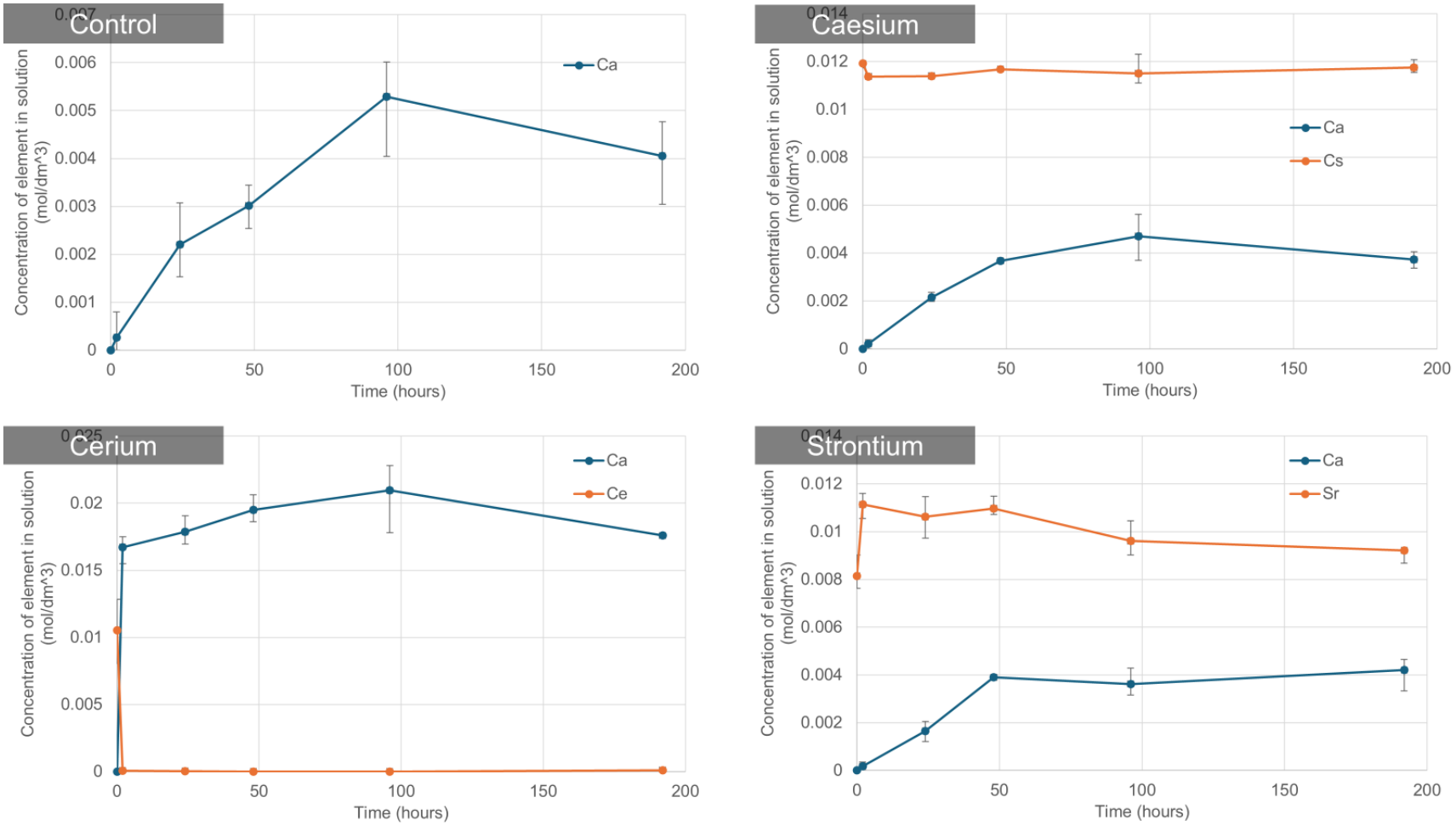


Figure 79: Graphs to show how the concentration of the radionuclide analogues changed concentration over the 8 day tests with reinhardbraunsite. The radionuclide analogues are orange and the concentration of calcium in solution is blue. The top left is the control, top right is caesium, bottom left is cerium and bottom right is strontium.

The concentration of calcium in solution in the sample of reinhardbraunsite mixed with deionised water increased to day four before decreasing slightly to day eight as shown in Figure 79. The rate tests using reinhardbraunsite as the mineral in the caesium solution showed no decrease of caesium. The reinhardbraunsite behaved similarly to how it behaved in deionised water where calcium was released into the solution until day four before the concentration of calcium in solution decreased slightly to day eight. The tests using reinhardbraunsite in a cerium solution showed the concentration of calcium following a similar trend to previous tests where the concentration increases to day four then decreases slightly. The concentration of cerium in solution was reduced to zero by two hours and remained at zero. The concentration of strontium in solution decreased slowly over the eight days. The concentration of calcium increased until day two before remaining fairly constant for the remaining six days of the experiment.

Jaffeite

Table 77 below shows the results of the rate tests testing how quickly jaffeite was able to reduce the concentration of radionuclides in solution.

Table 77: The results of the rate tests testing how quickly the addition of jaffeite reduces the concentration of radionuclides (Ce, Cs, Sr) in solution.

Test	**Time (hours)**					
Control	**0**	**2**	**24**	**48**	**96**	**192**
Ca concentration ($moldm^{-3}$)	0	0.004885	0.002872	0.005891	0.008087563	0.005661
Caesium	**0**	**2**	**24**	**48**	**96**	**192**
Ca concentration ($moldm^{-3}$)	0	0.004003	0.004446	0.005816	0.006804232	0.005954
Cs concentration ($moldm^{-3}$)	0.011918	0.011376	0.011554	0.011579	0.011321669	0.011974
Cerium	**0**	**2**	**24**	**48**	**96**	**192**
Ca concentration ($moldm^{-3}$)	0	0.014177	0.013485	0.01718	0.018778382	0
Ce concentration ($moldm^{-3}$)	0.010537	4.97E-05	0.000186	4.28E-06	2.81909E-05	8.71E-05
Strontium	**0**	**2**	**24**	**48**	**96**	**192**
Ca concentration ($moldm^{-3}$)	0	0.004661	0.004271	0.005493	0.005704709	0.005308
Sr concentration ($moldm^{-3}$)	0.008147	0.012079	0.010818	0.009942	0.010087499	0.009063

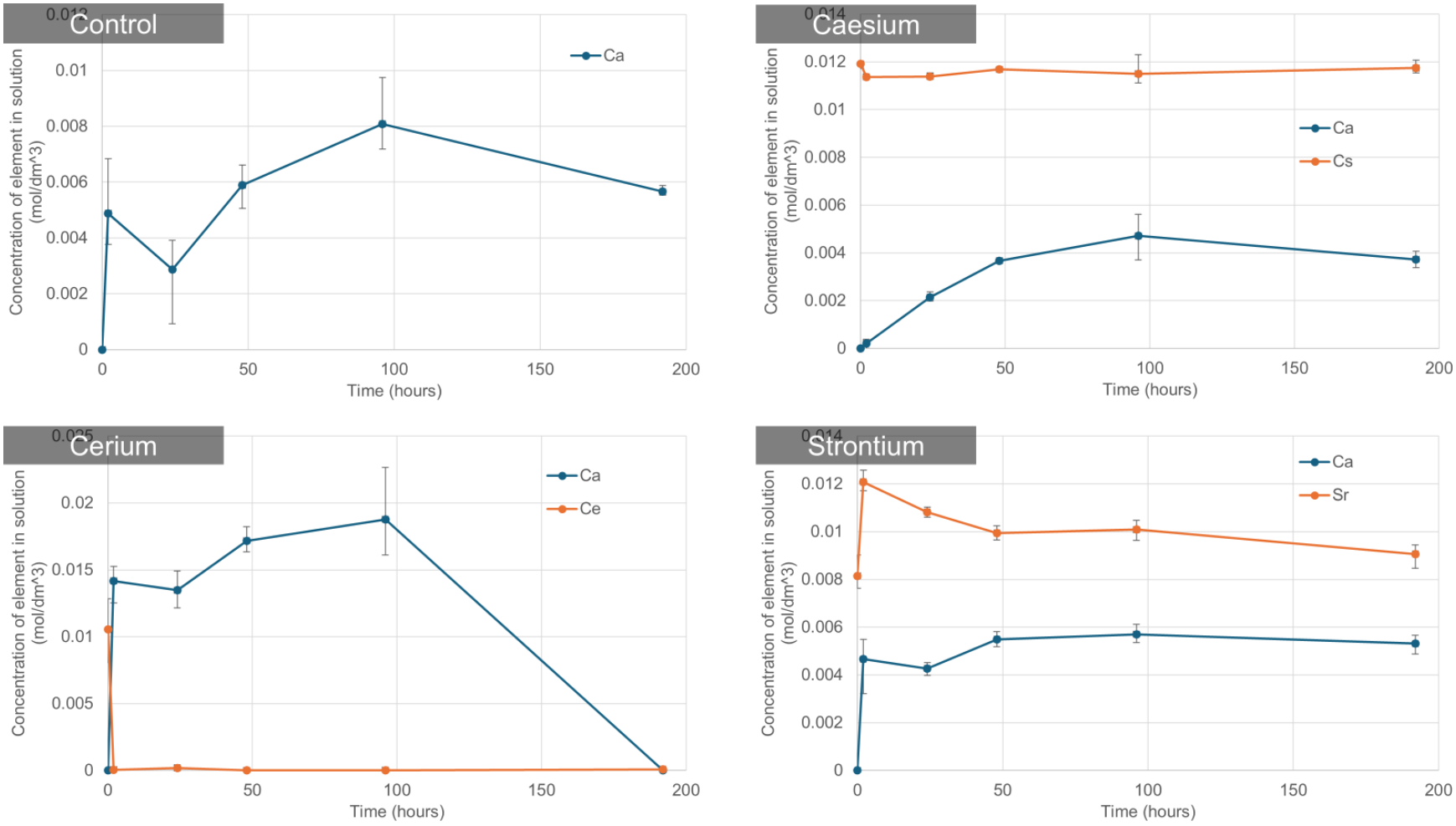


Figure 80: Graphs to show how the concentration of the radionuclide analogues changed concentration over the 8 day tests with jaffeite. The radionuclide analogues are orange and the concentration of calcium in solution is blue. The top left is the control, top right is caesium, bottom left is cerium and bottom right is strontium.

In the tests where jaffeite was mixed with deionised water the concentration of calcium in solution increased as shown in Figure 80. In the tests where jaffeite was mixed with caesium solution the concentration of caesium remained constant over the eight days. The concentration of calcium in solution was increased.

The concentration of cerium mixed with jaffeite was reduced to zero in two hours and remained at zero for the experiment. The concentration of calcium in solution rose rapidly in the first two hours, before continuing to rise slowly until day four then decreasing to zero in day eight.

Jaffeite mixed in the strontium solution rapidly released calcium into the solution in the first two hours, the concentration of calcite then remained fairly constant for the rest of the experiment. The concentration of strontium in solution slightly decreased over the eight days.

6.2.4.2.2 pH results

Once the rate tests were complete the samples were centrifuged and the solution was collected and removed from the mineral. This solution was sampled for ICP-OES or ICP-MS and the pH of the remaining solution was measured. The results are shown in Table 78. The measurement at time=0 is the pH of the stock solution before mineral was added. Before measurement the pH probe calibration was checked against three stock solutions to ensure for an accurate reading. The measurement for calcite at 24 hours with cerium is missing due to nitric acid being added to the sample accidentally.

As each timepoint was tested in a separate tube, so no samples were taken until the test was over, the volume remained constant so the only variable in this test was the time the sample was shaken with the radionuclide analogue solution.

Table 78: The pH measurement results of the different mineral tests in deionised water with caesium, cerium, and strontium.

Mineral	Solution	Radionuclide	0	2	24	48	96	192
Calcite	Deionised water	Control	7.469	8.79	8.93	9.781	9.09	9.279
Xonotlite	Deionised water	Control	7.469	10.086	10.055	10.19	10.243	10.171
α-C_2SH	Deionised water	Control	7.469	12.016	12.164	12.101	12.32	12.089
Reinhardbraunsite	Deionised water	Control	7.469	11.895	12.017	12.09	12.263	12.183
Jaffeite	Deionised water	Control	7.469	12.288	12.242	12.231	12.378	12.255
Calcite	Deionised water	Caesium	6.04	9.905	7.403	9.795	9.346	9.738
Xonotlite	Deionised water	Caesium	6.04	10.126	7.17	10.213	10.192	10.248
α-C_2SH	Deionised water	Caesium	6.04	12.03	6.907	12.143	12.335	12.085
Reinhardbraunsite	Deionised water	Caesium	6.04	11.983	7.305	12.122	12.292	12.182
Jaffeite	Deionised water	Caesium	6.04	12.295	11.829	12.245	12.376	12.253
Calcite	Deionised water	Cerium	4.7	7.945		7.072	7.566	6.188
Xonotlite	Deionised water	Cerium	4.7	7.502	8.126	7.072	7.337	6.385
α-C_2SH	Deionised water	Cerium	4.7	9.658	12.206	11.277	11.494	11.082
Reinhardbraunsite	Deionised water	Cerium	4.7	11.756	12.073	11.881	12.005	11.893
Jaffeite	Deionised water	Cerium	4.7	10.118	12.182	11.732	11.932	11.768
Calcite	Deionised water	Strontium	5.599	8.885	8.565	8.753	8.785	9.153
Xonotlite	Deionised water	Strontium	5.599	9.985	8.397	9.879	9.769	9.942
α-C_2SH	Deionised water	Strontium	5.599	8.637	10.104	12.071	12.315	12.148
Reinhardbraunsite	Deionised water	Strontium	5.599	8.524	12.025	12.039	12.243	12.161
Jaffeite	Deionised water	Strontium	5.599	12.288	11.994	12.218	12.354	12.248

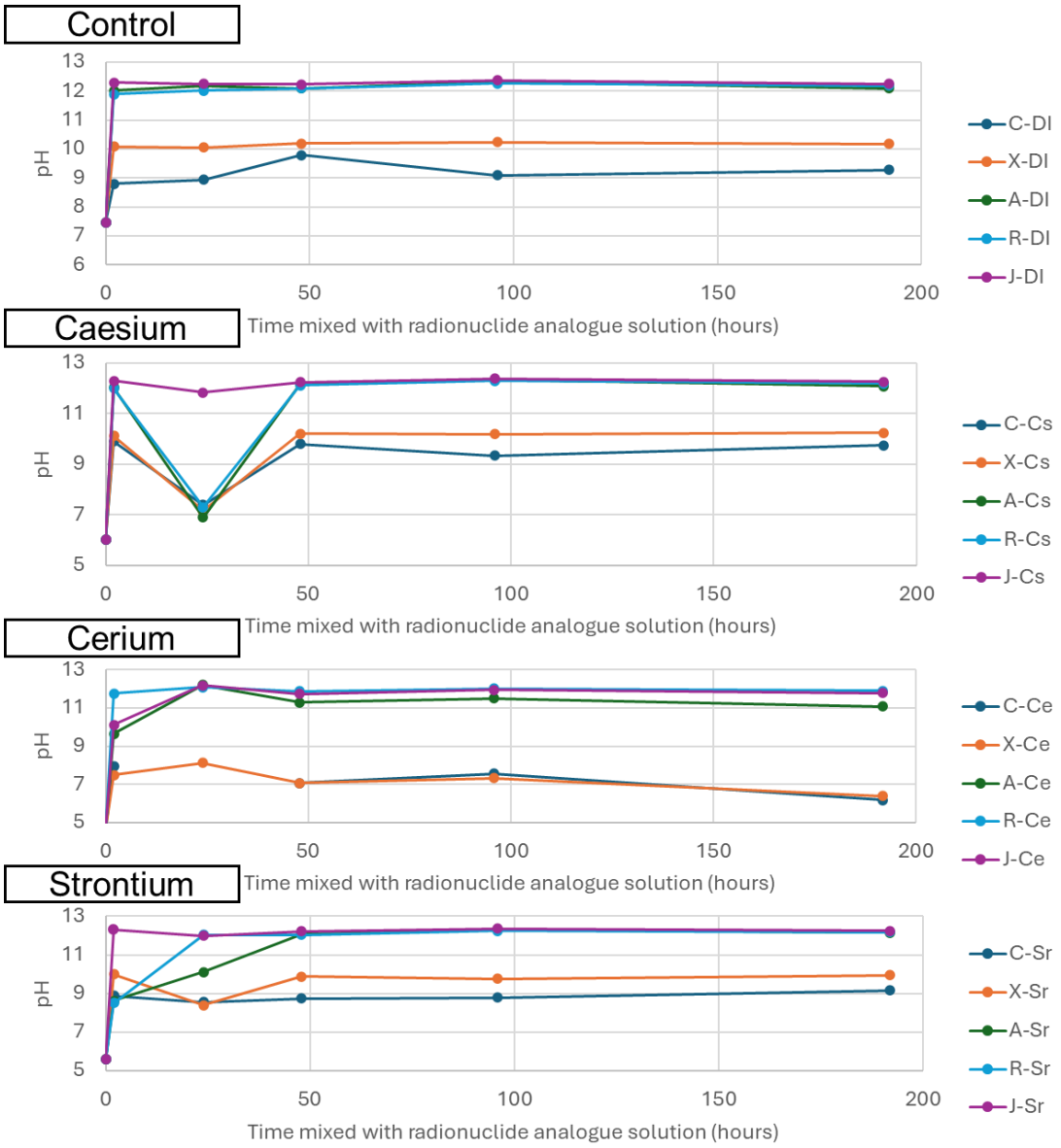


Figure 81: The results from measuring the pH of the solutions over the 8 day rate experiments. The top graph is the control sample, the second from top graph is the caesium solution, the third from top is the cerium solution, and the bottom graph is the strontium solution. The navy line is calcite, the orange line is xonotlite, the green line is α-C_2SH, the blue line is reinhardbraunsite, and the purple line is jaffeite.

As shown in Figure 81 all of the minerals raised the pH of the control sample, which was plain Millipore Deionised water. Xonotlite and calcite raised the pH the least, likely due to those samples containing either no or very little portlandite. After the minerals were added the pH of all samples rose and remained reasonably constant regardless of duration.

The results in the caesium solution were similar to the values in the control test. The ICP-MS results showed no significant reduction in the concentration of caesium so it is reasonable that the addition of caesium has similar results to the control. All minerals showed a drop in pH at 24 hours, where all but Jaffeite returned to a neutral pH. This test was repeated and gave the same result. The pH machine was calibrated against three buffer solutions before each reading, so it is not likely these drops in pH are error.

Xonotlite and calcite had a lower pH in the cerium tests than they did with other radionuclide analogues. Their pH was also lower than in the control tests. This suggests the cerium is lowering the pH and xonotlite and calcite have less buffering ability. They both have one calcium per molecule and show less calcium readily dissolves into solution this is likely the cause. The pH of the solutions with strontium were similar to the control tests. Reinhardbraunsite and α-C_2SH did not reach their final pH until 24 and 48 hours respectively, whilst in the control tests they both had within 2 hours. This suggests the strontium is interacting with the calcium or the minerals to delay the amount of calcium that can be dissolved into the solution.

6.3 Radionuclide sorption tests XRD

6.3.1 Introduction

After the phase 1 tests were complete, the samples were centrifuged. The solution was removed and collected for ICP-MS and ICP-OES to test how much of the radionuclide analogue was present in solution, and how much calcium and silicon had dissolved from the minerals into the solution. The remaining powder was dried under N_2 at room temperature until a constant mass was achieved. The mineral sample was then scanned using powder XRD . Due to the small volume of recoverable sample (50mg of sample was used for the tests), smaller volume zero background holders were used to accommodate the small sample volumes . A sample of the initial mineral was also scanned to observe any changes in the mineral crystalline structure. P-XRD results are presented below in Figure 82, Figure 83, Figure 84, Figure 85, and Figure 86. It is worth noting that XRD only detects crystalline phases, and that it is not reliable to identify minerals/ complexes present at a concentration less than 1% of the mass.

6.3.2 Calcite

The XRD patterns are shown below in Figure 82 and the minerals in each sample are shown in Table 79.

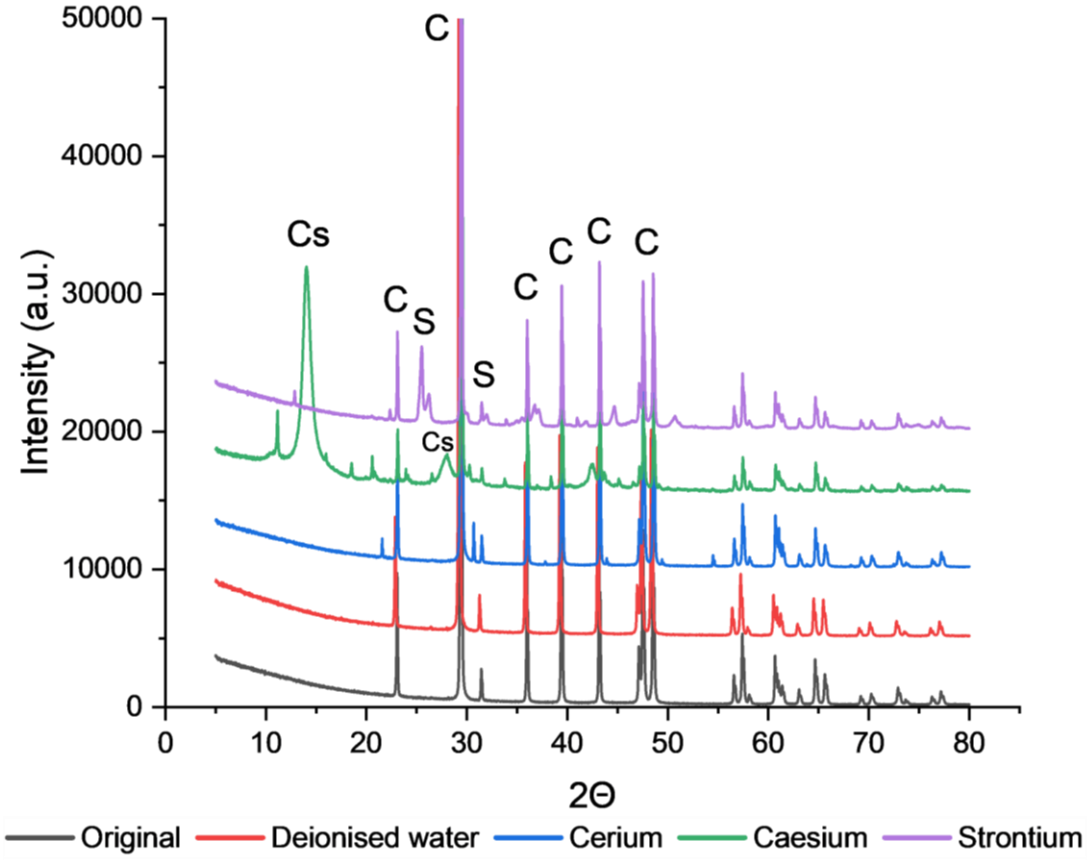


Figure 82: The XRD patterns of calcite (black) after being mixed with deionised water (red), cerium (blue), caesium (green) and strontium (purple) for 8 days. C = calcite, S = strontianite, Cs = caesium carbonate.

Table 79: The calcite samples, the minerals they contain and the COD ID used to identify the minerals.

Sample	Minerals [COD ID]	Reference
Original	Calcite [9000095]	191
Deionised water	Calcite [9000095]	191
Cerium	Calcite [9000095]	191
Caesium	Calcite [9000095] Caesium carbonate	191 258,259
Strontium	Calcite [9000095] Strontianite [5000093]	191 260

The sample of calcite in deionised water showed no changes in mineral formulation. This scan of the calcite sample mixed with the cerium solution also showed no changes.

The XRD pattern (Figure 82) for the calcite sample mixed with Caesium showed the presence of a new substance. There are several additional new peaks, and some wide 'humps' present in the calcite after it was exposed to caesium. There is a wide hump present at approximately 13 2Θ[258]. A broad hump in an XRD pattern indicates a poorly crystalline or an amorphous phase. It is possible these peaks are caused by the formation of caesium carbonate, of which the most significant peak is at approximately 14 2Θ. The peaks associated with caesium carbonate are broad, this can indicate reduction in crystallite size and/or an increase in lattice strain or structural disorder[259].

The XRD scan of the calcite sample mixed with strontium showed the formation of strontianite. Strontianite ($SrCO_3$) [261–263]. Previous studies found that mixing either a 1M or 0.5M Sr solution with a single calcite crystal induced the of strontianite after 3 days at 0.5M Sr and room temperature and just 1 day for the 1M solution[264]. This method differs in how this sample was treated, as it was mixed with 0.0114M SrCl at room temperature for 8 days. The formation of strontianite seems reasonable at this lower temperature as the mixing time is increased, this is in agreement with literature [264].

6.3.3 Xonotlite

The XRD patterns are shown below in Figure 83 and the minerals in each sample are shown in Table 80.

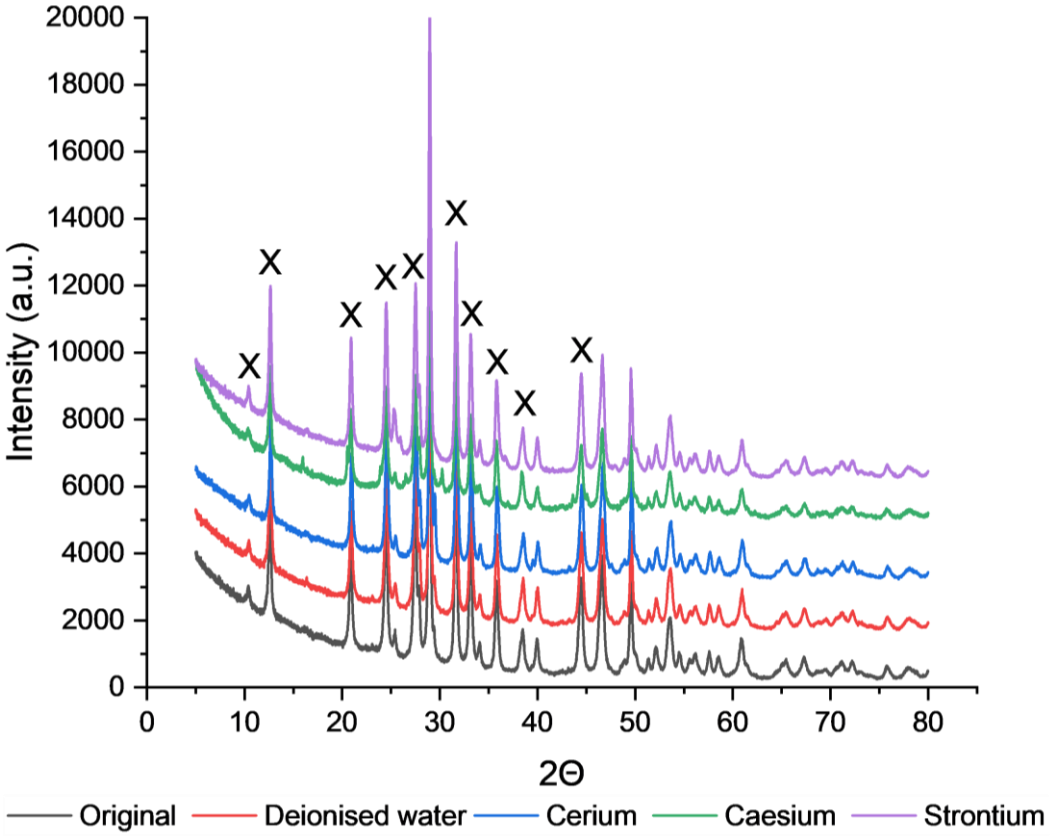


Figure 83: The XRD patterns of xonotlite (black) after being mixed with deionised water (red), cerium (blue), caesium (green) and strontium (purple) for 8 days. X = xonotlite, C = calcite.

Table 80: The xonotlite samples, the minerals they contain and the COD ID used to identify the minerals.

Sample	Minerals [COD ID]	Reference
Original	Xonotlite [9008437]	190
Deionised water	Xonotlite [9008437]	190
Cerium	Xonotlite [9008437]	190
Caesium	Xonotlite [9008437]	190
Strontium	Xonotlite [9008437] Strontianite [9008198]	190 265

The XRD pattern (of the xonotlite synthesised in the lab showed pure xonotlite was formed. The xonotlite sample mixed with Millipore deionised water for 8 days was unchanged, and the XRD was exactly the same as the original xonotlite sample. This

shows the xonotlite is stable in just pure deionised water, so any alternations to the mineral are due to the presence of the radionuclide analogue.

The xonotlite sample mixed with cerium showed no change in the XRD pattern after 8 days. The sorption test results from part 1 showed a reduction of 14% of cerium in the solution. The cerium was most likely precipitating and not reacting with the xonotlite. The cerium was only present at 0.00114 moles in a 10 ml volume, so 14% of this mass would be 0.000224g, there was 0.05g of xonotlite so the proportion of precipitated cerium would be 0.45% of the total solids. This is a very small proportion of the total solids and it is reasonable that it was not detected with XRD.

The xonotlite sample mixed with the caesium solution showed no change and had only pure xonotlite present.

The XRD pattern for the xonotlite sample tested with Strontium showed an abundance of the original xonotlite. However there were two new significant peaks at 26.015 and 36.674 2Θ, and an enlargement of one of the xonotlite peaks at 25.333. Analysis using DIFFRAC.EVA showed these peaks corresponded to strontianite, a mineral that was also found in the calcite sample mixed with strontium. Xonotlite and strontianite account for all peaks present in the XRD pattern. This reaction also explains the slight reduction of the quantity of strontium in solution.

6.3.4 Reinhardbraunsite

The XRD patterns are shown below in Figure 84 and the minerals in each sample are shown in Table 81.

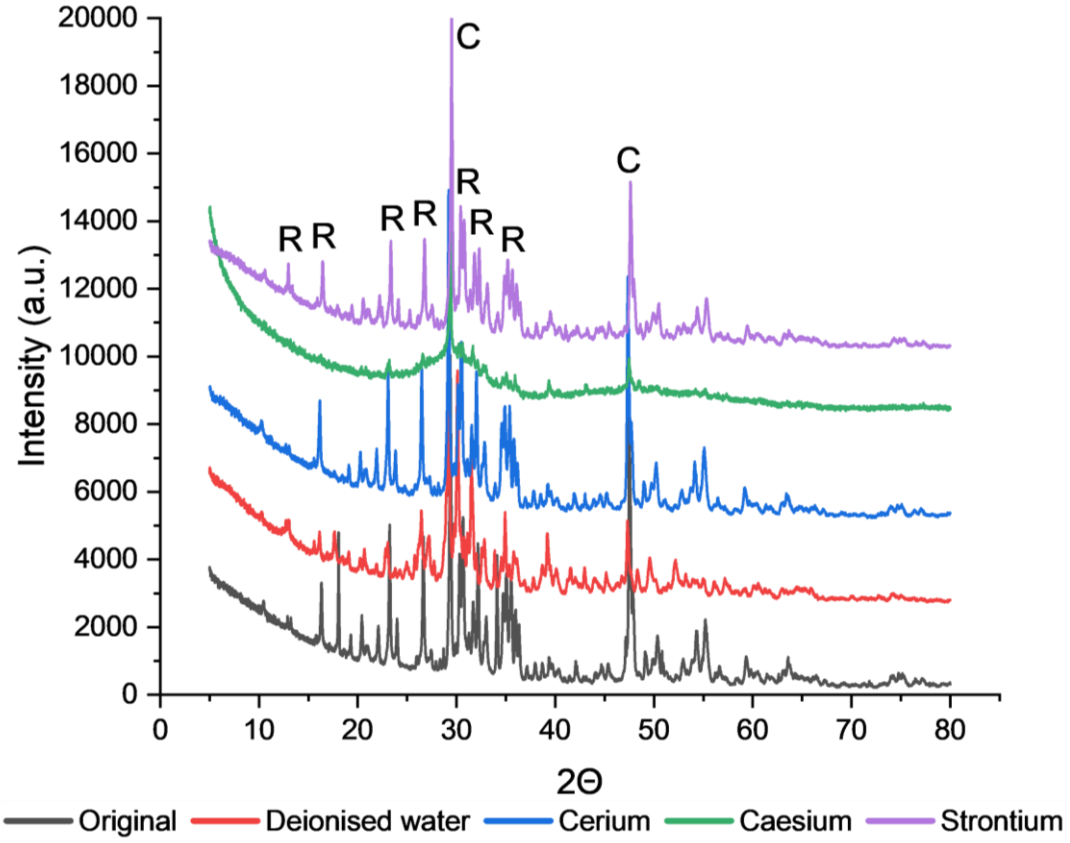


Figure 84: The XRD patterns of reinhardbraunsite (black) after being mixed with deionised water (red), cerium (blue), caesium (green) and strontium (purple) for 8 days. R = Reinhardbraunsite, C = calcite.

Table 81: The reinhardbraunsite samples, the minerals they contain and the COD ID used to identify the minerals.

Sample	Minerals [COD ID]	Reference
Original	Reinhardbraunsite [1529964] Portlandite [9000113]	192 266
Deionised water	Reinhardbraunsite [1529964] Portlandite [9000113]	192 266
Cerium	Reinhardbraunsite [1529964]	192
Caesium	Reinhardbraunsite [1529964]	192
Strontium	Reinhardbraunsite [1529964] Portlandite [9000113]	192 266

As shown in Figure 84 the original reinhardbraunsite sample contained both reinhardbraunsite and portlandite. The sample that was tested in deionised water also showed reinhardbraunsite and portlandite, however the peaks for portlandite were smaller suggesting some portlandite had dissolved into the solution. The reinhardbraunsite tested with cerium showed no portlandite, only pure reinhardbraunsite was present. The sample tested with caesium showed pure reinhardbraunsite. The reinhardbraunsite sample tested with strontium showed both reinhardbraunsite and portlandite present, there was however less portlandite present than in the original sample.

6.3.5 Jaffeite

The XRD patterns are shown below in Figure 85 and the minerals in each sample are shown in Table 82.

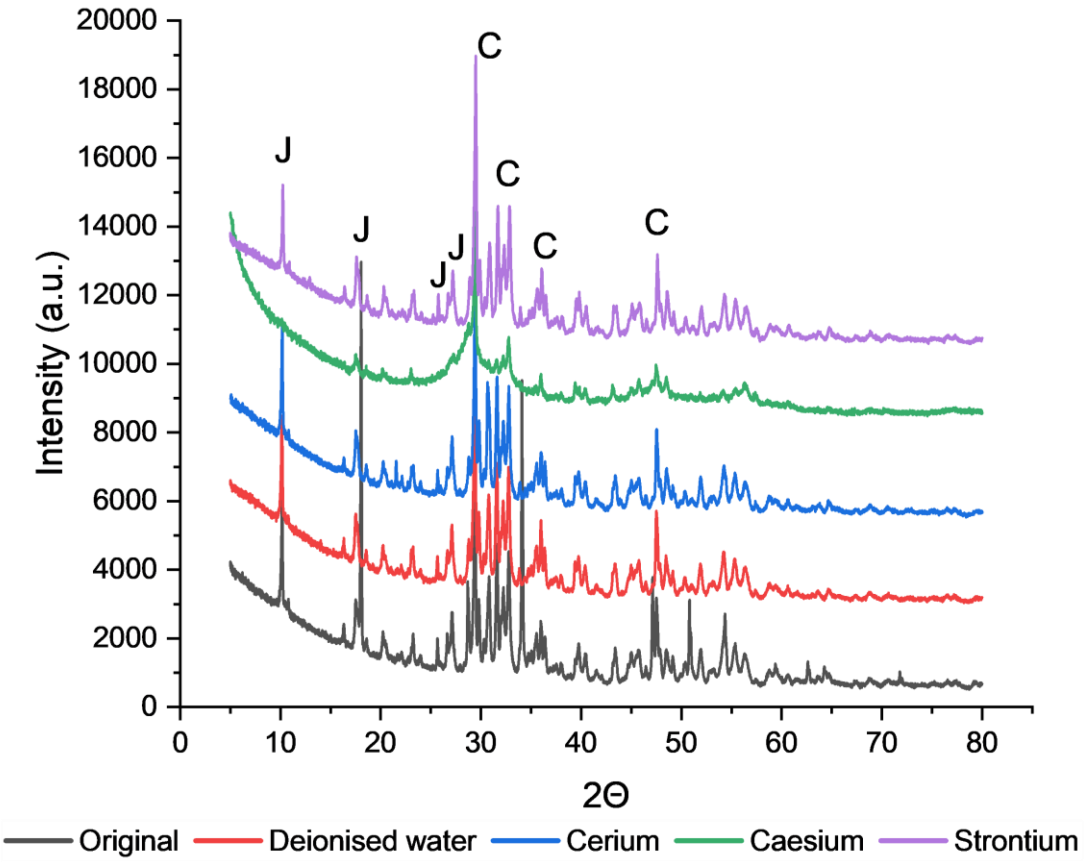


Figure 85: The XRD patterns of jaffeite (black) after being mixed with deionised water (red), cerium (blue), caesium (green) and strontium (purple) for 8 days. J = jaffeite, C = calcite.

Table 82: The jaffeite samples, the minerals they contain and the COD ID used to identify the minerals.

Sample	Minerals [COD ID]	Reference
Original	Calcite [9009668]	267
	Portlandite [1008781]	196
	Jaffeite [9012620]	197
	γ-C_2SH [9012681]	195
Deionised water	Calcite [9009668]	267
	Jaffeite [9012620]	197
	γ-C_2SH [9012681]	195
Cerium	Calcite [9009668]	267
	Jaffeite [9012620]	197
	γ-C_2SH [9012681]	195
Caesium	Calcite [9009668]	267
	Jaffeite [9012620]	197
	γ-C_2SH [9012681]	195
Strontium	Calcite [9009668]	267
	Jaffeite [9012620]	197
	γ-C_2SH [9012681]	195

The XRD patterns in Figure 85 of jaffeite showed very little difference after being tested in the different solutions. The original sample contained portlandite, none of the jaffeite samples that had been mixed in any of the solutions contained any portlandite which shows it had all dissolved into solution independently of whether radionuclides were present as it all also dissolved in the deionised water sample. The jaffeite samples also contained γ-C_2SH.

6.3.6 α-C_2SH

The XRD patterns are shown below in Figure 86 and the minerals in each sample are shown in Table 83.

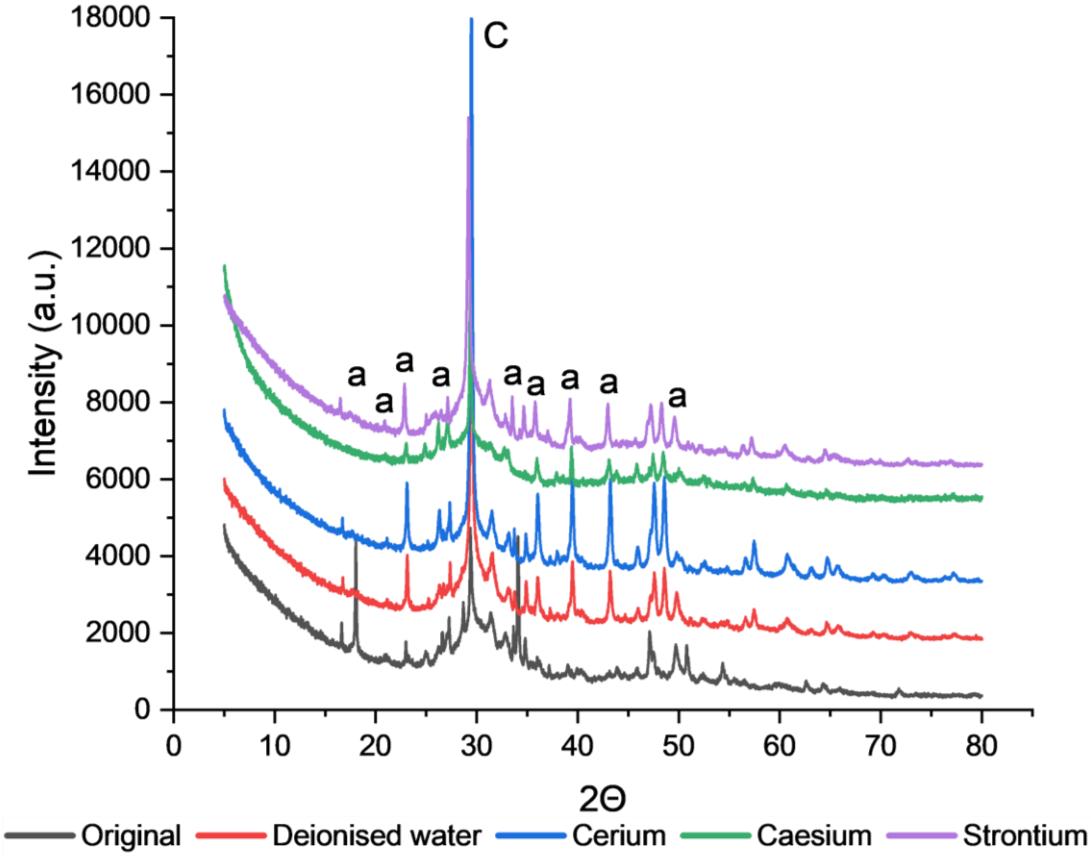


Figure 86: The XRD patterns of α-C_2SH (black) after being mixed with deionised water (red), cerium (blue), caesium (green) and strontium (purple) for 8 days. a = α-C_2SH, C = calcite.

Table 83: The α-C_2SH samples, the minerals they contain and the COD ID used to identify the minerals.

Sample	Minerals [COD ID]	Reference
Original	Calcite [9009667] αC_2SH [9011378] Quartz [9009666] Portlandite [9000113]	267 199 268 266
Deionised water	Calcite [9009667] αC_2SH [9011378] Quartz [9009666]	267 199 268
Cerium	Calcite [9009667] αC_2SH [9011378] Quartz [9009666]	267 199 268
Caesium	Calcite [9009667] αC_2SH [9011378] Quartz [9009666]	267 199 268
Strontium	Calcite [9009667] αC_2SH [9011378] Quartz [9009666] Strontianite [9013802]	267 199 268 265

The XRD patterns are shown in Figure 86. This mineral mix was not single phase, as a single phase synthesis route was not found. The mineral was a more complicated mix of portlandite, calcite, poldervaartite, and quartz. The portlandite and quartz present in the original mineral sample are unreacted from the initial starting mix. Calcite has formed from the reaction of portlandite with dissolved carbon dioxide in the water. Calcite has been tested so the effects of that are known. The effect of portlandite is also known as it was used to adjust the pH in the high pH solution used in the tests in phase 1. Quartz should be inert and this can be tested with the sample mixed with pure deionised water. Therefore any reductions on the radionuclide analogues beyond the results seen when calcite or the high pH solution were used can be attributed to poldervaartite or killalaite.

The α-C_2SH sample mixed in deionised water showed no portlandite, and a significantly higher amount of calcite. This is due to the carbonation reaction between the CO_2 dissolved in the water and the portlandite. The test tubes had a large amount of headspace and were mixed at a high rpm to ensure the water and mineral was

constantly agitated. This would allow for CO_2 to be dissolved into the water and for the limiting reactant to be the portlandite. Apart from the portlandite reacting to create more calcite the mineral mix is unchanged, this confirms the other minerals present (quartz, killalaite, and poldervaartite) are unreactive in water, so any change in the minerals are due to the radionuclide analogues.

The α-C_2SH samples mixed with cerium and caesium showed no difference in the XRD pattern to the sample mixed with deionised water. Like the sample mixed with deionised water it also showed no portlandite and an increase in the calcite peaks.

The α-C_2SH sample mixed with strontium showed the presence of calcite, α-C_2SH, killaite, quartz and a new mineral strontianite. It is likely the strontianite formed from strontium replacing calcium sites in calcite. This is an interesting result as it shows this process is possible even when calcite is present within a cement mixture.

6.4 Discussion and impact

6.4.1 Phase 1 results summary and conclusions

Single phase mineral tests

Table 84 shows the collated results of the mineral tests. The results from iodine testing are not included in this table as not all minerals were tested with iodine. The decision was made to stop investigating iodine as the ICP-OES measurements taken over 30 days were irregular, and the concentration kept increasing and decreasing randomly. As this trend was seen in all iodine tests across all minerals tested it was determined that this was an issue with the measurement technique. Investigating a technique to measure iodine concentration accurately is outside the scope of this project, and time constraints did not allow this.

Table 84: A summary table from the Phase 1 tests, showing the percentage of radionuclide remaining in solution after 8 days for each mineral in each solution.

Solution	Radionuclide	% of Radionuclide remaining in solution after 8 days					
		Calcite	Xonotlite	Reinhardbraunsite	α-CSH-1	α-CSH-2	Jaffeite
Deionised water	Strontium	33.1693	89.7019	96.1835	88.0955	95.6886	96.6181
	Cerium	8.19492	86.8821	0	0	0	0
	Caesium	96.114	92.75	95.5837	95.5257	99.9876	99.9876
High pH	Strontium	109.618	116.78	115.25	108.681	115.199	110.544
	Cerium	0	0	0	0	0	0.04492
	Caesium	97.9769	96.6895	0	97.1493	100.512	100.206
High Salinity	Strontium	47.0005	95.4335	100.043	95.035	116.03	103.661
	Cerium	104.287	92.2574	0	0	0.02326	1.96278
	Caesium	97.7529	97.9728	98.7474	96.8445	101.256	100.152

The graph in Figure 87 shows the percentage of radionuclide remaining in solution after 8 days. The concentration of strontium was most reduced by calcite in deionised water and high salinity solution. In the high pH solution none of the minerals reduced the concentration of strontium in solution. Xonotlite reduced cerium the least, calcite reduced the concentration of cerium in solution the second least. All other minerals reduced the concentration of cerium in solution completely. There was a small amount of cerium remaining in the high salinity solution tested with jaffeite. The concentration

of caesium in solution remained high regardless of the mineral used or the solution tested. It was most reduced by xonotlite in deionised water.

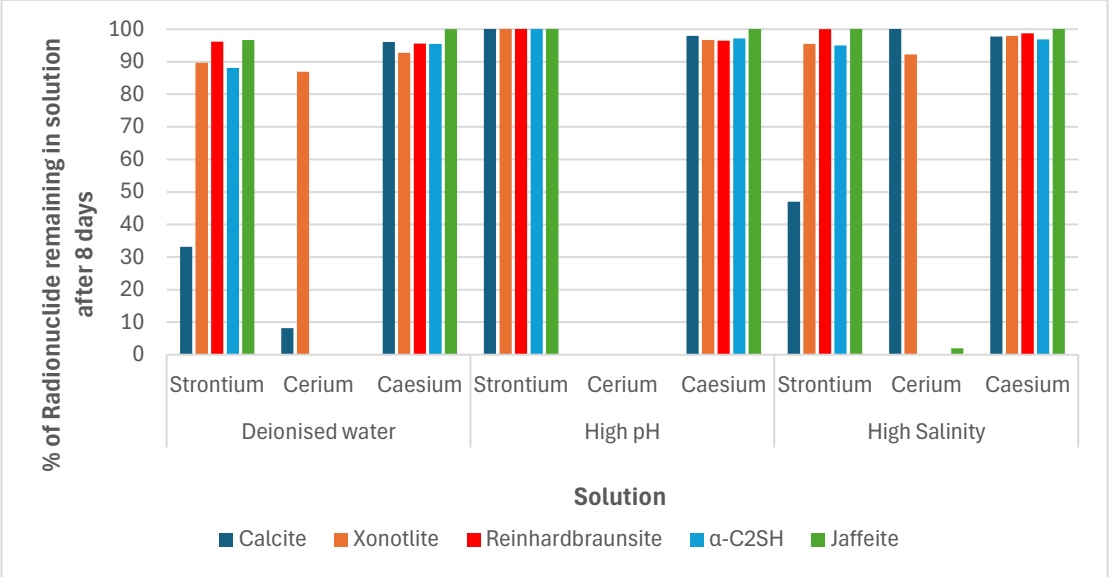


Figure 87: A graph showing the percentage of radionuclide remaining in solution after the 8 day tests. Navy = calcite, orange = xonotlite, red = reinhardbraunsite, blue = α-C_2SH, and green = jaffeite.

Cement tests

Table 85 below shows the percentage of radionuclide remaining in solution after 8 days of mixing with the different cements tested.

Table 85: A summary table from the Phase 1 tests, showing the percentage of radionuclide remaining in solution after 8 days for each cement in each solution.

Solution	**Radionuclide**	**% of Radionuclide remaining in solution after 8 days**		
		$CaO:SiO_2$ ratio 4 250°C	NRVB 200°C	NRVB 250°C
Deionised water	Strontium	82.6353	97.9395	97.0982
	Cerium	0.1691	0.03602	1.39484
	Caesium	100.389	100.372	0
High pH	Strontium	101.912	112.662	109.258
	Cerium	0.08359	0.09233	0.07985
	Caesium	99.2802	99.4307	99.8094
High Salinity	Strontium	108.057	97.8503	65.6177
	Cerium	0.28689	0.36331	0.03655
	Caesium	100.254	99.8594	102.496

The graph in Figure 88 below is the combined results of the tests from phase 1 on the cements. All three cements tested reduced the concentration of cerium in solution to a negligible amount. The cement $CaO:SiO_2$ ratio 4 250°C reduced the concentration of strontium in solution by more than the other two cements tested in deionised water. In the high salinity solution NRVB cured at 250°C reduced the concentration of strontium in solution by the most compared to the other two cements. Only NRVB cured at 250°C reduced the concentration of caesium in solution and it was only reduced in the deionised water solution.

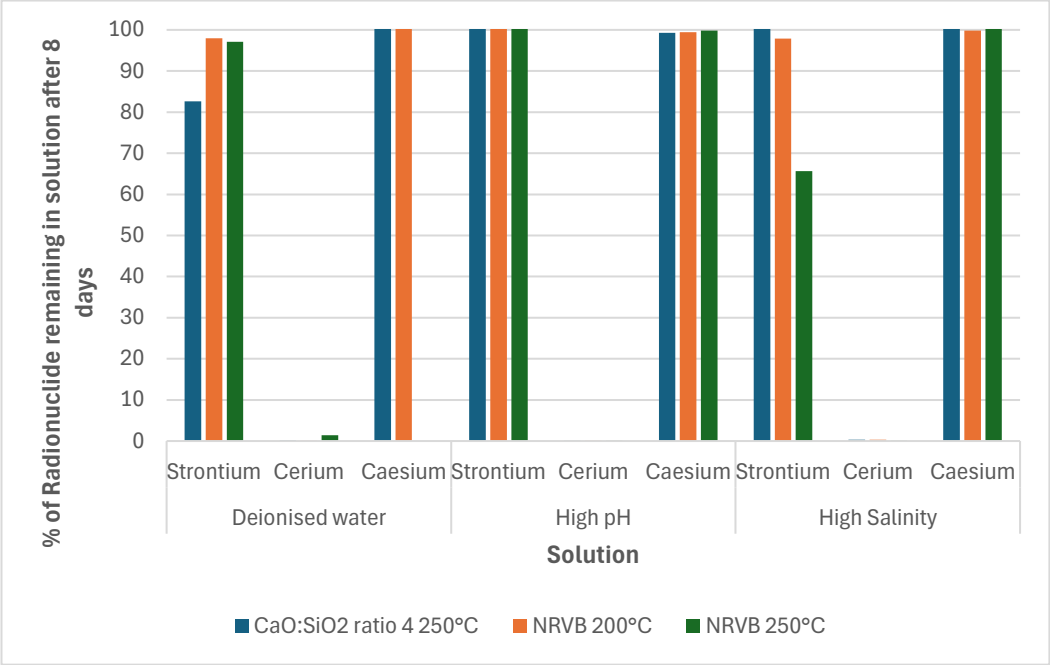


Figure 88: A graph showing the percentage of radionuclide remaining in solution after the 8 day tests. Navy = C:S 4 cured at 250°C, orange is NRVB cured at 200°C, and green is NRVB cured at 250°C.

6.4.2 Phase 2 results summary and conclusions

Table 86 shows the percentage of cerium remaining in solution after being mixed with the mineral for eight days.

Table 86: A summary of the results from the phase 2 tests regarding cerium.

Radionuclide concentration		**0.228**	**0.114**	**0.0552**	**0.0228**	**0.0114**
ICP-OES Start Concentration		100	100	100	100	100
Mineral	Calcite	96.48991	106.7785	86.23576	34.06182	2.018611
	Xonotlite	102.9385	109.2929	98.4071	77.0561	68.31782
	Reinhardbraunsite	83.0211	83.55946	45.34055	1.708878	2.333572
	Jaffeite	97.16051	84.60346	56.15193	0.816993	1.689334
	α-C_2SH	92.44724	85.47566	50.23224	3.159041	2.433787

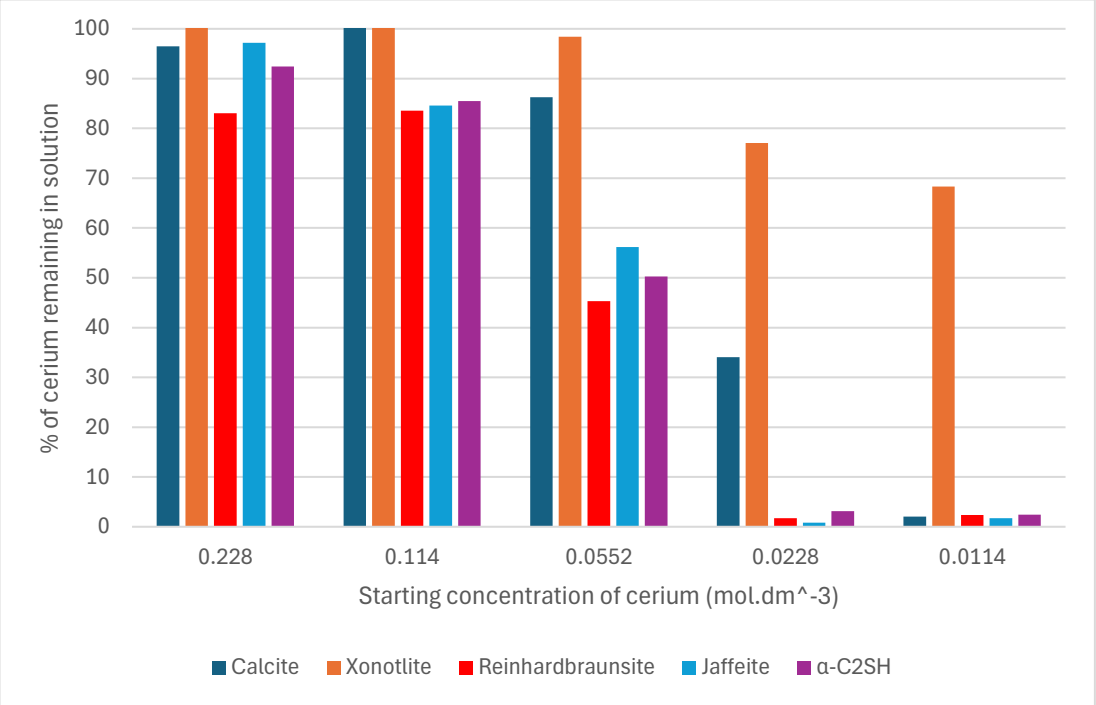


Figure 89: A graph showing the percentage of cerium in solution at different start concentrations after being mixed with individual minerals for 8 days. Navy = calcite, orange = xonotlite, red = reinhardbraunsite, blue = jaffeite, and purple = α-C_2SH.

At the lowest concentration the concentration of cerium in solution was reduced to approximately zero by all minerals except from xonotlite as shown in Figure 89. As the starting concentration was increased calcite became less effective at removing the cerium from solution. At the middle concentration tested, 0.0552 mol.dm^-3 all minerals could not remove all cerium from solution. At the highest concentration tested reinhardbraunsite was the most effective mineral, removing 17% of the cerium from solution. This is likely due to it having a C:S ratio of 5, meaning it contains more

calcium than the other minerals and so can more effectively buffer the pH to a level where cerium is less soluble and precipitates.

6.4.3 Phase 3 results summary and conclusions

The tests where the rate of reduction of radionuclides were plotted onto a graph, a straight line was taken as an approximation for the decrease of radionuclide in solution. The gradient of the line can be used to represent the rate change. Table 87 shows the gradients of the lines of best fit of the rate graphs. Where the number is negative this shows a decrease in concentration of radionuclide in solution.

Table 87: The gradients on the lines of best fit from the Phase 3 tests. Where the number is negative this shows the mineral reduced the concentration of radionuclide analogue in solution.

Mineral	Caesium	Cerium	Strontium
Calcite	0.000003	-0.00006	-0.00004
Xonotlite	0.000001	-0.00001	-5E-06
Reinhardbraunsite	0.000002	-0.00002	-4E-06
Jaffeite	0.000002	-0.00002	-6E-06
αC2SH	0.000002	-0.00002	-5E-06

In the solutions containing cerium and strontium all minerals decreased the concentration of radionuclide in solution. α-C_2SH, reinhardbraunsite, and jaffeite reduced the concentration of cerium in solution to 0 after two hours, so they had a quicker rate than calcite. None of the minerals decreased the concentration of caesium in solution.

6.4.4 Conclusions

All of the minerals performed differently. The effect of changing the solution to high salinity was minimal and had no significant impact on the results when compared to deionised water. This suggests that the minerals will perform similarly in sea water which has a comparable salinity.

Calcite was the most effective mineral at reducing the concentration of strontium in solution. XRD analysis confirmed this was due to the calcite reacting with strontium to form strontianite. At high concentrations of strontium in solution strontianite can form as a precipitate on the surface of calcite, it forms by Sr^{2+} ions bonding with CO_3^{2-}

ions in solution[269]. At lower strontium concentrations the strontium substitutes into calcium sites on the surface of the calcite[270].

Reinhardbraunsite was the most effective at reducing the concentration of cerium even at significant cerium concentrations. Ce(III) has a low solubility under alkaline conditions and can precipitate as $Ce(OH)_3$. In oxygen-containing systems, Ce(III) may subsequently oxidise to Ce(IV), resulting in the formation of Ce(IV)-bearing hydroxide or hydrous CeO_2 phases. Therefore, the apparent removal of cerium from solution is most likely from precipitation under the highly alkaline environments caused by the minerals[256,271].

None of the minerals were able to reduce the concentration of caesium, apart from the sample of NRVB cured at 250°C. Further work to verify this result should be undertaken. The reduction in caesium concentration within a cement containing solution is likely to be caused by sorption rather than precipitation. Caesium remains highly soluble under alkaline conditions, meaning that precipitation is unlikely to be the main mechanism responsible for its removal from solution. Previous studies investigating Caesium interaction with cementitious materials have shown that C-S-H is one of the main phases responsible for Cs retention within hydrated cement[272] . Caesium can interact with sorption sites on the C-S-H surface and within the interlayer regions, although the extent of retention is dependent on the C:S ratio of the C-S-H. Caesium adsorption decreases as the C:S ratio increases, as the higher concentration of Ca reduces the interaction of caesium with available surface sites[273], it has also been found that sorption sites had a greater affinity for caesium than sodium ions[274]. This is particularly relevant to NRVB due to its high C:S ratio and suggests that caesium retention by the cement may be relatively limited compared with lower C:S C-S-H phases. Therefore, any decrease in caesium concentration observed in these experiments is likely to result predominantly from sorption or ion-exchange processes rather than the formation of a Cs-containing precipitate.

XRD analysis showed that the minerals are stable in water, and don’t dissolve or form other minerals.

The work in this chapter was to evaluate how NRVB cured at higher temperatures performed against the safety function of buffering the pH to between 12-13 to precipitate radionuclides from groundwater solution. This chapter did this by testing the individual high temperature minerals, and cement mixes that contain the most high temperature minerals. This chapter shows that despite the NRVB cement

containing less portlandite than is present when NRVB is cured at lower temperatures, the high temperature minerals are still able to raise the pH and cause precipitation of cerium. These tests were conducted over very short timeframes compared to the lifetime of the GDF. This shows the minerals are effective at short term buffering, however more tests to study their efficacy on longer timescales is needed. Longer scale tests are particularly important following the results in Phase 3 which showed the initial calcium dissolution from most minerals occurred in the first 2 hours, this is consistent with the pH tests of these same experiments.

This chapter studied the efficacy of the minerals in deionised water, and in a high salinity groundwater analogue. Most of the high temperature minerals behaved exactly the same in deionised water and high salinity solution, this shows that the NRVB cured at higher temperatures is suitable for use in a high saline environment. This is useful information to inform both the GDF siting and the choice of backfill should the GDF be constructed in a region of the UK that has saline groundwater.

The results from this chapter are promising and show that NRVB is suitable for use in a high saline environment, and that it maintains its pH buffering properties when cured at higher temperatures. The results from this chapter could be used to design an ideal NRVB formulation by knowing the temperature of the vaults in which the backfill will be cured at, the C:S ratio can be adjusted to favour strengthening minerals such as xonotlite or minerals with a high buffering capacity such as reinhardbraunsite.

Chapter 7 Discussion of the implications for NRVB Cement in Nuclear Waste Disposal and repository design

7.1 Introduction

The current UK policy for ILW and HLW is disposal in a GDF. To get a license to construct the GDF the operator will need to demonstrate its long-term safety through a safety case built on claims, arguments and evidence. At least one of these claims will be about the backfill material chosen to encapsulate the waste containers. The backfill material that is chosen for the GDF will depend on a variety of factors, these include but are not limited to the host rock, the vault design, the characteristics of the waste being emplaced, and the location of the GDF. The properties of the backfill will influence which is chosen to be most appropriate. It is therefore essential that the properties of the backfill materials are fully understood, including their behaviour in potential repository conditions, and their long term evolution. Understanding the general properties of the different considered backfills, and the properties that are specific to the safety functions that are defined is important. This project should provide evidence for NRVB backfill under one or more of the arguments surrounding the selection and safety of a backfill material.

Prior to commencement of this thesis there was limited research on how NRVB cement behaves when cured or exposed to elevated temperatures. This research aimed to first investigate what the effect of high temperature curing on NRVB cement was, and to then begin to assess the implications of the changes in mineralogy and porosity on the safety function of radionuclide retention. The ability to retain radionuclides, and stop them from reaching the biosphere, is an important safety function of the backfill material. The GDF will need to demonstrate safety for 10,000 years so if the waste packages suffer any erosion or cracking in that time it could allow for radionuclides to egress from the packages. This will allow for the radionuclides to interact with the backfill, and if the backfill is not able to interact with the radionuclides and arrest them the radionuclides could escape from the GDF and cause harm to people, plants or animals.

7.1.1 The aims and objectives of this project

This thesis aimed to investigate how C:S ratio and curing temperature affect mineralogy, porosity, and radionuclide retention in NRVB-type cements.

This was achieved by the following approach:

- Development of preparation methodology by investigating hydration arrest and grinding methods.
- Mineralogical characterisation using XRD.
- Porosity analysis with XCT and helium pycnometry.
- Development of synthesis methods of individual high temperature mineral phases.
- Radionuclide analogue experiments with the synthesised minerals.

This discussion chapter analyses how the information and conclusions from these individual chapters can be integrated to help understand how the mineralogical evolution controls the long-term performance of NRVB cement systems. This chapter considers the impact and application of these results on the UK Geological Disposal Facility's design and safety, and suggests future work that could enhance the understanding of the NRVB backfill.

7.2 How Mineralogy affects the Porosity and Radionuclide Retention

The mineralogy of a cement affects its stability, pore structure, porewater chemistry and interactions with radionuclides. Understanding how the mineralogy of NRVB changes at elevated temperature is therefore important when considering its long-term performance in a GDF. NRVB was developed as a high-pH cementitious backfill which provides a chemical barrier to radionuclide release. Previous work has shown that relatively small differences in the raw materials used to make NRVB can affect its hydration, compressive strength and porosity[3]. The work in this thesis builds on this by showing that curing temperature and C:S ratio both affect the mineralogy of NRVB and that these changes also affect its pore structure, solution chemistry and interactions with radionuclide analogues.

Effect of temperature and C:S ratio on NRVB mineralogy

Chapter 3, Investigation into the effect of increasing the curing temperature and altering the C:S ratio of NRVB cement on the mineralogy, it was established using XRD analysis that the curing temperature and C:S ratio affect the mineralogy of the NRVB cement. It was found that at curing temperatures above 150°C, minerals that cause strength retrogression begin to form as the excess portlandite reacts. At room temperature the samples contained phases associated with the original cement, including calcite, portlandite, gypsum and larnite. As the curing temperature was increased, the original mineralogy was progressively replaced by crystalline calcium silicate hydrate phases.

These results are consistent with previous studies of cement under hydrothermal conditions. Previous studies investigating the C-A-S-H system between 200 and 350°C showed that relatively small changes in composition could substantially change mineral phase stability[56]. α-C_2SH was identified at curing temperatures below approximately 250°C and 1.1 nm tobermorite was identified at curing temperatures below approximately 300°C. Hydrogarnet was the only crystalline aluminium containing phase below 300°C, while additional aluminium phases, including $C_4A_3H_3$ and bicchulite, were present at higher temperatures[56]. Many of these phases were also identified in this study, showing that the hydrothermal alteration of NRVB broadly follows the behaviour previously reported for C-A-S-H cement systems.

The formation of α-C_2SH at approximately 200–250°C is particularly consistent with literature[56]. However, the amount of α-C_2SH formed in this study was dependent on the C:S ratio. Samples with a higher C:S ratio favoured calcium rich phases, whereas increasing the amount of silica promoted lower C:S calcium silicate hydrate phases. This shows that the mineralogical changes cannot be explained by temperature alone and that the starting composition of the cement is also important.

This can be seen clearly from the formation of xonotlite. At a C:S ratio of 4 and a curing temperature of 250°C, approximately 25% xonotlite was measured by quantitative XRD. Increasing the amount of silica further also promoted xonotlite formation, whereas the more calcium rich compositions (lower C:S ratio) favoured α-C_2SH, jaffeite and other calcium rich phases. The formation of a measurable amount of xonotlite at C:S 4 is important because it demonstrates that changing the C:S ratio

of NRVB can significantly alter the mineral assemblage even when the curing temperature remains the same.

This is consistent with previous studies that investigated Class G oil-well cement at 200 and 250°C and showed that adding silica changed the mineral assemblage produced during hydrothermal curing[51]. They found that unmodified cement contained calcium-rich phases including jaffeite and α-C_2SH, while silica addition promoted a different assemblage. The results from this thesis therefore support the conclusion that silica availability, and consequently C:S ratio, is an important control on the high-temperature mineralogy of NRVB.

Jaffeite was identified in several of the samples with a high C:S ratio. Its formation is consistent with previous work on Portland cement under hydrothermal conditions that identified jaffeite alongside α-C_2SH and portlandite in unmodified Class G cement cured hydrothermally[51]. Jaffeite is one of the crystalline calcium silicate hydrates found in hydrothermal cement systems[275]. The formation of jaffeite in the high-C:S samples in this study is therefore consistent with the large amount of calcium available relative to silica. This is particularly relevant to NRVB because its formulation contains a large amount of additional portlandite and has a bulk C:S ratio of approximately 7.27. This is substantially more calcium rich than silica enriched oil-well cement formulations. The formation of jaffeite therefore shows that NRVB follows the general behaviour reported for calcium rich hydrothermal cement systems, but its high initial C:S ratio results in a different mineral assemblage from formulations in which additional silica has been used to reduce the C:S ratio.

Reinhardbraunsite was also identified in some of the samples with a high C:S ratio. Both Reinhardbraunsite and jaffeite have been found to form when β-C_2S (larnite) is hydrothermally heated between 50 and 400°C[276]. Below 220°C, α-C_2SH formed directly from β-C_2S, whereas above 240°C the reaction pathway became more complicated and depended on how the hydrothermal reaction was carried out[276] . The formation of reinhardbraunsite in this study is therefore consistent with the high C:S ratio of the samples in which it was identified. However, it cannot be concluded that temperature alone caused its formation. In the previous study it was shown that the starting material and reaction pathway also affected the phases produced[276]. Their experiments were also carried out using β-C_2S rather than a cement formulation[276] . The comparison therefore supports reinhardbraunsite as a possible product of

calcium rich hydrothermal systems but does not demonstrate that the same reaction pathway occurred in NRVB.

The aluminium containing mineral phases identified in this study also agree with the published C-A-S-H literature. Hydrogarnet remained an important Al-bearing phase from 80 to 150°C. Hydrogarnet has been found in literature as the only crystalline aluminium bearing phase below 300°C, with additional phases becoming stable at higher temperatures[56]. Hydrogarnet composition is controlled mainly by curing temperature and, to a lesser extent, silica addition[277]. This is consistent with the hydrogarnet observed in this study.

γ-C_2SH was identified in some of the samples following hydrothermal curing at elevated temperatures. This is consistent with the literature where it was found that the hydration of β-C_2S under hydrothermal conditions between 50 and 400°C formed γ-C_2SH alongside a number of other calcium silicate phases, including α-C_2SH, jaffeite, reinhardbraunsite, kilchoanite and foshagite[276]. The phases that form from β-C_2S are strongly dependent on curing temperature and the hydrothermal reaction conditions[276]. Below approximately 220°C, α-C_2SH forms directly from β-C_2S, whereas above approximately 240°C the reaction pathway became more complex and a wider range of calcium silicate phases formed[276]. The identification of γ-C_2SH in the present study is therefore consistent with previous work showing that dicalcium silicate can form a range of crystalline calcium silicate hydrates under hydrothermal conditions.

However, in the study referenced above β-C_2S was used as the starting material[276] rather than a multiphase cement containing additional portlandite and calcite. Although the formation of γ-C_2SH in both studies provides evidence that it can form under hydrothermal conditions, it cannot be assumed that the reaction pathway was the same. The formation of γ-C_2SH in the present study is therefore likely to depend on both curing temperature and the high availability of calcium within NRVB. Further work using in-situ XRD or shorter curing periods would be required to determine when γ-C_2SH forms and which phases act as its precursors.

Overall, Chapter 3 shows that the cements with a higher C:S ratio followed a different mineralogical pathway from the samples containing additional silica. Cements with a higher C:S ratio favoured the formation of calcium rich minerals such as α-C_2SH, jaffeite and reinhardbraunsite, whereas reducing the C:S ratio increased the formation

of mineral phases such as xonotlite. The results therefore broadly agree with previous hydrothermal cement studies but extend this work to the higher C:S ratios relevant to NRVB.

Relationship between mineralogy and porosity

Chapter 4, The effect of increased curing temperature and different C:S ratio on porosity, the porosity of the cements made in Chapter 3 was studied. The results showed that the effect of temperature on porosity was dependent on C:S ratio and was more complicated than a simple increase in porosity with increasing temperature. The porosity was measured using XCT and helium pycnometry, and the pore space itself was investigated using SEM and EMPA. These techniques showed that at curing temperatures above 150°C the porosity increases in the cements. The SEM and EMPA images aligned with this finding, showing less defined porosity as the curing temperature was increased. These results are in agreement with those from Chapter 3 which found that above 150°C minerals that cause strength retrogression form in the cement.

At room temperature and 80°C, the measured porosities were generally between approximately 43 and 51%. At 150°C these increased to approximately 52–59%. However, greater differences between the different C:S ratios were observed at higher temperatures. At 200°C, the sample with a C:S ratio of 4 had a porosity of approximately 65%, compared with approximately 42% at C:S 7 and 50% for NRVB at its original C:S ratio of 7.27. At 250°C, the difference was greater, with porosities of approximately 80% at C:S 4, and 89% for NRVB at C:S 7.27. These results show that there was not a simple linear relationship between curing temperature and porosity. Instead, the effect of temperature depended strongly on the C:S ratio and therefore on the mineral assemblage that formed. This is an important result because it shows that increasing temperature alone cannot be used to predict the pore structure or porosity of NRVB.

The room temperature and 80°C experiments also showed an effect from the inclusion of $CaCO_3$. At C:S ratios of 4 and 5 there was little difference in porosity between samples made with and without $CaCO_3$. At C:S ratios of 6 and 7, however, the samples containing $CaCO_3$ had porosities approximately 9–15 percent higher than the equivalent samples without $CaCO_3$. This difference occurred when the cements were cured at both 25 and 80°C. This was unexpected because NRVB has a C:S ratio

of approximately 7.27 but did not show exactly the same behaviour. The high proportion of calcite also made identification and quantification of some of the lower-abundance hydration products by XRD difficult. It is therefore not possible from the mineralogical results alone to determine why the C:S 6 and 7 samples showed this difference.

The relationship between mineralogy and porosity observed in this study is consistent with previous work on C-A-S-H hydroceramics[52]. C-A-S-H hydroceramics cured between 200 and 350°C contained several of the same mineral phases identified in this study, including portlandite, jaffeite, xonotlite, tobermorite, and hydrogarnet[52]. Large differences in compressive strength and permeability were observed between samples with different compositions and mineral assemblages, demonstrating the relationship between hydrothermal phase formation, microstructure and engineering properties[52].

Prolonged curing of silica-enriched Class G cement at 200 °C has also been shown to result in microstructural coarsening together with changes in strength and permeability[278]. These changes occurred alongside the progressive conversion of semi-crystalline C-S-H to more crystalline calcium silicate hydrate phases, including tobermorite and xonotlite[278].

However, the results from this thesis also show why the mineralogical results cannot be used alone to predict porosity. For example, the C:S 4 sample at 250°C had a porosity of approximately 80% and contained approximately 25% xonotlite, but this does not demonstrate that xonotlite itself caused the high porosity. The pore structure will depend on the complete mineral assemblage and the morphology and distribution of those phases. This is particularly important because xonotlite has also been associated with dense microstructures under other hydrothermal conditions.

The increase in total porosity should also not be assumed to result directly in increased radionuclide transport. Transport is dependent on pore size, connectivity and tortuosity as well as total pore volume. XCT only resolves pores above the spatial resolution of the technique, while helium pycnometry measures accessible volume but does not determine whether those pores form connected transport pathways. Permeability and diffusivity measurements would therefore be required to determine whether the measured changes in porosity result in increased radionuclide transport.

Overall, Chapter 4 shows that curing temperature changes the pore structure of NRVB, but that the effect is strongly dependent on composition. The large difference between the C:S 4 and NRVB samples at 250°C demonstrates that the effect of temperature cannot be separated from the mineralogical changes caused by changing the C:S ratio.

Implications for the chemical buffering function of NRVB

The mineralogical and porosity changes identified in Chapter 3 and Chapter 4 could affect the chemical function of NRVB. NRVB is designed to provide a high pH chemical environment which contributes to limiting radionuclide mobility[4]. Portlandite provides a large reservoir of calcium and alkalinity in the original NRVB mineral assemblage and is designed to buffer the pH of NRVB to be between 12 and 13. This safety function would be applicable if the waste packages corrode or crack, and there is groundwater ingress that the radionuclides dissolve into. In Chapter 3 and Chapter 4 it was established that when NRVB cement is cured above 150°C there is a reduced amount of portlandite and greater porosity. These findings show that at higher curing temperatures there is less portlandite to buffer the pH, and a greater volume of pore space alongside a breakdown in pore structure. This suggests that not only will the NRVB cement be less effective at buffering pH to precipitate radionuclides, but there will also be more pore space so a larger flow network. This will make the NRVB cement less effective at prohibiting radionuclides from leaving the backfill. The reduction in portlandite observed at elevated temperatures could therefore reduce one component of its alkaline buffering capacity. However, this only considers the loss of the original phases and not the behaviour of the minerals which form in their place. Chapter 5 therefore developed methods to synthesise minerals representative of the high temperature phases identified in Chapter 3 so that their chemical behaviour could be investigated individually.

Chapter 6 showed that the solution chemistry produced by these minerals depended on their composition. Minerals with a higher C:S ratio generally produced more alkaline solutions than lower C:S minerals, primarily through the release of calcium into solution. The loss of portlandite during hydrothermal alteration therefore does not necessarily mean that all alkaline buffering capacity is lost. Secondary calcium-bearing phases may also contribute to maintaining alkaline conditions. However, the ability to maintain a high pH does not necessarily mean that a mineral will have a greater capacity to retain radionuclides. For example, C-A-S-H has been shown

experimentally to enhance Cs and Sr sorption in a cementitious material[279]. Atomistic modelling has similarly shown that Cs sorption within C-S-H interlayers decreases as the Ca:Si ratio increases[280].

The results from this thesis therefore show that the properties which favour alkaline buffering do not necessarily favour direct radionuclide sorption. A high C:S mineral may maintain a higher pH but have a lower sorption capacity for some radionuclides. The chemical performance of thermally altered NRVB therefore cannot be assessed from pH alone.

Radionuclide interactions with the altered mineral assemblage

The experiments in Chapter 6 showed that the mechanism and extent of removal from solution varied considerably between the different radionuclide analogues and minerals.

This can be seen particularly clearly for Ce. After eight days of contact with the cement samples, only approximately 0.17% of the initial Ce remained in solution for the C:S 4 cement cured at 250°C, 0.04% remained for NRVB cured at 200°C, and 1.39% remained for NRVB cured at 250°C. This corresponds to greater than approximately 98.6% removal from solution in all three cases. This is consistent with Ce having a very low solubility under the highly alkaline conditions produced by the cement and indicates that precipitation is likely to make an important contribution to its removal. The results therefore show that very high removal from solution does not necessarily demonstrate strong sorption by the cement minerals.

The Sr results were very different. After eight days, approximately 82.6% of Sr remained in solution for the C:S 4 cement cured at 250°C, while approximately 97.9% and 97.1% remained for NRVB cured at 200 and 250°C, respectively. The corresponding removal from solution was therefore only approximately 17.4%, 2.1% and 2.9%. This shows that Sr was retained much less strongly by these bulk cement samples than Ce under the conditions investigated.

However, the individual mineral experiments showed that Sr behaviour was strongly dependent on the mineral present. In the experiment with calcite, approximately 33.2% of the original Sr remained in solution after eight days, corresponding to approximately 66.8% removal. XRD also showed the formation of strontianite ($SrCO_3$). This demonstrates that the removal of Sr by calcite was not solely due to adsorption but also involved formation of a separate Sr-containing carbonate phase.

This agrees with previous work investigating Sr incorporation into calcium carbonate at pH 12.02–12.25[281]. Sr was shown to be incorporated into calcite, with strontianite also forming in some experiments where the Sr:Ca ratio was sufficiently high[281]. The formation of strontianite in this thesis is therefore consistent with previous work and provides a possible mechanism for Sr immobilisation in carbonate-containing cement systems.

In contrast, approximately 89.7% of Sr remained in solution in the xonotlite experiment, corresponding to only approximately 10.3% removal. The difference between approximately 66.8% removal by calcite and 10.3% by xonotlite demonstrates that mineralogy has a significant effect on Sr retention. It also shows why radionuclide behaviour cannot be predicted from the bulk C:S ratio or pH alone.

The Ce mineral experiments showed a similar dependence on mineralogy. Approximately 8.2% of Ce remained in solution after reaction with calcite, corresponding to approximately 91.8% removal, whereas approximately 86.9% remained in the xonotlite experiment, corresponding to only approximately 13.1% removal. This large difference further demonstrates that the behaviour observed in the bulk cement experiments cannot simply be assigned to all of the individual minerals present.

Cs showed a different behaviour again. Approximately 96.1% of Cs remained in solution after eight days in the calcite experiment, corresponding to only approximately 3.9% removal. This is consistent with calcite not providing the same strong removal mechanism for Cs as it did for Sr. Cs does not readily form an equivalent low-solubility carbonate under the conditions investigated and its interaction with cementitious materials is more dependent on sorption and ion-exchange processes.

The results for the bulk cement samples were more variable. Approximately 100% of the starting Cs concentration was measured after eight days for both the C:S 4 cement cured at 250°C and NRVB cured at 200°C, indicating there was no measurable removal within the uncertainty of the experiment. In contrast, no Cs was measured in solution after eight days for the NRVB sample cured at 250°C. This apparent difference is very large and should be treated with caution. The experiments were not sufficiently replicated to determine whether this represents a reproducible mineralogical effect or experimental variability despite each experiment being run three times.

It would therefore be inappropriate to conclude from the current Cs results that curing NRVB at 250°C necessarily causes complete Cs retention. Instead, the results show that Cs behaviour requires further investigation using repeat experiments. This is an important limitation of Chapter 6 and repeats of the experiments would be required before a quantitative relationship between curing temperature, mineralogy and Cs retention could be established.

The radionuclide analogue results therefore show that removal from solution is strongly dependent on both the element and the mineral assemblage. Ce was almost completely removed from solution by the bulk cement samples, most likely because of its low solubility at high pH. Sr showed much lower removal from the bulk cement samples but reacted strongly with calcite, where strontianite formed. Cs showed little removal by calcite and highly variable behaviour in the cement experiments. These results demonstrate that there is no single mechanism by which NRVB retains radionuclides and that a robust understanding of the mineralogic composition of the cement is essential to predict how NRVB will interact with radionuclides.

Overall implications for NRVB performance

Taken together, the results from this thesis show that curing NRVB at elevated temperatures cannot simply be described as beneficial or detrimental. Increasing the curing temperature changes the original mineral assemblage, consumes portlandite and changes the pore structure. However, the magnitude and direction of these changes depend strongly on the C:S ratio. This is particularly clear from the porosity results. At 250°C, porosity varied from approximately 80% at C:S 4 and 89% for NRVB at C:S 7.27. Therefore, temperature alone does not explain the change in pore structure. The mineralogical composition produced at each C:S ratio also needs to be considered.

The same conclusion can be drawn from the mineralogical results. At C:S 4 and 250°C, approximately 25% xonotlite was present, whereas the more calcium-rich systems favoured phases including α-C_2SH, jaffeite and reinhardbraunsite. These results broadly agree with previous hydrothermal cement studies[56,276,282], but also show that the high C:S ratio of NRVB results in a different mineral phase assemblage from the silica-enriched oil-well cements that are more commonly investigated in the literature.

The radionuclide experiments show why these mineralogical changes are important. The secondary phases are not chemically inactive and can continue to influence porewater chemistry and radionuclide behaviour. However, the effect depends on the radionuclide and mineral involved. More than 98.6% of Ce was removed from solution by all three bulk cement samples investigated, whereas Sr removal was only approximately 2–17%. Calcite removed approximately 67% of Sr, compared with only approximately 10% for xonotlite, and strontianite was identified following reaction with calcite. The Cs results were more variable and cannot currently be used to establish a reliable relationship between mineralogy and retention.

The main conclusion from this thesis is therefore not that higher curing temperatures causes a loss of NRVB performance. Instead, elevated curing temperatures change the minerals which are responsible for the physical and chemical properties of NRVB. Portlandite is consumed and the original mineral phase assemblage is replaced by more crystalline calcium silicate and calcium aluminosilicate phases. At the same time, the pore structure changes and in some compositions the porosity increases substantially. However, the new mineral phases remain chemically reactive and can contribute to alkaline buffering and, depending on the radionuclide, removal from solution.

There are important limitations to applying these results directly to the performance of NRVB in a GDF. The hydrothermal experiments used temperatures substantially higher than those expected throughout much of a GDF and were carried out for only five days. Previous studies have shown that mineralogical and microstructural changes can continue in cements cured at higher temperatures[278,282]. The phases measured after five days in this study therefore may not represent the final equilibrium phase assemblage.

There are also limitations associated with the radionuclide experiments. The individual minerals were used to identify mineral specific behaviour, whereas NRVB in a GDF will contain several phases which can dissolve, precipitate and react at the same time. Groundwater composition, competing ions, carbonation and interactions with the other engineered and geological barriers will also affect radionuclide behaviour. The limited repeatability of the current sorption experiments, particularly the Cs experiments, also means that some of the quantitative differences observed cannot yet be considered reproducible.

Similarly, although changes in porosity were measured, permeability and diffusivity were not measured directly. The results therefore show how temperature and C:S ratio affect the mineralogy and pore structure but do not directly demonstrate how quickly radionuclides would move through thermally altered NRVB.

Overall, this thesis demonstrates that temperature and C:S ratio are both important controls on the mineralogical evolution of NRVB. The high C:S ratio samples favoured calcium-rich phases including α-C_2SH, jaffeite and reinhardbraunsite, whereas increasing the silica content promoted phases including xonotlite. These mineralogical changes were accompanied by substantial differences in porosity and by differences in the chemical behaviour of the phases produced.

The main contribution of this work is therefore linking these three areas together. Curing temperature and C:S ratio both control the mineralogical composition of the cement; the mineral assemblage affects the pore structure and solution chemistry; and the mineral and solution chemistry affect radionuclide retention. The results show that the loss of portlandite or the formation of high-temperature phases cannot on their own be used to determine whether NRVB will continue to perform its intended functions. Instead, both the physical changes to the cement and the chemical behaviour of the new mineral assemblage need to be considered when assessing the long-term behaviour of thermally altered NRVB.

7.3 The impact on the current GDF design

The current design for how ILW and HLW will be emplaced within the GDF is shown in Figure 5. Both HLW and ILW will be disposed of within a waste container which, after emplacement in the GDF, will be backfilled with a suitable material. The backfill material forms part of the engineered barrier system, the primary objective of which is to keep the radioactive waste safely contained within the GDF and to inhibit any radionuclides from entering the groundwater. To fulfil this objective of preventing radioactivity from reaching the groundwater and the biosphere, requirements will be placed upon the backfill that is chosen. The requirements of the backfill will also be influenced by the waste form, and waste packaging.

The properties of the backfill will feed into the safety and engineering requirements of the GDF, and the backfill will need to be optimised to ensure it meets these requirements. This should be done through an optimisation process whereby the

safety requirements, the GDF design, and the properties of the backfill intrinsically feed into one another to inform decisions as illustrated in Figure 90.

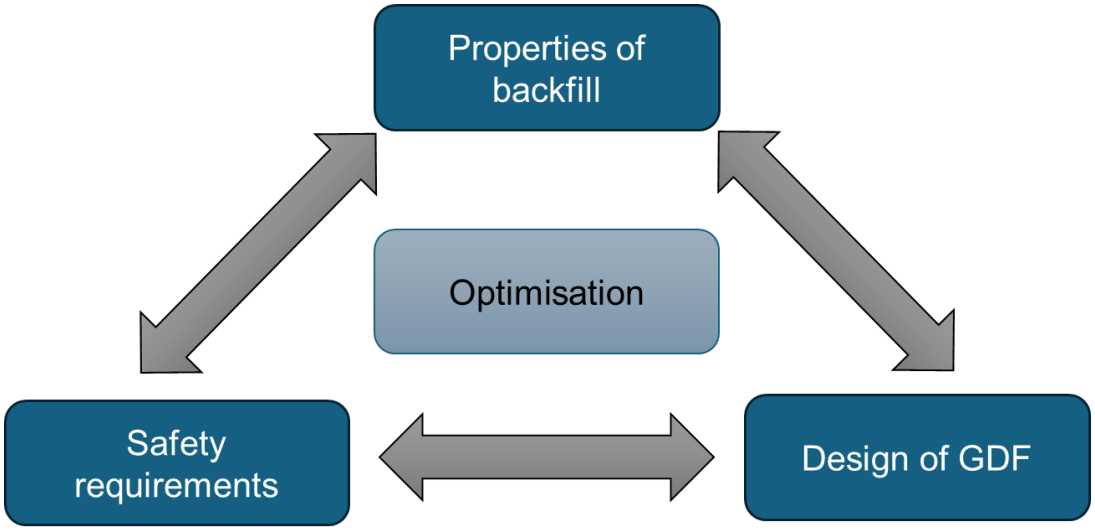


Figure 90: An illustration of how the properties of the backfill, the GDF design, and the safety requirements should feed into the designs and be underpinned by optimisation.

The first finding of this project that will affect the GDF design is that the temperature at which the NRVB cement is cured at affects the final mineralogy and porosity. This means that the waste packages emplaced within the GDF will need to be considered with regards to surface temperature as this will inform the mineralogical and physical (porosity) properties of the backfill directly. Alternatively, the C:S ratio of the NRVB could be altered to preferentially produce minerals with desirable properties once the waste package temperature is known. As was demonstrated in Chapter 3, Investigation into the effect of increasing the curing temperature and altering the C:S ratio of NRVB cement on the mineralogy, both the curing temperature and C:S ratio of NRVB cement can be altered to produce a particular mineralogy. If the temperature of the GDF is high enough to preferentially form strength reducing minerals then an additional barrier surrounding the backfill may be necessary depending on the host rock to account for the loss of strength triggered by the high temperature curing.

The second finding is that as the curing temperature is increased above 150°C the porosity increases. SEM images showed that above 150°C the porosity became less well defined, suggesting at higher curing temperatures there is a breakdown in structure as shown in Figure 91. This increase in porosity means groundwater and radionuclides will be able to move through the cement faster, assuming the pores are

interconnected. An important question that is raised by this finding is how long the cement is affected by this temperature gradient. If only the first few centimetres of backfill cement are impacted by the increased curing temperature and there is a significant amount of backfill then this is okay as the rest of the backfill will act as a barrier. However, if the temperature effects are far reaching within the backfill then this could affect the function of the backfill as a barrier if the porosity is increased to a depth that provides a pathway to groundwater. This finding could affect the required depth of backfill which has cost implications as a deeper backfill will require more volume within the GDF, or an additional barrier that provides containment may be added..



Figure 91: Diagram showing how the closer to the waste container the cement is cured the larger and more irregular the pores will be, this is due to the curing temperature being highest at the waste container.

The third finding that could impact on the design of the GDF arises from Chapter 6, The effect of mineralogical composition of NRVB cement on the mobility of radionuclides. In this chapter it was found that the high temperature minerals that form when the portlandite reacts are still able to buffer the pH and precipitate cerium out of solution. This finding is significant because cerium is an analogue for plutonium, a long lived radionuclide that will not have decayed to safe levels when the GDF is closed. The ability of the backfill to precipitate or bind radionuclides is important as it stops the radionuclides from entering the groundwater.

Calcite and xonotlite were able to reduce the concentration of strontium in solution. However, none of the minerals decreased the concentration of caesium in solution. This is not a concern as caesium has a short half-life so will have decayed to safe levels by the time the GDF is closed. However, if the minerals are investigated in the future for uses such as land remediation this is significant. If NRVB cement is chosen as the backfill for the GDF then further work to adapt the formulation or add an additive

that is able to capture caesium/ plutonium could be necessary depending on the final inventory that is disposed of in the GDF and the timescales the GDF is operated to.

7.4 Recommendations for Future Work

Throughout this project there are several research gaps identified that could inform future work. These are:

1. How the spatial arrangement of the minerals in regard to the pores within the cement affects their properties in regards to reducing the concentration of radionuclide in solution and buffering the pH.
2. How does NRVB cement perform in high salinity solution; what mineralogical changes occur when NRVB cement is exposed to high salinity solution, how is the porosity affected?
3. How is the mineralogy and porosity affected when the cement is cured against a temperature gradient?

More detail on these three suggested experimental questions is provided in sections 7.4.1, 7.4.2, and 7.4.3 below. The sections include a suggested experimental set up, what analysis should be undertaken, and the information this analysis would provide.

7.4.1 Proposed next experiment following Chapter 6: How the spatial arrangement of the minerals within the cement affects the properties in regards to reducing the concentration of radionuclide in solution and buffering the pH.

In Chapter 6 The effect of mineralogical composition of NRVB cement on the mobility of radionuclides, high temperature minerals and three NRVB cement mixes were tested to see how much radionuclide analogue they could remove from a solution. For these tests the minerals and cements were ground. This was due to the short experimental timeframes, to ensure there was as much surface area as possible to interact with the solution. The impact of doing this means there is no data as to the effect of where the minerals may be situated within a sample. For example, if a mineral is only found within the bulk of the cement it will be more difficult or impossible for the

radionuclide to reach it in a repository condition. Also, if a high ratio C:S mineral that can dissolve into the pore to buffer the pH is in the bulk of the cement it will not be able to dissolve into the pore water. Future experiments would involve testing a solid core of the cured NRVB cement in radionuclide solution. This would involve exposing one edge of the core to the solution as this would simulate repository conditions where the edge of backfill that is against the waste package would interact with the solution first (Figure 92). A vacuum would be applied to the other side of the cement core which would collect the solution once it had passed through. This solution would then be tested. Prior to this experiment the core should be scanned with the XCT, and the porosity measured using helium pycnometry. A marker should be attached to the outside of the core prior to XCT scanning so that once it is scanned after the tests the before and after scan can be aligned so the same pores can be compared to see if there is any degradation or accumulation. The core should be remeasured with helium pycnometry too. A limitation to this test is the size of the core that can be hydrothermally cured and then scanned with XCT to a high resolution. The core size will need to be carefully considered as will the duration of the test. The matrix used in the test will need to be carefully selected as if the radionuclide solution uses water this can cause further hydration reactions to occur within the cement.

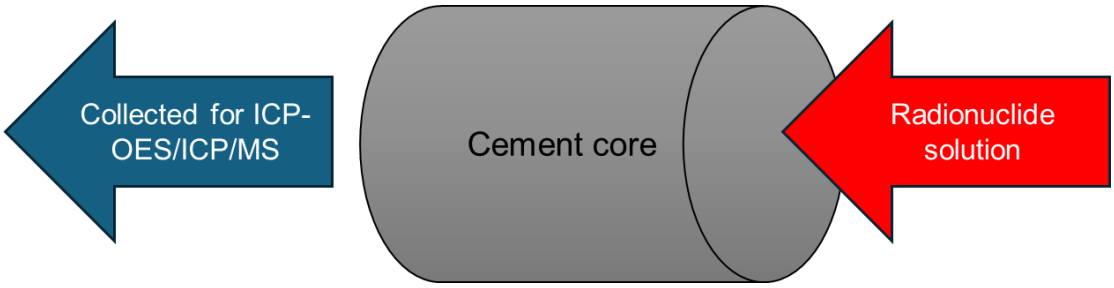


Figure 92: A suggested experimental setup to test how effective the cement cores are at removing radionuclide from solution.

Following the tests described above the strength of the cement cores should be measured. If high ratio C:S minerals are dissolving into solution, and/or minerals are reacting with radionuclides such as strontium, this could affect the strength and stability of the backfill.

A challenge with testing cores of the mineral is the strength of the individual minerals. Several tested in Chapter 6 formed as powders, and the NRVB cements with variable C:S ratios cured above 150°C were extremely fragile. A consideration could be to

compact the powders into a pellet and test this inside a plastic tube that offers stability, and to then use a very weak flow of radionuclide solution.

7.4.2 Proposed next experiment: How does NRVB cement perform in high salinity solution; what mineralogical changes occur when NRVB cement is exposed to high salinity solution, how is the porosity affected?

The location where the GDF will be built has not been determined yet, and some of the potential host rock around the UK has a high salinity. It will be important to understand how the NRVB cement backfill behaves when it is exposed to a high saline groundwater to underpin the decision as to where the GDF should be hosted. Groundwater ingress will occur once the engineered barrier systems begin to fail, so should not occur until after the cement has cured, therefore experiments should be undertaken with cured NRVB cement samples.

These experiments could be run by curing a NRVB cement sample then immersing it within a saline sample. This should be done within a plastic container as portlandite and other minerals from the cement may raise the pH of the saline solution and leach silicon from a glass container. The container should have an airtight seal to prevent additional CO_2 from entering the system, and to prevent water evaporating from the saline solution and altering the concentration of salt. This experiment could be run by having a level of saline solution that just covers the base of the cement sample, or where the sample is immersed in saline solution. A simple diagram of the experimental set up is illustrated in Figure 93.

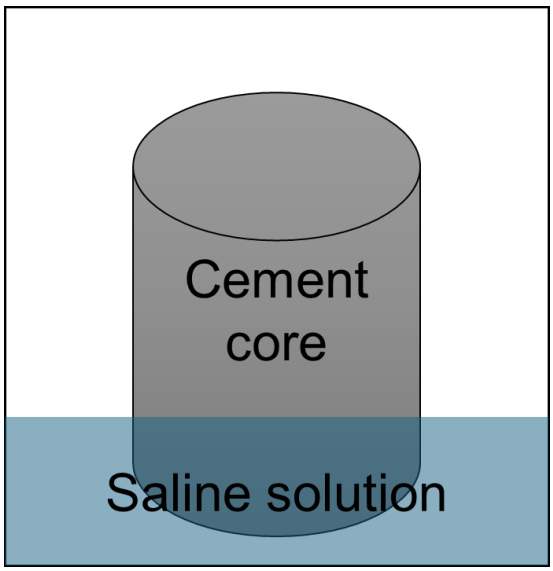


Figure 93: A suggested experimental setup to investigate how cured NRVB cement behaves when exposed to a saline solution that is acting as a groundwater analogue.

Over the duration of this experiment photographs of the sample should be taken at regular intervals so that the integrity of it can be measured. The sample could also have a marker embedded during curing so it can be scanned with XCT then rescanned during and after the experiment to measure the effect of the saline solution on individual pores. SEM and EMPA should be done on a sample that is not exposed to a saline solution, and the sample that has been exposed. Elemental maps of the salts included in the saline solution can be used to map the ingress of the salt into the cement. This would also show if the salt accumulates in the bulk or the pore space of the cement. XRD analysis of the cement before and after the experiment could be analysed quantitatively to assess if the concentrations of the minerals are affected by interacting with the saline solution.

These experiments would provide data about the stability of NRVB cement in a saline solution that would help provide evidence towards the argument of where the GDF could be sited. If these experiments show that NRVB cement is unstable and unsuitable for use in a high saline environment then a different backfill material will need to be chosen, alternatively if the NRVB cement is stable in the high saline groundwater then it is evidence for it to be incorporated into the GDF design should an appropriate site be selected.

7.4.3 Proposed next experiment: How is the mineralogy affected when the cement is cured against a temperature gradient?

This thesis studied the effects of curing NRVB cements at temperatures between 25 and 250°C, heating the cements to one single temperature for the duration of the cement curing. In real repository conditions it is unlikely that the whole cementitious system will be exposed to the same temperature. The waste packages will be producing heat, and the temperature of the host rock will mean the cement is cured at a range of temperatures, this is represented in a simple diagram in Figure 94. As the location of the GDF is not known, the host rock temperature is also unknown. The temperature the waste packages will emit is also unknown as there is no repository design. Factors that will affect the temperature emitted from the waste include the time the waste is stored before a GDF is available, how closely the waste is packaged, the fissile content of the waste, the packaging design, and what waste is chosen for disposal in the GDF.

Future experiments could try and simulate temperature gradients that the NRVB backfill could encounter whilst curing by heating one end of the cement whilst cooling the other. This will be challenging to replicate under hydrothermal conditions and to ensure the cement does not reach a constant temperature inside the reaction vessel temperature sensors will be needed.

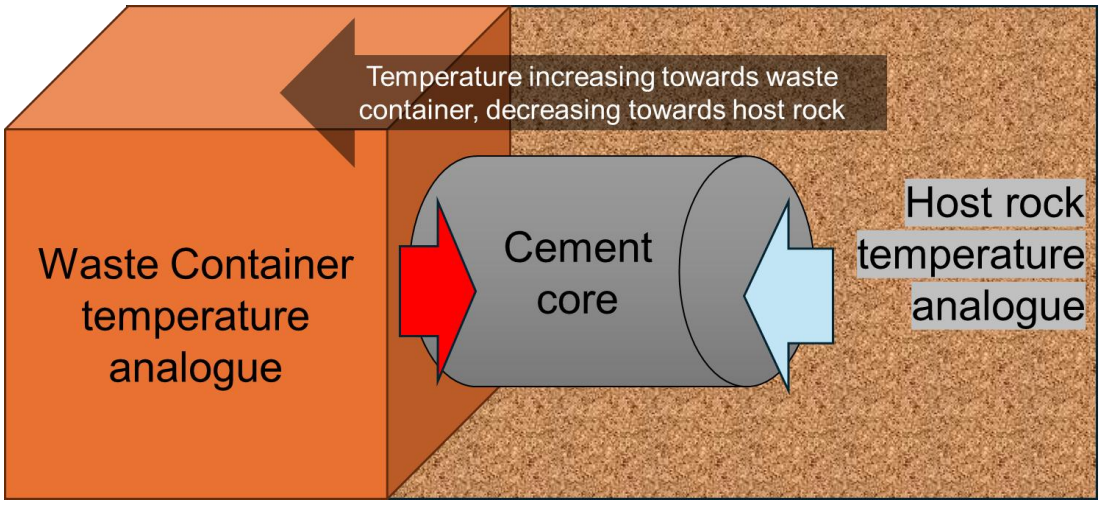


Figure 94: A suggestion for an experimental setup where a cement core is exposed to a temperature representative of the heat produced by a waste container at one end, and at the other it is exposed to the temperature of the GDF host rock.

After the cement has been exposed to the temperature gradient it would have the porosity measured to see if it is affected by the different curing temperatures. As shown below in Figure 95 the cement sample would then be prepared for SEM/EMPA analysis and XRD analysis. For SEM/EMPA analysis a section of the core would be taken across the temperature gradient, this would allow for study of how the porosity changes at the different curing temperatures and where minerals are forming. For XRD analysis samples would be taken in temperature increments so that the mineralogy evolution across the temperature gradient can be studied. In Figure 95 it is assumed that the core is in the same orientation as in Figure 94 where the left side of the core was heated and the right side cooled.

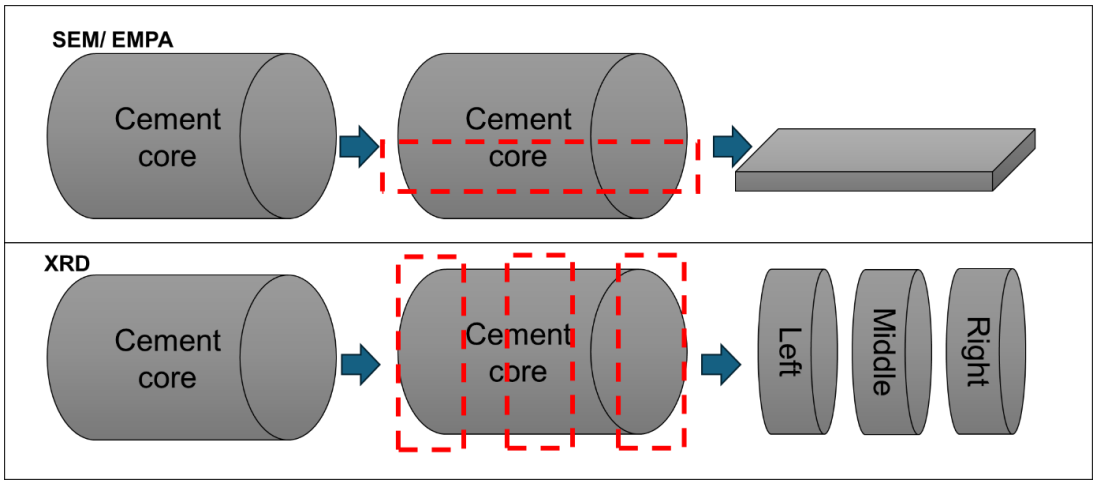


Figure 95: Two schematics showing how the cement sample would be prepared for SEM/EMPA (top) and XRD analysis (bottom).

These experiments would provide information as to repository conditions where there will be a temperature gradient once the backfill has been poured in, so the NRVB cement will cure at different temperatures. Information on how the mineralogy and porosity changes across the temperature gradient, and how long each temperature affects the mineralogy and porosity will provide useful information for the design of the repository. If the temperature of the backfill at the waste package is only affected for a short distance then less backfill may be needed, conversely if the effect of the higher temperature is longer reaching then a thicker layer of backfill will be necessary.

7.5 Overall Conclusions of the Discussion

The aim of this thesis project was to study the effect of high temperatures on NRVB cement. This was achieved by studying the mineralogical composition at different curing temperatures, the effect on porosity, and the consequences of curing at higher temperatures on the ability of the NRVB cement to arrest radionuclides.

The key findings of this thesis are:

- There is a direct relationship between the curing temperature and the mineralogy, which causes an increased porosity at higher curing temperatures.
- The C:S ratio and curing temperature can be controlled to preferentially form specific minerals that have desirable properties. This means the cement formulation can be optimised for the repository conditions (the heat of the external walls of the packages and temperature of the vaults).
- The mineral composition controls radionuclide immobilisation pathways, different minerals have different interaction methods with radionuclides and have different abilities to buffer the pH.

The overall implication of these findings is that the long-term cement performance and safety functions depend on both mineralogical and microstructural evolution which depend on the curing temperature and C:S ratio of the cement. Understanding the temperature of the surface of the waste packages will be an important parameter when choosing the backfill for the GDF, the thickness of the backfill, and the design of the backfill.

The research undertaken in this thesis provides important information on the mineralogy of higher temperature cements, and with higher C:S ratios than had previously been studied. It also contributes novel information on forming high temperature minerals and how they interact with radionuclides in solution.

References

1 What are the main waste categories? - UK Radioactive Waste & Materials Inventory, https://ukinventory.nda.gov.uk/information-hub/factsheets/what-are-the-main-waste-categories/, (accessed 26 May 2026).

2 H. R. Doran, C. S. Brown, I. Kolo, G. Falcone and D. C. W. Sanderson, Modelling a novel technique to remove excess decay heat from a geological disposal facility using a closed-loop geothermal system, *Thermal Science and Engineering Progress*, 2025, **57**, 103090.

3 R. G. W. Vasconcelos, A. Idiart, N. C. Hyatt, J. L. Provis and C. L. Corkhill, Leaching of Nirex Reference Vault Backfill cement by clay, granite and saline groundwaters, DOI:10.1557/adv.2018.248.

4 R. G. W. Vasconcelos, N. Beaudoin, A. Hamilton, N. C. Hyatt, J. L. Provis and C. L. Corkhill, Characterisation of a high pH cement backfill for the geological disposal of nuclear waste: The Nirex Reference Vault Backfill, *Applied Geochemistry*, 2018, **89**, 180–189.

5 Ministry of Defence and Foreign & Commonwealth Office, The History of the UK's Nuclear Weapons Programme, https://assets.publishing.service.gov.uk/government/uploads/system/uploads/attachment_data/file/27383/Cm6994_Factsheet5.pdf#:~:text=The%20United%20Kingdom%E2%80%99s%20nuclear%20weapons%20programme%20had%20its,a%20larger%20joint%20effort%20%E2%80%93%20the%20Manhattan%20Project., (accessed 13 March 2022).

6 Department for Business Energy & Industrial Strategy and NDA, *2019 UK Radioactive Waste Inventory*, 2019.

7 nuclear reactor - From production reactors to commercial power reactors | Britannica, https://www.britannica.com/technology/nuclear-reactor/From-production-reactors-to-commercial-power-reactors#ref1174534, (accessed 13 March 2022).

8 Demolition starts on Windscale chimney - GOV.UK, https://www.gov.uk/government/news/demolition-starts-on-windscale-chimney, (accessed 13 March 2022).

9 NDA, *PROGRESS ON PLUTONIUM CONSOLIDATION, STORAGE AND DISPOSITION*, 2019.

10 Nuclear Waste Services, What is radioactive waste? The science files, https://assets.publishing.service.gov.uk/government/uploads/system/uploads/attachment_data/file/1051061/What_is_radioactive_waste__NWS.pdf, (accessed 13 March 2022).

11 Deterministic vs. Stochastic Effects: What Are the Differences?, https://versantphysics.com/2021/04/21/deterministic-vs-stochastic-effects/, (accessed 13 March 2022).

12 E. Cardis, D. Krewski, M. Boniol, V. Drozdovitch, S. C. Darby, E. S. Gilbert, S. Akiba, J. Benichou, J. Ferlay, S. Gandini, C. Hill, G. Howe, A. Kesminiene, M. Moser, M. Sanchez, H. Storm, L. Voisin and P. Boyle, Estimates of the cancer burden in Europe from radioactive fallout from the Chernobyl accident, *Int. J. Cancer*, 2006, **119**, 1224–1235.

13 *NRC REVIEW OF THE TOKAI-MURA CRITICALITY ACCIDENT APRIL 2000 DIVISION OF FUEL CYCLE SAFETY AND SAFEGUARDS OFFICE OF NUCLEAR MATERIAL SAFETY AND SAFEGUARDS US NUCLEAR REGULATORY COMMISSION NRC REVIEW OF THE TOKAI-MURA CRITICALITY ACCIDENT*, .

14 Tokaimura Criticality Accident - World Nuclear Association, https://world-nuclear.org/information-library/safety-and-security/safety-of-plants/tokaimura-criticality-accident.aspx?msclkid=c7a8e603b92f11eca26dadcd3b758738, (accessed 11 April 2022).

15 Nuclear Power in the United Kingdom |UK Nuclear Energy - World Nuclear Association, https://www.world-nuclear.org/information-library/country-profiles/countries-t-z/united-kingdom.aspx?msclkid=c42585b8b93211ec9cad4b9c8dfb7b43, (accessed 11 April 2022).

16 P. Stein and S. Macfarlane-Smith, Nuclear designs on a low-carbon future, *Ingenia*.

17 J. Tang, *OFFICE OF CIVILIAN RADIOACTIVE WASTE MANAGEMENT CALCULATION COVER SHEET 1. OA-Page: OA 1 Of: 67 2. Calculation Title Decay Heat of Major Radionuclides for PWR Spent Fuels to 10,000 Years MOL.20020107.0154 3. Document Identifier (including Revision Number) Waste Package Project Calculation CONTENTS*, 2001.

18 RWM, Geological Disposal Engineered Barrier System Status Report.

19 RWM, Geological Disposal Engineered Barrier System Status Report.

20 NDA Report no DSSC/402/01 - Geological Disposal: Generic Disposal System Specification Part B: Technical Specification.

21 Nuclear Power in the United Kingdom |UK Nuclear Energy - World Nuclear Association, https://www.world-nuclear.org/information-library/country-profiles/countries-t-z/united-kingdom.aspx?msclkid=28d653b1bf0b11eca4ada00e880fa481, (accessed 18 April 2022).

22 Radioactive Waste Management | Nuclear Waste Disposal - World Nuclear Association, https://world-nuclear.org/information-library/nuclear-fuel-cycle/nuclear-wastes/radioactive-waste-management.aspx?msclkid=28d4623cbf0b11eca3214aa0e7afbf45, (accessed 18 April 2022).

23 Radioactive Waste Strategy September 2019 - GOV.UK, https://www.gov.uk/government/consultations/nda-radioactive-waste-

management-strategy/outcome/radioactive-waste-strategy-september-2019, (accessed 3 June 2026).

24 Nuclear Waste Services, *GDF Annual Report 2020-2021*, 2022.

25 Nuclear Waste Services, What will a GDF look like?, https://assets.publishing.service.gov.uk/government/uploads/system/uploads/attachment_data/file/1051119/What_will_a_GDF_look_like__NWS.pdf, (accessed 14 March 2022).

26 Explaining the multi-barrier approach of a GDF - South Copeland GDF Community Partnership, https://southcopeland.workinginpartnership.org.uk/2024/07/23/explaining-the-multi-barrier-approach-of-a-gdf/, (accessed 25 March 2026).

27 The Infrastructure Planning (Radioactive Waste Geological Disposal Facilities) Order 2015.

28 The Infrastructure Planning (Radioactive Waste Geological Disposal Facilities) Order 2015, https://www.legislation.gov.uk/uksi/2015/949/article/2/made?, (accessed 2 October 2026).

29 National Policy Statement for Geological Disposal Infrastructure - GOV.UK, https://www.gov.uk/government/publications/national-policy-statement-for-geological-disposal-infrastructure, (accessed 2 October 2026).

30 The Environmental Permitting (England and Wales) Regulations 2016.

31 Regulating the geological disposal of radioactive waste: environmental protection - GOV.UK, https://www.gov.uk/guidance/regulating-the-geological-disposal-of-radioactive-waste-environmental-protection, (accessed 2 October 2026).

32 Regulating geological disposal an overview.

33 R. G. W. Vasconcelos, B. Walkley, S. Day, C. C. Tang, H. Paraskevoulakos, L. J. Gardner and C. L. Corkhill, 18-month hydration of a low-pH cement for geological disposal of radioactive waste: The Cebama reference cement, DOI:10.1016/j.apgeochem.2020.104536.

34 T. Vehmas, V. Montoya, M. C. Alonso, R. Vašíček, E. Rastrick, S. Gaboreau, P. Večerník, M. Leivo, E. Holt, N. Fink, N. A. Mouheb, J. Svoboda, D. Read, R. Radekˇradekčervinka, R. Vasconcelos and C. Corkhill, Characterization of Cebama low-pH reference concrete and assessment of its alteration with representative waters in radioactive waste repositories, *Applied Geochemistry*, 2020, **121**, 104703.

35 M. A. Saghiri, J. Orangi, A. Asatourian, J. L. Gutmann, F. Garcia-Godoy, M. Lotfi and N. Sheibani, Calcium silicate-based cements and functional impacts of various constituents, *Dent. Mater. J.*, 2017, **36**, 8.

36 P. Brown, Hydration of cementitious materials, DOI:10.1680/mocm.35973.0069.

37 T. Vehmas, V. Montoya, M. C. Alonso, R. Vašíček, E. Rastrick, S. Gaboreau, P. Večerník, M. Leivo, E. Holt, N. Fink, N. A. Mouheb, J. Svoboda, D. Read, R. Radekˇradekčervinka, R. Vasconcelos and C. Corkhill, Characterization of Cebama low-pH reference concrete and assessment of its alteration with representative waters in radioactive waste repositories, *Applied Geochemistry*, 2020, **121**, 104703.

38 M. Felipe-Sotelo, J. Hinchliff, L. P. Field, A. E. Milodowski, O. Preedy and D. Read, Retardation of uranium and thorium by a cementitious backfill developed for radioactive waste disposal, *Chemosphere*, 2017, **179**, 127–138.

39 T. Heath, J. Schofield and A. Shelton, Understanding cementitious backfill interactions with groundwater components, *Applied Geochemistry*, 2020, **113**, 104495.

40 G. M. N. Baston, M. M. Cowper and T. A. Marshall, Sorption properties of aged cements, *Mineral. Mag.*, 2012, **76**, 3411–3423.

41 G. M. N. Baston, M. M. Cowper and T. A. Marshall, Sorption properties of aged cements, *Mineral. Mag.*, 2012, **76**, 3411–3423.

42 N. C. Collier, D. W. Heyes, E. J. Butcher, J. Borwick, A. E. Milodowski, L. P. Field, S. J. Kemp, I. Mounteney, S. A. Bernal, C. L. Corkhill, N. C. Hyatt, J. L. Provis and L. Black, Gaseous carbonation of cementitious backfill for geological disposal of radioactive waste: Nirex Reference Vault Backfill, *Applied Geochemistry*, 2019, **106**, 120–133.

43 Radioactivity : Carbon-14, https://www.radioactivity.eu.com/site/pages/RadioCarbon.htm, (accessed 11 April 2022).

44 T. Heath, J. Schofield and A. Shelton, Understanding cementitious backfill interactions with groundwater components, *Applied Geochemistry*, 2020, **113**, 104495.

45 E. Asadi Amirabadi, M. Salimi, N. Ghal-Eh, G. reza Etaati, C. Author, M. Salimi, G. Reza Etaati and H. Asadi, Study of Neutron and Gamma Radiation Protective Shield Iran View project Study of Neutron and Gamma Radiation Protective Shield, *Int. J. Innov. Appl. Stud.*, **3**, 1079–1085.

46 D. A. Costa, M. E. Cournoyer, J. F. Merhege, V. E. Garcia and A. N. Sandoval, A primer on criticality safety, *J. Chem. Health Saf.*, 2017, **24**, 7–13.

47 M. Michaux, E. Nelson and B. Vidick, Chemistry and Characterization of Portland Cement, *Well Cementing*, 1–17.

48 P. Brown, Hydration of cementitious materials, DOI:10.1680/mocm.35973.0069.

49 N. Meller, K. Kyritsis and C. Hall, The mineralogy of the CaO-Al 2 O 3-SiO 2-H 2 O (CASH) hydroceramic system from 200 to 350 °C, *Cem. Concr. Res.*, 2008, **39**, 45–53.

50 N. Meller, C. Hall and J. S. Phipps, A new phase diagram for the CaO-Al 2 O 3-SiO 2-H 2 O hydroceramic system at 200 8C, DOI:10.1016/j.materresbull.2005.03.001.

51 N. Meller, C. Hall, K. Kyritsis and G. Giriat, Synthesis of cement based CaO-Al 2 O 3-SiO 2-H 2 O (CASH) hydroceramics at 200 and 250 °C: Ex-situ and in-situ diffraction, DOI:10.1016/j.cemconres.2007.03.006.

52 K. Kyritsis, C. Hall, D. P. Bentz, N. Meller and M. A. Wilson, Relationship Between Engineering Properties, Mineralogy, and Microstructure in Cement-Based Hydroceramic Materials Cured at 2001-3501C, DOI:10.1111/j.1551-2916.2008.02914.x.

53 K. Kyritsis, N. Meller and C. Hall, Chemistry and Morphology of Hydrogarnets Formed in Cement-Based CASH Hydroceramics Cured at 2001 to 3501C, DOI:10.1111/j.1551-2916.2009.02958.x.

54 S. A. Kärnbränslehantering, Svensk Kärnbränslehantering AB Horizontal deposition of canisters for spent nuclear fuel Horizontal deposition of canisters for spent nuclear fuel.

55 J. Castro, D. Bentz and J. Weiss, Effect of sample conditioning on the water absorption of concrete, DOI:10.1016/j.cemconcomp.2011.05.007.

56 N. Meller, K. Kyritsis and C. Hall, The mineralogy of the CaO-Al 2 O 3-SiO 2-H 2 O (CASH) hydroceramic system from 200 to 350 °C, DOI:10.1016/j.cemconres.2008.10.002.

57 K. L. Scrivener, R. Snellings and B. Lothenbach, A Practical Guide to Microstructural Analysis of Cementitious Materials,CRC Press, Taylor & Francis Group, *CRC Press, Taylor & Francis Group*.

58 H. F. W. (Harry F. W.) Taylor, Cement chemistry (2nd edition), *Thomas Telford Publishing*, 1997, 0–470.

59 K. Scrivener, R. Snellings and B. Lothenbach, A practical guide to microstructural analysis of cementitious materials, *A Practical Guide to Microstructural Analysis of Cementitious Materials*, 2016, 1–531.

60 F. P. Glasser, CEMENTS IN RADIOACTIVE WASTE DISPOSAL.

61 U. R. Berner, Evolution of pore water chemistry during degradation of cement in a radioactive waste repository environment, *Waste Management*, 1992, **12**, 201–219.

62 N. Saeki, R. Kurihara and I. Maruyama, Applicability of XRD/Rietveld Analysis with an External Standard Method for the Quantification of Mineral Components in Carbonated Hardened Cement Paste, *Journal of Advanced Concrete Technology*, 2024, **22**, 602–619.

63 R. Snellings, A. Salze and K. L. Scrivener, Use of X-ray diffraction to quantify amorphous supplementary cementitious materials in anhydrous and hydrated blended cements, *Cem. Concr. Res.*, 2014, **64**, 89–98.

64 C. E. Boyd, Carbon Dioxide, pH, and Alkalinity, *Water Quality*, 2020, 177–203.

65 R. Ylmén and U. Jäglid, Carbonation of Portland Cement Studied by Diffuse Reflection Fourier Transform Infrared Spectroscopy, *International Journal of Concrete Structures and Materials 2013 7:2*, 2013, **7**, 119–125.

66 S. T. Pham and W. Prince, Effects of Carbonation on the Microstructure of Cement Materials: Influence of Measuring Methods and of Types of Cement, *Int. J. Concr. Struct. Mater.*, 2014, **8**, 327–333.

67 J. Zhang and G. W. Scherer, Comparison of methods for arresting hydration of cement, *Cem. Concr. Res.*, 2011, **41**, 1024–1036.

68 V. Shah, K. Scrivener, B. Bhattacharjee and S. Bishnoi, Changes in microstructure characteristics of cement paste on carbonation, *Cem. Concr. Res.*, 2018, **109**, 184–197.

69 N. V. Y. Scarlett, I. C. Madsen, L. M. D. Cranswick, T. Lwin, E. Groleau, G. Stephenson, M. Aylmore and N. Agron-Olshina, Outcomes of the International Union of Crystallography Commission on Powder Diffraction round robin on quantitative phase analysis: Samples 2, 3, 4, synthetic bauxite, natural granodiorite and pharmaceuticals, *J. Appl. Crystallogr.*, 2002, **35**, 383–400.

70 Z. Zhang, G. W. Scherer and A. Bauer, Morphology of cementitious material during early hydration, *Cem. Concr. Res.*, 2018, **107**, 85–100.

71 K. Scrivener, R. Snellings and B. Lothenbach, *A practical guide to microstructural analysis of cementitious materials*, CRC Press, 2016.

72 J. Epp, X-ray diffraction (XRD) techniques for materials characterization, *Materials Characterization Using Nondestructive Evaluation (NDE) Methods*, 2016, 81–124.

73 H. M. Rietveld, A profile refinement method for nuclear and magnetic structures, *urn:issn:0021-8898*, 1969, **2**, 65–71.

74 B. D. . Cullity, *Elements of x-ray diffraction*, Addison-Wesley Publishing Company, Inc., 1978.

75 R. Snellings, X-ray powder diffraction applied to cement, *A Practical Guide to Microstructural Analysis of Cementitious Materials*, 2016, 107–176.

76 D. Zagorac, H. Muller, S. Ruehl, J. Zagorac and S. Rehme, Recent developments in the Inorganic Crystal Structure Database: Theoretical crystal structure data and related features, *J. Appl. Crystallogr.*, 2019, **52**, 918–925.

77 D. L. Bish and S. A. Howard, Quantitative phase analysis using the Rietveld method, *J. Appl. Crystallogr.*, 1988, **21**, 86–91.

78 H. M. Jennings, Refinements to colloid model of C-S-H in cement: CM-II, *Cem. Concr. Res.*, 2008, **38**, 275–289.

79 K. L. Scrivener, Backscattered electron imaging of cementitious microstructures: Understanding and quantification, *Cem. Concr. Compos.*, 2004, **26**, 935–945.

80 W. A. Gutteridge, On the dissolution of the interstitial phases in Portland cement, *Cem. Concr. Res.*, 1979, **9**, 319–324.

81 M. Pedrotti, A. Tarantino, A. Annese, F. Cotecchia and C. Vitone, Manuscript title: A microstructural insight into the compression behaviour of scaly clays, DOI:10.1680/jgeot.23.00269.

82 T. Degen, M. Sadki, E. Bron, U. König and G. Nénert, The HighScore suite, *Powder Diffr.*, 2014, **29**, S13–S18.

83 A. A. Coelho, TOPAS and TOPAS-Academic: An optimization program integrating computer algebra and crystallographic objects written in C++: An, *J. Appl. Crystallogr.*, 2018, **51**, 210–218.

84 J. Li, W. Zhang and P. J. M. Monteiro, Preferred orientation of calcium aluminosilicate hydrate compacts: Implications for creep and indentation, *Cem. Concr. Res.*, DOI:10.1016/j.cemconres.2021.106371.

85 S. Medina-Carrasco and J. M. Valverde, The Calcium Looping process for energy storage: Insights from in situ XRD analysis, *Chemical Engineering Journal*, DOI:10.1016/j.cej.2021.132244.

86 B. Šavija and M. Luković, Carbonation of cement paste: Understanding, challenges, and opportunities, *Elsevier Ltd*, 2016, preprint, DOI: 10.1016/j.conbuildmat.2016.04.138.

87 W. Ashraf, Carbonation of cement-based materials: Challenges and opportunities, *Elsevier Ltd*, 2016, preprint, DOI: 10.1016/j.conbuildmat.2016.05.080.

88 C. Boyd and W. Quality, pH, Carbon Dioxide, and Alkalinity, *Water Quality*, 2015, 153–178.

89 R. G. W. Vasconcelos, N. Beaudoin, A. Hamilton, N. C. Hyatt, J. L. Provis and C. L. Corkhill, Characterisation of a high pH cement backfill for the geological disposal of nuclear waste: The Nirex Reference Vault Backfill, *Applied Geochemistry*, 2018, **89**, 180–189.

90 T. Heath, J. Schofield and A. Shelton, Understanding cementitious backfill interactions with groundwater components, *Applied Geochemistry*, 2020, **113**, 104495.

91 Radioactive Waste Management, *Geological Disposal Engineered Barrier System Status Report*, 2016.

92 British Geological Survey, Potential Natural Changes and Implications for a UK GDF Minerals and Waste Programme Commissioned Report CR/12/127 N, 2012.

93 R. Waste Management Limited, *RWM - Geological Disposal - Science and Technology Plan 2020*, 2020.

94 Geothermal technologies - British Geological Survey, https://www.bgs.ac.uk/geology-projects/geothermal-energy/geothermal-technologies, (accessed 22 December 2025).

95 Bulk cement products | Hanson UK, https://www.hanson.co.uk/en/products/bulk-cement, (accessed 11 April 2022).

96 Hydrated Lime | Tarmac Buxton Lime, http://tarmacbuxtonlime.com/products/lime/hydrated-lime/, (accessed 11 April 2022).

97 Limestone Powders | Tarmac Buxton Lime, http://tarmacbuxtonlime.com/products/limestone-powders/, (accessed 11 April 2022).

98 R. M. Kroc, X-ray Fluorescence Spectrometry X-ray Fluorescence.

99 What is X-Ray Fluorescence (XRF) - Scimed, https://www.scimed.co.uk/education/what-is-x-ray-fluorescence-xrf, (accessed 22 December 2025).

100 Hanson Cement, Chemical Report - Composition of Ribblesdale PC, https://www.hanson.co.uk/system/files/assets/document/cc/05/chem_wk_2021-44_ribblesdale_pc_-_ribblesdale.pdf, (accessed 24 October 2022).

101 T. Wei, F. Wei, J. Zhou, Z. Wu, C. Zhang, J. Zhuang and X. Cheng, Formation and strengthening mechanisms of xonotlite in C3S-silica and C2S-silica powder systems under high temperature and pressure, *Cem. Concr. Res.*, 2022, **157**, 106812.

102 A. Quennoz and K. L. Scrivener, Hydration of C3A–gypsum systems, *Cem. Concr. Res.*, 2012, **42**, 1032–1041.

103 N. Meller, C. Hall and J. S. Phipps, A new phase diagram for the CaO-Al 2 O 3-SiO 2-H 2 O hydroceramic system at 200 8C, DOI:10.1016/j.materresbull.2005.03.001.

104 N. Meller, K. Kyritsis and C. Hall, The mineralogy of the CaO-Al 2 O 3-SiO 2-H 2 O (CASH) hydroceramic system from 200 to 350 °C, *Cem. Concr. Res.*, 2008, **39**, 45–53.

105 L. P. Esteves, On the hydration of water-entrained cement-silica systems: Combined SEM, XRD and thermal analysis in cement pastes, *Thermochim. Acta*, DOI:10.1016/j.tca.2011.02.003.

106 L. Black, C. Breen, J. Yarwood, C. S. Deng, J. Phipps and G. Maitland, Hydration of tricalcium aluminate (C3A) in the presence and absence of gypsum—studied by Raman spectroscopy and X-ray diffraction, *J. Mater. Chem.*, 2006, **16**, 1263–1272.

107 N. Meller, K. Kyritsis and C. Hall, The mineralogy of the CaO-Al 2 O 3-SiO 2-H 2 O (CASH) hydroceramic system from 200 to 350 °C, DOI:10.1016/j.cemconres.2008.10.002.

108 K. Kyritsis, C. Hall, D. P. Bentz, N. Meller and M. A. Wilson, Relationship Between Engineering Properties, Mineralogy, and Microstructure in Cement-Based Hydroceramic Materials Cured at 2001-3501C, DOI:10.1111/j.1551-2916.2008.02914.x.

109 T. Mohammed, A. Torres, F. Aguayo, P. Huynh, I. K. Okechi and A. Mankar, Heat of hydration and chemical shrinkage of early-age hardening cement paste produced with calcium sulfoaluminate cement incorporating fly ash and limestone powder, *Journal of Building Pathology and Rehabilitation 2025 10:2*, 2025, **10**, 152.

110 N. Chitvoranund, B. Lothenbach, D. Londono-Zuluaga, F. Winnefeld and K. Scrivener, Influence of temperature on phase assemblages of belite-ye'elimite cement, *Cem. Concr. Res.*, 2023, **174**, 107339.

111 B. D. Cullity and S. R. Stock, *Elements of X-Ray Diffraction Textbook*, Prentice Hall, Upper Saddle River, NJ., 3rd edn., 2001.

112 D. Stephan and S. Wistuba, Crystal structure refinement and hydration behaviour of doped tricalcium aluminate, *Cem. Concr. Res.*, 2006, **36**, 2011–2020.

113 S. B. Singh, P. Munjal and N. Thammishetti, Role of water/cement ratio on strength development of cement mortar, *Journal of Building Engineering*, 2015, **4**, 94–100.

114 T. Slamečka and F. Škvára, *THE EFFECT OF WATER RATIO ON MICROSTRUCTRE AND COMPOSITION OF THE HYDRATION PRODUCTS OF PORTLAND CEMENT PASTES*, 2002, vol. 46.

115 C. Hejny and T. Armbruster, Polytypism in xonotlite Ca6Si6O17(OH)2, *Z. Kristallogr. Cryst. Mater.*, 2001, **216**, 396–408.

116 T. P. Kuznetsova, N. N. Nevskii, V. V. Ilyukhin and N. V. Belov, Refinement of the crystal structure of calcium chondrodite Ca5[SiO4]2(OH)2=Ca(OH)2*2Ca2SiO4 Locality: synthetic.

117 N. A. Yamnova, K. Sarp, E.-T. Y. K and D. Y. Pushcharovskii, Crystal structure of jaffeite.

118 S. Udagawa, K. Urabe, M. Natsume and T. Yano, Refinement of the crystal structure of gamma-Ca2SiO4.

119 R. E. Marsh, A revised structure for alpha-dicalcium silicate hydrate.

120 T. Runčevski, R. E. Dinnebier, O. V. Magdysyuk and H. Pöllmann, Crystal structures of calcium hemicarboaluminate and carbonated calcium hemicarboaluminate from synchrotron powder diffraction data.

121 L. Schropfer and H. Bartl, Oriented decomposition and reconstruction of hydrogarnet, Ca3.Al2.(OH)12 Sample: specimen C12A7H15, intermediate phase resulting from the decomposition of hydrogarnet. Ca12Al14O33(H2O)15.

122 A. Kyono and S. Arora, Crystal structure change in grossular-Si-free katoite solid solution: Oxygen position splitting in katoite.

123 L. Desgranges, D. Grebille, g Calvarin, G. Chevrier, N. Floquet and J.-C. Niepce, Hydrogen thermal motion in calcium hydroxide: Ca (O H)2.

124 K. Kihara, An X-ray study of the temperature dependence of the quartz structure Sample: at T = 298 K.

125 T. Tsurumi, Y. Hirano, H. Kato, T. Kamiya and M. Daimon, Crystal structure and hydration of belite.

126 W. A. Wooster, On the crystal structure of gypsum Ca S O4 (H2 O)2.

127 S. A. Markgraf and R. J. Reeder, High-temperature structure refinements of calcite and magnesite Sample: T = 24 C.

128 E. Kuzielová, M. Žemlička, J. Másilko and M. T. Palou, Pore structure development of blended G-oil well cement submitted to hydrothermal curing conditions, *Geothermics*, 2017, **68**, 86–93.

129 R. B. Pernites and A. K. Santra, Portland cement solutions for ultra-high temperature wellbore applications, *Cem. Concr. Compos.*, 2016, **72**, 89–103.

130 M. Palou, V. Živica, T. Ifka, M. Boháč and M. Zmrzlý, in *Journal of Thermal Analysis and Calorimetry*, Kluwer Academic Publishers, 2014, vol. 116, pp. 597–603.

131 D. T. Tran, Y. Lee, H. S. Lee, H. M. Yang and J. K. Singh, Effects of γ-C2S on the Properties of Ground Granulated Blast-Furnace Slag Mortar in Natural and Accelerated Carbonation Curing, *Sustainability 2021, Vol. 13, Page 357*, 2021, **13**, 357.

132 J. Chang, T. Jiang and K. Cui, Influence on compressive strength and CO2 capture after accelerated carbonation of combination β-C2S with γ-C2S, *Constr. Build. Mater.*, 2021, **312**, 125359.

133 T. Wei, F. Wei, J. Zhou, Z. Wu, C. Zhang, J. Zhuang and X. Cheng, Formation and strengthening mechanisms of xonotlite in C3S-silica and C2S-silica powder systems under high temperature and pressure, *Cem. Concr. Res.*, 2022, **157**, 106812.

134 T. Matschei, B. Lothenbach and F. P. Glasser, The role of calcium carbonate in cement hydration, *Cem. Concr. Res.*, 2007, **37**, 551–558.

135 A. Ipavec, R. Gabrovšek, T. Vuk, V. Kaučič, J. MačEk and A. Meden, Carboaluminate Phases Formation During the Hydration of Calcite-Containing Portland Cement, *Journal of the American Ceramic Society*, 2011, **94**, 1238–1242.

136 Y. Y. Kim, K. M. Lee, J. W. Bang and S. J. Kwon, Effect of W/C ratio on durability and porosity in cement mortar with constant cement amount, *Advances in Materials Science and Engineering*, DOI:10.1155/2014/273460.

137 H. Zhao, Q. Xiao, D. Huang and S. Zhang, Influence of pore structure on compressive strength of cement mortar, *ScientificWorldJournal.*, DOI:10.1155/2014/247058.

138 S. Zheng, T. Liu, G. Jiang, C. Fang, B. Qu, P. Gao, L. Li and Y. Feng, Effects of Water-to-Cement Ratio on Pore Structure Evolution and Strength Development

of Cement Slurry Based on HYMOSTRUC3D and Micro-CT, *Applied Sciences 2021, Vol. 11,* DOI:10.3390/app11073063.

139 S. Zheng, T. Liu, G. Jiang, C. Fang, B. Qu, P. Gao, L. Li and Y. Feng, Effects of Water-to-Cement Ratio on Pore Structure Evolution and Strength Development of Cement Slurry Based on HYMOSTRUC3D and Micro-CT, *Applied Sciences 2021, Vol. 11, Page 3063*, 2021, **11**, 3063.

140 N. M. Bassil, A. D. Bewsher, O. R. Thompson and J. R. Lloyd, Microbial degradation of cellulosic material under intermediate-level waste simulated conditions, *Mineral. Mag.*, 2015, **79**, 1433–1441.

141 P. J. Withers, C. Bouman, S. Carmignato, V. Cnudde, D. Grimaldi, C. K. Hagen, E. Maire, M. Manley, A. Du Plessis and S. R. Stock, X-ray computed tomography, *Nature Reviews Methods Primers 2021 1:1*, 2021, **1**, 18-.

142 R. G. W. Vasconcelos, N. Beaudoin, A. Hamilton, N. C. Hyatt, J. L. Provis and C. L. Corkhill, Characterisation of a high pH cement backfill for the geological disposal of nuclear waste: The Nirex Reference Vault Backfill, *Applied Geochemistry*, 2018, **89**, 180–189.

143 Y. Yang, J. Liu, L. Liu, J. Li, Q. Liu, Z. Chen and C. Shi, Quantifying the water saturation degree of cement-based materials by hydrogen nuclear magnetic resonance (1H NMR), *Constr. Build. Mater.*, 2024, **438**, 137340.

144 M. Safiuddin and N. Hearn, Comparison of ASTM saturation techniques for measuring the permeable porosity of concrete, *Cem. Concr. Res.*, 2005, **35**, 1008–1013.

145 P. Rivard, M. A. Bérubé, G. Ballivy and J. P. Ollivier, Effect of drying–rewetting on the alkali concentration of the concrete pore solution, *Cem. Concr. Res.*, 2003, **33**, 927–929.

146 F. Fu, L. Lin and E. Xu, Functional pretreatments of natural raw materials, *Advanced High Strength Natural Fibre Composites in Construction*, 2017, 87–114.

147 The Control of Mercury (Amendment) (EU Exit) Regulations 2022 - GOV.UK, https://www.gov.uk/eu-withdrawal-act-2018-statutory-instruments/the-control-of-mercury-amendment-eu-exit-regulations-2022, (accessed 19 August 2025).

148 H. G. T. Nguyen, J. C. Horn, M. Bleakney, D. W. Siderius, L. Espinal, H. G. T. Nguyen, J. C. Horn, M. Bleakney, D. W. Siderius and L. Espinal, Understanding Material Characteristics through Signature Traits from He Pycnometry, *Langmuir*, 2019, **35**, 2115–2122.

149 Gas Pycnometry | Density Measurement | Covalent, https://covalent.com/techniques/morphology-structural-analysis/gas-pycnometry, (accessed 9 February 2026).

150 S. Y. Chang, C. Wang and C. C. Sun, Relationship between hydrate stability and accuracy of true density measured by helium pycnometry, *Int. J. Pharm.*, 2019, **567**, 118444.

151 Facilities – Semiconductor Spectroscopy and Devices, https://ssd.phys.strath.ac.uk/facilities/, (accessed 18 August 2025).

152 N. J. Cochrane, Y. Iijima, P. Shen, Y. Yuan, G. D. Walker, C. Reynolds, C. M. Macrae, N. C. Wilson, G. G. Adams and E. C. Reynolds, Comparative Study of the Measurement of Enamel Demineralization and Remineralization Using Transverse Microradiography and Electron Probe Microanalysis, *Microscopy and Microanalysis*, 2014, **20**, 937–945.

153 E. D. Banks, N. M. Taylor, J. Gulley, B. R. Lubbers, J. G. Giarrizo, H. A. Bullen, T. M. Hoehler and H. A. Barton, Bacterial calcium carbonate precipitation in cave environments: A function of calcium homeostasis, *Geomicrobiol. J.*, 2010, **27**, 444–454.

154 B. Lothenbach, G. Le Saout, E. Gallucci and K. Scrivener, Influence of limestone on the hydration of Portland cements, *Cem. Concr. Res.*, 2008, **38**, 848–860.

155 A. A. Elgalhud, R. K. Dhir and G. Ghataora, Limestone addition effects on concrete porosity, *Cem. Concr. Compos.*, 2016, **72**, 222–234.

156 D. Wang, C. Shi, N. Farzadnia, Z. Shi, H. Jia and Z. Ou, A review on use of limestone powder in cement-based materials: Mechanism, hydration and microstructures, *Constr. Build. Mater.*, 2018, **181**, 659–672.

157 G. W. Scherer and F. Bellmann, Kinetic analysis of C-S-H growth on calcite, *Cem. Concr. Res.*, 2018, **103**, 226–235.

158 I. G. Richardson, The nature of C-S-H in hardened cements, *Cem. Concr. Res.*, 1999, **29**, 1131–1147.

159 Y. Tao, Y. Gao, Y. Sun, R. J. M. Pellenq and C. S. Poon, C-S-H decalcification in seawater: The view from the nanoscale, *Cem. Concr. Res.*, 2024, **175**, 107385.

160 H. Yang, Y. Che and F. Leng, Calcium leaching behavior of cementitious materials in hydrochloric acid solution, *Scientific Reports 2018 8:1*, 2018, **8**, 8806-.

161 X. Liu, P. Feng, X. Yu and J. Huang, Decalcification of calcium silicate hydrate (C-S-H) under aggressive solution attack, *Constr. Build. Mater.*, 2022, **342**, 127988.

162 T. Tracz and T. Zdeb, Effect of Hydration and Carbonation Progress on the Porosity and Permeability of Cement Pastes, *Materials*, 2019, **12**, 192.

163 X. Liu, P. Feng, X. Yu and J. Huang, Decalcification of calcium silicate hydrate (C-S-H) under aggressive solution attack, *Constr. Build. Mater.*, 2022, **342**, 127988.

164 R. Wang and J. Wang, A Review on Dehydration of C(-A)-S-H and Rehydration of Dehydrated C(-A)-S-H for Recycled Cement, *Materials 2026, Vol. 19,* 2026, **19**, 1133.

165 H. Yang, Y. Che and F. Leng, Calcium leaching behavior of cementitious materials in hydrochloric acid solution, *Scientific Reports 2018 8:1*, 2018, **8**, 8806-.

166 T. Wei, F. Wei, J. Zhou, Z. Wu, C. Zhang, J. Zhuang and X. Cheng, Formation and strengthening mechanisms of xonotlite in C3S-silica and C2S-silica powder systems under high temperature and pressure, *Cem. Concr. Res.*, 2022, **157**, 106812.

167 S. Shaw, S. M. Clark and C. M. B. Henderson, Hydrothermal formation of the calcium silicate hydrates, tobermorite (Ca5Si6O16(OH)2·4H2O) and xonotlite (Ca6Si6O17(OH)2): an in situ synchrotron study, *Chem. Geol.*, 2000, **167**, 129–140.

168 G. Smalakys and R. Siauciunas, Peculiarities of xonotlite synthesis from the raw materials with different SiO2 activities, *Journal of Thermal Analysis and Calorimetry 2020 142:5*, 2020, **142**, 1671–1679.

169 N. Duc Van, K. Imasawa and Y. Hama, Influence of hydrothermal synthesis conditions and carbonation on physical properties of xonotlite-based lightweight material, *Constr. Build. Mater.*, 2022, **321**, 126328.

170 T. Matschei, B. Lothenbach and F. P. Glasser, The role of calcium carbonate in cement hydration, *Cem. Concr. Res.*, 2007, **37**, 551–558.

171 B. Lothenbach, G. Le Saout, E. Gallucci and K. Scrivener, Influence of limestone on the hydration of Portland cements, *Cem. Concr. Res.*, 2008, **38**, 848–860.

172 A. Kirfel, H. M. Hamm and G. Will, The crystal structure of reinhardbraunsite, Ca5(SiO4)2(OH,F)2, a new mineral of the calcio-chondrodite type, *TMPM Tschermaks Mineralogische und Petrographische Mitteilungen*, 1983, **31**, 137–150.

173 Calcium analogue of chondrodite | American Mineralogist | GeoScienceWorld, https://pubs.geoscienceworld.org/msa/ammin/article-abstract/43/9-10/818/541408/Calcium-analogue-of-chondrodite, (accessed 28 October 2025).

174 S. Wang, Z. Niu, D. Jin, J. He, Y. Mu and G. Ye, Effect of Reactivity of Hydrated Portland Cement on Hydrothermal Synthesis of Xonotlite, *Materials 2023, Vol. 16, Page 1578*, 2023, **16**, 1578.

175 T. Wei, X. Cheng, H. Liu, H. Zhang, L. Zhang, K. Mei, C. Zhang, K. Liu and J. Zhuang, Crystallization of tricalcium silicate blended with different silica powder dosages at high temperature, *Constr. Build. Mater.*, 2022, **316**, 125884.

176 S. Wang, X. Peng, L. Tang, L. Zeng and C. Lan, Influence of Hydrothermal Synthesis Conditions on the Formation of Calcium Silicate Hydrates: from Amorphous to Crystalline Phases, *J. Wuhan Univ. Technol. Mater. Sci. Ed.*, 2025, **33**, 1150.

177 E. Kuzielová, M. Žemlička, J. Másilko and M. T. Palou, Development of G-oil well cement phase composition during long therm hydrothermal curing, *Geothermics*, 2019, **80**, 129–137.

178 E. Kuzielová, M. Slaný, M. Žemlička, J. Másilko and M. T. Palou, Phase Composition of Silica Fume—Portland Cement Systems Formed under Hydrothermal Curing Evaluated by FTIR, XRD, and TGA, *Materials 2021, Vol. 14, Page 2786*, 2021, **14**, 2786.

179 M. Palou, V. Živica, T. Ifka, M. Boháč and M. Zmrzlý, Effect of hydrothermal curing on early hydration of G-Oil well cement, *J. Therm. Anal. Calorim.*, 2014, **116**, 597–603.

180 S. Wang, Z. Niu, D. Jin, J. He, Y. Mu and G. Ye, Effect of Reactivity of Hydrated Portland Cement on Hydrothermal Synthesis of Xonotlite, *Materials 2023, Vol. 16, Page 1578*, 2023, **16**, 1578.

181 S. Wang, X. Peng, L. Tang, L. Zeng and C. Lan, Influence of Hydrothermal Synthesis Conditions on the Formation of Calcium Silicate Hydrates: from Amorphous to Crystalline Phases, *J. Wuhan Univ. Technol. Mater. Sci. Ed.*, 2025, **33**, 1150.

182 R. Gendvilas and R. Siauciunas, The Influence of Temperature and Nature of CaO Component on the Formation of α-C2SH, *Solid State Phenomena*, 2016, **244**, 12–18.

183 R. Siauciunas, Z. Takulinskas, E. Prichockiene and A. Selskiene, Hydrothermal synthesis of α-C2SH and kilchoanite mixture and its application in CO2 hardening mortar, *Ceram. Int.*, 2023, **49**, 14864–14874.

184 B. Bresson, F. Meducin, H. Zanni and C. Noik, Hydration of tricalcium silicate (C 3 S) at high temperature and high pressure.

185 M. Zhao, Quantitative Control of C2S Crystal Transformation, *Applied Mechanics and Materials*, 2012, **121–126**, 311–315.

186 S. Zhao, Z. Liu, F. Wang and S. Hu, Elucidating factors on the strength of carbonated compacts: Insights from the carbonation of γ-C2S, β-C2S and C3S, *Cem. Concr. Compos.*, 2025, **155**, 105806.

187 Z. X. Chen, N. T. Zhang and S. H. Chu, Role of alkalinity in CO2 sequestration of γ-belite, *Constr. Build. Mater.*, 2024, **432**, 136508.

188 A. Kunhi Mohamed, S. C. Parker, P. Bowen and S. Galmarini, An atomistic building block description of C-S-H - Towards a realistic C-S-H model, *Cem. Concr. Res.*, 2018, **107**, 221–235.

189 Z. X. Chen, N. T. Zhang and S. H. Chu, Role of alkalinity in CO2 sequestration of γ-belite, *Constr. Build. Mater.*, 2024, **432**, 136508.

190 C. Hejny and T. Armbruster, Polytypism in xonotlite Ca6Si6O17(OH)2 Note: polytype derived from structure in Kudoh and Takeuchi (1979).

191 D. L. Graf, Crystallographic tables for the rhombohedral carbonates.

192 R. M. Ganiev, Yu. A. Kharitonov, V. V. Ilyukhin and N. V. Belov, The crystal structure of calcium chondrodite Ca5 (Si O4)2 (O H)2 = Ca (O H)2 (Ca2 Si O4)2.

193 T. Armbruster, B. Lazic, I. O. Galuskina, E. V. Galuskin, E. Gnos, K. M. Marzec and V. M. Gazeev, Trabzonite, Ca4[Si3O9(OH)]OH: crystal structure, revised formula, new occurrence and relation to killalaite.

194 R. Basso, A. D. Giusta and L. Zefiro, Crystal structure refinement of plazolite: a highly hydrated natural hydrogrossular.

195 E. R. Gobechiya, N. A. Yamnova, A. E. Zadov and V. M. Gazeev, Calcio-olivine gamma-Ca2SiO4: I. Rietveld refinement of the crystal structure.

196 W. R. Busing and H. A. Levy, Neutron diffraction study of calcium hydroxide.

197 N. A. Yamnova, K. Sarp, E.-T. Y. K and D. Y. Pushcharovskii, Crystal structure of jaffeite.

198 B. P. Onac, H. Effenberger, K. Ettinger and S. P. Panzaru, Hydroxylellestadite from Cioclovina Cave (Romania): Microanalytical, structural, and vibrational spectroscopy data Locality: Cioclovina Cave, Sureanu Mountains, Romania.

199 R. E. Marsh, A revised structure for alpha-dicalcium silicate hydrate.

200 L. Levien, C. T. Prewitt and D. J. Weidner, Structure and elastic properties of quartz at pressure P = 20.7 kbar.

201 A. Kyono and S. Arora, Crystal structure change in grossular-Si-free katoite solid solution: Oxygen position splitting in katoite : Ca3Al2(SiO4)0.57(O4H4)2.43 unspilt oxygen model.

202 S. Onthong, W. Hanpongpun, S. Sinthupinyo, E. A. O'Rear and T. Pongprayoon, Bifunctional Multiwall Carbon Nanotubes and Their Effect on Hydration, Conductivity, and Mechanical Properties of Cement Composites, *International Journal of Concrete Structures and Materials 2025 19:1*, 2025, **19**, 69-.

203 H. Saalfeld and W. Depmeier, Silicon-free compounds with sodalite structure Note: Very short S-O bondlength of 1.26 angstroms.

204 F. C. Hawthorne and R. B. Ferguson, Anhydrous sulphates. II. Refinement of the crystal structure of anhydrite.

205 G. Natta and L. Passerini, Soluzioni solide, isomorfismo e simmorfismo tra gli ossidi dei metalli bivalenti. - 1. Sistemi: CaO-CdO, CaO-MnO, CaO-CoO, CaO-NiO, CaO-MgO.

206 C. Ma, A. R. Kampf, H. C. Connolly, J. R. Beckett, G. R. Rossman, S. A. Sweeney Smith and D. L. Schrader, Krotite, CaAl2O4, a new refractory mineral from the NWA 1934 meteorite.

207 S. Saburi, I. Kusachi, C. Henmi, A. Kawahara, K. Henmi and I. Kawada, Refinement of the structure of rankinite.

208 D. R. Peacor, High-temperature single-crystal study of the cristobalite inversion Note: Cell has been corrected Sample: T = 28 C.

209 Y. El Khessaimi, Y. El Hafiane and A. Smith, Examination of ye'elimite formation mechanisms, *J. Eur. Ceram. Soc.*, 2019, **39**, 5086–5095.

210 O. Almendros-Ginestà, M. A. Clavero-Sánchez, M. García-Gutiérrez and T. Missana, Radionuclide retention by portlandite in the presence of isosaccharinate and phthalate and possible role of ternary complexes, *Chemosphere*, 2025, **374**, 144224.

211 F. P. Glasser, Mineralogical aspects of cement in radioactive waste disposal, *Mineral. Mag.*, 2001, **65**, 621–633.

212 O. Almendros-Ginestà, T. Missana, M. García-Gutiérrez and U. Alonso, Analysis of radionuclide retention by the cement hydrate phase portlandite: A novel modelling approach, *Progress in Nuclear Energy*, 2023, **159**, 104636.

213 S. P. Gregory, J. R. M. Mackie and M. J. Barnett, Radioactive waste microbiology: predicting microbial survival and activity in changing extreme environments, *FEMS Microbiol. Rev.*, DOI:10.1093/FEMSRE/FUAE001.

214 M. Vikman, K. Marjamaa, M. Nykyri, J. S. Small, H. Miettinen, L. Heikinheimo, T. Haavisto and M. Itävaara, The biogeochemistry of gas generation from low-level nuclear waste: Microbiological characterization during 18 years study under in situ conditions, *Applied Geochemistry*, 2019, **105**, 55–67.

215 J. S. Small, M. Nykyri, M. Vikman, M. Itävaara and L. Heikinheimo, The biogeochemistry of gas generation from low-level nuclear waste: Modelling after 18 years study under in situ conditions, *Applied Geochemistry*, 2017, **84**, 360–372.

216 F. Druyts, S. Caes and P. Thomas, Carbon-14 release and speciation from carbon steel in highly alkaline conditions, *Radiocarbon*, 2018, **60**, 1683–1690.

217 T. Guillemot, G. Salazar, M. Rauber, D. Kunz, S. Szidat and E. Wieland, Carbon-14 release and speciation during corrosion of irradiated steel under radioactive waste disposal conditions, *Science of the Total Environment*, DOI:10.1016/j.scitotenv.2021.152596.

218 A. I. Marsh, L. G. Williams and J. A. Lawrence, The important role and performance of engineered barriers in a UK geological disposal facility for higher activity radioactive waste, *Progress in Nuclear Energy*, 2021, **137**, 103736.

219 J. Bu, R. Gonzalez Teresa, K. G. Brown and F. Sanchez, Adsorption mechanisms of cesium at calcium-silicate-hydrate surfaces using molecular dynamics simulations, *Journal of Nuclear Materials*, 2019, **515**, 35–51.

220 X. Gaona, D. A. Kulik, N. Macé and E. Wieland, Aqueous-solid solution thermodynamic model of U(VI) uptake in C-S-H phases, *Applied Geochemistry*, 2012, **27**, 81–95.

221 M. L. Schlegel, I. Pointeau, N. Coreau and P. Reiller, Mechanism of europium retention by calcium silicate hydrates: an EXAFS study, *Environ. Sci. Technol.*, 2004, **38**, 4423–4431.

222 T. Matschei, B. Lothenbach and F. P. Glasser, The role of calcium carbonate in cement hydration, *Cem. Concr. Res.*, 2007, **37**, 551–558.

223 N. P. Qafoku, A. R. Lawter, E. C. Gillispie, E. McElroy, F. N. Smith, R. Sahajpal, K. Cantrell and V. Freedman, Calcium carbonate minerals as scavengers of metals and radionuclides: Their role in natural attenuation and remediation, *Advances in Agronomy*, 2022, **176**, 115–152.

224 E. Curti, Coprecipitation of radionuclides with calcite: estimation of partition coefficients based on a review of laboratory investigations and geochemical data, *Applied Geochemistry*, 1999, **14**, 433–445.

225 E. J. Elzinga, C. D. Tait, R. J. Reeder, K. D. Rector, R. J. Donohoe and D. E. Morris, Spectroscopic investigation of U(VI) sorption at the calcite-water interface, *Geochim. Cosmochim. Acta*, 2004, **68**, 2437–2448.

226 S. E. Hellebrandt, S. Hofmann, N. Jordan, A. Barkleit and M. Schmidt, Incorporation of Eu(III) into Calcite under Recrystallization conditions, *Scientific Reports 2016 6:1*, 2016, **6**, 33137-.

227 R. E. Guidone, N. Huber, F. Heberling, T. Sittel, N. Palina, F. Bocchese, S. St´, S. Brassinnes, M. Altmaier and X. Gaona, Uptake of H 14 CO 3 − / 14 CO 3 2− by calcite: impact of ISA and chloride, *RSC Adv.*, 2025, **15**, 38762–38773.

228 A. Hamilton, P. Bots, H. Zhou, B. Liu and C. Hall, Clean-up of divalent cobalt ions by massive sequestration in a low-cost calcium silicate hydrate material, *Scientific Reports 2024 14:1*, 2024, **14**, 7052-.

229 J. Chang, T. Jiang and K. Cui, Influence on compressive strength and CO2 capture after accelerated carbonation of combination β-C2S with γ-C2S, *Constr. Build. Mater.*, 2021, **312**, 125359.

230 B. E. Klamm, C. J. Windorff, M. L. Marsh, D. S. Meeker and T. E. Albrecht-Schmitt, Schiff-base coordination complexes with plutonium(IV) and cerium(IV), *Chemical Communications*, 2018, **54**, 8634–8636.

231 W. Gashier, T. Miura, K. Hashimoto, R. J. Hand and H. Kinoshita, Leaching behaviour of cementitious nuclear wasteforms containing caesium and strontium, *Advances in Applied Ceramics*, 2014, **113**, 447–452.

232 H. Ren, Y. Li, L. Xu, P. Wang and Y. Cao, A review of recent advances in health risks and detection of 129I and 131I in environmental and biological samples, *Environ. Technol. Innov.*, 2025, **38**, 104146.

233 P. Belli, R. Bernabei, F. A. Danevich, A. Incicchitti and V. I. Tretyak, Experimental searches for rare alpha and beta decays, *The European Physical Journal A 2019 55:8*, 2019, **55**, 1–43.

234 Standardization of 90Sr (SRM 4329a) | NIST, https://www.nist.gov/pml/radiation-physics/standardization-90sr-srm-4329a, (accessed 12 March 2025).

235 Radioactive Properties of Key Cesium Isotopes and an Associated Radionuclide.

236 T. Masumitsu, K. Masaaki, U. Hiroaki, M. Norimasa, F. Hiroshi, M. Takuya and S. Noriyuki, Iodine Sorption onto Mixed Solid Alumina Cement and Calcium Compounds, *J. Nucl. Sci. Technol.*, 2000, **37**, 970–978.

237 P. Martin, M. Ripert, T. Petit, T. Reich, C. Hennig, F. D'Acapito, J. L. Hazemann and O. Proux, A XAS study of the local environments of cations in (U, Ce)O2, *Journal of Nuclear Materials*, 2003, **312**, 103–110.

238 [Table, WHAT IS PLUTONIUM?]. - Toxicological Profile for Plutonium - NCBI Bookshelf, https://www.ncbi.nlm.nih.gov/books/NBK599413/table/ch1.tab1/, (accessed 12 March 2025).

239 NDA group welcomes Government decision on plutonium disposition - GOV.UK, https://www.gov.uk/government/news/nda-group-welcomes-government-decision-on-plutonium-disposition, (accessed 12 March 2025).

240 W. Bodel, A. Bull, G. Butler, R. Harrison, J. Matthews, D. Warrilow-Brennan and C. Sharrad, Managing the UK plutonium stockpile: no easy choices.

241 James and Martin, 2022 Inventory for Geological Disposal Main Report.

242 Z. Franic, N. Lokobauer and G. Marovic, Radiostrontium activity concentrations in milk in the Republic of Croatia for 1961 - 2001 and dose assessment.

243 A. Burger and I. Lichtscheidl, Strontium in the environment: Review about reactions of plants towards stable and radioactive strontium isotopes, *Science of The Total Environment*, 2019, **653**, 1458–1512.

244 F. Deng and F. Lin, Measurement of 90Sr in Marine Biological Samples, *Molecules 2022, Vol. 27, Page 3730*, 2022, **27**, 3730.

245 Radionuclide Basics: Cesium-137 | US EPA, https://www.epa.gov/radiation/radionuclide-basics-cesium-137, (accessed 8 May 2025).

246 R. O. Abdel Rahman and M. I. Ojovan, Toward Sustainable Cementitious Radioactive Waste Forms: Immobilization of Problematic Operational Wastes, *Sustainability 2021, Vol. 13, Page 11992*, 2021, **13**, 11992.

247 R. M. Asmussen, J. Turner, S. Chong and B. J. Riley, Review of recent developments in iodine wasteform production, *Front. Chem.*, 2022, **10**, 1043653.

248 R. M. Asmussen, J. Turner, S. Chong and B. J. Riley, Review of recent developments in iodine wasteform production, *Front. Chem.*, 2022, **10**, 1043653.

249 Iodine-129 | I | CID 175671713 - PubChem, https://pubchem.ncbi.nlm.nih.gov/compound/Iodine-129#section=Toxicity-Summary, (accessed 23 December 2025).

250 T. J. Robshaw, J. Turner, S. Kearney, B. Walkley, C. A. Sharrad and M. D. Ogden, Capture of aqueous radioiodine species by metallated adsorbents from wastestreams of the nuclear power industry: a review, *SN Appl. Sci.*, 2021, **3**, 1–15.

251 S. A. Cumberland, A. Hamilton, J. C. Renshaw, K. M. Tierney and R. J. Lunn, Hydroxyapatite coatings on cement paste as barriers against radiological contamination, DOI:10.1038/s41598-023-37822-6.

252 Guide to Reference Groundwater and Porewater Compositions in Support of the UK GDF Programme.

253 Enhancing Cesium Analysis Using the Expanded Wavelength Range of the Avio 220 Max ICP-OES | PerkinElmer, https://www.perkinelmer.com/uk/libraries/tch-636207-avio220-max-icp-oes-enhancing-cesium-analysis, (accessed 14 January 2025).

254 S. N. Kerisit, F. N. Smith, S. A. Saslow, M. E. Hoover, A. R. Lawter and N. P. Qafoku, Incorporation Modes of Iodate in Calcite, DOI:10.1021/acs.est.8b00339.

255 S. Zhang, C. Xu, D. Creeley, Y.-F. Ho, H.-P. Li, R. Grandbois, K. A. Schwehr, D. I. Kaplan, C. M. Yeager, D. Wellman and P. H. Santschi, Iodine-129 and Iodine-127 Speciation in Groundwater at the Hanford Site, U.S.: Iodate Incorporation into Calcite, DOI:10.1021/es401816e.

256 P. Abellan, T. H. Moser, I. T. Lucas, J. W. Grate, J. E. Evans and N. D. Browning, The formation of cerium(III) hydroxide nanoparticles by a radiation mediated increase in local pH †, DOI:10.1039/c6ra27066b.

257 E. Wieland, J. Tits, D. Kunz and R. Dähn, Strontium Uptake by Cementitious Materials, *Environ. Sci. Technol.*, 2007, **42**, 403–409.

258 M. I. Hossain, B. Aïssa, I. Zimmermann, M. Khaja, N. Abdelhak, B. Mohammad, I. Hossain, M. K. Nazeeruddin and A. Belaidi, Development of an inorganic cesium carbonate-based electron transport material for a 17% power conversion efficiency perovskite solar cell device, *https://doi.org/10.1117/1.JPE.10.015502*, 2020, **10**, 015502.

259 P. Marin-Troya, C. Espinosa, L. Monasterio-Guillot and P. Alvarez-Lloret, Carbonate Minerals' Precipitation in the Presence of Background Electrolytes: Sr, Cs, and Li with Different Transporting Anions, *Crystals 2023, Vol. 13, Page 796*, 2023, **13**, 796.

260 J. P. R. de Villiers, Crystal structures of aragonite, strontianite, and witherite.

261 A. S. Lea, J. E. Amonette, D. R. Baer, Y. Liang and N. G. Colton, Microscopic effects of carbonate, manganese, and strontium ions on calcite dissolution, *Geochim. Cosmochim. Acta*, 2001, **65**, 369–379.

262 Z. Hu, Y. Li, C. Zhang and B. Ao, Structural, electronic, optical and bonding properties of strontianite, SrCO3: First-principles calculations, *Journal of Physics and Chemistry of Solids*, 2016, **98**, 65–70.

263 R. I. Gabitov and E. B. Watson, Partitioning of strontium between calcite and fluid, *Geochemistry, Geophysics, Geosystems*, DOI:10.1029/2005GC001216.

264 P. Forjanes, C. Pérez-Garrido, P. Álvarez-Lloret, J. M. Astilleros and L. Fernández-Díaz, Formation of Strontianite and Witherite Cohesive Layers on Calcite Surfaces for Building Stone Conservation, *Cryst. Growth Des.*, 2022, **22**, 6418–6428.

265 W. Pannhorst and J. Lohn, Zur kristallstruktur von strontianit, SrCO3.

266 D. M. Henderson and H. S. Gutowsky, A nuclear magnetic resonance determination of the hydrogen positions in Ca(OH)2 T = 25 C.

267 H. Sitepu, O. B. H and D. Li, Comparative evaluation of the March and generalized spherical harmonic preferred orientation models using X-ray diffraction data for molybdite and calcite powders Note: GSH model.

268 A. F. Gualtieri, Accuracy of XRPD QPA using the combined Rietveld-RIR method.

269 K. Zeppenfeld, Crystallization kinetics of strontianite from Sr(HCO3)2 solutions, *Geochemistry*, 2006, **66**, 319–323.

270 R. H. Parkman, J. M. Charnock, F. R. Livens and D. J. Vaughan, A study of the interaction of strontium ions in aqueous solution with the surfaces of calcite and kaolinite, *Geochim. Cosmochim. Acta*, 1998, **62**, 1481–1492.

271 P. Yu, S. A. Hayes, T. J. O'Keefe, M. J. O'Keefe and J. O. Stoffer, The Phase Stability of Cerium Species in Aqueous Systems, *J. Electrochem. Soc.*, 2006, **153**, C74.

272 M. Ochs, I. Pointeau and E. Giffaut, Caesium sorption by hydrated cement as a function of degradation state: Experiments and modelling, *Waste Management*, 2006, **26**, 725–732.

273 E. Duque-Redondo, K. Yamada and H. Manzano, Cs retention and diffusion in C-S-H at different Ca/Si ratio, *Cem. Concr. Res.*, 2021, **140**, 106294.

274 T. Missana, M. García-Gutiérrez, M. Mingarro and U. Alonso, Comparison between cesium and sodium retention on calcium silicate hydrate (CSH) phases, *Applied Geochemistry*, 2018, **98**, 36–44.

275 I. G. Richardson, The calcium silicate hydrates, *Cem. Concr. Res.*, 2008, **38**, 137–158.

276 K. Yanagisawa, X. Hu, A. Onda and K. Kajiyoshi, Hydration of β-dicalcium silicate at high temperatures under hydrothermal conditions, *Cem. Concr. Res.*, 2006, **36**, 810–816.

277 K. Kyritsis, N. Meller and C. Hall, Chemistry and morphology of hydrogarnets formed in cement-based CASH hydroceramics cured at 200° to 350°C, *Journal of the American Ceramic Society*, 2009, **92**, 1105–1111.

278 X. Pang, J. Qin, L. Sun, G. Zhang and H. Wang, Long-term strength retrogression of silica-enriched oil well cement: A comprehensive multi-approach analysis, *Cem. Concr. Res.*, 2021, **144**, 106424.

279 K. Li and X. Pang, Sorption of radionuclides by cement-based barrier materials, *Cem. Concr. Res.*, 2014, **65**, 52–57.

280 J. Arayro, A. Dufresne, T. Zhou, K. Ioannidou, J. F. Ulm, R. Pellenq and L. K. Béland, Thermodynamics, kinetics, and mechanics of cesium sorption in cement paste: A multiscale assessment, *Phys. Rev. Mater.*, 2018, **2**, 053608.

281 D. J. Hodkin, D. I. Stewart, J. T. Graham, G. Cibin and I. T. Burke, Enhanced Crystallographic Incorporation of Strontium(II) Ions into Calcite via Preferential Adsorption at Obtuse Growth Steps, *Cryst. Growth Des.*, 2018, **18**, 2836–2843.

282 K. Luke, H. F. W. Taylor and G. L. Kalousek, Some factors affecting formation of truscottite and xonotlite at 300–350°C, *Cem. Concr. Res.*, 1981, **11**, 197–203.

Appendices

Appendix 1 XRD pattern of cements cured at 80°C with calcite in initial mix

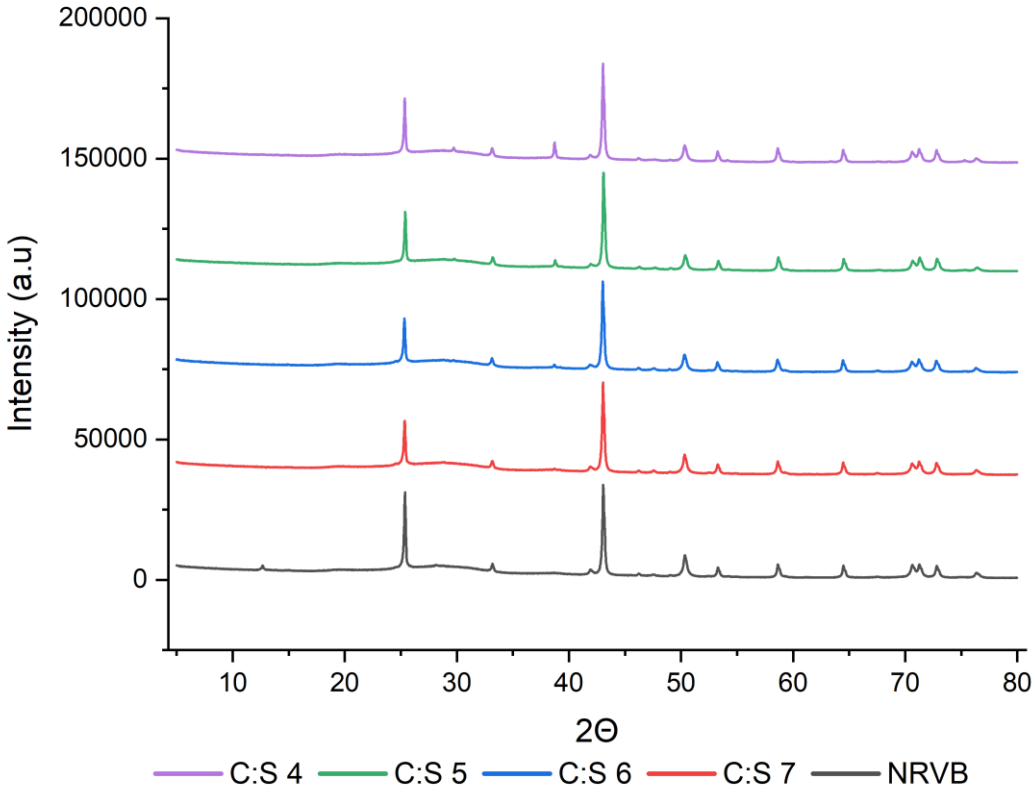


Figure 96: Diffractogram for cements cured at 80°C with $CaO:SiO_2$ ratios between 4 and 7.27 (NRVB).

Appendix 2 XRD pattern of cements cured at 25°C with calcite in initial mix

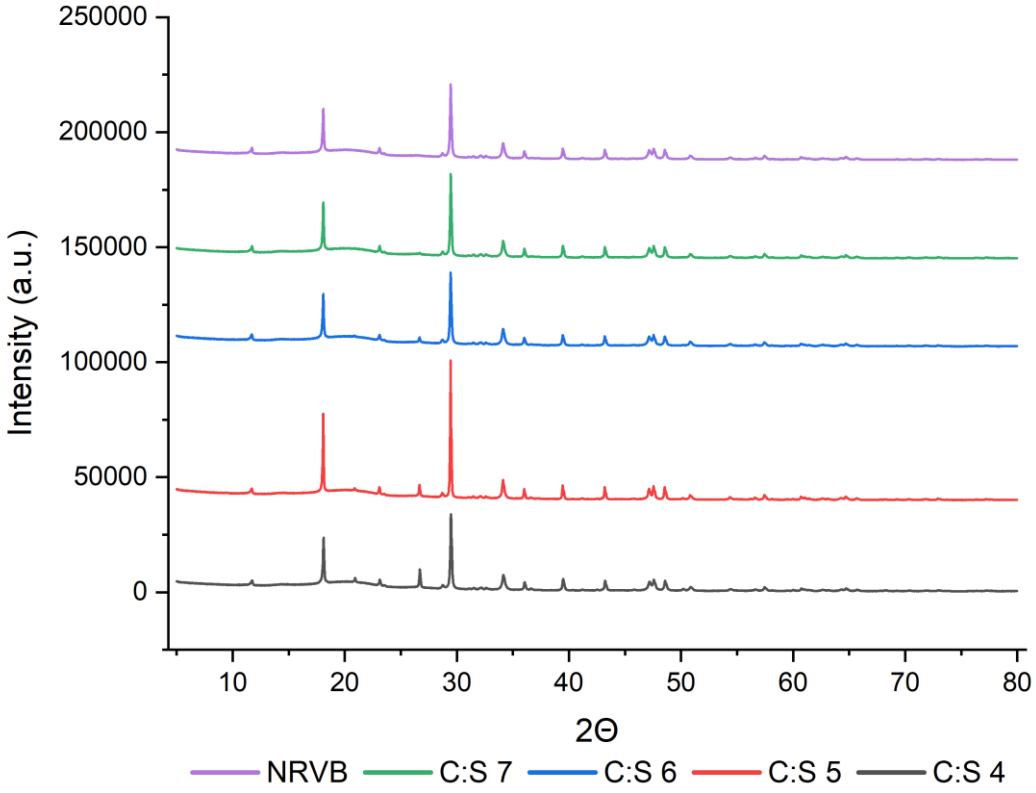


Figure 97: Diffractogram for cements cured at 25°C with CaO:SiO2 ratios between 4 and 7.27 (NRVB).

Appendix 3 NRVB cement cured at 250°C

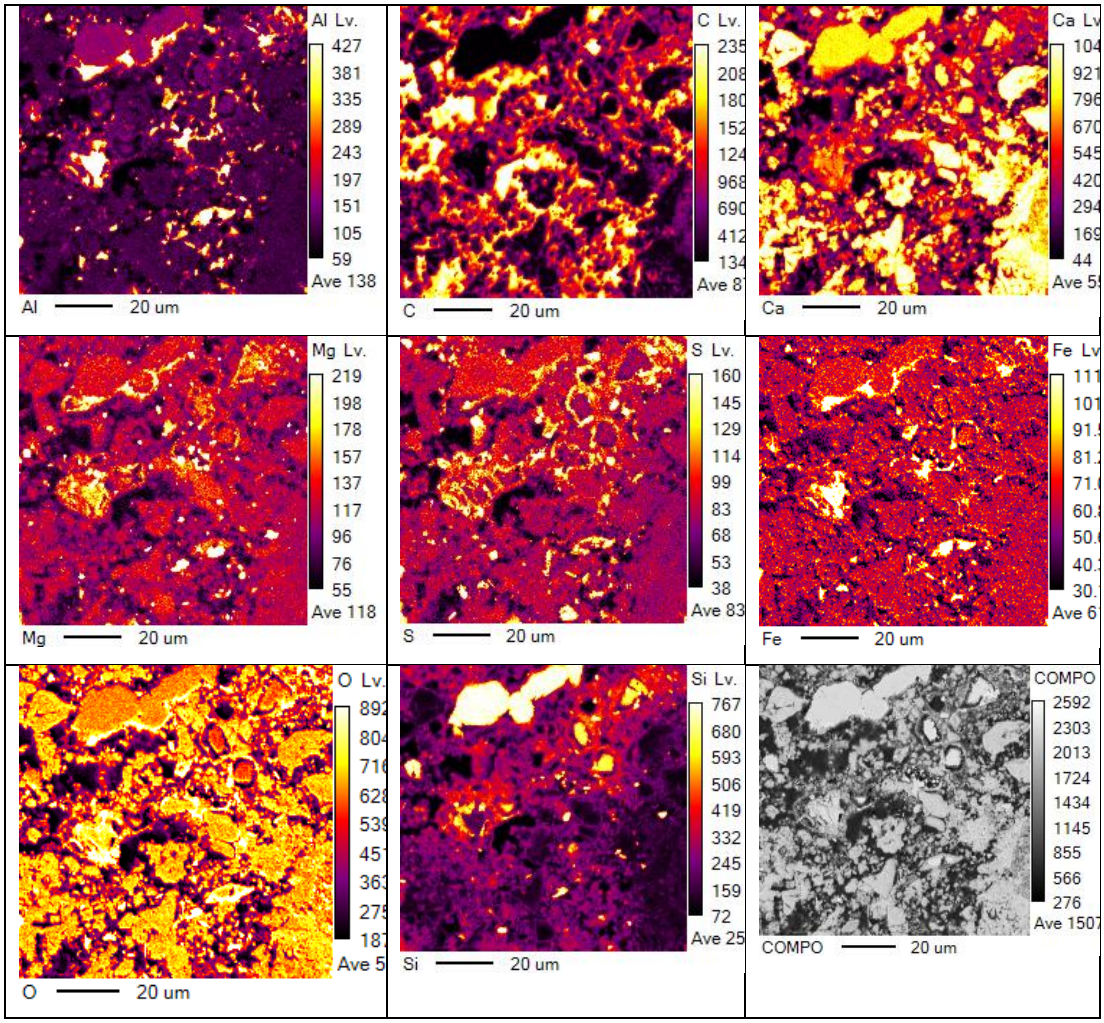
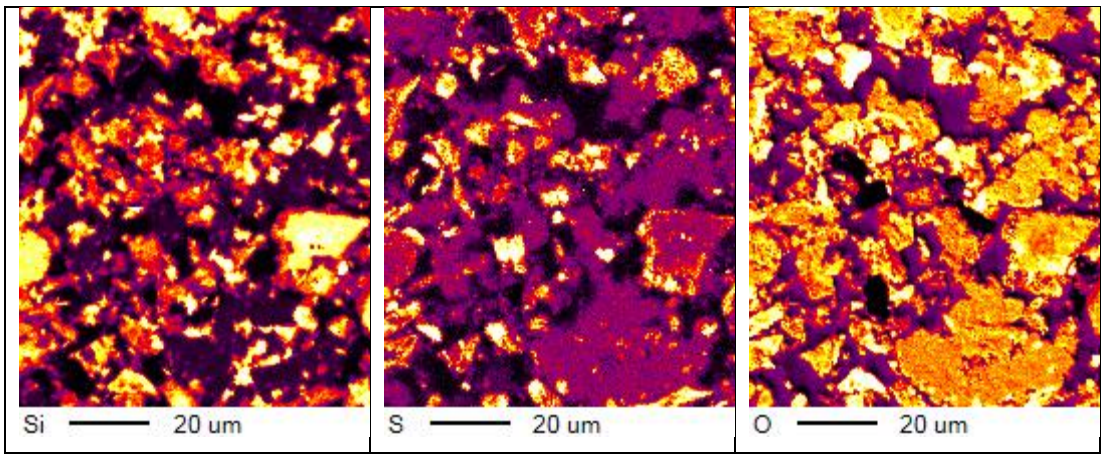


Figure 98: EMPA elemental scans for the NRVB cement cured at 250°C. Starting top left Al, C, Ca, middle left Mg, S, Fe, bottom left O, Si, and the compositional elemental scan.

Appendix 4 NRVB cement cured at 200°C



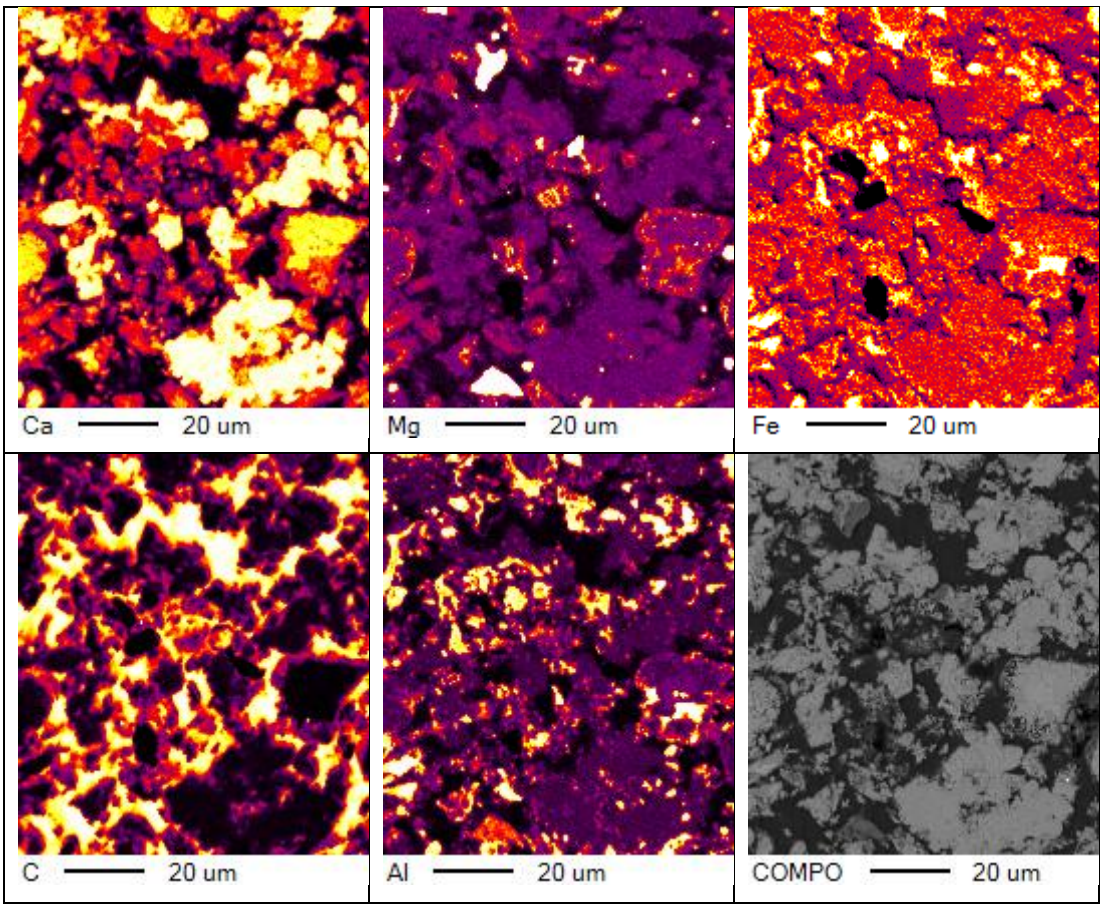
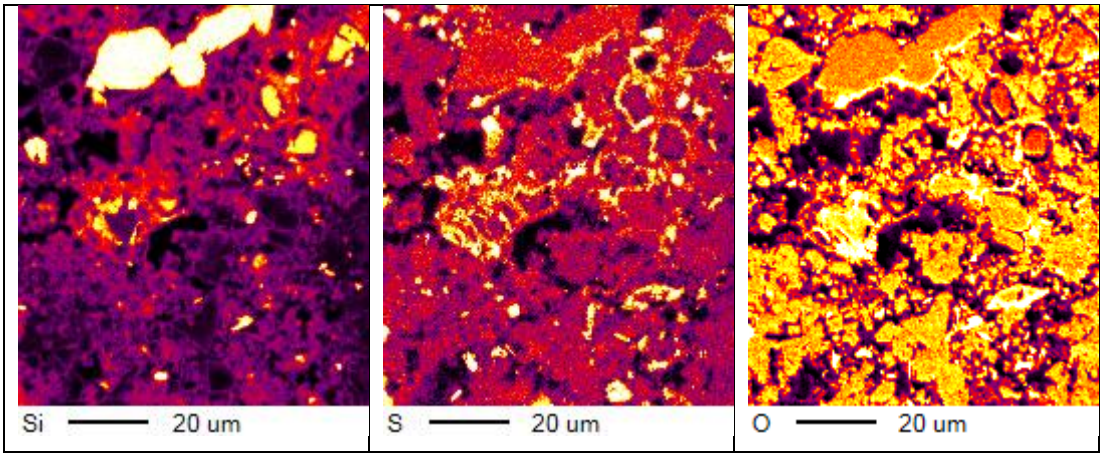


Figure 99: EMPA elemental scans for the NRVB cement cured at 200°C. Starting top left Al, C, Ca, middle left Mg, S, Fe, bottom left O, Si, and the compositional elemental scan.

Appendix 5 NRVB cement cured at 150°C



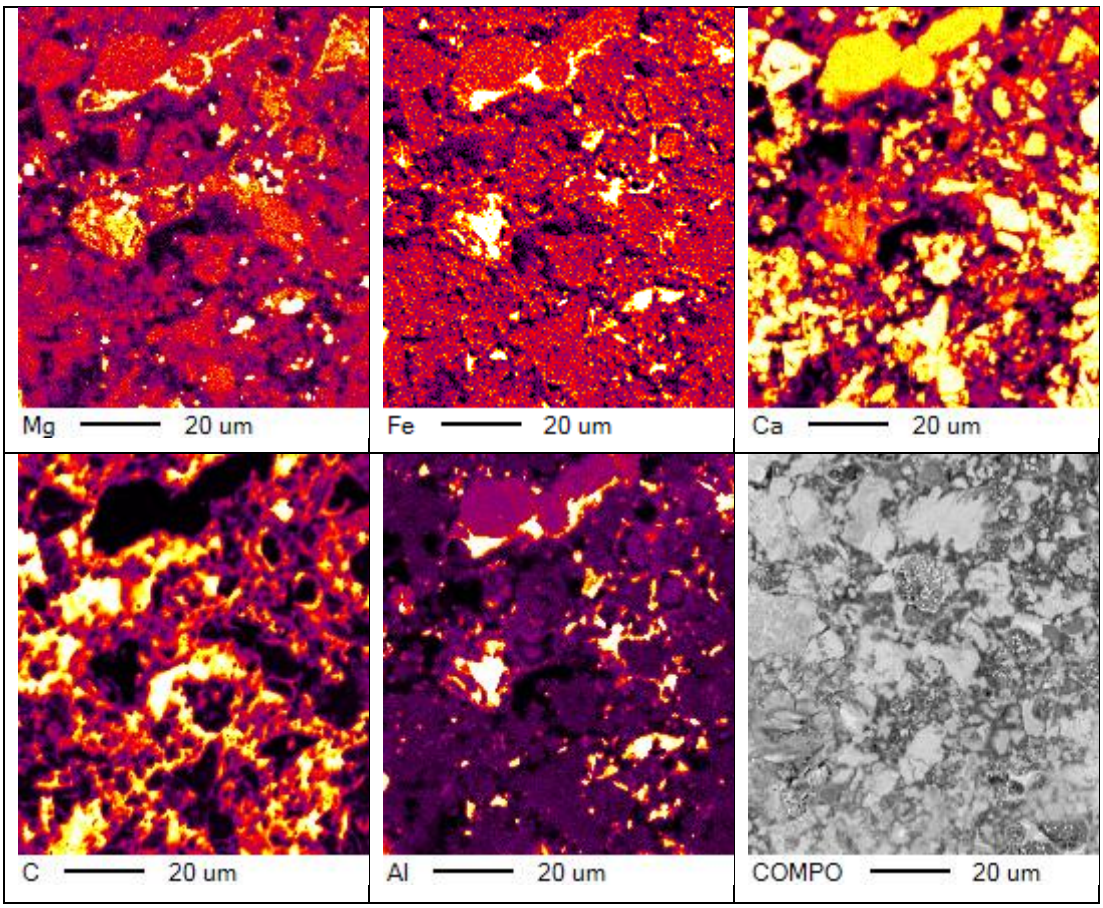
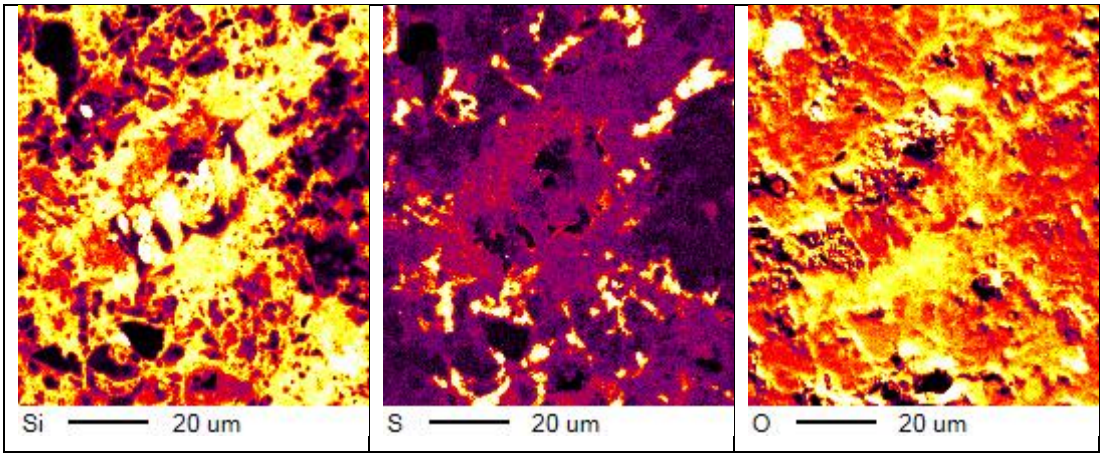


Figure 100: EMPA elemental scans for the NRVB cement cured at 150°C. Starting top left Al, C, Ca, middle left Mg, S, Fe, bottom left O, Si, and the compositional elemental scan.

Appendix 6 NRVB cement cured at 80°C



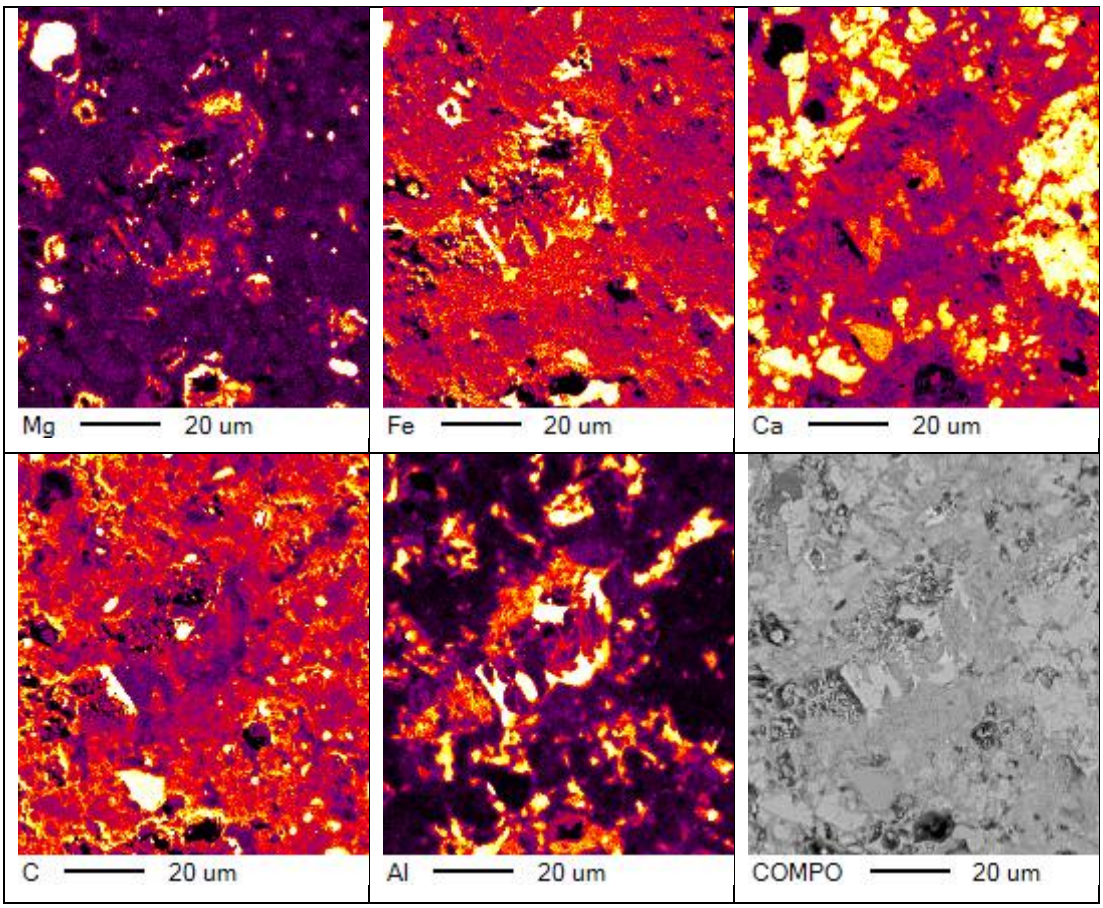
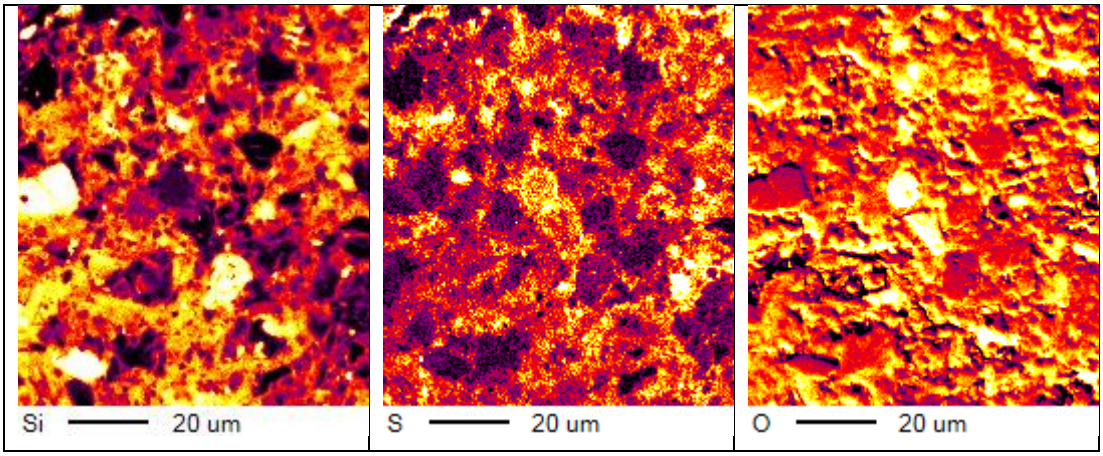


Figure 101: EMPA elemental scans for the NRVB cement cured at 80°C. Starting top left Al, C, Ca, middle left Mg, S, Fe, bottom left O, Si, and the compositional elemental scan.

Appendix 7 NRVB cement cured at 25°C



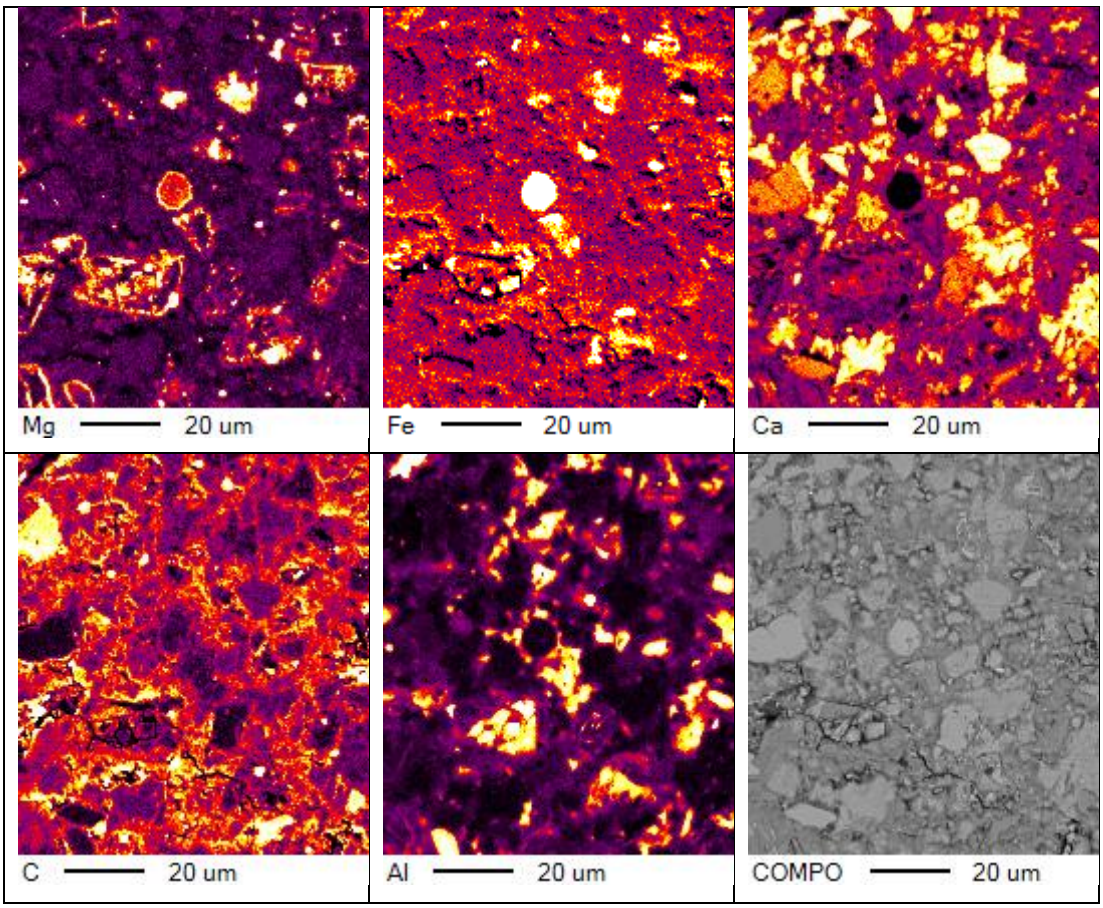
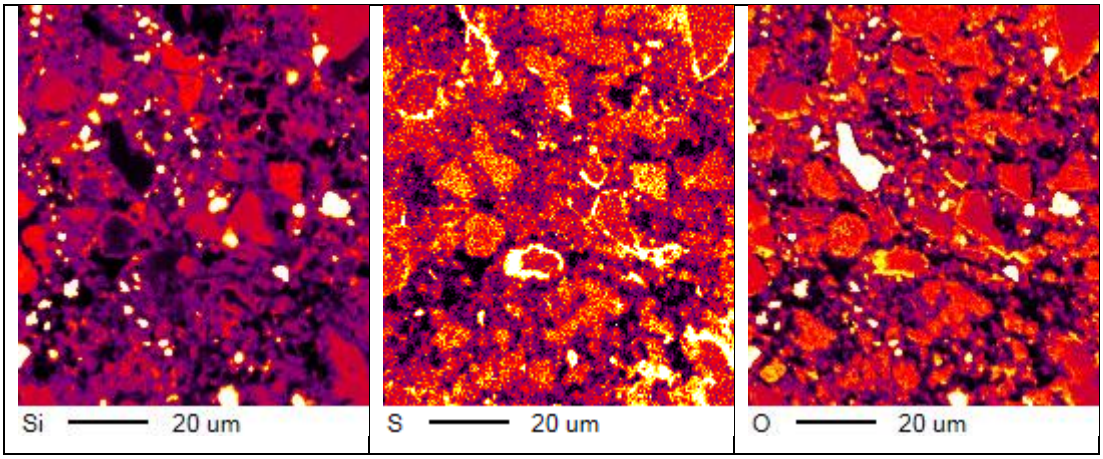


Figure 102: EMPA elemental scans for the NRVB cement cured at 25°C. Starting top left Al, C, Ca, middle left Mg, S, Fe, bottom left O, Si, and the compositional elemental scan.

Appendix 8 C:S 4 cement cured at 250°C



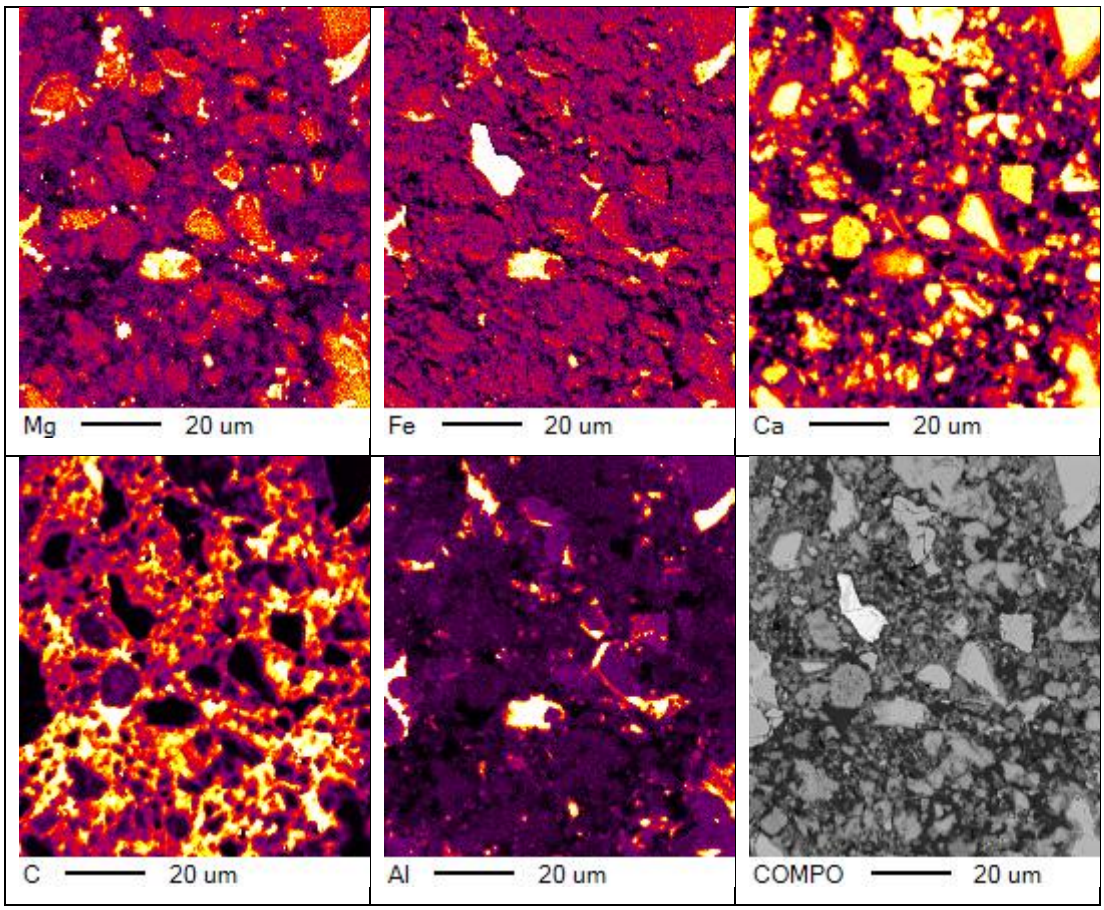
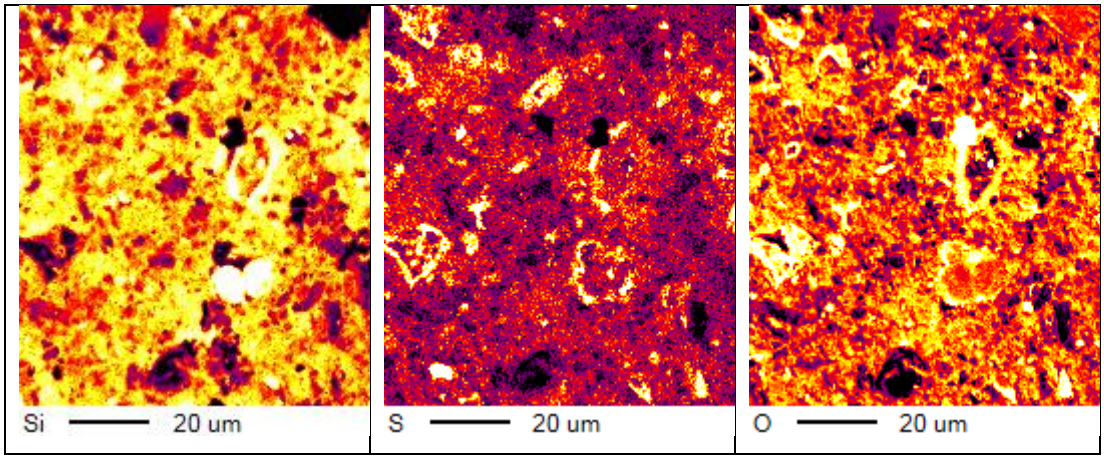


Figure 103: EMPA elemental scans for the C:S 4 cement cured at 250°C. Starting top left Al, C, Ca, middle left Mg, S, Fe, bottom left O, Si, and the compositional elemental scan.

Appendix 9 C:S 4 cement cured at 200°C



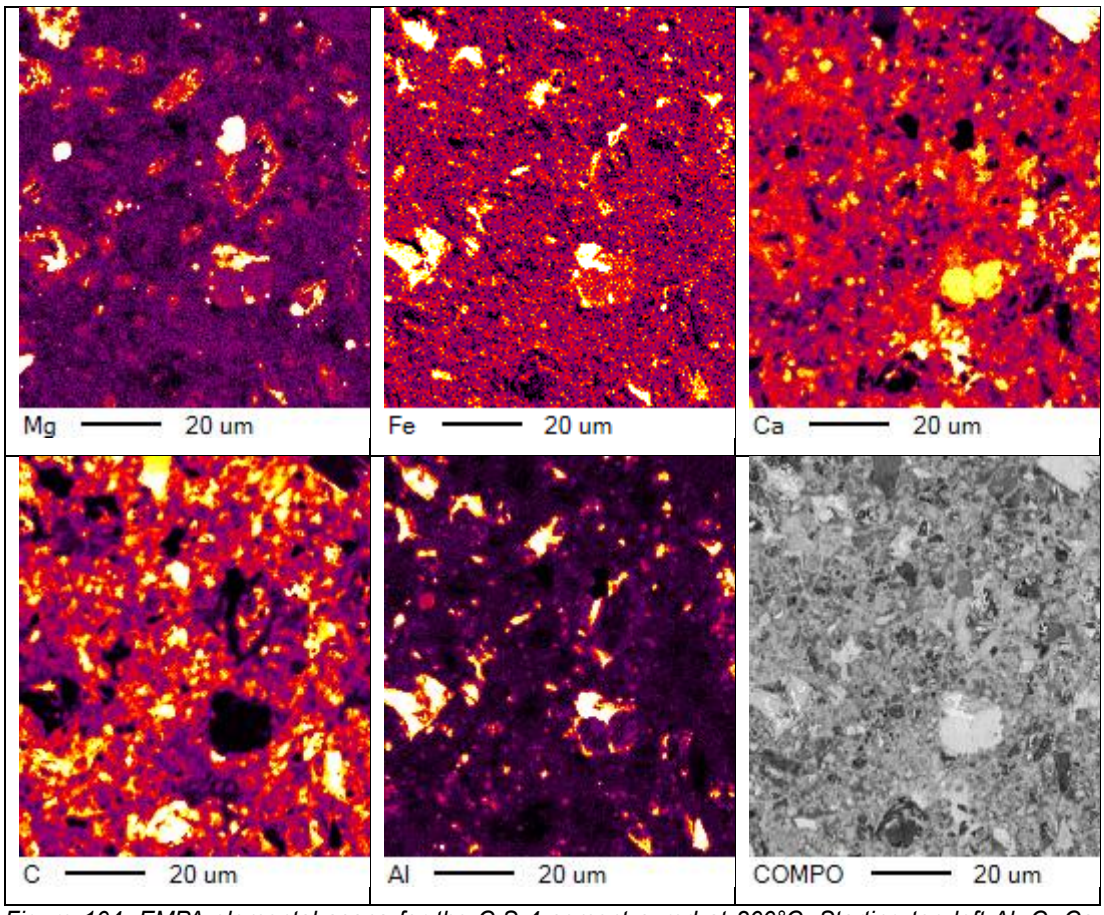
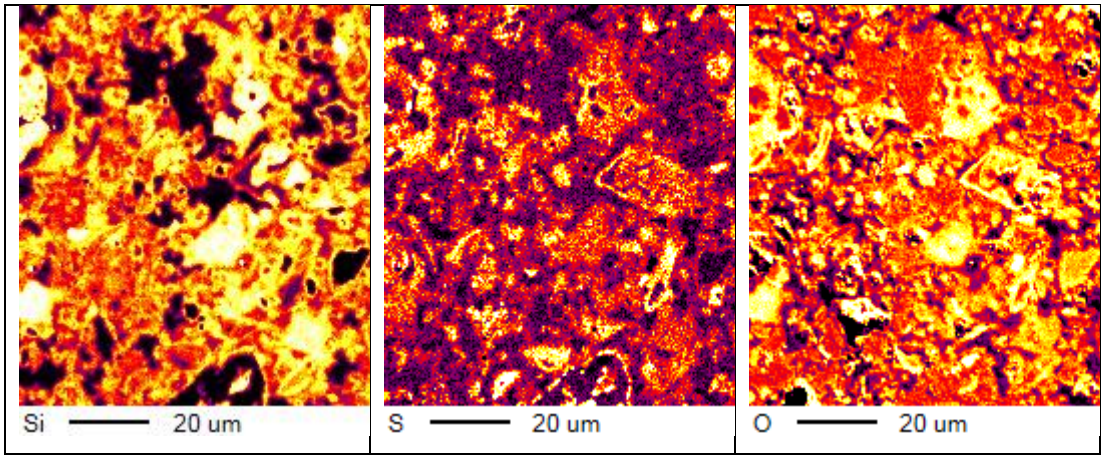


Figure 104: EMPA elemental scans for the C:S 4 cement cured at 200°C. Starting top left Al, C, Ca, middle left Mg, S, Fe, bottom left O, Si, and the compositional elemental scan.

Appendix 10 C:S 4 cement cured at 150°C



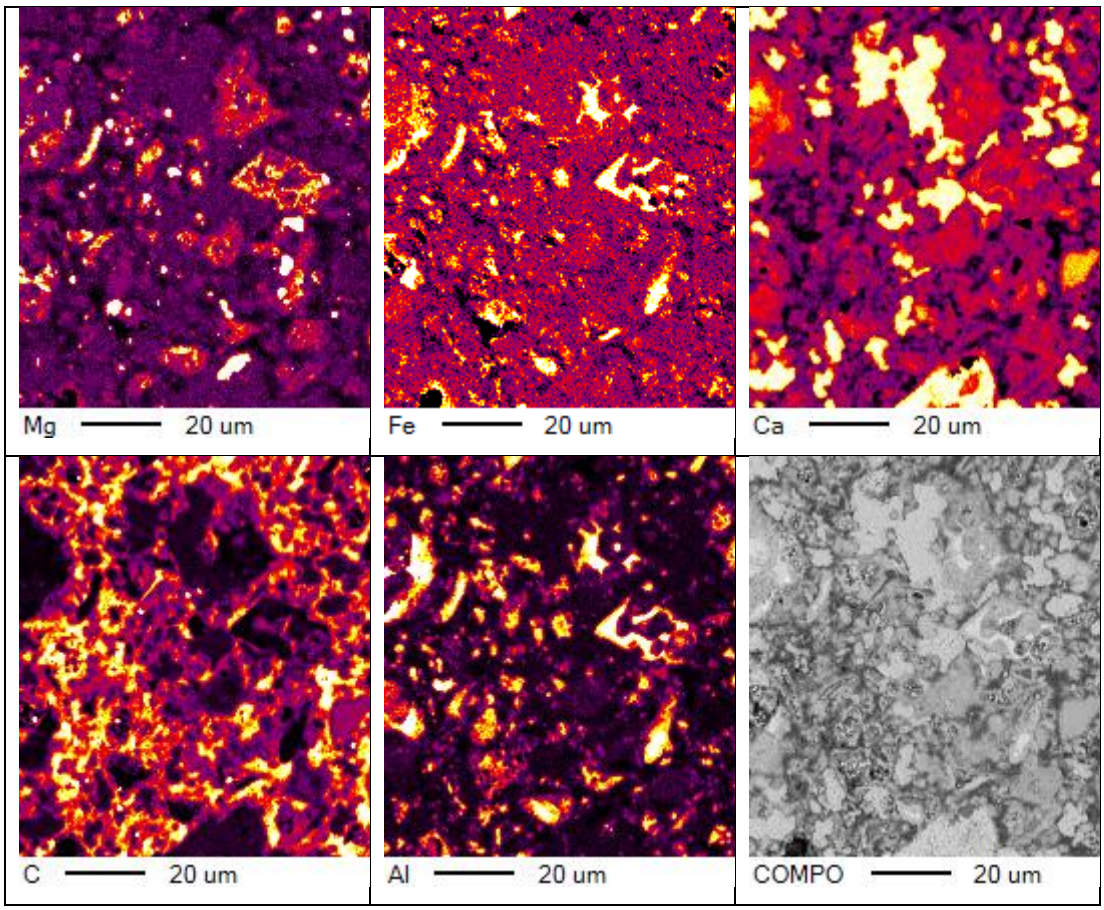
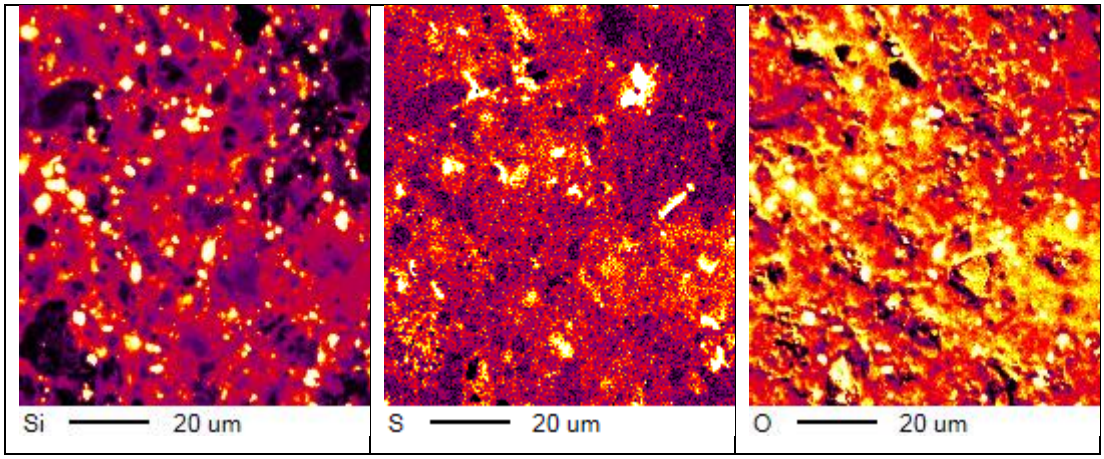


Figure 105: EMPA elemental scans for the C:S 4 cement cured at 150°C. Starting top left Al, C, Ca, middle left Mg, S, Fe, bottom left O, Si, and the compositional elemental scan.

Appendix 11 C:S 4 cement cured at 80°C



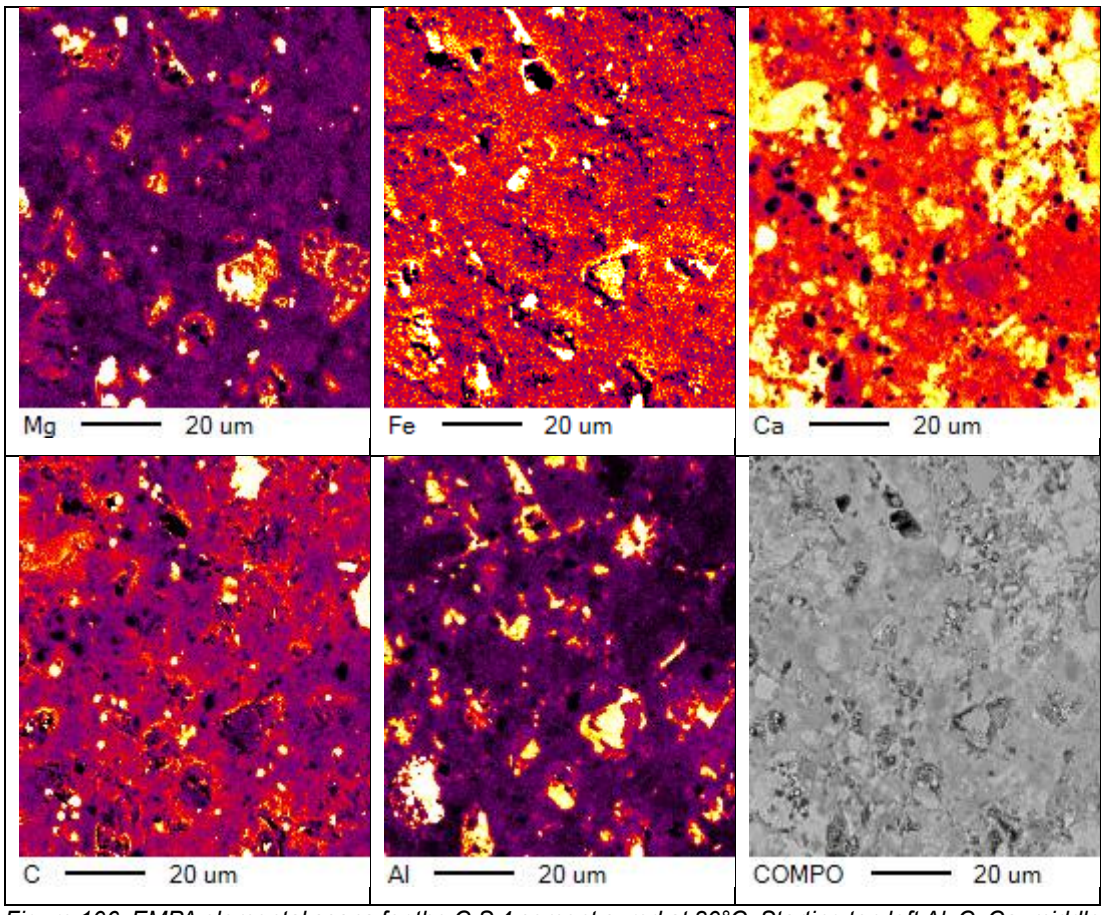
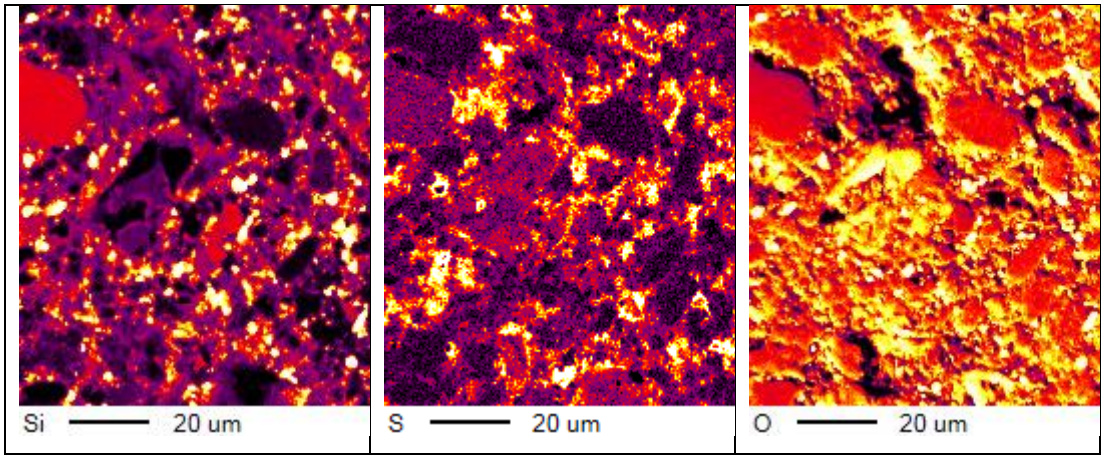


Figure 106: EMPA elemental scans for the C:S 4 cement cured at 80°C. Starting top left Al, C, Ca, middle left Mg, S, Fe, bottom left O, Si, and the compositional elemental scan.

Appendix 12 C:S 4 cement cured at 25°C



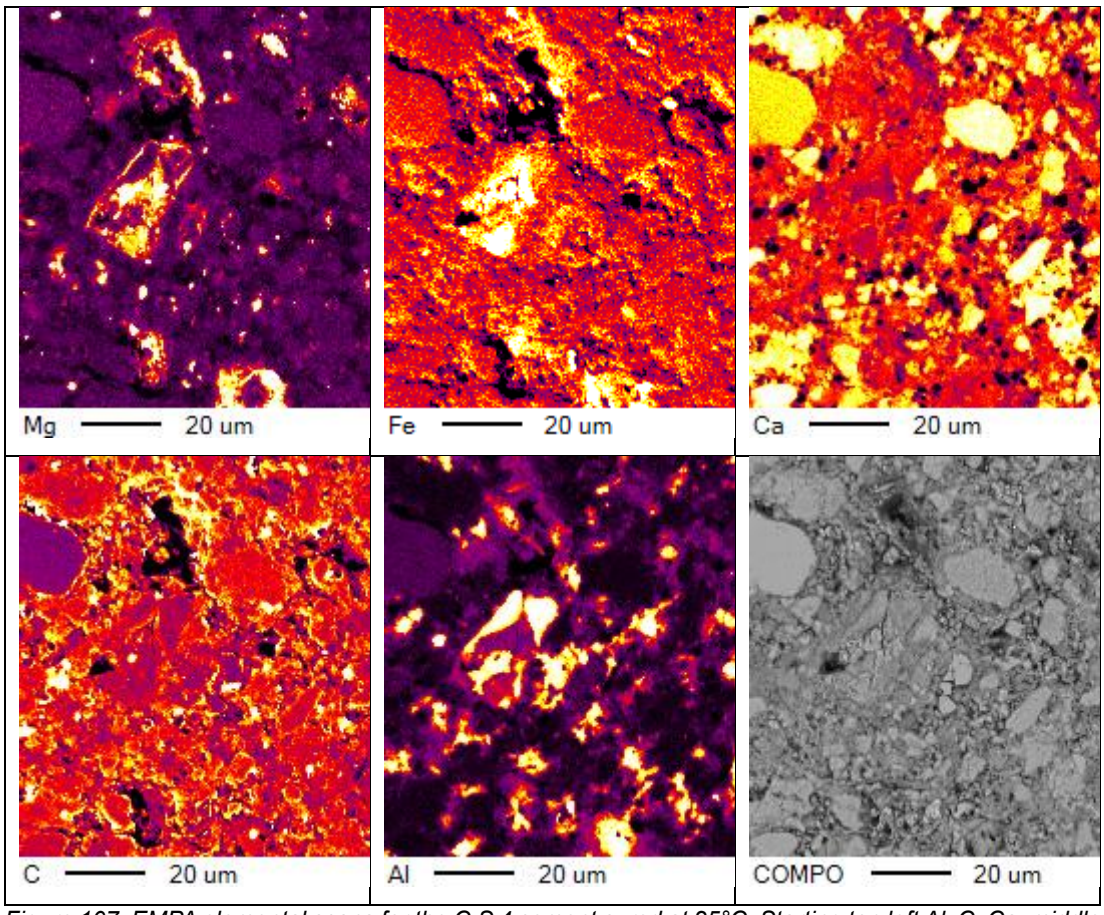


Figure 107: EMPA elemental scans for the C:S 4 cement cured at 25°C. Starting top left Al, C, Ca, middle left Mg, S, Fe, bottom left O, Si, and the compositional elemental scan.